INVESTIGATION OF WAKE STRUCTURE OF ISOLATED AND INTERSECTING FLAT PLATES

by

JAIME Arturo DONOSO Parra

Thesis submitted for the degree of Master of Philosophy in the Faculty of Engineering, University of London and for the Diploma of Imperial College.

SUMMARY

The aerodynamics of two thin flat plates intersecting at right angles and placed perpendicular to an air stream has been studied. Some basic measurements on an isolated flat plate, to investigate the effect of end-plates, have also been made.

It is found that for the isolated plates the inclusion of end-plates promotes two-dimensionality of both time-averaged shedding process and mean base pressure, and increases considerably the base suction ($-Cp_b$). An aspect ratio of about 20 appears to be important for transverse correlations of velocity fluctuations arising from vortex shedding. Below this value a high transverse correlation is produced, showing that end-plates are able to enhance the spanwise correlation of the shedding. Above this value they are unable to produce high correlations although base pressure is uniform across the span. Stream turbulence is shown to diminish the effect of end-plates on base pressure and it decreases the correlation too.

Measurements of mean pressure were made in the base of the intersecting members, together with hot-wire estimates of shedding frequencies, mean and fluctuating velocities across the span and velocity correlations in the near wake. These tests were conducted in smooth flow only.

The base suction in the region of the intersection is considerably lower than that on an isolated flat plate. Three dimensionality in the junction region manifests itself as a spanwise variation of base pressure. The Strouhal number remains constant across the span and shedding actually ceases close to the intersection. The wake around the intersection experiences no regular vortex shedding and its high base pressure bleeds air into the wake toward the end-plates.Thus, the largest aspect ratio intersection tested (AR=27) showed that the mean convection speed and

vortex spacing are lower (in the vicinity of the end-plates) compared with that of an isolated model presented by other workers (see references 8 and 18). Spanwise correlations showed vortex filament slightly staggered across the span, those near the intersection leading.

The investigation emphasised that the true "Isolated Intersection" is only likely to be reached for aspect ratios somewhat beyond 27.

ACKNOWLEDGMENTS

I should like to express my deepest gratitude to the head of the Department of Aeronautics of Imperial College London. Profesor P. R. Owen who made working facilities available to me and cooperated in the friendliest manner during the investigation.

I want particularly to thank my supervisor, Dr. R. Hillier for his lasting interest which is so very valuable to me.

To the technical staff, Mr. J. Coles, K. Sage, J. O'Leary and L. Eales, I am obliged for their valuable help.

I also owe a debt of gratitude to World University Service which gave me financial support.

CONTENTS

List of Symbols

a	Longitudinal vortex spacing
h	Width of plate
x,y,z	Streamwise,normal and spanwise coordinates
p	Presure
p_b	Base pressure
$p_{o\infty}$	Stagnation pressure
p	Static pressure in free stream
p_1	Static pressure at the contraction exit
p_2	Static pressure in the settling chamber
K	Wind tunnel calibration factor, $\frac{1}{2}\rho U_o^2 \;/\; (p_2 - p_1)$
l	Distance
l_w	Distance between hot-wires
l_p	Distance between end-plates
n	Vortex shedding frequency
U	Mean velocity in x-direction
U_o	Velocity of the free stream
U_n	Vortex velocity relative to free stream
$\sqrt{\bar{u}'^2}$	Root mean square of the velocity fluctuations
$\sqrt{\bar{u}'^2}/U_o$	Definition of the turbulence intensity
t	Time
AR	Aspect ratio, $l_p \;/\; h$, $l \;/\; h$
C_D	Drag coefficient
C_p	Pressure coefficient, $p - p_\infty \;/\; \frac{1}{2}\rho U_o^2$, $1 + \frac{p - p_{o\infty}}{(p_2 - p_1)\,K}$
C_{pb}	Base pressure coefficient
$\hat{C}_p$	Pressure recovery parameter, $(C_p - C_{pb}) \;/\; (1 - C_{pb})$
R	Bubble closure
Re	Reynolds number, $U_o h/\nu$
St	Strouhal number, nh/U_o
$\delta .995$	Boundary layer thickness

List of Symbols (cont)

t_c	Time per cycle
t_{max}	Lag time to get maximum correlation
τ	Time, tU_o / h
ν, δ, μ	Fluids properties, viscosity, density, kinematic viscosity
$R_{u_1u_1}(\tau)$	Autocorrelation function
$R_{u_1u_2}(\tau)$	Crosscorrelation function
$\rho_{u_1u_2}$	Correlation coefficient, $\overline{u_1u_2} / \sqrt{\overline{u_1'^2}} \sqrt{\overline{u_2'^2}}$
$\overline{u_1u_2} / U_o^2$	Correlated energy at shedding frequency

Subscripts

c	Denotes corrected for wind tunnel blockage
1, 2	1 for fixed hot-wire, 2 for moving hot-wire
o	Free stream conditions

Chapter 1

INTRODUCTION

-o-o-0-o-o-

Many engineering structures are of the lattice-type and as such may pose particularly difficult problems from the view point of designig for fluid dynamic loading because of the complex interactions at the junctions between adjacent bars or members. This involves interaction between shears flows and wakes, and depends on the distribution of the members, three-dimensional effects, etc. Data for estimating the mean fluid forces on lattice frameworks has been presented in the past (see reference 5). Such frameworks are normally constructed from flat-sided members, round sections or a combination of these shapes. Depending on the shape of the cross section of its members, the fluid forces on a lattice structure may or may not be influenced by changes in Reynolds number. There are two main methods for calculating the fluid forces acting on a framework. In the first (bulk method) the forces are obtained from "empirical" data relating the force coefficient for a single framework to its overall shape and solidity ratio, together with an allowance for the effect of shielding for downstream frames. The second method (summation method) involves summing the forces acting on individual members of the framework calculated from the force coefficient for separate members in two-dimensional flow (infinitely long member or structure) factored to account for the effect of shielding by other members, and adding to those forces the sum of the interference forces due to the joints.

Little is known about any of these features, so that there is a very strong case for developing a more fundamental understanding of them.

A different approach has been taken in this project. Here we consider simply the aerodynamics of a single interaction formed by two thin flat plates crossing at right angles, the whole assembly being placed normal to the stream. The flat plates have been chosen as the basic shape: partially because it provides some considerable advantages from the experimental viewpoint such as, fixed flow separation at the sharp edges, independance of Reynolds number effect, easy model making, etc; partially because it is representative of a common and practical shape. The intention is to study the effect of this gross disruption of vortex shedding; later projects could then increase the complexity of interference between components and progressively develop the understanding of lattice structure aerodynamics.

Although the general project in this dissertation is an investigation of intersecting bodies, it was decided that initial tests should concentrate on defining the basic data for an isolated flat plate normal to the stream. In particular it is necessary first to quantify the effects of end-plates or end-wall constraint, so that ultimately these could be separated from the effects of body intersection. It is well known that the objective of end-plates is to improve flow two-dimensionality, but it is clear from the literature that there may be some difficulty in defining precisely what is meant by this state. In principle, with end-plates a much more highly correlated motion across the span may arise. This will be dealt with in chapter 4.

Likewise, relatively little is known about the effects of turbulence intensity on isolated flat plates, which does present a particular form of basic wake interference in its own right. This feature has been the subject of our first investigation on wake interference.

In recent years there have been a number of interesting experiments on separated base flows, and in particular the use of various devices to interfere with the wake has produced revealing results. Bearman (45) and Wood (44) for example, have both examined the wakes behind blunt based aerofoils with either splitter plates or base bleed used to interfere with vortex formation. They found for example that with a sufficiently large bleed quantity the regular vortex street pattern disappeared and the base drag of the section was reduced to about a third of its value without bleed. From a comparison of base bleed and splitter plate results they concluded that the base pressure is dependant on the vortex formation distance but apparently independant of the method adopted to interfere with vortex formation (see Roshko (9) and Nash (35)). Castro (43) studied two-dimensional perforated flat plates placed normal to the stream. He showed that with porosity the base pressure and Strouhal number increase. If the porosity is high enough the sheddings stop completely. These are all factors of great relevance to the intersection study presented here. The only other study of an isolated intersection between bluff bodies placed normal to the stream is the work of Nakamura et al (62), who investigated the wake structure behind a crossed circular cylinders.

The preliminary results in the present study showed many points of similarity to results given by these (and others) workers in relation with the fundamental mechanism of wake interference. Since there is still much to be explained in the field of intersecting body flows, it was felt desirable to extend the scope of the test to attempt to gain more understanding of the nature of the flow.

It was planned to approach the problem in two phases. Firstly, surface pressures on the intersecting flat plates with end-plates would be studied, to assess the importance of end effects. Next mean and fluctuating velocity measurements could be made in the wake, particularly to obtain shedding frequencies, to determine how far the effects of the intersection persists along the span of this gross form of interference with the vortex shedding process.

Chapter 2

Experimental Apparatus

o-o-0-o-o

2.1 Wind Tunnels

The experiments were performed in the 0.91 m x 0.61 m (3'x2', small wind tunnel) and in the 0.91 m x 0.91 m (3'x3', large wind tunnel), both wind tunnels of the Department of Aeronautics, Imperial College of Science and Technology, London. The tunnels are both of the low speed and low turbulence closed-return type. The turbulence intensity level in the tunnels working section are 0.1 % in the small tunnel and 0.04 % in the large tunnel. The experiments were conducted in a range of stream velocities, from 12 to 30 m/s, which gives a Reynolds number range (based on body height) of $2x10^4$ to 10^5. The undisturbed tunnel speed was obtained from the pressure drop down the contraction, which was calibrated against dynamic pressure in the working section. The tunnel calibration was carried out with van Essen water manometers.

2.2 Bluff Body Models

2.2.1 Isolated Flat Plates

Two 2.54 cm (model 1) and one 5.08 cm (model 2) height flat plates with sharp edges bevelled at 45^o were tested spanning the tunnels at mid-height. Details of the models and pressure tapping are presented in figure 2.1. The thickness/height, t/h, of the models was 0.125. The pressure tappings were manufactured from steel tubing of internal diameter 1 mm running through the models and were used for mean pressure measurements only. Narrow-bore plastic tubing conected the pressure tapping tube to inclined Alcohol Multitube manometers. The models were simply supported in slots cut in the side walls of the working section by means of mounting blocks fitted outside of the tunnel's wall. The slots were carefully sealed with sellotape.

2.2.2. Intersecting Flat Plates

Two intersection geometries were achieved by crossing two flat plate models of type 1 at right angles. This was tested normal to the stream. Firstly, an "overlapped" junction was used , that is one model lying immediately in front of the other (see figure 6.1). The maximum aspect ratio based upon distance between end-plates/model height was 20 (this experiment was carried out in the small tunnel only).Secondly, the models were cut at mid-span to form the "intersecting" (halflapped) junction (see figure 6.5), with both vertical and horizontal separation edges lying in the same plane. This truly intersecting model was tested in both wind tunnels. The maximum aspect ratio was 27, which was obtained in the large tunnel only. A general view of the experiment set up is shown in figure 2.2

2.3 End-Plates

Three sets of round edged end-plates with rounded corners were tested on the isolated models in order to remove the three-dimensional effects of the growing tunnel wall boundary layer. This effect has long been recognised but little detailed work has been done on the resulting body-wall interference problem. However, it still remains unclear as to which type of end-plate best improves the reasonably good 2-D flow produced with sharp edged bodies. The three sets of end-plates were made of aluminium sheet of 1.58 mm (1/16") thickness. They were rigidly attached to the models by means of light perpex adjustable sliders (see figure 2.3). More details including the dimension of the end-plates and pressure tappings along their centre line are provided in figure 2.3, 2.4 and 2.5 respectively. The end-plates were mounted on each model at a minimum distance of 5.08 cm from the tunnel's wall, so that they were just outside of the tunnel wall boundary layer (see figure 3.5). To prevent any flow of air between the end-plates and the model, the small gaps were sealed with plasticine and sellotape.

2.4 Instrumentation

A large part of the experimental work, involved the measurement of mean and fluctuating velocity in the wake. This was done by means of constant temperature hot-wire anemometers. A hot-wire probe with a 5 micron platinum wire as a sensor was used in conjuction with Disa M01 and D01 series anemometer units. The probe was mounted in the "slide rule" type traverse gear of the wind tunnels. The traverse mechanism was used to position the probe in the streamwise and spanwise direction of the models. A Disa voltmeter, with variable damping, was used to measure mean voltages and a Disa RMS meter measured the variance. Statistical properties of the velocity signals were obtained through a Hewlett Packard 3721A digital correlator; the auto and cross correlation being particularly useful "quick-look" facilities. An additional facility, for obtaining permanent hard copy recordings of the signal, was the four channel "brush" pen recorder. The vortex shedding frequency was measured with a Muirhead wave analyser and directly from recorded autocorrelation functions.
Other instruments used in the experiments are listed below:
Oscilloscope, Fixed Gain Amplifier and 30 V Power Supply Units. Figure 2.2 shows the set up of the instrumentation together with the intersecting model in the large tunnel.

Chapter 3

EXPERIMENTAL TECHNIQUES AND DATA REDUCTION

o-o-0-o-o

3.1 Wind tunnel calibrations

A freestream calibration of the wind tunnels was performed for both a uniform stream and with the grids present in the tunnel. The dynamic pressure was measured at several positions along the tunnel centre line using a pitot static probe, this was done for several values of $p_2 - p_1$, where p_2 is the static pressure in the settling chamber and p_1 is the pressure measured at the contraction exit. The values of $q = p_\infty - p_{0\infty} = 1/2 \rho U_0^2$ at each position were also measured with a van Essen water manometer. Calibration graphs of the dynamic pressure q against $p_2 - p_1$ were then drawn for smooth and turbulent flows. Figure 3.1 shows the tunnel calibration in smooth flow and figure 3.2 is the grid B calibration. Non-uniformities where observed for calibrations close to the grids, which are due to the probe position with respect to the mesh. This is shown for grid B test in figure 3.3.

Table 3.1 below shows the calibration factor $K = q/(p_2 - p_1)$ for both smooth and turbulent flows at the position to be occupied by the model in the working section along the tunnels.

Small Tunnel			
Position downstream	0.83 m	1.30 m	2.46 m
Smooth Flow	1.012	1.030	1.037
Grid A	0.960	0.910	0.890
Grid B	0.970	0.960	0.970
Grid C	1.020	1.020	1.028
Large Tunnel			
Position downstream	1.50 m		
Smooth Flow	1.055		

Table 3.1 Calibration of Dynamic Head along Working Section
(all measurements from mid-plane of Grid)

Test on isolated models were run for a range of grid conditions (small tunnel only) and these are given in table 3.2 for three model test positions along the working section. Other intensities will be specified where necessary in the text. Figure 3.4 shows the corresponding graphs of turbulence intensity along the working section.

		Grid A	Grid B	Grid C
Mesh size, M, (cm)		15.24	7.62	3.18
Test position	Intensity %		6.80	3.50
0.83 m	L_x cm		3.05	1.83
1.30 m	Intensity %	9.50	4.90	2.60
	L_x cm	5.72	3.62	2.10
2.46 m	Intensity %	5.70	3.10	1.50
	L_x cm	8.00	4.65	2.51

Table 3.2 Test Conditions

3.2 Evaluation of mean pressure coefficient Cp

The contraction and working section of the wind tunnel is shown below.

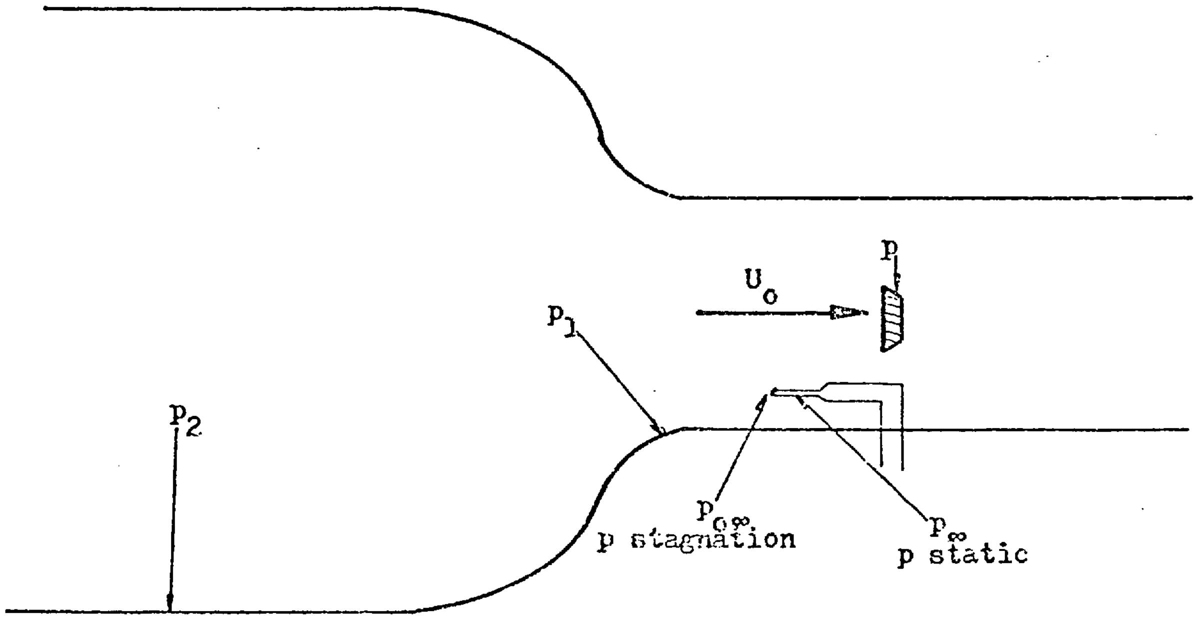

With the notation in the sketch the desired pressure coefficient Cp is defined as

$$Cp = \frac{p - p_\infty}{1/2 \rho U_o^2} \qquad (3.1)$$

Equation (3.1) can be written as

$$Cp = \frac{p - p_{o\infty}}{1/2 \rho U_o^2} + \frac{p_{o\infty} - p_\infty}{1/2 \rho U_o^2}$$

with the definition

$$\begin{aligned} 1/2 \rho U_o^2 &= (p_2 - p_1)\, K \quad \text{and} \\ 1/2 \rho U_o^2 &= p_{o\infty} - p_\infty \end{aligned} \qquad (3.2)$$

$$Cp = 1 + \frac{p - p_{o\infty}}{(p_2 - p_1)\, K} \qquad (3.3)$$

where p_∞ and $1/2 \rho U_o^2$ are the static and the dynamic pressure at the location of the center section of the model in the empty wind tunnel and $p_{o\infty}$ is the stagnation pressure which is recorded at the central tapping on the front face of the model*, p is the pressure at the surface of the model and p_2 and p_1 are static pressures at the begining and the end of the wind tunnel contraction respectively.

3.3 Boundary layer thickness

In the absence of the model the mean velocity profile was measured at the rearmost model position (x = 2.46 m) in the small tunnel. These profiles are shown in figure 3.5 for the smooth flow and for grid B (Turb. Inten. 3.1 %) respectively. The velocities are shown non-dimensionalized with respect to the maximum velocity on the traverse, U_e, measured in the tunnel centre line. The tunnel wall boundary layer thickness, $\delta_{0.995}$ is taken as the position for $U/U_e = 0.995$.

* (This compared within better than 1% of q_∞ with the reading given by a pitot tube)

3.4 Oil flow visualisation

The surface oil flow technique used in this investigation consisted in applying to the model surface a thin coat of paint. The oil mixture used was a suspension of Titanium dioxide in Speedivac oil (or paraffin), with Oleic acid acting as dispersant. This layer of paint flows under the combined action of the gravitational,friction and pressure forces. The air flow spreads the mixture along the surface streamlines (shear stress lines) and a streaky deposit of the powder remains marking the the flow direction after the tunnel has been stopped. The optimum mixture for any speed was found by trial and error.

3.5 Hot-wire data reduction

The hot-wire is assumed to respond to normal velocities only, i.e. lateral cooling is considered to have a negligible effect. The wire is cooled similarly, whatever the direction of the normal velocity. It is an inappropiate instrument for a recirculating flow situation, and its use in the wake was restricted to positions outside the formation region immediately behind the body.

3.5.1 Velocity fluctuations

A single wire, in a fluctuating velocity field, carried with a uniform mean flow, respond to a velocity vector, with modulus, $\left[(\bar{U} + \bar{u}')^2 + \bar{v}'^2\right]^{1/2}$, if placed in the horizontal plane normal to the U (mean flow) direction. $\left[(\bar{U} + \bar{u}')^2 + \bar{v}'^2\right]^{1/2} \simeq \bar{U}(1 + \bar{u}'/\bar{U})$, for small turbulent intensity.

Using a simple King's Law, for the hot-wire response,

$$E^2 = A + B\bar{U}^n(1 + \bar{u}'/\bar{U})^n$$

i.e. $\bar{E}^2 + 2\bar{e}\bar{E} + \bar{e}^2 = A + B\bar{U}^n(1 + n(\bar{u}'/\bar{U}) + \text{-----------})$

where $E = \bar{E} + \bar{e}$

Equating like orders,

$$\bar{E}^2 = A + B\bar{U}^n$$

$$B = (E^2 - A)/\bar{U}^n$$

$$2\bar{e}\bar{E} = B\bar{U}^n n(\bar{u}'/\bar{U})$$

Hence,

$$\frac{\sqrt{\bar{u}'^2}}{U} = \frac{2}{n}\,\frac{\bar{E}^2}{\bar{E}^2 - A}\,\frac{\bar{e}}{\bar{E}}\text{, is obtained}$$

Which expresses the linearity of voltage to velocity fluctuations, for small intensities.

The hot-wire was calibrated (for A and B) in the empty working section, with an assumed exponent $n = 0.45$ (see appendix B).

Thus we can measure velocity fluctuations as a fraction of the local mean velocity without measuring the latter directly.

3.5.2 Correlations

The auto and cross correlation functions, $R_{u_1u_1}(\tau)$ and $R_{u_1u_2}(\tau)$ have been defined in Appendix C (see formulas C2 and C4). They are, respectively, Fourier transform pairs. The commonly used and physically understood correlation coefficient $\rho_{u_1u_2}(0)$ (unlagged coefficient) was calculated from equation (C1). The maximum correlation coefficient was calculated from

$$(\rho_{u_1u_2})_{max} = \frac{(\overline{u_1u_2})_{max}}{\sqrt{\bar{u}_1'^2}\sqrt{\bar{u}_2'^2}}$$

(see equation (C5) in appendix C). From the first maximum of $R_{u_1u_2}(\tau)$ i.e. $(\overline{u_1u_2})_{max}$ (for τ increasing) at $t = t_{max}$ it was estimated the phase angle between the two signals (see appendix C). Finally, the correlated energy at shedding frequency was calculated from equation C7 of appendix C.

CHAPTER 4

Experiments on Isolated Flat Plate

Aspect Ratio and End Effects

-o-o-0-o-o-

4.1 Introduction

This thesis is a study of the aerodynamics of an intersection between two flat plates, which is a particularly gross form of interference with the vortex shedding process. It is necessary to start this work, therefore, by defining clearly the datum case of an isolated flat plate placed normal to a non-turbulent stream. The earliest reliable experiment on a flat plate appears to be that of Fage and Johansen (7, 1927). Their results are shown in table 4.1 below compared with the measurements of Fail et al (8), Nakaguchi et al (19), Davies (51) and others. Fage and Johansen's results have been corrected for the effects of wind tunnel blockage by Maskell (10). The plate Fage and Johansen used was flat on the front face and the rear face was slightly tapered from the centre (where the thickness was 3 per cent of the width) towards the sharp edges. The plate was mounted with small clearances between its ends and tunnel walls. No end-plates were used and the aspect ratio was 14., so that it may be influenced by three-dimensional effects. Fail et al's (8) model was mounted on the upstream end of a rod; thus the model did not span the wind tunnel, having free ends, and their results were highly influenced by three-dimensional effects. The plate of Arie and Rouse's (22) experiment spanned completely the tunnel width having a thickness/width ratio of 0.083 and bevelled at an angle of 60° along the edge on the rear side. They did not use end-plates so that their results may be also influenced by three-dimensional effects due to the wind tunnel wall boundary layers. Arie and Rouse's results have been corrected for the effects of wind tunnel blockage by Maskell (10). The only data found for a flat plate with end-plates is that of Davies (51).

Author	$-C_{pb}$	C_D	S_t	AR	t/h	End-Plates	Solid Blockage	Corrected	Model end
Fage & Johansen	1.38 1.09	2.13 1.87	0.146 0.155	14 14	0.03 0.03	no no	0.071 0.071	no yes	Terminated at tunnel wall
Fail et al	0.68	1.50	0.109	20	0.16	no	0.015	yes	S_t uncorrected free ends
Davies	1.24		0.142	15.8	0.25	yes	0.055	yes	Across tunnel wall
Arie & Rouse	1.36	2.1		12	0.083	no	0.083	no	"
Nakaguchi et al	1.25	2.0	0.135		0.25	no		no	"
Bearman & Trueman	1.28	2.1	0.140	28	0.20	no	0.070	yes	"

Table 4.1 Data on Flat Plates

His model spanned the (0.91 m.square) wind tunnel, at mid-height. The end-plates used were made of light perspex rigidly attached to the model, at about 5.0 cm from the tunnel wall. The plate Davies used was flat on the front face, having a thickness/width ratio of 0.25, its depth was due to the presence of stiffening ribs on the rear face. The separation of the end-plates was about 16 body widths (i.e. AR=16). Although the design of his end-plates was rather arbitrary, it seems likely that he approached a more two-dimensional flow by removing the three-dimensional effects of the growing tunnel wall boundary layer. His results are shown in figure 4 compared with other bluff bodies fitted with end-plates too.

The work by Nakaguchi et al (19) has shown that the base pressure Cp_b and therefore the drag coefficient C_D of a rectangular cross-section cylinder in smooth flow, with one face normal to the stream is extremely sensitive to changes in the thickness ratio t/h. They showed that Cp_b for a thin flat plate is -1.25 ($C_D \simeq 2$) and Cp_b decreases to a minimum value of about -2.2 ($C_D \simeq 3$) as t/h is increased to 0.6. Their measurement of base pressure and drag coefficient are reproduced in figure 4.1 together with those of Bearman and Trueman (18). In this latter reference it is argued that with further increases in t/h the rear corners of the rectangular section begin to interfere with the highly curved free shear layer. Thus, the interference (afterbody) weakens the strength of the shed vortices, consequently the base pressure increases (drag falls) and therefore "flat plates" will show a thickness effect.

Lateral velocity correlation on flat plates (with end-plates) has been investigated by Davies (51) and on rectangular sharp-edged cylinder t/h = 0.2 without end-plates by Bearman and Trueman (18). They have found that the signals from two hot-wires are highly correlated across the span.

Their results are shown compared with various other bluff bodies in figure 4.2 taken from reference (51). It can be seen that the signals are better correlated for thin bodies (i.e. low t/h). Much work has been done on square section cylinders. Vickery (38), Lee (30), Obasaju (53) and others have investigated the spanwise correlation of fluctuating pressures on square cylinders; their results are presented in figure 4.3. The square section shows a steady decrease of correlation with transducer separation and that is clearly lower than the flat plate case.

It therefore appears that mean base pressures and shedding frequencies are known fairly reliably already, and that these can be used as a check on our own experimental accuracy. It also appears that relatively little is still known about end effects; including the importance of end-plate design, model aspect ratio and shedding correlation across the span which are all factors of great relevance to the intersection study. These features therefore were the subject of our first investigation. Because it could also be conducted with relatively little difficulty, and also because it does present a particular form of interference with the wake, Chapter 5 will investigate the effects of stream turbulence on the isolated flat plate.

4.2 Development and use of end-plates

Although it is commonly accepted that end-plates should be used to inhibit three-dimensional effects in nominally two-dimensional bluff body flows, there are in fact no absolute rules governing their precise design. Clearly they must be located sufficiently far inboard from the tunnel wall, and protrude far enough forward that the model is fully isolated from the effects of tunnel wall boundary layer.

Downstream of the model the end-plates must at least isolate the "cavity region" of the model from the corresponding region outboard of the end-plates. Probably they should also extend sufficiently far downstream as to include full pressure recovery (and for this reason pressure measurements were also made on the end-plates during the present tests) although in practice this could lead to unnecessarily long designs. Stansby's (13) experiments on a circular cylinder (see figure 4.4) have shown that end effects influence the flow for considerable spanwise distances, and he has noted that a constant pressure - or near constant pressure - across the base region does not identify a flow as being uniquely two-dimensional; he obtained nearly constant distributions, but at different levels, for tests with and without end-plates. End-plates have a clear influence on vortex shedding. They can produce more highly correlated shedding across the span, particularly at low aspect ratios where there is strong enhancement (Keeffe (25), Graham (17)).

Lee (32) suggests that two-dimensional bodies with sharp-edged separations are the least critically dependent on end conditions, his tests on square-section cylinders showing little change between those with and without end-plates. Although the fixed separations line removes one obvious source of three-dimensionality, it would be surprising if bleed into the low pressure cavity region near the tunnel wall were to be unimportant or somehow only confined within the immediate vicinity of the tunnel wall. Lee's end-plates were very small, however, by any of the criteria previously suggested, and it is possible that they were too small to have any real effect. This is especially likely since the earlier work of Cowdrey (14), on the same geometry, shows end-plates to be essential (see figure 4.5).

He found that they could reduce base pressures by 0.1 or more in Cp_b, a conclusion supported by Obasaju (16) in a later work. Cowdrey also noted that under some circumstances a gross breakdown of the flow could occur if the end-plates were too short to isolate properly the cavity region.

4.2.1 Use of short end-plates

The first end-plates tested are shown schematically in figure 2.3 (End-plates A). These are close to Stansby's dimensions (for a circular cylinder in his case) and although in the event they transpired to be too small in the downstream direction it appeared a reasonable decision at the time. Because it was also necessary to change the model aspect ratio, or end-plate separation, adjustable sliders (shown in figure 2.3) on the outside of the end-plate enabled them to be moved along the model. The tunnel wall boundary layer thickness ($\delta_{0.995}$) was some 50 mm at the rearmost test position and the end-plates were never operated closer to the wall than 53 mm, which corresponds to maximum aspect ratios of 20 and 36 for model 1 (horizontal and vertically respectively) and 10 for model 2 in the 1.02 m x 0.61 m wind tunnel (3' x 2'). Later aspect ratio tests (figure 4.9) indicate no effect of wall proximity in this case.

Figures 4.6, 4.7 and 4.8 compare spanwise base pressure distributions for tests with and without end-plates A at maximum available aspect ratios. The end-plates produce a significant effect both reducing the base pressure and giving a much more constant distribution across the span. It is noticeable that although the spanwise pressure changes are weak - indeed strictly they are barely significant compared with the experimental accuracy - the adjustment in base pressure level appears almost out of all proportion to these variations.

Clearly weak spanwise gradients still indicate significant ventilation of, or crossflows within, the bubble. Obviously figures 4.6, 4.7 and 4.8 cannot be compared precisely, because of the different effect of blockage and aspect ratio, and for this reason further tests were made to record the sensitivity of base pressure to aspect ratio or end-plates spacing as shown in figure 4.9. Provided that the aspect ratio was above some critical value (about 5.5 for model 1 and 3.5 for model 2) the pressure changes at mid-span were weak. Below the critical aspect ratio, however, there was a breakdown of the flow. Vortex shedding (as detected by a hot-wire) ceased and the base pressure rose by about 1.0 in Cp_b. The demarcation between the two regimes was fairly abrupt, separated only by a narrow band (as indicated in figure 4.9) in which the flow was bistable, switching intermittently from one to the other. Pressure distributions on the end-plates confirmed the gross alteration in wake behaviour, figure 4.10 comparing the low pressure, short bubble characteristic of strong shedding with higher pressure, long bubble for aspect ratios below critical. The latter case agrees fairly closely with the flat plate normal to the stream/downstream splitter plate combination tested by Arie and Rouse (22). The end-plate distributions of figure 4.10 show that pressure recovery is nowhere near completed by the trailing edge once shedding has ceased so that bubble closure will not have occurred, and wool tuft visualisation confirmed that there was a massive inflow into this wake region from outside of the end-plates at the trailing edge. The precise flow developments which lead to flow breakdown were unclear, since there was no evidence of significant changes in base pressure prior to this condition either inside or outside of the end-plates. The initiator of the breakdown transpired to be the slider used to move the side plate along the model, since near the critical aspect ratio the flow became very sensitive to disturbances placed just outside the end-plates.

Although probably not of immediate practical interest some curious features of the flow were noticed. It appeared that with aspect ratios well below the critical value strong shedding could be restarted simply by placing an obstacle some distance (approximate 6h) downstream of the plate. Possibly the long bubble associated with the flow breakdown extended this far and was then able to convect disturbances upstream to the base region and stimulate shedding again. Although such a feedback mechanism may be of interest to the general problem of complex lattice structures it was not further studied here.

Clearly the "short" end-plates are inadequate, at least for low aspect ratio tests. It also became evident that small obstacles placed on the outside of the end plates could only interfere with the central flow (near the critical AR) if they were located at its trailing edge within some 2h of the centre line, that is within the likely cavity width. Thus it is probably only strictly necessary to lengthen the end-plates. Two designs were used with the plate length nearly doubled, as shown in figures 2.4 and 2.5 respectively, results being indistinguishable between the two for all subsequent tests.

4.2.2 Use of long end-plates

Figure 4.11 now compares the pressure distributions with this new design - end-plates B. Again the mean pressure level has been further reduced and within measurement accuracy the pressure is constant across the span. The figure provides an interesting reminder that weak lateral gradients of pressure do not imply in any way that the mean level is close to a "two dimensional limit" if one can even be uniquely defined; end effects are able to penetrate large lateral distances.

Figure 4.12 shows the effect of aspect ratio, or end-plate spacing, on base pressure with these large end-plates. There is now no flow breakdown over the range tested but there is a "slight" reduction in base pressure as the aspect ratio is reduced. This may reflect an increased coherence of the shedding at the lower aspect ratios which will be discussed further in the next section. It might also result from experimental factors such as an increasing contribution to the overall blockage (from the relatively higher pressure) flow over the model sections external to the end-plate.

Henceforth all references to end-plates and base pressures will refer to the end-plates B (long end-plates) unless it is expecified so. It should be noted that further increase in end-plate size has no further effect on base pressure.

4.3 Measurement of shedding frequency

The vortex shedding frequency was measured both on the Muirhead wave analyser and on the Hewllet-Packard correlator from the output of a hot-wire anemometer. The hot-wire probe was positioned off the model centre line, thus the trace from it was virtually a sine wave and one cycle represented the passage of one vortex now springing from the sharp edge of separation of the model. A hot-wire position which gave a strong shedding signal was found by trial and error to be $x = 1h$, $y = 1h$. A very high degree of agreement was found between the values of St obtained from the Muirhead wave analyser and from the Hewllet-Packard autocorrelograms.

Figure 4.13 shows the Strouhal number, defined as $St = nh/Uo$ (where Uo is the measured free stream velocity, h is the frontal face flat plate width and n is the shedding frequency) plotted against aspect ratio.

The figure shows a range of values of Strouhal number between 0.143 and 0.149 (uncorrected for blockage). It should be noted that there is no discernible variation of Strouhal number with end-plates separation. It was also observed that the amplitude of the signal from the hot-wire suggested that the vortices were similarly strong for tests both with and without end-plates. No significant variation of Strouhal number either with plate width or aspect ratio was found. It appears then that end-plates separation do not affect vortex shedding frequencies. The figure also shows that the results are in good agreement with those of Fage and Johansen (7), Fail et al (8) and the rectangular section flat plate ($t/h = 0.2$) of Bearman and Trueman (18).

The Strouhal number was measured over a range of Reynolds numbers too, $2 \times 10^4 < Re < 10^5$. St did not show any significant variation over the range of Re for the different aspect ratios considered. This confirms the findings of Castro (43) and Davies (51) for flat plates in smooth flow.

4.4 Corrections due to blockage effect

In order to compare the pressure data on different sizes of flat plates, the results were corrected for blockage effects. Two correction methods were compared. The method of Maskell (10) and the method of Allen and Vincenti (12), which are discussed in more detail in Appendix A.

The model configurations discussed earlier provide three possible blockage ratios and figure 4.14 shows the corrections of base pressure, Cp_b, at mid-span for these cases. Although aspect ratio effects have been shown to be weak the comparisons are all made at an aspect ratio of 10 by suitable positioning of the end-plates. It can be seen that the method of Maskell gives the best results, since the corrected data collapse with the measured values extrapolated to zero blockage (i.e.

assuming a linear variation of Cp_b -measured value- with S/C -blockage-). This is in agreement with the conclusion of Fackrell (11) who found that for a normal flat plate Maskell's corrections were best below 0.1 solid blockage. Although Allen and Vincenti's method showed a good agreement within the experimental accuracy the corrected data did not collapse at zero blockage and as it was reported in reference 11, it appears to under correct at these lower solid blockage ratios. In the light of these experimental evidences the Maskell correction method has been used here.

Figure 4.15 shows the corrected spanwise pressure distribution by the method of Maskell for fixed aspect ratio as indicated. It can be clearly seen that the data collapse at Cp_{bc} of about -1.24 for these three different blockage ratios.

Henceforth all references to corrected base pressures will refer to the Maskell method.

4.5 Measurements of lateral correlations of shedding in the near wake

The influence of end-plates on the shedding process can be clearly seen by measurements of lateral velocity correlations. For convenience these tests were usually confined to model 1, with the hot-wire located at $x = 2h$, $y = 1.5h$ where a fairly clear shedding signal was obtained.

4.5.1 Correlation without end-plates

Two lateral correlations for the no end-plates case are shown in figure 4.16. In one the fixed hot-wire was placed 3h (i.e. 7.62 cm) from the tunnel wall whilst the moving wire was traversed across the span;

in the other the fixed wire was located on the tunnel centre line (℄) and produces a generally higher unlagged correlation. Looking first at the correlations taken at zero time delay, the flow is clearly not two-dimensional with regard to the space correlation of the shedding process, despite the nearly uniform base pressure distribution shown in figure 4.11. The correlations of figure 4.16 also show a slight negative lobe at the larger wire separations, which indicates a change in the phase relationship of the shedding across the span. This is seen more clearly from the typical space-time correlations of figure 4.17 where the shedding becomes progressively delayed as the tunnel walls are approached. Figure 4.18 presents t max, the time delay to maximum correlation (see Appendix C), which reaches a maximum of about 30% of the shedding cycle for the largest wire separation tested. Because of the stagger, or retardation, of the mean vortex line a useful indication of the coherence of the filament is given by the maximum correlation ($\rho_{u_1 u_2}$ at t max) rather than the zero time delay value. These values are also shown in figure 4.16, where there is now much less difference between the two fixed wire positions.

4.5.2 Correlation with end-plates

With end-plates (only end-plates B were tested) there is a much more highly correlated motion across the span without the strong retardation noticed above near the tunnel walls. Figure 4.19 shows that for an end-plates separation of 20h the correlation no longer falls to zero but appears to asymtote to values in the range $0.4 < \rho_{u_1 u_2} < 0.5$. Davies' (51) data for a flat plate (t/h = 0.25) indicates a similar trend, although both his aspect ratio (AR = 15.8) and his range of wire separations (up to 8h) are less than here.

The effect appears to be similar to that noted by (say) Graham (17) and Keefe (25), although in their cases for aspect ratios (based on model width, h) considerably less than those used here (Graham's model AR = 4 and Keefe's model AR = 5). Even using an aspect ratio based upon wake widthness, rather than model widthness, the present geometry appears able to correlate the shedding at higher spans than these previous tests. Within the experimental accuracy there was virtually no discernible phase lag in shedding across the span and the shape of the correlation was independent of fixed wire position indicating a highly two-dimensional behaviour of the time-averaged shedding process.

This coherence was not due to any locking-in between the vortex shedding and model or end-plate vibration: firstly, the correlations were unchanged with alterations in wind speed; secondly, accelerometer measurements showed no significant vibration at the shedding frequency, twice shedding frequency or other harmonic, the principle end-plate motion (with amplitude < 3 mm) being normal to its plane at a natural frequency which was well separated from that of the shedding; finally, additional stiffening of the model/end-plate assembly produced no effect upon the velocity correlations.

Larger aspect ratios or end-plate separations were unable, however, to produce such high correlations. With an aspect ratio of 34 and 27, figure 4.20 shows that the correlation falls to zero by a wire separation of 14h followed by an extensive, but nonetheless weak, negative lobe. This was accompanied by a mean phase angle change along the span (figure 4.21) so that, on average, a shed vortex filament is staggered with respect to the model. There was no obvious reason why the delay should be biased towards one end of the model rather than the other.

With the model located at its main position in the tunnel, the sense of the asymmetry and the measured results were always reproducible. When the model was moved to the larger wind tunnel, the asymmetry established in the opposite sense, so that although great care was taken in setting up the geometry it appears that the mean asymmetric mode is established very readily by weak disturbance. Obviously the staggered shedding must represent some stable mode, the sense of the atagger being presumably triggered by some asymmetry in the model and end-plates, tunnel or approach flow. It was noted incidentally that there was a significant random phase modulation so that it was only possible to obtain repeatable correlations by operating at the longest sample times (0.45 seconds). This was not observed for the lower end-plates separations ($AR = 20$ and for no end-plate case, $AR = 24$). This gave the impression of a fairly random variation of inclination with time, possibly so that individual vortex filaments could even be staggered in either sense of the model and the mean result simply indicates a preponderance of those with one particular orientation. The aspect ratio below which end-plates can strongly correlate the shedding appears to be in the approximate range $18 < AR < 20$ as shown in figure 4.22 where the correlation between hot-wires fixed close to (1h from) each end-plate is shown. The good coherence of the mean vortex line is shown by the maximum correlation $\rho_{u_1u_2}$ at $t = t_{max}$, but presumably it is the random phase modulation which largely carries the fall in correlation. Going back to figure 4.20 it can be seen that end-plates are still managing to correlate phase of shedding for hot-wire separation of about 8h or so from end-plate, this is assumed due to the lateral correlation $\rho_{u_1u_2}$ is maximum at $\tau = 0$ in this range of separation.

Chapter 5

Measurements on Isolated Flat Plates in Turbulent Streams

-o-o-O-o-o-

5.1 Introduction

The previous chapter has studied in detail the isolated flat plate in a non-turbulent stream, to provide a set of basic data to compare with experiments on any deliberate interference with vortex shedding. Our main interference study is that due to intersection between two flat plates which will be discussed in Chapter 6. However, because it also forms a basic wake interference study in its own right and because it also presents a problem of practical interest, the present chapter will deal briefly with the effects of stream turbulence on an isolated flat plate.

The effect of stream turbulence on bluff-body separated flow is a problem which has received considerable study, although there is as yet no clear overall picture of the mechanism of the interaction. Confining our attention initially to two-dimensional flows only, it is convenient to consider the flows from two broad viewpoints:

1) whether or not the separation is fixed, by geometry, to occur at a sharp edge,
2) whether or not the flow experiences regular vortex shedding.

If separation occurs on a smoothly curved surface, such as a circular cylinder or a sphere, then it is well-known that the position of separation and hence the overall aerodynamics, are strongly determined by the location of transition relative to the separation points. Thus, even in a non-turbulent stream, such flows show a strong dependence upon Reynold's number (or at least a Reynolds number dependent range). Hence the drag of a circular cylinder falls from $C_D = 1.2$ to $C_D \doteqdot 0.23$ over the Reynolds number range $2 \times 10^5 < Re < 4 \times 10^5$ and similar results are found for the sphere (see Goldstein (2)).

With a sharp-edged separation as occurs for our flat plate geometries, square and rectangular section cylinders etc., there is no equivalent sensitivity to Reynolds number. If transition occurs before separation it cannot of course influence the position of separation anyway and sharp-edged geometries seem generally insensitive to Reynolds number, so that it appears that whether or not transition occurs before separation, or where transition occurs in the shear layer for a laminar separation, has little effect on the flow. Roshko and Lau (42) have remarked, in fact, that the position of shear layer transition for laminar separation appears not to scale so much upon a Reynolds number so much as simple multiple (they suggest about 50) of the thickness of the shear layer at separation. Since this is likely to be considerably less than the body thickness it means that transition will commence very soon after separation (compared say with typical body scales or distances to reattachement or mean bubble closure). This observation is supported by Roshko and Lau's original measurements, by Bearman's study of flat plates normal to a stream (ref.60) and by Hilliers(59) study of flow past a long two-dimensional rectangular body.

Since one effect of stream turbulence is to promote earlier transition, then the smooth surface geometries shows a strong effect of turbulence on transition, and hence on separation positions. Indeed the sensitivity of a sphere to stream turbulence was, for a long while, used as a measure of turbulence levels in tunnel working sections (Goldstein, (2) Chap XI) and in this case Taylor (63) showed that drag data could be correlated satisfactorily by the turbulence parameter $(\sqrt{\overline{u'^2}}/U_o)/(Lx/D)^{1/5}$.

The earlier data of Fage and Warsap (61) showed that stream turbulence promotes transition on a circular cylinder at a lower Reynolds number than the smooth flow, and Bearman (64) has shown that Taylor's parameter can correlate the data again.

Stream turbulence clearly cannot change the separation position for sharp edges bodies, and hence we should not expect these data to correlate on Taylor's parameter which is essentially a boundary layer transition parameter. Stream turbulence does appear to affect shear layer development, however, for sharp-edged separations, and here it is best to now consider the flows under the second classification of whether or not regular vortex shedding occurs.

The regular formation and shedding of vortices from a body is a powerful mechanism for extracting energy from the free stream and as such it generates high drags and low base pressures. For example, we have seen from the previous chapter that vortex shedding from a thin flat plate gives base pressures of order -1.24 whereas the same geometry, with vortex shedding inhibited (for the short end-plate test of chapter 4 or -0.57 by using splitter plate, Arie and Rouse (22)) gives only -0.5.

When regular shedding is absent, stream turbulence appears steadily to reduce base pressures and to contract bubble lengths (Hillier and Cherry (70) for reattachment on long rectangular blocks; Bearman (26) for reattachment on the splitter plate downstream of a square cylinder; Bearman (60) and Humphries and Vincent (65) for the flow behind a flat disc; Hillier and Cherry (70) for the flow over blunt ended cylinders placed parallel to the stream). Apart from the disc experiments the others quoted above found virtually no systematic effects of integral scale of turbulence but a strong dependence on intensity (see figure 5.1 reproduced from reference 26). The disc experiment shows less clear results (perhaps because it has been the most intensely studied of these flows) indicating significant scale effects.

These range from the combined parameter $(\sqrt{\overline{u'^2}}/U_o)\ (Lx/D)^2$ of Bearman (whose tests are the most extensive and perhaps the most accurate (see figure 5.2) to $(\sqrt{\overline{u'^2}}/U_o)\ (Lx/D)$ of Humphries and Vincent, and an interesting observation by Melbourne W.(67) that neither parameter correlates his data and what is instead required is a measure of the energy in the high frequency end of the stream turbulence spectrum which, he argues, is the correct scale to interact with the shear layer at separation.

The action of turbulence on shedding bodies is less distinct, the flow being further complicated by the fact that the afterbody length appears as an essential part of the interaction. It has already been analysed in chapter 4 that the base pressure of a rectangular cross-section cylinder in smooth flow, with one face normal to the stream is extremely sensitive to changes in the ratio of the cylinder thickness to frontal face height (see Nakaguchi et al (19), Bearman and Trueman (18) and Nakamura et al (40) figure 5.3). If t/h is about 2.8 the flow reattaches to the sides, the vortex strength weakens and the base pressure increases considerably.

Nakamura and Tomonari (40), Lanaville and Williams (29) and Petty (34) have shown that the base pressure and therefore the drag of rectangular cross-section cylinder are affected by approaching turbulence in two different ways. Their results presented in figures 5.4, 5.5 and 5.6 respectively, summarise the effects of the turbulence on Cp_b and C_D of rectangular 2-D cylinders. Firstly Cp_b increases (C_D decreases) as the turbulence intensity increases for cylinders with $t/h \geq 0.63$ approximately (figure 5.5 and 5.6). Secondly, for cylinders with $0.43 \leq t/h \leq 0.63$ Cp_b decreases (C_D increases) to a relative minimum value as the turbulence intensity increases from an initial value of zero and then Cp_b increases again (figure 5.5 and 5.6).

If $t/h \leq 0.4$, the trend is similar, but the minima base pressure coefficients are not so pronounced. Square section cylinders have been intensely studied (this is a good example of 2-D bluff body with sharp edges of separation and strong regular shedding which can be related to our basic thin flat plate). Vickery (38), Laneville et al (28), Laneville and Williams (29), Lee (30), Petty (33), Petty (34), Kavur (27) and Bearman (26) for example, have shown that when a 2-D square section is placed in turbulent flow the base pressure is increased. The general form of the trend is presented in figure 5.7 (reproduced from Bearman (26)). Apart from Lee's experiments the other workers quoted above found virtually no systematic effects of integral scale. This is shown in figure 5.8 reproduced from reference 29. It appears then that over a broad range of Lx/h the base pressure (consequently the drag) responds to the turbulence intensity and is insensitive to its scale.

5.2.1 The effects of turbulence on use of end-plates

The effects of turbulence intensity on flat plate tests with and without end-plates are shown in the table 5.1 below (base pressure corrected for wind tunnel blockage by the method of Maskell (10)).

It can be seen that for intensity of about 9.5% the reduction in base pressure due to the end-plates was only 0.05 in Cp_{bc}, compared with the smooth flow case in which the base pressure decreases 0.18 in Cp_{bc}. Therefore the addition of turbulence to the flow has the effect of reducing the end-plate effect due to the model penetration into the boundary layer on the tunnel walls. The information given in table 5.1 indicates that one of the effects of turbulence is to make the flat plate behave as if it were longer in the spanwise direction, since model 1 showed that the end-plates reduce the base pressure less on higher aspect ratio tests (see figure 4.7 and 4.8).

Turbulence Intensity $\sqrt{\overline{u'^2}}/U_o$ %	Cp_{bc} Without End-plate	Cp_{bc} With End-plate	Decrease in Cp_{bc}
Smooth	-1.06	-1.24	-0.18
2.6	-1.17	-1.30	-0.13
5.7	-1.19	-1.27	-0.08
9.5	-1.14	-1.19	-0.05

Table 5.1 Effect of Turbulence Intensity on Use of End-Plates.

The magnitude of this difference is surprising. It is suggested that the turbulence alters the interference between the tunnel wall boundary layer (thicker in turbulent flow, see figure 3.5) with the shear layer and vortex formation patterns to bring about these changes, or presumably the addition of turbulence into the flow produces a boundary layer on the end-plates which is thick enough to reduce their effect compared with the smooth flow test. This was not investigated further. It is noted, however, that Keefe (25) and Gerrard (68) have both demonstrated the considerable effect that end disturbances can have on vortex shedding mechanisms on circular cylinders.

5.2.2 Turbulence effect on flat plate base pressure

Very few workers have investigated the effect of turbulence on thin two-dimensional flat plates, therefore there are few experimental data to establish clearly the overall picture of the mechanism of the interaction. Thus, as part of interference tests, model 1 and model 2 (with end-plates) were tested in the small tunnel (0.91m x 0.61m) in turbulent flows. The data was corrected for the effect of wind tunnel blockage by the method of Maskell (10).

It should be noted that in section 4.2.2 it was shown that the effect of aspect ratio on base pressure is negligible in smooth flow. The same hold in turbulent flow since model 1 for an aspect ratio of 36, 20, 10 did not show any significant effect on base pressure.

Figure 5.9 shows the effect of turbulence intensity on base pressure coefficient at mid span of the models for an aspect ratio of 10. The results are presented uncorrected too and compared with those of Petty (34). It can be seen that Cp_{bc} decreases to a relative minimum ($Cp_{bc} = -1.3$) as the intensity increases (say 3%). The slight decrease was about -0.06 in Cp_{bc} with respect to the smooth flow value (it should be remembered that the accuracy of the data is of order ± 0.03 in Cp_b). Further increases in turbulence intensity (up to $\sqrt{\overline{u'^2}}/U_0$ of about 9.5%) causes a weak but steady increase to a value of -1.19 (at 9.5% intensity) compared with the smooth flow value of -1.24. Petty's results (uncorrected, blockage unknown) agree closely with the present measured pressure coefficient (S/C = 0.025) shown in figure 5.9. The differences between these two sets of data is slightly larger for the higher intensities, the difference in distributions presumably reflecting the different accuracy in grid flow calibration to some extent.

It was also observed that base pressure showed no dependence on the scale of turbulence since the Cp_{bc} values were identical within the experimental accuracy for model 1 and 2 (i.e. h = 2.54cm and 5.08cm respectively). The overall range of Lx/h is from 0.36 to 3.5 although at any given intensity the range is of course much less (but at least a minimum range of 2 from the change of model scale).

An attempt to obtain data at very high turbulence intensities was also made. The models were placed close to the grids, i.e. $X/M < 10$ (where M is mesh size), region in which the turbulence shows a degree of anisotropy (see Vickery (39)). It is particularly important to remember that the grid flow calibrations even for dynamic head is rather uncertain close to the grids (for example, K was about 1.02 behind mesh point and K = 0.95 behind grid point for grid B, see figure 3.3), therefore the data for high intensity levels is probably only accurate to ± 0.06 in Cp_{bc}.

Figure 5.10 shows the general trend of data for higher intensity tests, the base pressure being of order -1.22 for intensity of about 19% compared with the smooth flow value of -1.24. It can be seen that the high turbulence intensity does not introduce any significant variation in Cp_{bc}. Although the results are a little scattered for the higher intensities, it appears that the vortex shedding or at least those aspects of vortex shedding which affect Cp_b is so strong that it is not influenced significantly by turbulence intensity and is insensitive to its scale.

It is instructive, however, to compare the pressure distribution on the end-plate centre line for smooth and turbulent flows. Figure 5.11 shows the pressure coefficient, Cp, distribution on the end-plate, for the smooth stream and two turbulence conditions (4.9% and 9.5%).

The main differences are in the level of the pressure - although these are weak - and there appears to be little difference in bubble length. This latter point is shown more clearly in figure 5.12 where the pressure recovery $\hat{Cp}=(Cp-Cp_b)/(1-Cp_b)$ is plotted against x/h (see appendix A and Roshko and Lau (48) for further discussion of $\hat{Cp}$). Figure 5.12 illustrates the strong similarity in the distributions, and apart from the values immediately downstream of separation there are virtually no differences in bubble scale.

5.3 The effect of turbulence on Strouhal number

The vortex shedding frequency was measured on a Hewlett-Packard correlator directly from the autocorrelation signals which gives an accuracy of about 2%. The hot wire was positioned 2h downstream of the model 1 (h = 2.54cm) and 1.5h off its centre line as shown in table 5.2 The observation of Strouhal number in turbulent flows did not show any significant variation compared with those obtained in smooth flow.

Data on $St = nh/U_0$ (n and U_0 uncorrected for blockage), are presented in table 5.2. It decreases slightly from 0.146 in smooth flow to about 0.142 in turbulent flow ($\sqrt{\overline{u'^2}}/U_0=19\ \%$) which is barely significant compared with experimental accuracy.

Turb. Int.	Smooth	1.5 %	5.7 %	9.5 %	19 %
St	0.146	0.146	0.144	0.144	0.142
AR	20	20	20	20	20

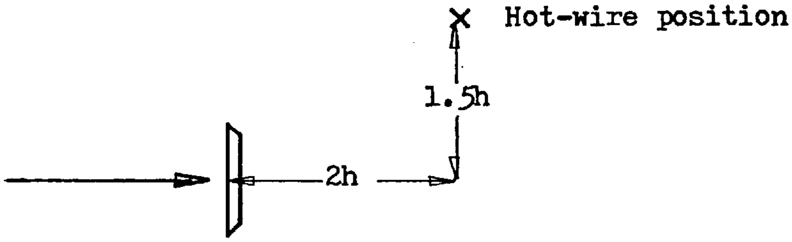

Table 5.2 Effect of Turbulence Intensity on Strouhal Number

5.4 The effects of stream turbulence on velocity correlations

Figures 5.13, 5.14 and 5.15 respectively show the autocorrelation function $\overline{u_1 u_1}(\tau)/U_o^2$ versus the dimensionless time $\tau = tU_o/h$ (where t is the real time and U_o is the uncorrected free stream velocity) and cover a period slightly greater than that of the first complete shedding cycle ($\tau \cong 7$). The probe was positioned at mid-span as shown in table 5.2. It should be noted that the errors due to H.P. correlator and hot wire inaccuracies are of about ± 5% (H.P. Correlator's Operation Manual).

Two main points should be emphasised at this stage. Firstly, the amplitude of the signal at $\tau = 0$ (i.e. the mean square turbulence intensity at the probe position) increases steadily with stream turbulence intensity to a value of $\overline{u_1 u_1}(0)/U_o^2 = 3.35 \times 10^{-2}$ (at 9.5% intensity) compared with the smooth flow value of 2.2×10^{-2}. Secondly, the amplitude after one shedding cycle ($\tau \cong 7$) hardly changes from the smooth to the two turbulence cases (within measurement accuracy) suggesting little alteration in the turbulent energy actually at the shedding frequency. This implies that the correlated energy at the shedding frequency between two successive vortices, at the probe position, responds only weakly to stream turbulence initially, but that there is a progressive disruption of this coherence as the intensity is increased. This is shown in figures 5.16 (smooth flow), 5.17 (4.9% intensity) by means of autocorrelations for τ covering a period of about 3 cycles and in figure 5.18 (9.5% intensity) for τ covering a period of about 7 cycles.

Cross correlations between two hot wires were achieved by fixing one wire at z = o and traversing the other in the span-wise direction.

Both wires were maintained at the same values of x and y shown in table 5.2. The measurements of velocity cross correlations for an aspect ratio, between end-plates, of 20 were made in the small tunnel (S/C = 0.025). The cross correlations (unlagged) are shown both as correlation coefficients, $\rho_{u_1u_2} = \overline{u_1u_2}(0)/\sqrt{\overline{u_1'^2}}\sqrt{\overline{u_2'^2}}$, in figure 5.19 or as the $\overline{u_1u_2}(0)/U_o^2$ coefficient in figure 5.20. The advantage of the former is that it is more convenient to measure experimentally, being less prone to hot wire calibration errors. The advantage of the latter is that for large wire separations (i.e. for z>Lx) it enables a direct comparison to be made between correlated energies at the shedding frequency. That is if we regard the turbulence signals to comprise two components

$$\begin{aligned} u_1 &= u_{1V} + u_{1T} \\ u_2 &= u_{2V} + u_{2T} \end{aligned} \qquad (5.4.1)$$

where subscript V refers to the fluctuations specifically at the shedding frequency, and subscript T refers to the remaining fluctuations (which come from the stream turbulence and from turbulence within the vortices), we can write

$$\overline{u_1u_2} = \overline{u_{1V}u_{2V}} + \overline{u_{1T}u_{2T}} + \overline{u_{1T}u_{2V}} + \overline{u_{2T}u_{1V}} \qquad (5.4.2)$$

now

$$\overline{u_{1T}u_{2V}} = \overline{u_{2T}u_{1V}} = 0 \qquad . \text{ (assumed uncorrelated)}$$

so that

$$\overline{u_1u_2} = \overline{u_{1T}u_{2T}} + \overline{u_{1V}u_{2V}} \qquad (5.4.3)$$

or since at large separations , i.e. z>Lx

$$\overline{u_{1V}u_{2V}} \longrightarrow 0, \qquad \overline{u_1u_2} = \overline{u_{1T}u_{2T}} \qquad (5.4.4)$$

Thus figure 5.19 shows clearly that with increasing stream turbulence intensity the spanwise correlation coefficient $\rho_{u_1u_2}$ decreases more sharply with wire separation.

Figure 5.20 shows that at large wire separation there is a genuine fall in the correlated shedding component with stream turbulence. This reduction shows a much greater sensitivity than that found in the previous autocorrelation results. In a sense this is similar to the results found in chapter 4 for the effects of aspect ratio on the models in smooth stream. In that case the transition from "low aspect ratio" to "high aspect ratio" had little effect upon the autocorrelation as such, but showed a strong effect of course on the transverse correlations. In these turbulent studies measurement was actually made of the time-lagged cross correlations for an AR=20. The results showed clearly that there was not a mean phase-angle change across the model (i.e. the mean vortex filament in turbulent flows was not inclined with respect to the plate axis) since the maximum correlation occurred at zero time delay (in fact for both smooth and turbulent cases t_{max}/t_c was less than 0.03 which is within the H.P. correlator accuracy). It can therefore be stated that the decay in cross correlation results probably are from the apperance of a random modulations in phase and/or amplitude. In other words, the randomly distributed vorticity introduced into the wake in turbulent streams causes random fluctuating velocities which are poorly correlated across the span. Hence the energy of the fluctuating velocities at the shedding frequency in turbulent flows is lower than in smooth flow for large wire separations. Which means that the stream turbulence produces three-dimensional effects in the wake. It clearly requires fairly high intensities to begin to have a dicernible effect on the cross correlation.

In the light of the present results it can be stated that the introduction of turbulence into the mean flow decreases the spanwise coherency of the vortices, as a result the correlation coefficient, $\rho_{u_1u_2}(\tau)$, decreases much more sharply with wire separation. It appears again that one of the effects of turbulence is to make the body behave as if it were longer in the spanwise direction, since it was stated in chapter 4 that the correlation coefficient decreases much more sharply with increasing aspect ratio.

5.5 Conclusions

The main observations on the effects of turbulence on thin two-dimensional flat plates may be summarised as follows:-

(i) The mean base pressure measured was found to be considerably insensitive to turbulence intensity even up to 20%. The results of this investigation confirm the findings of Nakamura et al (40) and Petty (34). It was found that for t/h = 0.125, the base pressure decreases slightly to a relative minimum as the intensity of turbulence increases and then increases. This suggests that the vortex shedding instability is so strong that it is not influenced significantly by turbulence. It is also confirmed that the scale of the free stream turbulence plays a secondary role in the mean flow.

(ii) The addition of turbulence into the flow minimised the end effect due to the model interaction with boundary layer on tunnel walls. Thus, when the end-plates were fitted the base pressure decreased less than in smooth flow.

(iii) The Strouhal number appears not to be affected with the addition of turbulence into the flow.

St decreases about 3% with turbulence intensity of about 19% (barely compared with experimental accuracy).

(iv) Turbulence intensity in the mean flow reduces the lateral velocity correlation.

(v) The bubble length, at the end-plates, is not affected by turbulence intensity.

CHAPTER 6

THE INTERSECTING MODEL

-o-o-0-o-o-

6.1 Introduction

It has already been stated earlier that the intention was to generate an intersection geometry by crossing two flat plate models at right angles and placing the combination normal to the stream. This gives geometries which are simple to machine and to assemble, and which also present fixed separation lines and a probable independence to Reynolds number changes. Little is known about intersecting bluff bodies. The only other study of an isolated intersection is the work of Nakamura et al (62). They investigated the intersection between two circular cylinders. Although this latter geometry may give a shape which is slightly more representative geometrically of components of a lattice structure, from our viewpoint circular cylinders would only confuse the fundamental mechanism of wake interference due to the geometry with possible Reynolds number effects.

It was planned to approach the problem in three phases:-

i) mean pressure distribution on the intersecting models and on the end-plates to establish, if possible, at what aspect ratio the flow at the intersection becomes isolated from end effects.

ii) oil flow, smoke and wool tuft visualisation to study the mean flow pattern in the wake.

iii) hot wire measurements in the wake to establish,

   1) mean velocity and turbulence contours
   2) vortex shedding frequencies and both spanwise and streamwise correlations.

6.2 Basic pressure distributions

For convenience, in the first exploratory tests carried out in the 0.91 x 0.61 m (3' x 2') wind tunnel, one flat plate model simply overlapped the other as shown in figure 6.1. These models were 2.54 cm in breadth. There was no gap between the models (the central joint was in fact sealed by a thin sheet of double-sided sellotape), so that the leading edge plane of one was upstream of the other by one model thickness (0.35 cm compared with the model breadth of 2.54 cm). The solid blockage of the combination is 6.6% in the small tunnel and 5.1% in the large tunnel and will therefore give a high interference. Because of the difficulties in correcting pressures for blockage, all data for the intersecting geometries are left uncorrected (see appendix A). It should be noted, however, that the largest solid blockage for an isolated model (h = 5.08 cm) was 5%. The Maskell correction applied to this 2-D case increased the base pressure from -1.42 to -1.24, i.e. an increase of about 0.18 in Cp_b.

Figure 6.2 shows the measured spanwise pressure distribution for an aspect ratio between end-plates of 20. The full details of the pressure distribution will be discussed for later tests, but two main points should be emphasised at this stage. Firstly, the distributions were unchanged if the end-plate size was increased (see the geometries in figure 6.2) so that the end-plates B can be considered sufficiently large. Secondly, although any one member of the intersecting pair produces symmetrical distributions about the intersection there is a clear difference between members due to their upstream/downstream positioning. A similar effect may be noted for the pressure distributions on the end-plates (figure 6.3).

Since the tunnel was rectangular in section, there was a slight possibility that the differences between members in figure 6.2 was also due to vertical/horizontal positioning rather than solely the upstream/downstream effect. Figure 6.4 presents data for the different possible combinations. There appears only to be a weak effect due to horizontal/vertical positioning (see the two distributions for the downstream member) which may in turn be a tunnel shape effect or possible misalignment of the models during reassembly, but the real effect appears to be the one of upstream/downstream positioning.

The magnitude of this difference is surprising. It was not investigated further, however, since it was decided that the effect should be eliminated for this basic test of an isolated intersection. Identical distributions on all four members, for example, means that the line bisecting the angle between any two members is an axis of symmetry, which would considerably reduce the number of velocity measurements required later. The models were therefore re-machined with appropriate slots at their centre-spans as shown in figure 6.5, so that a truly intersecting combination is generated with both models lying in the same plane normal to the flow. This geometry was used for all subsequent tests and is the shape implied by any future reference to an intersection.

The tests were repeated in the 0.91m x 0.61m wind tunnel (small tunnel). Figure 6.6 shows that these geometrical changes to the model produce very similar distributions on the two members. Near the intersection there is a region of marked disturbance, the base pressure Cp_b at the centre being - 0.84 compared with an isolated model value of - 1.24 (corrected for blockage).

Of course the intersecting model data are not corrected for blockage so that the actual difference will be greater. The region of large disturbance extends almost three body widths from the centre, where it changes quite abruptly to a much more gradual variation.
The intersection raises the base pressure above that of the isolated model, which is only to be expected from an interference with the vortex shedding process which is the mechanism which sustains low base pressures. Since the pressure variation persists as far as the end-plates it is unlikely that the aspect ratio of 20 provides independence between the central intersection and the end-plate. Because of the blockage difficulties it is not possible to compare pressure data absolutely with the isolated model. It is instructive, however, to compare pressure distribution on the end-plates for intersecting and isolated models. Figure 6.7 for example, shows a marked increase of streamwise scale and also presumably the bubble length, at the end-plate, due to the intersection. There was also identical pressure distributions on the end-plates of both members of the intersection, which showed the symmetry of the flow.

Reducing the aspect ratio below 20 in fact produced a pronounced effect on the pressure distributions. Figure 6.8 shows that mid-span values are relatively little affected, Cp_b only increasing from -0.84 to -0.80 in the aspect ratio range 20 to 12, but outboard of the immediate intersection zone large differences develop . These differences are clearly seen on the end-plate distributions (figure 6.9) as a raising of pressure, and an increase of bubble length, as the aspect ratio is reduced. It was not possible to operate at aspect ratios greater than 20 in the 0.91 x 0.61m tunnel, although measurements at an aspect ratio of 27 were made in the 0.91 x 0.91m (3' x 3') wind tunnel.

Figure 6.10 first compares a test at an aspect ratio of 20 in both tunnels, the difference in distributions presumably reflecting the different blockage to some extent (6.6% in 0.91m x 0.61m tunnel, and 5.1% in 0.91m x 0.91m tunnel). Figure 6.11 then compares tests at an aspect ratio of 20 and 27 in this larger wind tunnel. The transposed symbols in figures 6.10 and 6.11 are assuming symmetry in the flow. Still there is a difference in distribution although now it is nowhere near as sensitive to aspect ratio changes as were the results of figure 6.8. The mid-span and "core" values - up to a l/h of ± 2.5 - are virtually unaffected by aspect ratio. It is only outboard of this region that differences arise again. It should be noted that the increase of Cp_b as the intersection is approached presumably means a decrease of separation velocity and hence presumably a generation of trailing vorticity in the vicinity of the intersection is expected.

Following the work of Nash (35), Roshko and Lau (42) and others on separation bubbles we define a "pressure recovery" coefficient, $\hat{Cp} = (Cp - Cp_b)/(1 - Cp_b)$, where Cp is the pressure coefficient on the end-plate centre line and Cp_b is the minimum pressure coefficient on the model base (i.e. in the vicinity of the end-plates). $\hat{Cp}$ essentially records the pressure recovery $(Cp - Cp_b)$ as a fraction of the dynamic head at separation (proportional to $(1 - Cp_b)$). It has been shown in appendix A that it is not possible to correct data for intersecting models for blockage. Therefore pressure measurements cannot be compared quantitatively with that on isolated model tests. However, it is shown (see appendix A, formula 19) that the pressure recovery coefficient $\hat{Cp}$ is independent of blockage - i.e. $\hat{Cp} = \hat{Cp}_c$ - provided that the effect of blockage is simply a uniform overall increase of dynamic head.

Figure 6.12 compares tests at an aspect ratio of 20 in both tunnels. It is clear that there is no difference in $\hat{Cp}$ distribution (within the experimental accuracy) on the end-plate. It is also clear that the pressure recovery at an aspect ratio of 27 is similar to that of the isolated flat plate. This figure suggests that for an aspect ratio of 27 the streamwise scale looks similar to the isolated model and that the main difference is simply in pressure level. It also suggests that for an aspect ratio of 20 the bubble has lengthened (this will be discussed next in the flow visualisation section). It should be noted that even for an aspect ratio of 27 the base pressure is still falling as the end-plates are reached, so that perhaps the true "isolated" intersection is only likely to be reached for aspect ratios beyond this. Nevertheless, it is suggested that the results at an aspect ratio of 27 are illustrative of the general mechanism of intersection, although a fully "isolated case" i.e. aspect ratio infinite, has not been reached yet.

6.3 Flow visualisation

The flow about the intersecting model is complex and would require extensive velocity measurements to define it properly. A brief study was therefore first made using smoke flow, wool tufts and oil flow, to determine the overall features of the flow field.

Smoke was first introduced upstream of the model (about 0.5 metre upstream), as a thin filament directly in line with the intersection. This smoke was rapidly entrained into the wake in the vicinity of the intersection. As well as diffusing downstream of the intersection it also spread outwards along the span of the members (as far as the vicinity of the end-plates).

Thus four well defined columns of smoke were observed in the near wake bleeding air from the intersection to the regions outboard. This is of course associated with the large spanwise gradient of pressure observed in figures 6.10 and 6.11. Smoke introduced upstream in the vicinity of the end-plate was rapidly entrained into the wake filling the region from the position of injection up to the end-plate and diffusing downstream in this area only. A similar behaviour was noted for smoke injected directly into the wake. That is there was no diffusion towards the centre. This is similar to flow observed over smoke stack too. Smoke emerges from top of stack and is sucked down towards base in immediate nearfield.

The corresponding oil flow in the base region is shown in figure 6.13. The visualisation is not as clear as could be desired, but there is still the evidence of a strong outflow from the centre again. The oil begins to accumulate at some 6-7 body widths outboard from the centre. Obviously the precise position is dependent upon the oil mixture consistency and this effect was not studied in detail but coupled with the pressure distributions of figure 6.10, it does suggest a strong reduction of the cross flow velocity in the vicinity of the end-plates.

Ideally, the flow at the end-plates would not be of interest, simply because they should be located sufficiently far from the intersection that they do not influence it. That is the flow near the end-plate would be identical to that of the isolated model. In practice the pressure distributions have shown that the end-plates still influence the central flow and are not yet isolated from the effects of the intersection.

A brief oil visualisation study was made of the flow on the end-plates, only for aspect ratios of 12 and 20, and these results are shown in figures 6.14 and 6.15. The flow in the vicinity of the end-plates will be very complicated, combining the effect of the outwash from the intersection region with the horseshoe vortex flow induced by the separation of the end-plate boundary layer upstream of the model. This particular separation (primary separation) can be seen in figure 6.15, commencing about 1.5 model widths upstream of the model; the horseshoe vortex and the vortices shed from either sharp edges of the flat plate are identifiable as well (for further discussion on this very complex flow see Belik (52)).

6.3.1 Bubble length measurements

Even on the end-plates (figure 6.14) the bubble size appears longer than that presented by Fail et al (8) and Bradbury (41) for isolated models, so in an attempt to gain a clear understanding of the mechanism of the intersecting model flows, measurements have been made of the bubble size. Unfortunately no oil flow tests were carried out at the highest aspect ratio (AR = 27).

Figure 6.16 (obtained from oil flow), for example, shows a marked increase of bubble length R, at the end-plate, as the aspect ratio is reduced. This is compared with the bubble length suggested by Fail et al (8) for an isolated flat plate (i.e. two-dimensional flow). The impression from figure 6.16 is that the bubble size approaches the 2-D case with increasing aspect ratio, but is still longer than the isolated model.

A simple attempt was made to estimate the bubble length across the span using a wool tuft on the end of a long, thin rod. The closure position was simply taken as the position where, on average, the tuft appeared to spend equal time between the upstream and downstream directions. Although the flow is highly turbulent, successive measurements always located the closure position within about ± 1.5cm (± 0.6h). It should be noted that wool tuft and oil flow values showed good agreement at the end-plates. Figure 6.17 shows the bubble length estimated for aspect ratios of 12 and 20 of the intersecting models. This suggests a longer bubble near the intersection. It can be seen that the longer bubble is associated with a higher base pressure at mid-span (see figure 6.8) and the shorter length with the relatively low base pressure near the end-plates. It is also seen that the bubble length at mid-span is increased as the aspect ratio is reduced.

It is instructive to compare our pressure data and bubble length on the end-plate with other work reported on the effect of wake interference. That is, interference with the separated shear layer forming the vortex street, particularly with the interference generated by base bleed, since this will be similar to the bleed of air in the present work from the intersection to the outer region of vortex shedding.

Bearman (45) and Wood (44) for example, have both shown that if some bleed air is introduced into the wake of a blunt-based aerofoil, the vortex formation point moves downstream. There is a corresponding increase in Strouhal number and base pressure. With sufficiently large bleed quantity the regular vortex street pattern disappeared.

Castro (43) has shown that porosity on flat plates normal to the stream increases the shedding frequency and the drag drops (Cp_b increases) and also the reversed flow and the vortex formation region moves downstream with increasing porosity. He suggests that the vortex street may not be present at high porosity. These cases of base bleed present similar features to the present test since as was earlier stated the large spanwise gradient of pressure bleeds air from the intersection to the region outboard.

It is also instructive to show the effect of aspect ratio on $\hat{Cp}$ at the end-plate. This is shown in figure 6.18 for various aspect ratios compared with the isolated flat plate test. It should be noted that the earlier measured bubble closure, R, for an aspect ratio of 12 was about 5.5 and 3.5 for aspect ratio 20. It appears interesting then that this closure shows about 70 ± 2% of pressure rise from separation to reattachment. The corresponding $\hat{Cp}$ are, 0.25 (AR = 12), 0.3 (AR = 20) and about 0.34 (AR = 27, taken from figure 6.12). For the isolated model the estimated bubble closure, $R = x/h$, to 70% recovery appears to be of about 3.1h and $\hat{Cp} = 0.35$ (the closure for isolated model was not measured). Although we have no oil flows for the intersection at an aspect ratio of 27 the evidence from figures 6.12 and 6.18 is that bubble length near the end-plate approaches the 2-D value as the aspect ratio is increased and is very close to that of isolated model for an aspect ratio of 27.

A discussion on recovery coefficient has been presented by R. Hillier (59). He defined the recovery coefficient

$$\hat{Cp} = (Cp - Cp_s) / (1 - Cp_s)$$

based upon the suction immediately of separation, Cp_s, rather than on the maximum suction Cp_b.

His analyses are based upon nominally 2-D geometries without vortex shedding (separated and reattached flows). Hillier for convenience defined the streamwise scale, R, as the distance to 70% recovery which would be close to but perhaps not identical with the reattachment length. For example, he found values of $\hat{Cp}$ in the range $0.25 < \hat{Cp} < 0.32$ for a bubble closure of about $4.2 < x/h < 4.8$ on his 2-D geometries.

It is surprising then that the agreement appears reasonable considering the likely errors caused by three-dimensionality and vortex shedding in the present tests.

6.4 Mean and fluctuating velocity measurements

The mean velocity and the intensity of the velocity fluctuations were measured across the span of the intersecting members. The hot-wire probe was aligned normal to the free stream with its axis in z direction for the horizontal member and in y direction for the vertical. This is important in view of the work presented by Bradbury (41) for high intensity or reversing flow. Results of his experiments are shown in figure 6.19. It is noted that the readings are influenced in the recirculating regions and this depends on hot-wire alignment. Corrections for probe misalignment could not be applied in the present work since the mean flow direction was not determined. Measurements are also subject to errors arising from the fluctuating nature of the flow behind the model. Therefore caution must be observed in the interpretation of the hot-wire data in the highly turbulent flow ($\sqrt{\overline{u'^2}}/U_o$, up to about 0.3 and $\sqrt{\overline{u'^2}}/U$ up to 0.2, where U_o is the free stream velocity and U is the local velocity at the probe position) immediately downstream of the model, though it is considered here that a local intensity of 20% will lead to only small errors.

Mean velocity measurements are presented for the intersecting model in the large tunnel (i.e. S/C = 0.051, AR = 27). Figure 6.20 shows a traverse in the plane two body widths downstream from the separation edge. Clearly the intersection exerts a significant perturbation on the mean velocity field. The velocity distribution shows a gradual increase of mean velocity towards the corner until a maximum is reached at about z/h = 2. This was associated with the interaction of the two separated shear layers from the edge of the intersecting arms. Figure 6.21c shows the corresponding chordwise velocity distribution uncorrected for blockage at z/h = 12 (i.e. in the vicinity of the end-plates), this is compared with that of Bradbury (41) measured 2h downstream but corrected for blockage, S/C = 0.1, with end-plates in figure 6.21a and with that of Fail et al (8) (measurements taken 1.25h downstream and corrected for blockage) in figure 6.21b. It can be seen that the results agree closely, but even this large aspect ratio test shows that the mean velocity has not reached the true isolated value.

From graphs such as that of figure 6.20 mean velocity contours were plotted. Results are presented in figure 6.22. The distribution is symmetrical about the bisector since identical velocities (within experimental accuracy) were measured at symmetrical positions about this bisector.

Figure 6.23 presents the corresponding plots for intensity of velocity fluctuations. The results show clearly how the high intensities associated with the strong vortex shedding in the outboard regions decreases continuously toward the intersection. This weakening occurs progressively from y/h = 10 to about 3, where there was no significant energy at the shedding frequency (this is supported by further measurements to be presented in section 6.4).

The increase of intensity for $y/h < 3$ occurs as the probe enters the centre bubble where the flow does not appear to contain energy at any discrete frequency.

The effect of aspect ratio on intensity distributions for the intersecting model was estimated by comparing aspect ratios of 20 and 27 from the tests in the large tunnel ($S/C = 0.051$) with the mean value of the isolated model in the same tunnel ($S/C = 0.028$, $AR = 27$). Results are shown in figure 6.24a. Caution must be observed in the interpretation of the turbulence intensities, since a possible error in positioning the probe with respect to the model is estimated as ± 2mm. This in the chordwise direction would infer an error or about 1.6% in $\sqrt{\overline{u'^2}}/U_0$. The corresponding chordwise traverse test (intersecting model $AR = 27$ at $z/h = 12$) is shown in figure 6.24b compared with the isolated case data reproduced from Bradbury (41) in figure 6.24c. The distributions presented in figure 6.24a show that the turbulence intensity in the vicinity of the intersection is almost unaffected by aspect ratio (less than 0.01 in $\sqrt{\overline{u'^2}}/U_0$ up to $z/h = 4$). Outboard of this region the difference increases. This was associated with the stronger vortex shedding of the higher aspect ratio model in the outboard region. However, turbulence intensity distributions compared with mean pressure data (figure 6.11) show a similar effect. That is even for an aspect ratio of 27 the intensity is still rising as the end-plates are reached. Its value is about 0.03 in $\sqrt{\overline{u'^2}}/U_0$ below the present isolated test. The difference could reflect blockage effects to some extent, but this would not affect the main conclusion of the present investigation. That is, for the intersection at an aspect ratio of 27 the turbulence intensity approaches the 2-D test in the vicinity of the end-plates.

Probably a better comparison to show the approach of the intersecting model to the 2-D limit would be to compare data based upon local intensities, which to an extent will allow for the effects of different blockage. At $z/h = 12$, $y/h = 1.5$, this gives $\sqrt{u'^2}/U = 12\%$ compared with a value of about 13% for the isolated model.

Intensity of fluctuating velocity contours in the plane two body widths downstream from the separation edge are shown in figure 6.25. The graph reflects the same kind of symmetry observed in mean velocity distributions discussed previously in the present section (see figure 6.22). Mean velocity and turbulence intensity contours taken from the work of Nakamura et al (62) measured at very large x/h behind crossed circular cylinders are presented in figure 6.26 (this was the only available work on intersecting bluff body flows). The difference in turbulence intensity and mean velocity distributions compared with the present results also reflect the fundamental mechanism of wake interference due to the geometry of their model, with possible Reynolds number effects and wind tunnel wall boundary layer effects, since they did not isolate the intersection by means of end-plates.

Finally, figure 6.27 shows intensity distributions measured across the span at different stations downstream (intersecting model AR = 27). It is remarkable that the intensities are more uniform in the spanwise direction downstream (it may depend also on y/h value), in particular at $x/h = 9$. It should be noted, however, that the further the hot-wire is from the wake the more it becomes influenced by the large scale eddies rather than the small scale turbulence whose scale decays rapidly away from the wake. A long way from the wake, probably tends to produce large lateral correlations. It is therefore difficult to compare precisely the different downstream stations. This will be discussed in more detail in the following section.

6.5 Shedding frequency and velocity correlations

6.5.1 Shedding frequencies and autocorrelations

The vortex shedding frequency was measured on a Hewlett-Packard correlator from the output of a hot-wire anemometer. It was obtained directly from autocorrelation signals. The hot-wire was positioned 2h downstream of the intersecting model and 1.5h off the central line.

The Strouhal number is identical for each of the four arms of the intersecting model, measured at 12.4h from the intersection. A detailed investigation of the variation of Strouhal number with distance from the origin was conducted as well, figure 6.28 showing values (uncorrected for blockage) measured along two opposite arms of the intersection. The symmetry is clear and it is noted that the frequency remains constant with position. As in the base pressure results there appeared to be no discernible Reynolds numbers effect over the range investigated ($2.5 \times 10^4 < Re < 5 \times 10^4$). The intersection had an aspect ratio of 20 in the small tunnel and 27 in the large tunnel. The Strouhal number remains constant across the span until detectable shedding actually ceases close to the intersection, with this result symmetrical about the intersection. St is slightly higher for the highest blockage test (roughly St = 0.160 compared with St = 0.155) and both are higher than the isolated case (St = 0.146). The region of particular interest on this curve is the position where regular shedding is undetectable. This corresponds to the position on the base pressure curve (see figure 6.10) at which Cp_b suddenly increases. Similar effects have been observed on a circular cylinder with a free end (reference (71)). Clearly this introduces three-dimensionality but perhaps an important effect is that in the near wake, at the tip, interacts with the flow over the top of the body. Air feeds into the low pressure region behind the body and vortex formation is modified by the effective introduction of entrainment fluid. It also corresponds to the position on the turbulence intensity curve where the fluctuating velocities are the lowest (see figure 6.23) as well as the mean local velocity is highest (figure 6.20). Towards the intersection point (i.e. $z/h = \pm 2$) the shedding signal becomes very weak (as shown in figure 6.29d) suggesting little energy at the shedding frequency. This is shown schematically in figure 6.29a to d for an aspect of 27. The plots show $\overline{u_1 u_1(\tau)}/U_o^2$ which for large time delays, represent correlated energy at shedding frequency between successive vortices.

It seems reasonable to argue that in the vicinity of the intersection the shear layer separated from the sharp side of the intersecting member rapidly mix up and distort, so that they are not free to interact with the opposite shear layer and roll up to form the 2-D vortex street. Thus, around the intersection, the wake had taken up a configuration with no regular vortex shedding and with high base pressure bleeding air into the wake toward the end-plates. It has been earlier stated that with another kind of wake interference such as bleeding air into the wake (Bearman (45) and Wood (44)) and perforations on flat plates (Castro (43)) the base pressure and Strouhal number increase. If bleed rate is high enough or there is a high plate porosity the shedding stops completely. It should also be noted that a study of aspect ratio changes (AR = 27, 16, 12) showed that St remained unchanged with alterations in aspect ratio, although there was a significant reduction in energy at the shedding frequency for the lower values.

An instructive work related to the influence of a slight three-dimensionality in the model on vortex shedding has been reported by Gaster (50). His experiments on two cones of taper ratio 36 : 1 and 18 : 1 have shown that the frequency of vortex shedding was controlled by the "local diameter" of the taper cone and had a value which was slightly lower than that on a parallel cylinder of the same size, and the coupling between regions of different characteristic frequencies introduced a certain amount of amplitude modulation to the motion. Thus the vortex shed in patches with predominant frequency in the patch which varied continuously along the model while the frequency of the packets remained constant.

It should be noted that the present experiment on intersecting flat plates shows clearly that the shedding frequency is independent of the position along the span of the model (this ceases close to the intersection). However, signals recorded at different spanwise stations are different in amplitude (amplitude decreases towards the intersection). It is also clear that the Strouhal number appeared to be slightly higher on the intersecting model than on isolated plates (this may reflect blockage effect to some extent).

6.5.2 Velocity cross-correlations

The aspect ratio of 27 produces strong regular vortex shedding, which ceases close to the intersection. The purpose of this section is to study the coherency of this shedding across the span and to compare it with the behaviour found with the isolated model.

Although the four members were shedding at the same frequency, it was found that there was zero correlation between any two arms for hot-wire placed close to the end-plates. Since, however, the frequencies were so close, a short integration on the Hewlett-Packard correlator would always give an apparent correlation, perhaps with a phase lag, between the two arms. These values were not repeatable with subsequent short integrations showing that the phase relationship was in fact random. As stated above, the longer integrations produced zero correlation.

Second measurements provided an estimate of the vortex spacing, a, close to the end-plate. With a hot-wire fixed at 1.5h above the centre line, 2h downstream and 1.1h from the end-plate, figure 6.30 shows the (unlagged) cross correlation with a wire moved downstream. The correlation peak at $x/h = 4.4$ corresponds to a 360° phase change in shedding between the two wires (time delay is also shown upon figure 6.30), so that this is taken as the mean vortex spacing. It can be seen that t_{max}/t_c varies linearly with x/h within experimental accuracy, so downstream of this fixed wire position the vortex convection speed can be regarded as effectively constant. Given a Strouhal number of 0.155, a mean convection speed of $0.68U_o$ is found. This compares with a vortex spacing of 5.2h and a convection speed of $0.76U_o$ found by Fage and Johansen (7).

The spanwise inclination or "stagger" of a vortex filament was also determined by spanwise correlations. One wire was again located close to the end-plate, the other was traversed in the spanwise direction toward the intersection (see figure 6.31) to record space-time cross correlations between the two wires which are shown in figure 6.32a.

It is noted that there is an initial rapid fall in correlation, which reflects turbulent fluctuations which are not well correlated across the span and whose magnitude is probably sensitive to precise location of the hot-wire. The sensitivity of the correlated energy at the shedding frequency $\overline{u_1 u_2}/U_o^2$ across the span due to the location of the hot-wire from the centre line of the model is shown in figure 6.37. It can be clearly seen that it is noticeable the effect of the hot-wire location on the correlations. Going back to figure 6.32a it can be observed that there is a region of nearly constant correlation for wire separations of 2h to 6h, after which the correlation falls rapidly as the intersection is approached and which correlates reasonably closely with the region of rapid pressure rise noted earlier in this chapter in figure 6.11. This final fall is accompanied by the appearance of a mean phase difference (although the basic fall is not associated with this, as seen by comparing the unlagged correlation with the maximum in figure 6.32a). Thus the vortex filament gives the impression of being slightly staggered on the average across the span so that it leads near the centre line. An estimate of this "lead" distance was obtained for one wire separation of 9.4h (fixed wire still 1.1h from the end-plate). The moving wire was traversed downstream until the maximum correlation was achieved (similar to the measurements discussed in figure 6.30) which gave a streamwise wire separation of 0.6h. Coupled with the phase lag of figure 6.32b this suggests a mean convection speed of 0.47Uo, significantly lower than that determined near the end-plates.

No spanwise correlations were made closer to the model than x/h = 2, but the above results infer either that on average the vortex filament sheds earlier towards the model intersection than in the outboard regions, or that if shedding is simultaneous along the span the interference of the mean velocity fields between adjacent arms provides initially a higher convection speed near the centre line. It should be appreciated, however, that the large spanwise gradients of mean pressure towards the intersection imply a spanwise variation in the rate of shedding of vorticity and hence in vortex strength (as seen for example in the velocity fluctuation intensities of figures 6.23 and 6.27). Thus one should not regard the flowfield as composing a series of single, staggered vortices, but rather that in the immediate approach to the intersection there is a rapid appearance of trailing vorticity. To illustrate these latter statements figure 6.33 shows comparatively the mean velocity fields along the span together with the spanwise gradient of mean base pressure and the variation of the velocity fluctuations. It can be clearly seen that for $2<z/h<3$ the mean velocity reaches its maximum value, the fluctuating velocity its minimum level and this correlates reasonably with the region of rapid pressure rise.

Two more streamwise inclinations of the vortex filament were determined by spanwise correlation at $x/h = 6.5$ which is about the streamwise location of the closure point of the central bubble, and 9h. Different y locations were taken in each case so that it is not possible to compare the data precisely between each station (fixed wire 1.1h from end-plate in either case), for example the initial fall in correlation at small hot-wire separations which reflects turbulent velocity fluctuations rather than those due to vortex shedding will be very sensitive to the vertical positioning of the wire in the shear layer. These two further correlation coefficients ($\rho_{u_1u_2}$) are shown in figure 6.34a and 6.35a.

Again the same general form as figure 6.32a is apparent, although with different absolute levels to the coefficients. Therefore, it appears instructive to compare the spanwise correlation of the energy at the shedding frequency in the three stations downstream, to bear in mind that the absolute levels of the correlation coefficient are highly influenced with the position of the wires in the shear layer, since these measurements were taken at different y locations in each case. This is shown in figure 6.36. It is noted that the correlated energy at St freq. drops to zero for l_w/h of about 10 (i.e. at $z \simeq 2.4$) in the three stations downstream. The same holds for the measurements 2h downstream at different y locations shown in figure 6.37. This suggests that the vortex shedding actually ceases in the core of the wake.

The corresponding time delay function (t_{max}/t_c) are shown in figures 6.34b and 6.35b respectively. A comparison between the time delay function measured at different stations downstream shows that t_{max}/t_c (for example for $l_w/h = 8.5$) decreases continuously, suggesting that the vortex filament is becoming parallel to the intersecting arm. This is because the convection velocity is higher near the end-plates than near the intersection. Therefore the lagged vortices (close to the end-plates) reach those shed first but with lower convection velocity close to the intersection.

Chapter 7

CONCLUSIONS

FOR INTERSECTING MODEL

-o-o-0-o-o-

The intersecting flat plate model appears to be a useful tool for studying the basic flow on intersecting bluff bodies with fixed flow separation at the sharp edges. It avoids serious problems of Reynolds number dependence and shifting of separation positions, and enables the study to concentrate on the interaction between shear flows and wake interferences. The mean flow shows an increase of base pressure towards the intersection which means a decrease of separation velocity and, (although the velocity is not known on the rear of the model) presumably a decrease in the rate at which vorticity is being shed from the separation edge. In the outer parts of the span the shed vortex sheets are able to interact with those shed from the other side to form a regular vortex street. In the central part of the model shedding at a discrete frequency does not appear possible, the vortex sheets shed from each separate arm rapidly interacting (three-dimensionally) to form a turbulent central wake. The transition from the regular shedding zone to the central zone is interesting and probably still requires further investigation. The large fall in the rate of shedding of vorticity (spanwise) occurs over a short distance and appears to correlate with a reduction of energy at the shedding frequency. Presumably this means that from the meanflow point-of-view the transition from the outer to inner regions is accompanied by the appearance of trailing vorticity, rather in the manner suggested schematically by figure 7.1. This trailing vorticity is generated through the whole region of changing spanwise pressure, but is obviously strongly concentrated very close to the intersection ($z<2.5h$)

There is a difficulty in the visualisation of the unsteady generation and shedding of vorticity. Since the rate of shedding varies along the model span, any elemental vortex filament shedding from the outer regions of the span may not necessarily penetrate as far as the centre (or even continue along the neighbouring arm of the intersection) but must instead turn in the streamwise sense. As a filament is just shedding from the arm however, it is clearly not possible for the filament to extend to infinity downstream; the possibility is therefore that it links with the filaments (or vortices) shedding from the other side of the arm. In the outer regions, the two-dimensional nature of the vortex sheets shed from either side of the arm leads to the periodic roll-up as a Karman vortex sheet. In the inner region the strongly three-dimensional nature of the flow prevents this.

Further work on this project could usefully pursue the detailed physics of the unsteady roll-up and shedding of the vortex sheet.

Finally, the main observations on the effect of the Junction placed normal to the stream may be summarized as follows:

(i) A truly intersecting combination - That is both models laying in the same plane normal to the flow -, produces a very symmetrical distribution of base pressure, mean velocity and turbulence intensities of the two intersecting members. Thus, the mean flow is symmetrical about the intersection.

(ii) Even for an aspect ratio of 27 between end-plates the base pressure is still falling and turbulence intensity is rising as the end-plates are reached. Therefore the true "Isolated Intersection" is only likely to be reached for aspect ratios beyond this.

(iii) Reducing the aspect ratio of the intersecting members produced a pronounced effect on the base pressure distribution particularly outboard of the inmediate intersection. The base pressure raises and the bubble legth increases.

(iv) The Strouhal number remains constant across the span and there is no variation of St with intersecting members aspect ratio, but St is higher than the isolated flat plate case.

(v) The mean convection velocity of the vortices relative to the shedding arm is constant downstream beyond $x/h = 2$ in the vicinity of the end-plates, that is lower than the velocity found on isolated models. The longitudinal spacing between two consecutive vortices downstream is also shorter than that on isolated model.

(vi) The vortices across the span are not shed simultaneously. Those close to the intersection are shed first, as a result the vortex filament two body widths downstream from the edge of the members is inclined, central part leading,although the "average convection velocity" in the vicinity of the junction is lower than that close to the end-plate.

(vii) The vortex filament becomes parallel to the intersecting arm downstream. As a consecuence the turbulence intensity and the energy at shedding frequency show a uniform distribution across the span. Therefore there is a better coherancy of the vortices downstream.

REFERENCES

(1)	Houghton, E. and Brock, A.	"Aerodynamics for Engineering Students", Edwards Arnold (Publishers) Ltd. , 1974.
(2)	Goldstein.	"Modern Development in Fluid Dynamics", Dover Publications INC. N.Y. 1965.
(3)	ESDU Data.	"Fluid Forces on Non-Streamline Bodies", Item 71012, 1971.
(4)	ESDU Data.	"Fluid Forces, Pressures and Moments on Rectangular Blocks", Item 71016, 1971.
(5)	ESDU Data.	"Fluid Forces on Lattice Structures", Item 75011, 1975.
(6)	Parkinson, G. and Jandali, T.	"A Wake Source for Bluff Body Potential Flow", J.F.M. vol 40, pp.577, 1970.
(7)	Fage, A. and Johansen, F.	"On the Flow of Air Behind an Inclined Flat Plate of Infinite Span", R. & M. 1104, 1927.
(8)	Fail, R. Lawford, J. and Eyre, R.	"Low Speed Experiments on the Wake Characteristics of Flat Plates Normal to an Air Stream", R. & M. 3120, 1957.
(9)	Roshko, A.	"On the Drag and Shedding Frequency of Two-Dimensional Bluff Bodies", NACA. TN. 3169, 1954.
(10)	Maskell, E.	"A Theory of the Blockage Effects on Bluff Bodies and Stalled Wings in a Closed Wind Tunnel", R.& M. 3400, 1966.
(11)	Fackrell, J.	"Blockage Effects on Two-Dimensional Bluff Body Flow", Aero Q. 26, 1975.

(12) Allen, H. and Vincenti, W. "Wall Interference in a Two-Dimensional Flow Wind Tunnel", NACA. TN. 782, 1944.

(13) Stansby, P. "The Effect of End-Plates on the Base Pressure Coefficient of a Circular Cylinder", Aeronautical Journal, 1974.

(14) Cowdrey, C "A Note on the Use of End-Plates to Prevent Three-Dimensional Flow at the End of Bluff Cylinder", NPL. Aero Report 1025, 1962.

(15) Maull, D. "Mechanisms of Two and Three-Dimensional Drag", Symposium on Aerodynamic Drag Mechanisms of Bluff Bodies and Road Vehicles, Plenum Press, N.Y., 1978.

(16) Obasaju, E. "On the Effect of End-Plates on the Mean Forces on Square Section Cylinders", I.C. Dep. of Aeronautics Report, 1979.

(17) Graham, J. "The Effect of End-Plates on the Two-Dimensionality of Vortex Wake", The Aeronautical Quarterly, 1979.

(18) Bearman, P. and Trueman, D. "An Investigation of the Flow Around Rectangular Cylinders", The Aeronautical Quarterly, Vol. 23, 1972.

(19) Nakaguchi, H. , Hashimoto, K. and Muto, S. "An Experimental Study on Aerodynamic Drag of Rectangular Cylinders", Journal of the Japan Society of Aeronautical and Space Sciences, Vol. 16, pp. 1-5, 1968.

(20) Bearman, P. "Investigation of the Flow Behind a Two-Dimensional Model with a Blunt Trailing Edge and Fitted with Splitter Plates", J.F.M., Vol. 21, pp. 241, 1965.

(21) Clements, R. "An Inviscid Model of Two-Dimensional Vortex Shedding", J.F.M., 57, 2, 1973

(22) Arie, M. and Rouse, H. "Experiments on Two-Dimensional Flow over a Normal Wall", J.F.M., 1, pp.129, 1956.

(23) Nakamura, Y. and Tomonari, Y. "Pressure Distributions on Rectangular Prisms at Small Incidences", Journal Japan Soc. Aero. and Space Sc. vol. 21, 1979.

(24) Gerrard, J. "The Three-Dimensional Structure of the Wake of a Circular Cylinder", J.F.M., vol. 25, part 1, pp.187, 1966.

(25) Keefe, R. "Fluctuating Forces Acting on a Stationary Circular Cylinder in a Subsonic Flow", U.T.I.A., Report 76, 1961.

(26) Bearman, P. "Turbulence Effect on Bluff Body Mean Flow", The Third U.S. Nat. Conf. Wind Engineering Research, University of Florida, 1978.

(27) Kavur, C. "An Investigation of the Effect of Turbulence on the Flow Around Cylinders of Square Cross-Section", M.Sc. Thesis, I.C. London 1971.

(28) Laneville, A., Gartshore, I. and Parkinson, G. "An Exploration of some Effects of Turbulence on Bluff Bodies", Proc. 4th. Int. Conf. on Wind Effects on Building and Structures, London 1975, (Cambridge University Press).

(29) Laneville, A. and Williams, C. "The Effect of Intensity and Large Scale Turbulence on the Mean Pressure and Drag Coefficient of 2-D Rectangular Cylinder", Fifth Int. Conf. on Wind Engineering, Colorado State, July, 1979.

(30) Lee, B. "The Effect of Turbulence on the Surface Pressure Field of a Square Prism", J.F.M., 69, pp. 263, 1975.

(31) Lee, B. "Some Effect of Turbulence Scale on the Mean Forces on a Bluff Body", J. Ind. Aer., 1, pp. 361, 1976.

(32) Lee, B. "The Susceptibility of Tests on 2-D Bluff Bodies to Incident Flow Variations", J.Ind. Aer., 2, pp. 133, 1977.

(33) Petty, D. "The Effect of Turbulence Intensity and Scale on the Flow Past Square Prisms", 3rd. Colloquium on Industrial Aerodynamics, 1978.

(34) Petty, D. "The Effect of Turbulence Intensity on 2-D. Bluff Bodies", Euromech Conference I.C.1979.

(35) Nash, J. "A Review on Two-Dimensional Base Flow" R.& M., 3323, 1962.

(36) Simmons, J. "The Relationship Between the Base Pressure on a Bluff Body and the Velocity at Separation", The Aeronautical Journal, vol 78 pp. 330, 1974.

(37) Simmons, J. "Phase Angle Measurements Between Hot-Wire Signals in the Turbulent Flow of a 2-D Bluff Body", J.F.M., 64, pp. 599, 1974.

(38) Vickery, B. "Fluctuating Lift and Drag on a Long Cylinder of Square Cross-Section in a Smooth and in Turbulent Stream", J.F.M., vol. 25, part 3, pp. 481, 1966.

(39) Vickery, B. "On the Flow Behind a Coarse Grid and its Use as a Model of Atmospheric Turbulence in Studies Related to Wind Loads on Buildings", N.P.L. Aero Rep., 1143, 1965.

(40) Nakamura, Y. and Tomonari, Y. "The Effect of Turbulence on the Drag of Rectangular Prisms", Trans. Japan Soc. Aero and Space Sci., vol.19, pp.81, 1976.

(41) Bradbury, L. "Measurements with a Pulse-Wire and Hot-Wire Anemometer in the Highly Turbulent Wake of a Normal Flat Plate", J.F.M., vol. 77, part 3, pp.473, 1976.

(42) Roshko, A. and Lau, J. "Some Observations on Transition and Reattachment of a Free Shear Layer in Incompressible Flow", Proc. Heat Transfer Fluid Mech. Inst., 18, pp. 157, 1965.

(43) Castro, I. P. "Wake Characteristics of Two-Dimensional Perforated Plates Normal to an Air Stream", J.F.M., vol. 46, part 3, pp.599, 1971.

(44) Wood, C. J. "The Effect of Base Bleed on a Periodic Wake", J.Royal Aero. Soc., 68, pp.477, 1964

(45) Bearman, P. W. "The Effect of Base Bleed on the Flow Behind a Two-Dimensional Model with a Blunt Trailing Edge", The Aero Quart. vol. XVIII, 1967.

(46) Bearman, P. W. "Investigation of the Flow Behind a 2-D Model with a Blunt Trailing Edge and Fitted with Splitter Plates", J.F.M. vol.21, part 2, pp. 241, 1965.

(47) Prassad, J. K. and Grupta, A. K. "Velocity Correlation Structure in the Turbulent Near Wake of Bluff Bodies", A.I.A.A. Journal, 11, vol. 15, 1977

(48) El Baroudi, M. Y. "Measurements of Two point Correlations of Velocity Near a Circular Cylinder Shedding a Karman Vortex Street", T.N.,31 Univ. of Toronto, Inst. of Aerophysics., 1961.

(49) Fiedler, H. E. and Willie, R. "Some Observations in the Near Wake of Blunt Bodies", A.I.A.A., 6, vol. 8, 1970.

(50) Gaster, M. "Vortex Shedding from Slender Cones at Low Reynolds Numbers", J.F.M., vol. 38, part 3, pp. 565, 1969.

(51) Davies, M. E. "Wakes of Oscilating Bluff Bodies", Ph.D. Thesis, University of London, 1975.

(52) Belik, L. "The Secondary Flow about Circular Cylinders Mounted Normal to a Flat Plate", Aero. Quarterly, 1973.

(53) Obasaju, E. D. "Pressure Fluctuation on Stationary and Oscillating Square Section Cylinders", Ph.D. Thesis, University of London, 1977.

(54) Prendergast, V. "Measurements of Two Point Correlations of the Surface Pressure on a Circular Cylinder", T.N., 23, Univ. of Toronto, Inst. of Aerophysics, 1958.

(55) Wilkinson, R. H. "On the Vortex Induced Loading on Long Bluff Cylinders", Ph.D. Thesis, Faculty of Engineering Univ. of Bristol.

(56) Bradshaw, P. "An Introduction to Turbulence and its Measurements", Pergamon Press, 1971.

(57) Bryer, D. W. and Pankhurst, R. "Pressure-Probe Methods for Determining Wind Speed and Flow Direction", N.P.L., 1971

(58) Tanner, M. "The Wake Pressure Behind Wedges as Influenced by Splitter Plates and Suction", AGARD, CP 4, 1965.

(59) Hillier, R. "Further Measurements in a Separated-and-Reataching Flow", I.C. Aero Report, 1978.

(60) Bearman, P. "An Investigation of the Forces on Flat Plates in Turbulent Flow", N.P.L. Report 1296, 1969.

(61) Fage, A. and Warsap, J. "The Effect of Turbulence and Surface Roughness on the Drag of a Circular Cylinder", R. & M. 1283, 1929.

(62) Nakamura, I., Osaka, H., and Yamada, H. "An Experimental Investigation of Turbulent Wake Structure Behind a Crossed Circular Cylinder", Japan Soc. Mech. Eng. , 790-15, 1970. (in Japanese).

(63) Taylor, G.I. "Scientific Papers", vol II, Cambridge University Press, 1960.

(64) Bearman, P. "The Flow Around a Circular Cylinder in the Critical Reynolds Number Regime", N.P.L. Aero Report, 1257, 1968.

(65) Humphries, W. and Vincent, J. "Experiments to Investigate Transport Processes in the Near Wakes of Disks in Turbulent Air Flow", J.F.M., vol 75, part 4 pp. 737, 1976.

(66) Bendat, J. and Piersol, A. "Measurement and Analysis of Random Data", J. Wiley and Sons, Inc. 1966.

(67) Melbourne W. Personal contact

(68)	Gerrard, J.	"Measurements of the Fluctuating Pressure on the Surface of a Circular Cylinder", A.R.C., 19, pp.844, 1958.
(69)	Pocha, J.J.	"On Unsteady flow Past Cylinders of Square Cross-section", Ph.D. Thesis, Dep. of Aeronautics Q.M.C. Univ. of London, 1971.
(70)	Hillier, R. and Cherry, N.	"The Effect of Stream Turbulence on Separated Bubbles", 4th Colloquium on Industrial Aerodynamics, Aacher, 1980.
(71)	Gould, R.W.F., Raymer, W.G., and Ponsford, P.J.	"Wind tunnel test on Chimneys of Circular Section at High Reynolds Number", Symposium on Wind Effects on Building and Structures, Loughborough University,1968.

APPENDICES

* * *

APPENDIX A

The Evaluation of Blockage Corrections.

A.1 Isolated Models

It is doubtful whether any wind tunnel blockage correction method can correctly compensate for the effect of blockage, since no entirely satisfactory correction method has been proposed to account for the effects of wind tunnel blockage on the flow past two-dimensinal bluff bodies. Nevertheless, two correction method are compared here. They are:

(i) The Method of Allen and Vincenti (12).

Potential Flow theory is applied where a plane surface can be modelled by an Image system and they have represented the effect of wind tunnel walls by an infinite series of images. It is assumed that the only effect of blockage is to produce an apparent increase in the free stream velocity. This is then assumed to consist of two independant parts, a solid blockage due to the presence of the model and the wake blockage. The base pressure coefficient

$$Cp_b = 1 - U_s^2 \quad (U_s \text{ tangential velocity at separation}) \qquad (A1)$$

the corrected separation velocity , U_{sc} , given by

$$\frac{U_{sc}}{U_s} = 1 + \frac{\Delta\pi^2}{48}\left(\frac{h}{T}\right)^2 + \frac{1}{4}C_{Dm}\left(\frac{h}{T}\right) \qquad (A2)$$

where is determined by the body shape ($\Delta = 0$ for flat plates) and C_D is the measured drag coefficient. Thus,

$$\frac{U_c}{U} = 1 + 0.25\, C_D\left(\frac{h}{T}\right) \qquad (A3)$$

$$\frac{C_D}{C_{Dc}} = 1 - 0.50\, C_D\left(\frac{h}{T}\right) \qquad (A4)$$

$$\frac{1 - Cp_c}{1 - Cp} = \frac{U^2}{U_c^2} = \frac{K_c^2}{K^2} \qquad (A5)$$

The corrected values of U_c , C_{Dc} , Cp_c are given in terms of the measured values U, C_D, and Cp, where h is the plate width and T is the tunnel height.

The method quoted above was originally developed for flow past streamlined bodies where the wake effect is small. However, for bluff bodies, the accuracy of this method is limited by their inability to accurately represent the potential flow about both the body and its wake.

(ii) The Method of Maskell (10)

This method obtains a blockage correction for the confined flow past bluff bodies by using a very simple free-streamline representation of the wake and considering the momentum balance in the external flow neglecting all effects assumed to be $O((S/C)^2)$ (where S/C is the blockage ratio, S being the body surface and C cross sectional area of the tunnel). It has been shown that this method gives good results for flat plates normal to the flow up to about 10 % blockage ratio. It is notable that the correction given by Maskell's method for flat plates is about twice that given by the wake blockage of the other method.

The equations to be applied are:

$$1 - Cp_b = K^2 \tag{A6}$$

$$\varepsilon = 1 / (K_c^2 - 1) \tag{A7}$$

$$\frac{C_D}{C_{Dc}} = \frac{1 - Cp_b}{1 - Cp_{bc}} = \frac{K^2}{K_c^2} = 1 + C_D \frac{S}{C} \frac{1}{K_c^2 - 1} \tag{A8}$$

$$K_c^2 = \frac{K^2 + 1 - C_D \frac{S}{C} + \sqrt{(K^2 + 1 - C_D \frac{S}{C})^2 - 4K^2}}{2} \tag{A9}$$

where the subscript c denotes the corrected value.

Both Allen and Vincenti and Maskell methods require measured drag coefficient C_D , to find the base pressure coefficient K_c . So a Wake Source model for Bluff Bodies Potencial Flow by Parkinson and Jandali (6) was used to calculate the Drag Coefficient of flat plates.

where,

$$C_D = 3 - \pi \cos\delta + \frac{\cos 2\delta}{\sin\delta} \ln \frac{1 + \cos\delta + \sin\delta}{1 + \cos\delta - \sin\delta} + \tan\delta \qquad (A10)$$

and

$$\cos\delta = \frac{1}{K} \qquad (A11)$$

C_D expresed in terms of Cp_b (experimental measured value) can be written as

$$C_D = 3 - \frac{\pi}{\sqrt{1 - Cp_b}} + \frac{1 + Cp_b}{\sqrt{1 - Cp_b}\,\sqrt{-Cp_b}} \ln \frac{\sqrt{1 - Cp_b} + 1 + \sqrt{-Cp_b}}{\sqrt{1 - Cp_b} + 1 - \sqrt{-Cp_b}}$$

$$+ \sqrt{-Cp_b} \qquad (A12)$$

Formula (A12) was computed and is presented in figure A1. The plotted values were fitted on a straight line as follows:

If C_{Di} $(i=1,2,\ldots\ldots,n)$ are the obtained values of C_D at chosen (exact) value of Cp_{bi} of the variable Cp_b , then the line of "best fit" passes through the centroid

$$\overline{C}_D = \frac{1}{n} \sum_{i=1}^{n} C_{Di} \quad , \quad \overline{Cp}_b = \frac{1}{n} \sum_{i=1}^{n} Cp_{bi} \qquad (A13)$$

and is given by

$$Cp_b = mC_D + C \qquad (A14)$$

where

$$m = \frac{\sum (C_{Di} + \overline{C}_D)(Cp_{bi} - Cp_b)}{\sum (C_{Di} - \overline{C}_D)^2} , \qquad (A15)$$

and

$$C = \overline{Cp}_b - m\overline{C}_D . \qquad (A16)$$

These formulas were computed and

$$C_D = - 0.934 Cp_b + 0.846 , \qquad (A17)$$

was obtained, which was plotted in figure A1 compared with formula (A12) and with experimental data from different sources. It can be seen that a good agreement was found. Therefore, formula (A17) was used to calculate drag coefficient C_D of the isolated flat plates. It should be noted that when it is related C_D to Cp_b (measured values) by Maskell it is assumed the same relation by Parkinson and Jandali's theory as if there were no blockage.

A.2 Intersecting Models

Section 4.3 shows that the method of Maskell(10) gave good agreement for our isolated models. The base pressure was uniform across the span therefore the parameter $K = 1 - Cp_b$ was determined straighforwardly from a single measurement of static pressure somewhere on the base of the body. It was also straightforward to obtain C_D which is required for the corrections by using the method of Parkinson and Jandali(6) (i.e. as if there were no blockage). Therefore it was possible to determine the blockage factor $= 1 / (K_c^2 - 1)$. Maskell showed that even a substantial non-uniformity in base pressure did not invalidate the theory. It was proposed that the theory held for almost all 2-D bluff body flows, and for a wide range of 3-D flows for which the wake is closely "axi-symmetric" at the downstream plane of reference.

Because our intersecting flat plates showed a substantial non-uniformity in base pressure across the span (figure 6.10) and velocity measurements downstream in the wake showed no axial symmetry (figure 6.21) i.e. the wake is fully three-dimensional, and partially because it was not possible to identify the measured drag to be included in the blockage parameter $C_D\ S\ /\ C$ in formula (A8),all intersecting data is presented in its measured form. Nevertheless, an attempt to correct the base pressure of the intersecting plates for blockage was carried out by using the method of Maskell. Firstly, the parameter K (Form.(A6)), was determined from the base pressure at mid-span and the corresponding C_D applying formula (A17). Secondly, K was determined from the average base pressure across the span and C_D from formula (A17) as before in order to allow subsequent correction of the observed pressures. Then the corrected base pressure (at mid-span of the models) was compared with the measured values in both wind tunnels in figures A2 and A3 respectively.

A.3 Pressure Recovery Coefficient Independance of Constraint

For a given

$$\hat{Cp} = \frac{Cp - Cp_b}{1 - Cp_b} \qquad (A18)$$

can be reduced as

$$\hat{Cp} = \frac{-(1 - Cp) + (1 - Cp_b)}{1 - Cp_b}$$

applying Maskell corrections i.e. equation (A8). The equation (A18) can then be written as

$$\hat{Cp} = \frac{-\frac{K^2}{K_c^2}(1 - Cp_c) + \frac{K^2}{K_c^2}(1 - Cp_{bc})}{\frac{K^2}{K_c^2}(1 - Cp_{bc})}$$

therefore

$$\hat{Cp} = \frac{Cp_c - Cp_{bc}}{1 - Cp_{bc}} = \hat{Cp}_c$$

or

$$\frac{Cp - Cp_b}{1 - Cp_b} = \frac{Cp_c - Cp_{bc}}{1 - Cp_{bc}} \qquad (A19)$$

Thus, it has been shown that Cp is independant of constraint

APPENDIX B

Turbulence Intensity Formula

The general relation between the airstream velocity U and the voltage E registered by the hot-wire can be expressed as follows:

$$E^2 = A + BU^n \qquad \text{(calibration formula)} \qquad \text{(B1)},$$

Where A, B and n are constant.

Differentiating

$$2EdE = nBU^{n-1}\,dU$$

and at 'zero' velocity

$$E_o^2 = A$$

Therefore

$$E^2 - E_o^2 = \frac{U^n\,2EdE}{nU^{n-1}dU}$$

and rearranging

$$\frac{dU}{U} = \frac{2EdE}{n(E^2 - E_o^2)}$$

Experimentally, it was found $n = 0.45$

Hence finally

$$\frac{dU}{U} = 4.444\,\frac{EdE}{E^2 - A}$$

If dU is replaced by the r.m.s. value of the turbulent velocity and dE by the r.m.s. value of the fluctuating component of the voltage signal, the formula used in calculating turbulence intensities is obtained:

$$\frac{\sqrt{\overline{u'^2}}}{U} = 4.444\,\frac{E\sqrt{\overline{e'^2}}}{E^2 - A} \qquad \text{(B2)}.$$

APPENDIX C

The Correlation Coefficient

We define the Correlation Coefficient $\rho_{u_1u_2}$ of two velocity signals as

$$\rho_{u_1u_2} = \frac{\overline{u_1u_2}}{\sqrt{\overline{u_1'^2}}\sqrt{\overline{u_2'^2}}} = \frac{\overline{e_1e_2}}{\sqrt{\overline{e_1'^2}}\sqrt{\overline{e_2'^2}}} \qquad \text{(C1)}$$

since $\bar{e}_1 = K_1u_1$, $\bar{e}_2 = K_2\bar{u}_2$ and $\overline{e_1e_2} = K_1K_2\overline{u_1u_2}$;
where $\bar{e}_1^2$ and $\bar{e}_2^2$ are the autocorrelation function, and $\overline{e_1e_2}$ is the crosscorrelation function at $t = 0$.

Using Hewlett Packard model 3721A Correlator the Autocorrelation Function was obtained as follows:

$$R_{x_1x_1}(\tau) = \lim_{T\to\infty} \frac{1}{T}\int_0^T x(t)x(t-\tau)dt \qquad \text{(C2)}$$

where τ is the time delay of the signal.

$R_{x_1x_1}(\tau)$, is a measure of the similarity between a signal and a time-delayed form of itself given by (C2).

The propierties of this function are:

(i) $R_{x_1x_1}(\tau)$ is a maximum positive value at $\tau = 0$, specifically $R_x(0) = \psi_x^2$ (Probability density function) = 1.0

(ii) $R_{x_1x_1}(\tau)$ tends to the square of the mean value as $\tau \to \infty$, if the signal is Random

(iii) $R_{x_1x_1}(\tau) = R_{x_1x_1}(-\tau)$, the Autocorrelation Function is symmetrical for positive and negative values of τ .

(iv) If two uncorrelated signal are added together, the autocorrelation function of the resulting signal is equal to the sum of the separate autocorrelation functions, i.e. , if $z = x + y$ then

$$R_{zz} = R_{xx} + R_{yy}$$

The Autocorrelation Function can be expressed in dimensionless form as follows

$$R_{u_1u_1} = \frac{\overline{u_1u_1}}{U_o^2} = \left(\frac{2}{n}\right)^2\left(\frac{E_1}{E_1^2 - A_1}\right)^2 \bar{e}_1'^2 \left(\frac{U_1}{U_o}\right)^2 \qquad \text{(C3)}$$

Where n and A_1 are constant (Appendix B), U_1 is the local velocity, U_o is the airstream velocity in the tunnel and $\bar{e}'^2$ is the mean square volt (i.e. autocorrelation function at t = 0)

The Crosscorrelation Function , $R_{x_1x_2}(\tau)$, is a measure of the similarity between two signals as a function of a time shift , τ , between them , given by

$$R_{x_1x_2}(\tau) = \lim_{T\to\infty}\frac{1}{T}\int_0^T x_1(t-\tau)x_2(\tau)dt \qquad \text{(C4)}$$

where one signal, $x_1(t)$, is delayed an amount τ with respect to the other signal, $x_2(t)$.

The propierties of crosscorrelation function are:

(i) $R_{x_1x_2}(\tau)$ is generaly not equal to $R_{x_1x_2}(-\tau)$

(ii) The first maximum (for τ increasing) at $t = t_{max}$, where t is the real time, is a measure of the phase between the two signals, representing the delay necessary to optimise the match between $x_1(t)$ and $x_2(t)$. Further maxima indicate the periodicity in the signals, though spread of the dominant frequency band, diminishes their amplitude.

As the H-P correlator provides $R_{x_1x_2}(\tau)$ inmediately at the experimental site (see Fig. C1), the estimates of phase angle were made from t_{max} , and also the first maximum (for τ increasing) at $t = t_{max}$ is a measure of the maximum $R_{x_1x_2}(\tau)$, i.e. $R_{x_1x_2}(t_{max}) = (R_{x_1x_2}(\tau))_{max}$.

Thus we define the maximum correlation coefficient as

$$(\rho_{u_1u_2})_{max} = \frac{(\overline{e_1e_2})_{max}}{\sqrt{\bar{e}_1'^2}\sqrt{\bar{e}_2'^2}} = \frac{(\overline{u_1u_2})_{max}}{\sqrt{\bar{u}_1'^2}\sqrt{\bar{u}_2'^2}} \qquad \text{(C5)}$$

The correlation legth, λ , is a characteristic length associated with the average size of the eddies being shed from the cylinder and it is given by

$$\lambda = \int_0^\infty \rho_{x_1x_2}(\tau)dx \qquad \text{(C6)}$$

i.e. the area under the correlation coefficient versus span separation between the signals.

The correlated energy at shedding frequency u_1u_2 can be expresed

$$\frac{\overline{u_1u_2}}{U_1U_2} = \left(\frac{2}{n}\right)\frac{E_1}{E_1^2 - A_1}\left(\frac{2}{n}\right)\frac{E_2}{E_2^2 - A_2}\,\overline{e_1e_2} \; ,$$

where U_1 and U_2 are the local velocities (at the hot-wire positions) , A_1 , A_2 and n are constants (hot-wire calibration).

The results are presented in dimensionless form with respect to the free stream velocity U_o.

therefore

$$\frac{\overline{u_1u_2}}{U_o^2} = \left(\frac{2}{n}\right)^2\frac{E_1}{E_1^2 - A_1}\;\frac{E_2}{E_2^2 - A_2}\;\overline{e_1e_2}\;\frac{U_1U_2}{U_o^2}$$

Experimentally, it was found $n = 0.45$ (see Appendix B)

hence finally

$$\frac{\overline{u_1u_2}}{U_o^2} = 19.75\,\frac{E_1}{E_1^2 - A_1}\;\frac{E_2}{E_2^2 - A_2}\;\overline{e_1e_2}\,\frac{U_1U_2}{U_o^2} \qquad \text{(C7)} \; .$$

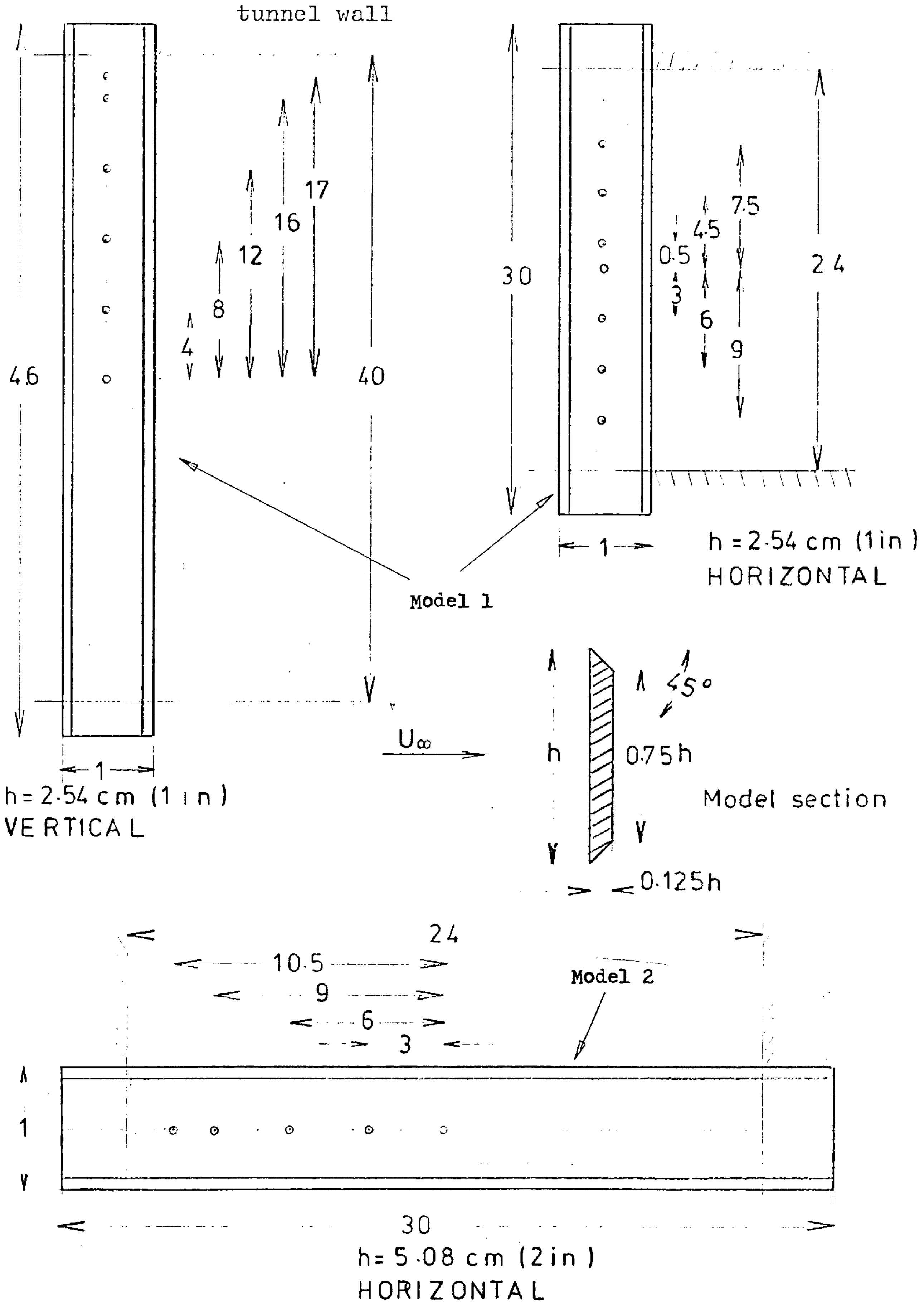

Fig **2.1** Dimension of the models not to Scale
(all dimensions normalized with respect to the body width h)

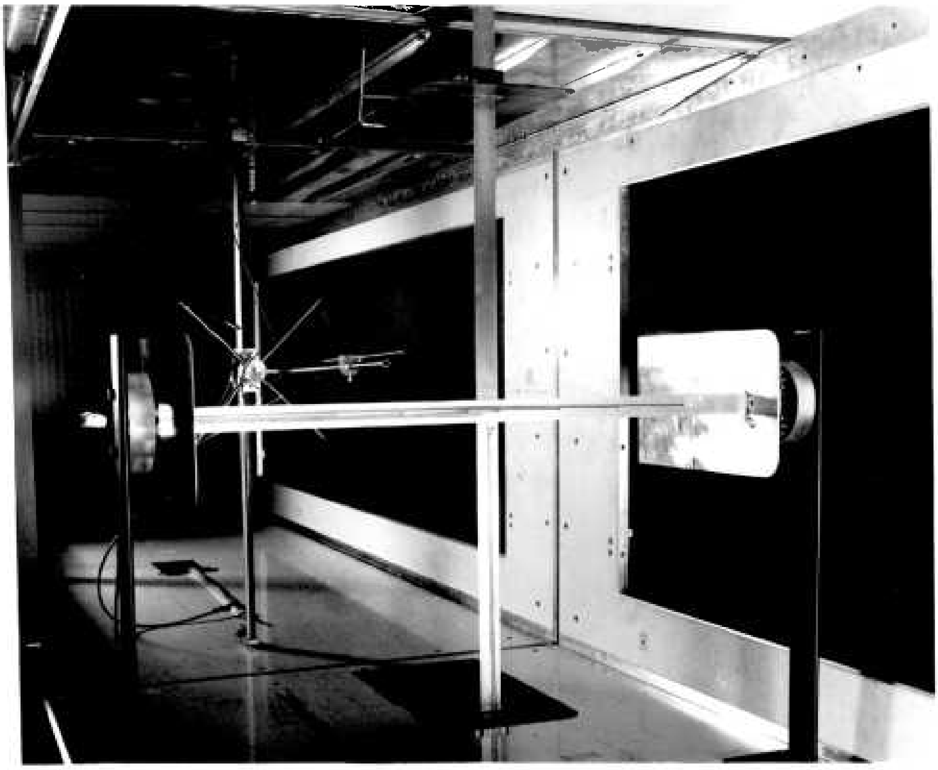

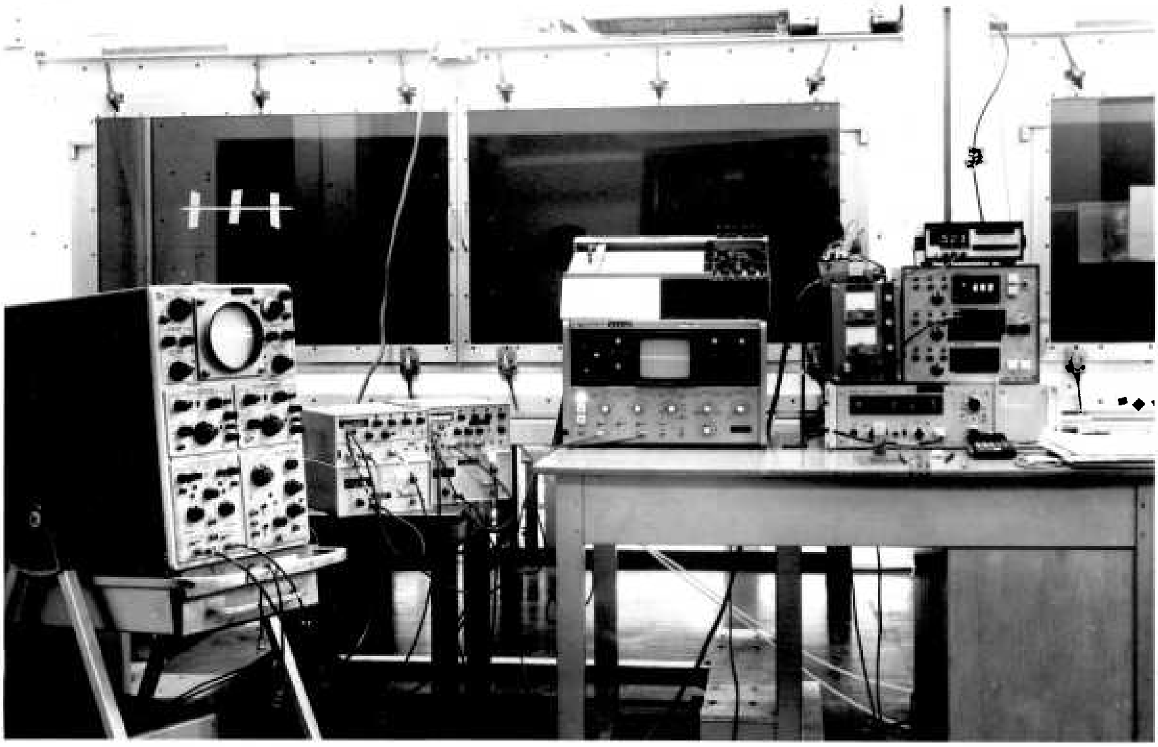

Figure 2.2 Intersecting flat plates in the large wind tunnel and set-up of the instrumentation

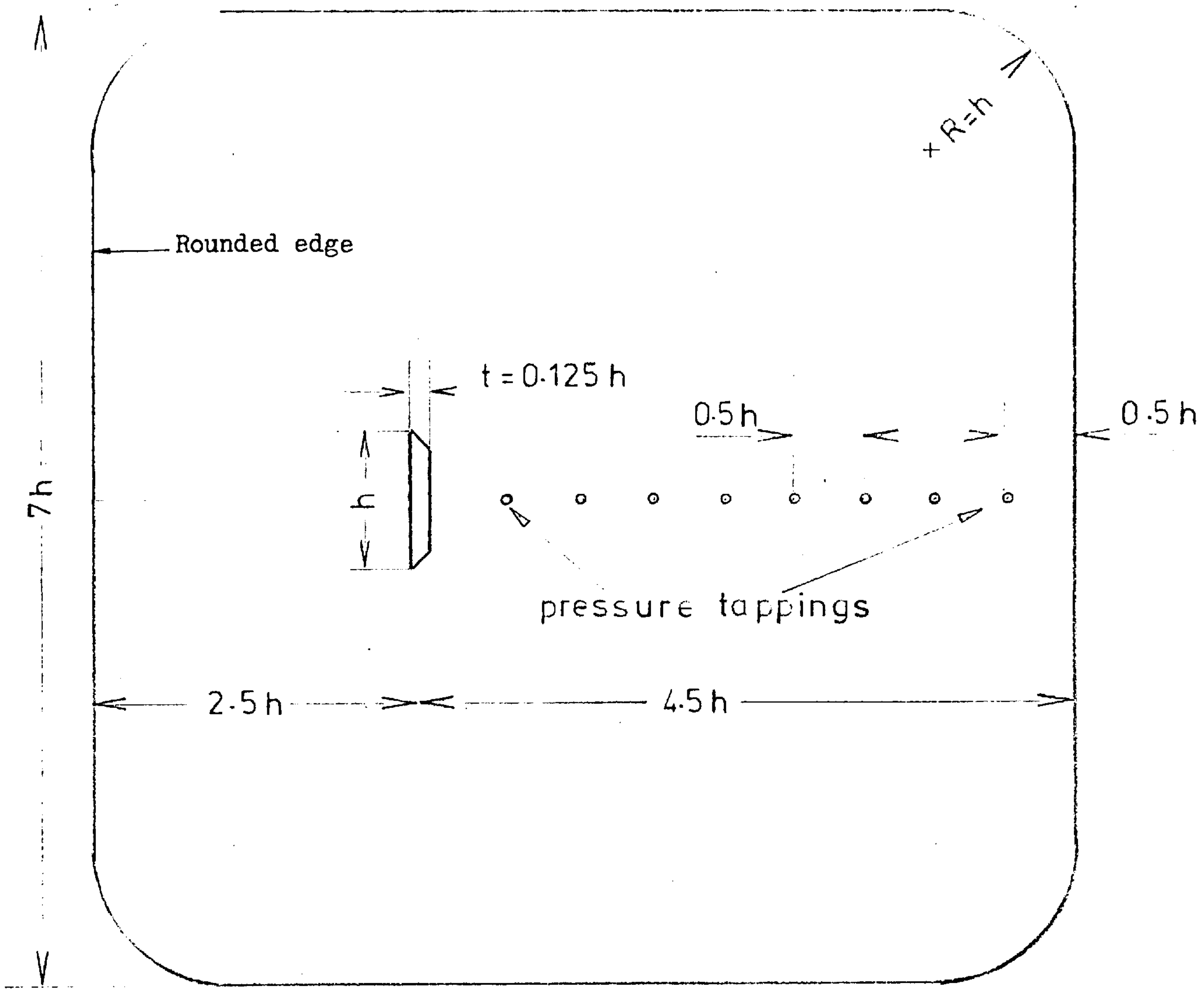

End Plates A

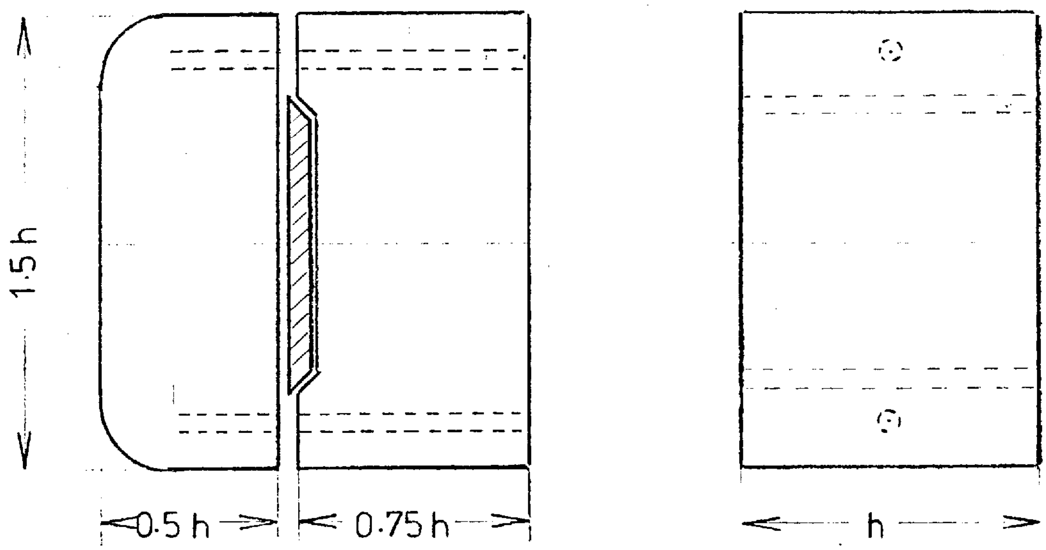

Fig 2.3 Adjustable slider

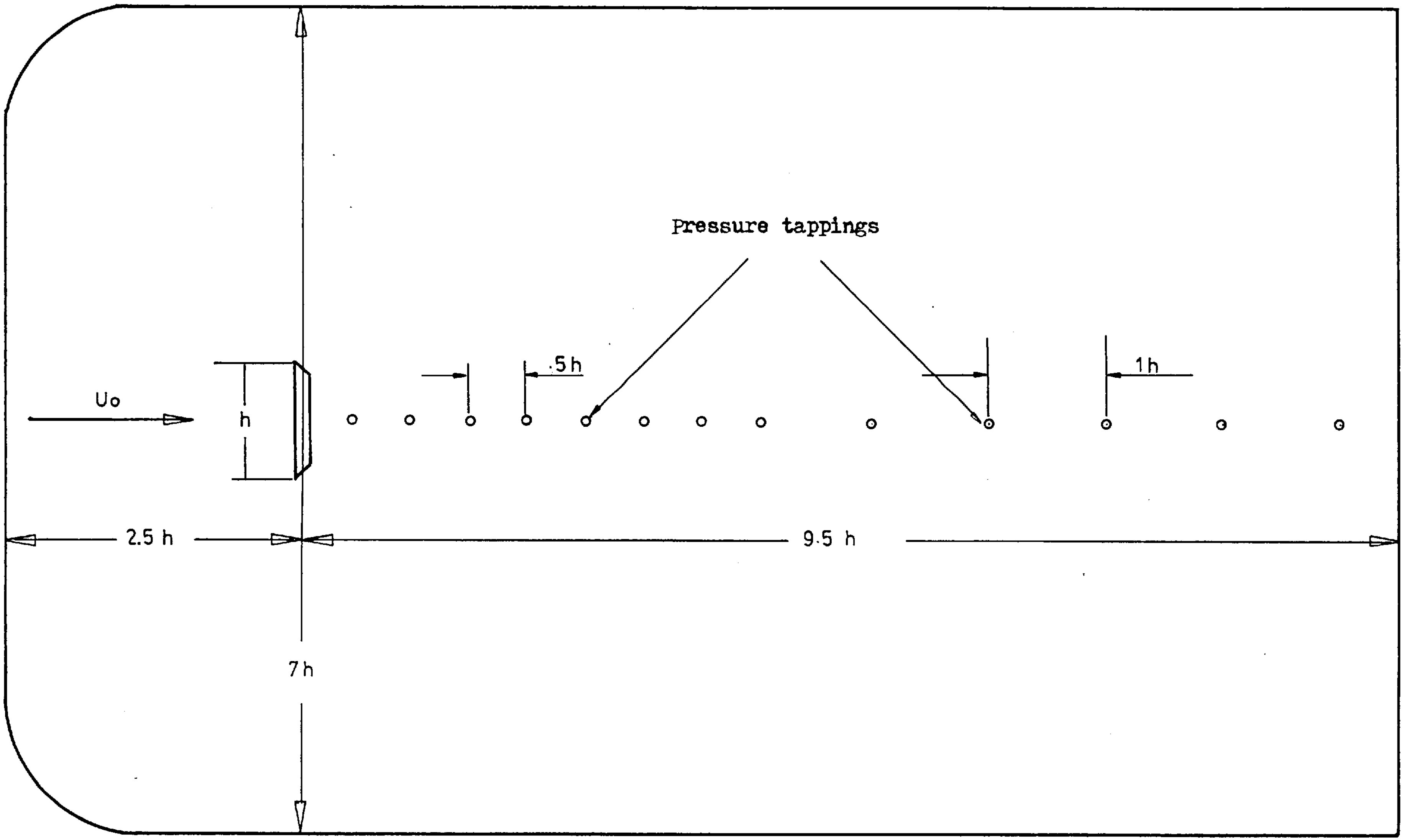

Figure 2.4 End Plate B

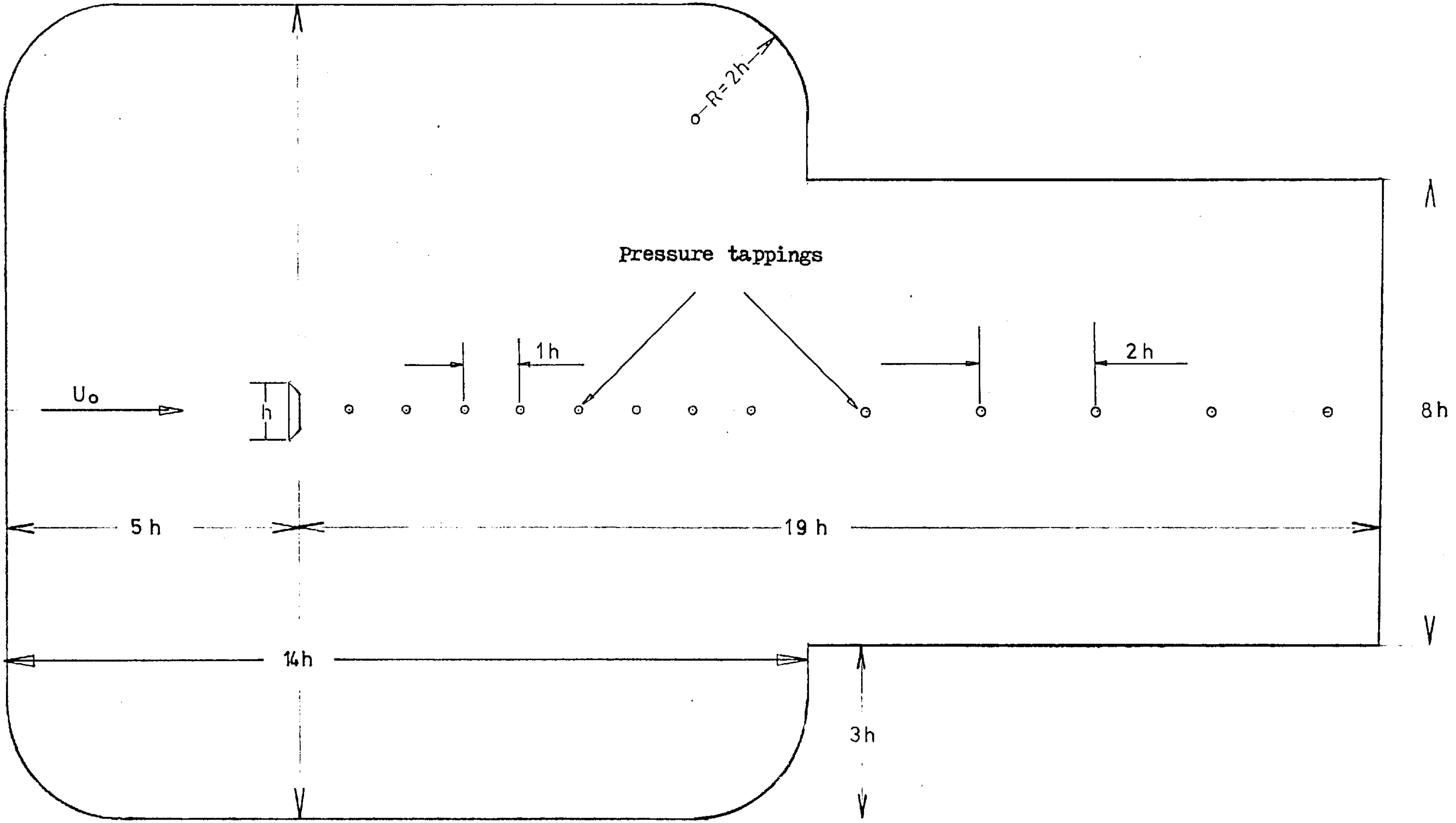

Figure 2.5 End plate C

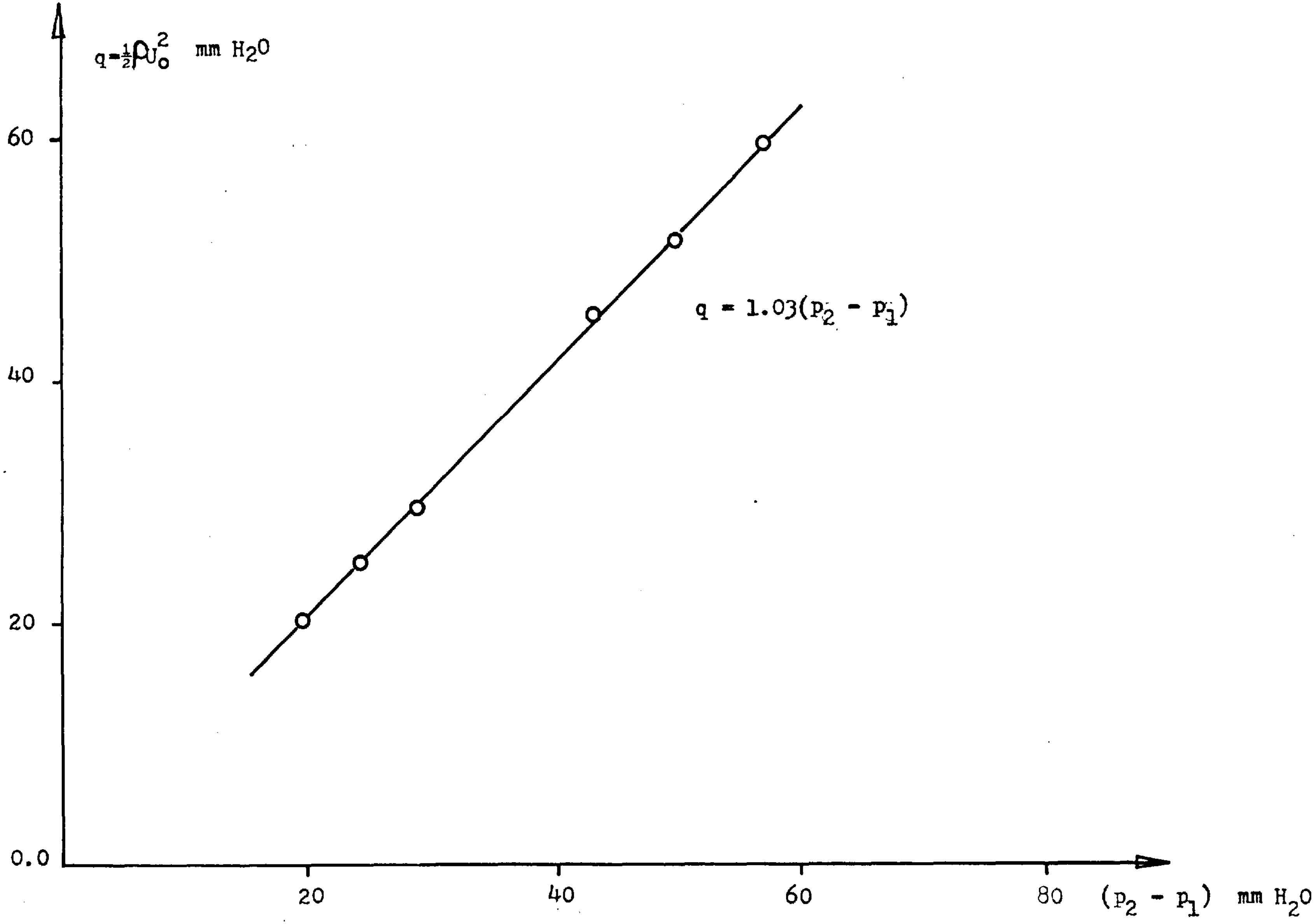

Figure 3.1 Smooth Stream Calibration of Dynamic Head (x = 1.3 m downstream)

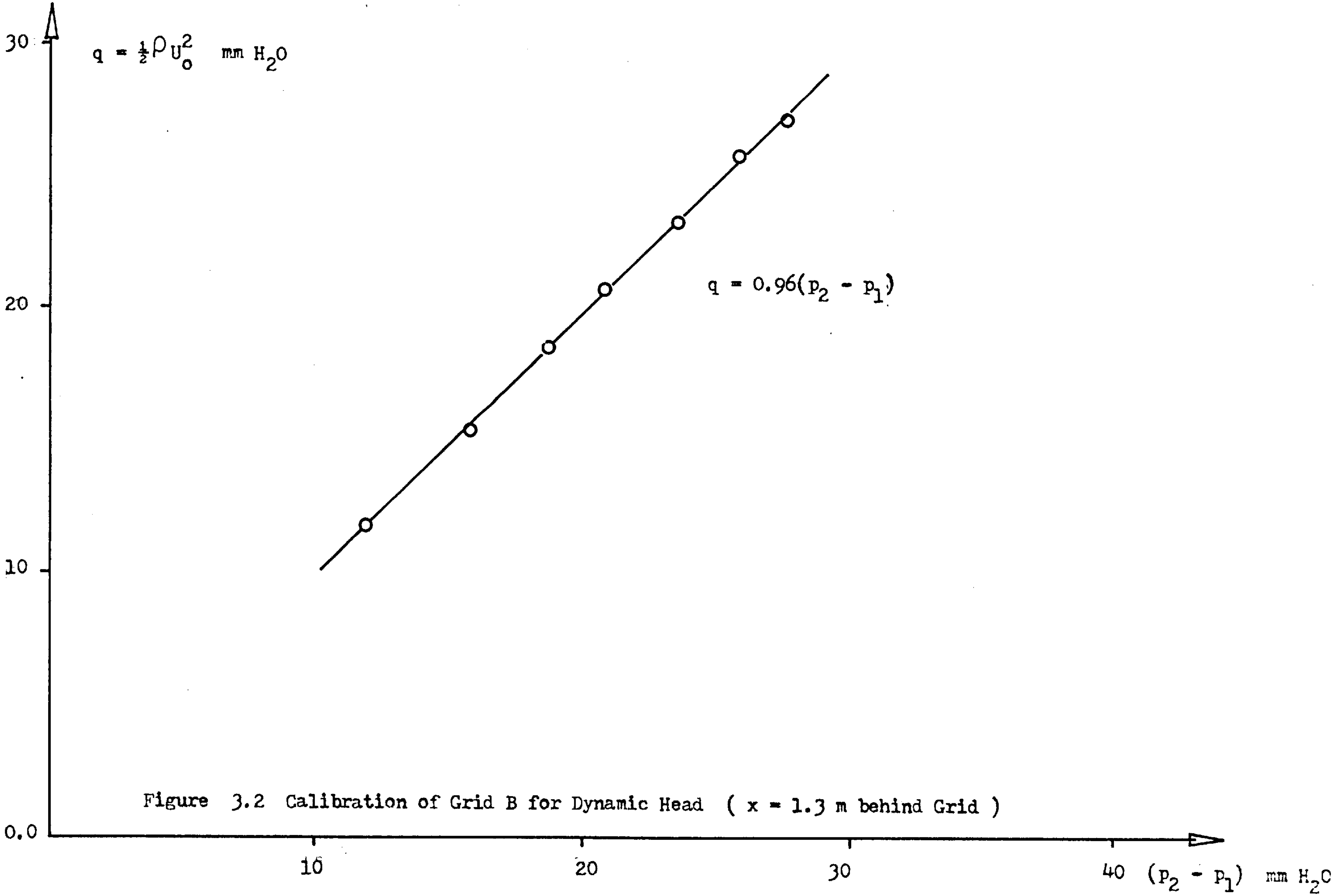

Figure 3.2 Calibration of Grid B for Dynamic Head (x = 1.3 m behind Grid)

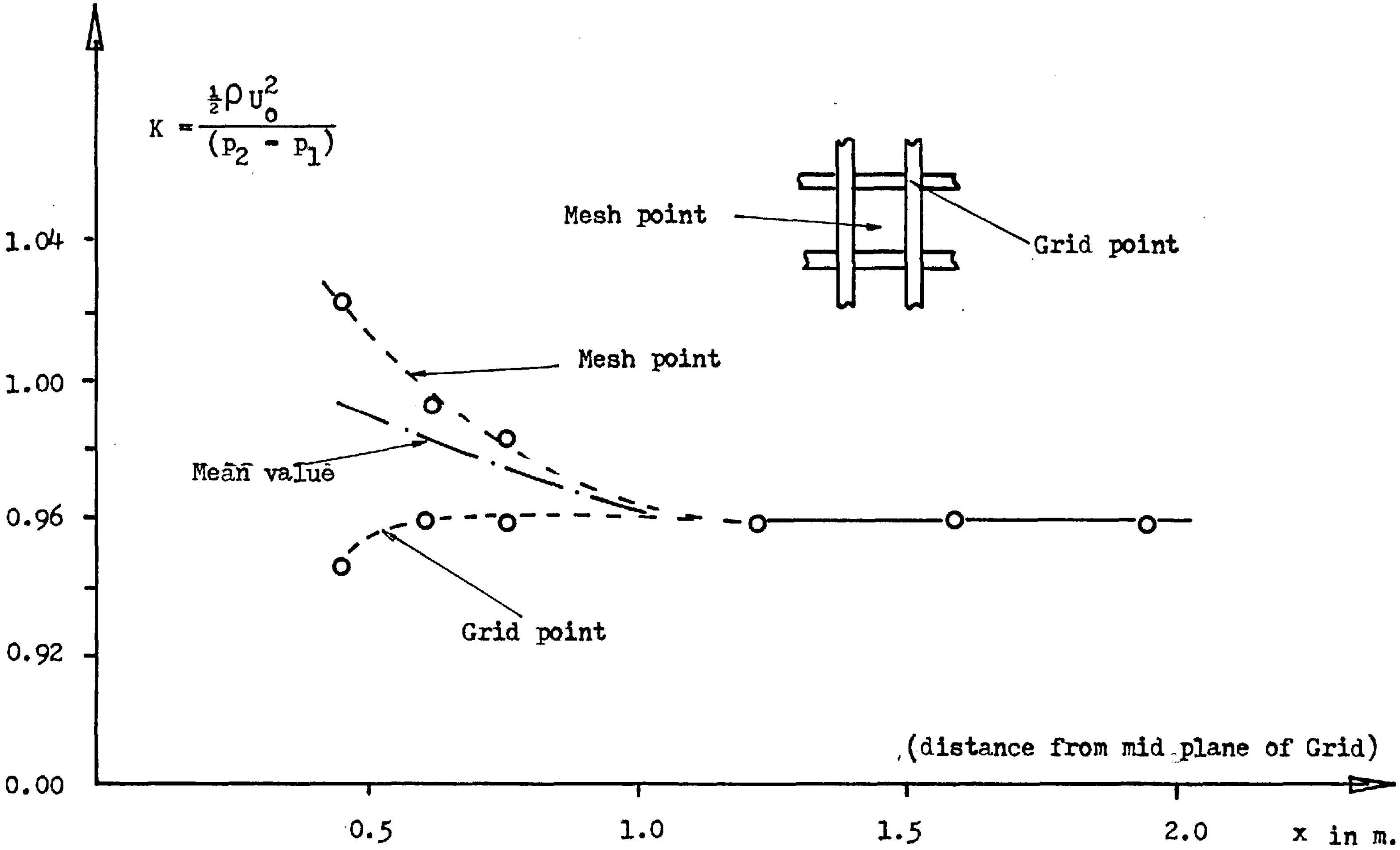

Figure 3.3 Non-Uniformities Behind Grid B

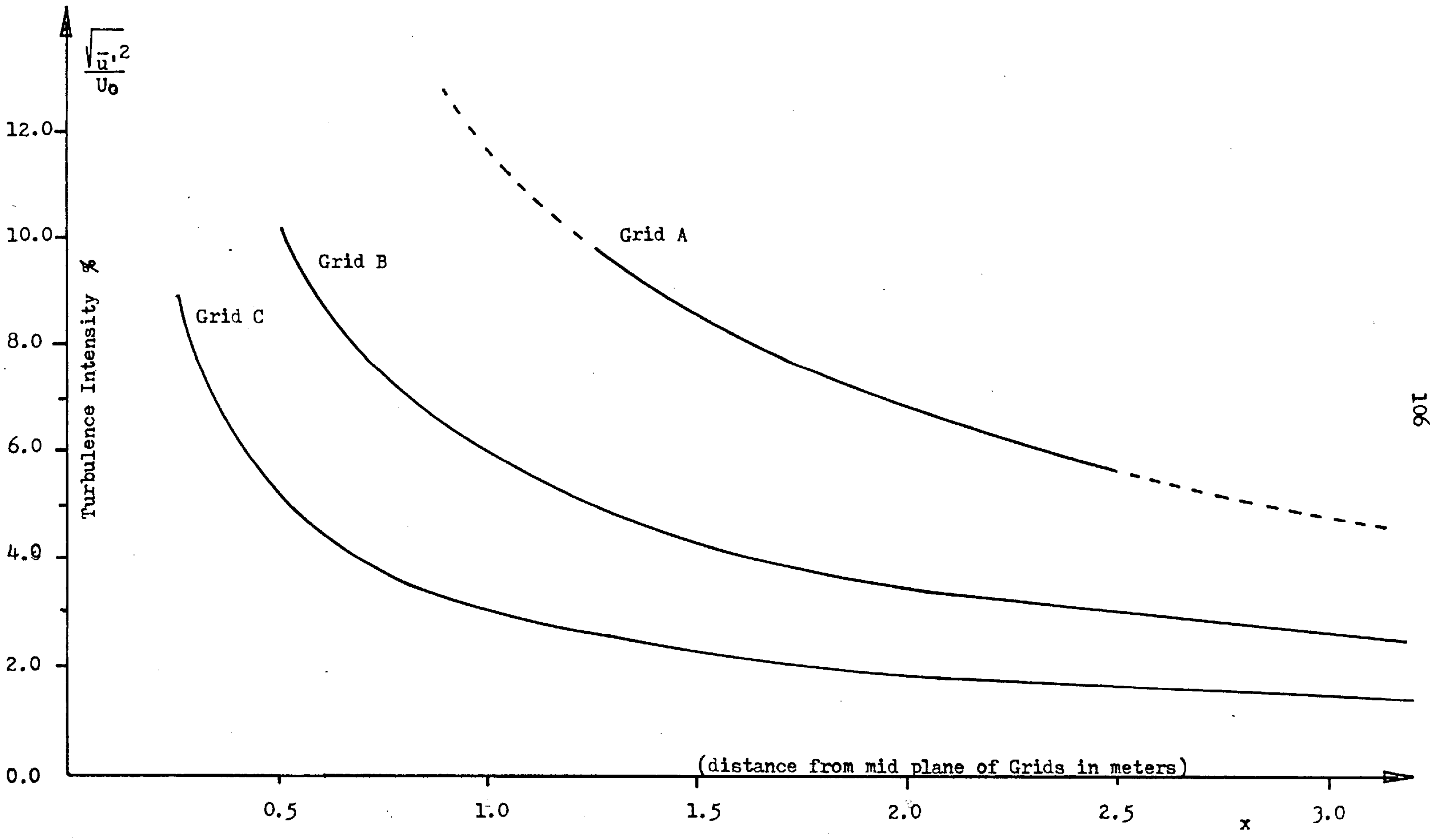

Figure 3.4 Turbulence Intesities Behind Grids

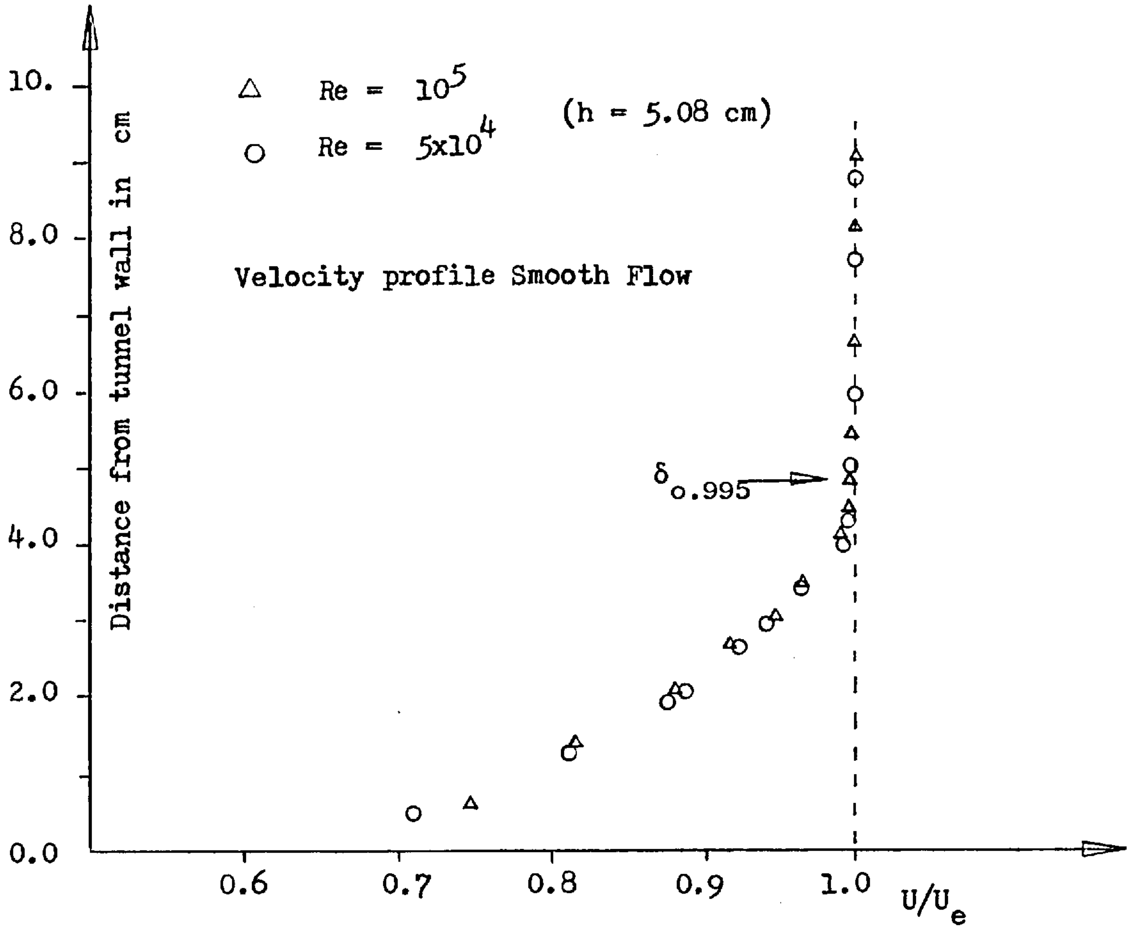

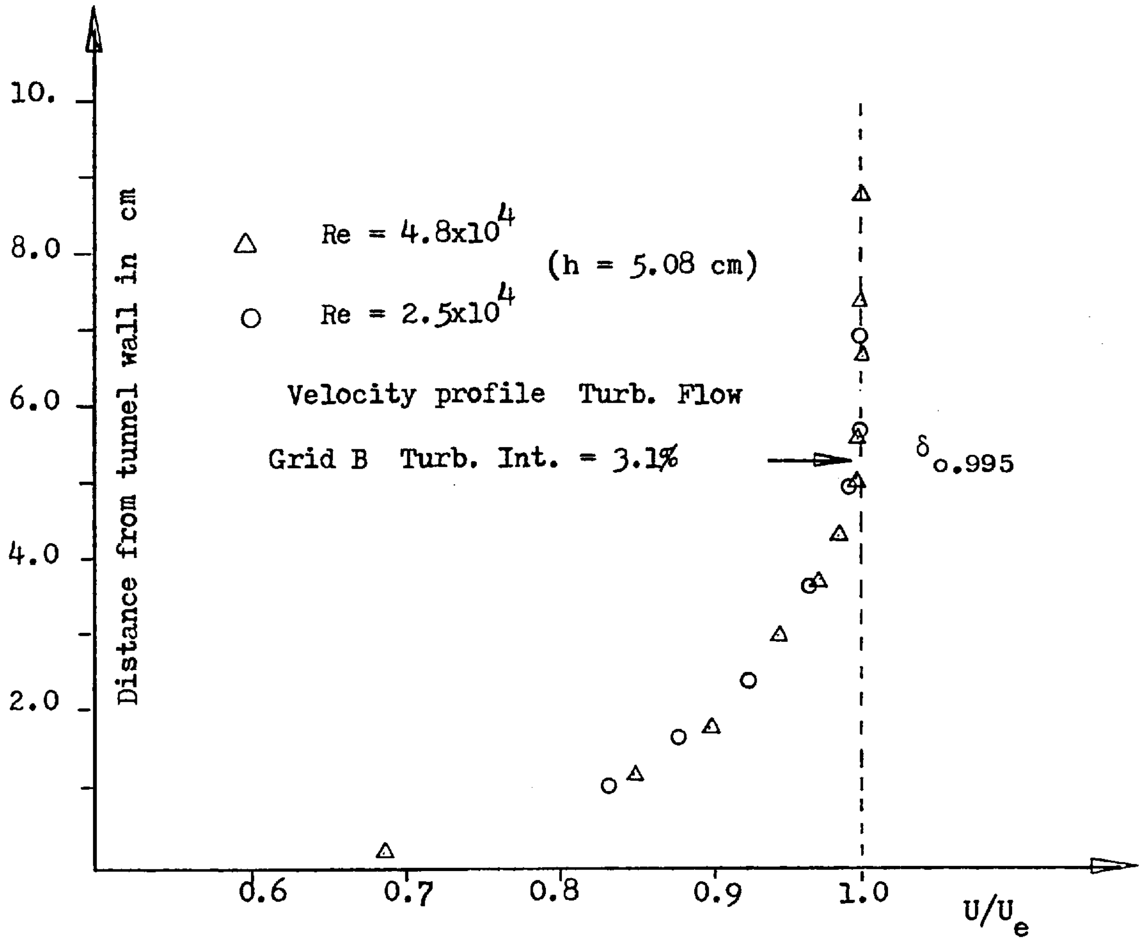

Figure 3.5 Velocity Profiles (2.46 m downstream)

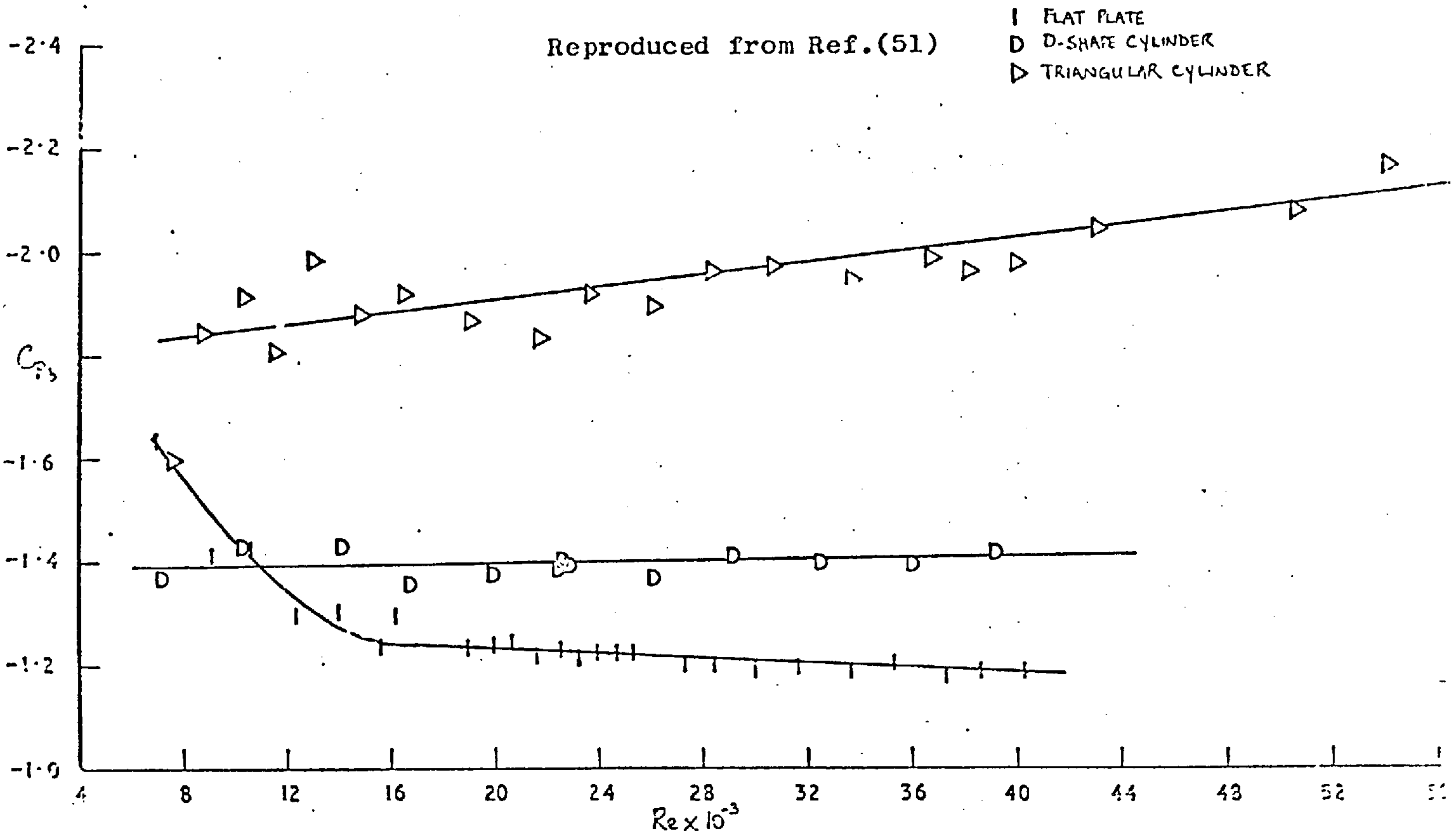

FIGURE 4 VARIATION OF BASE PRESSURE, WITH REYNOLDS NUMBER, FOR THREE STATIONARY BLUFF BODIES IN UNIFORM SMOOTH FLOW.

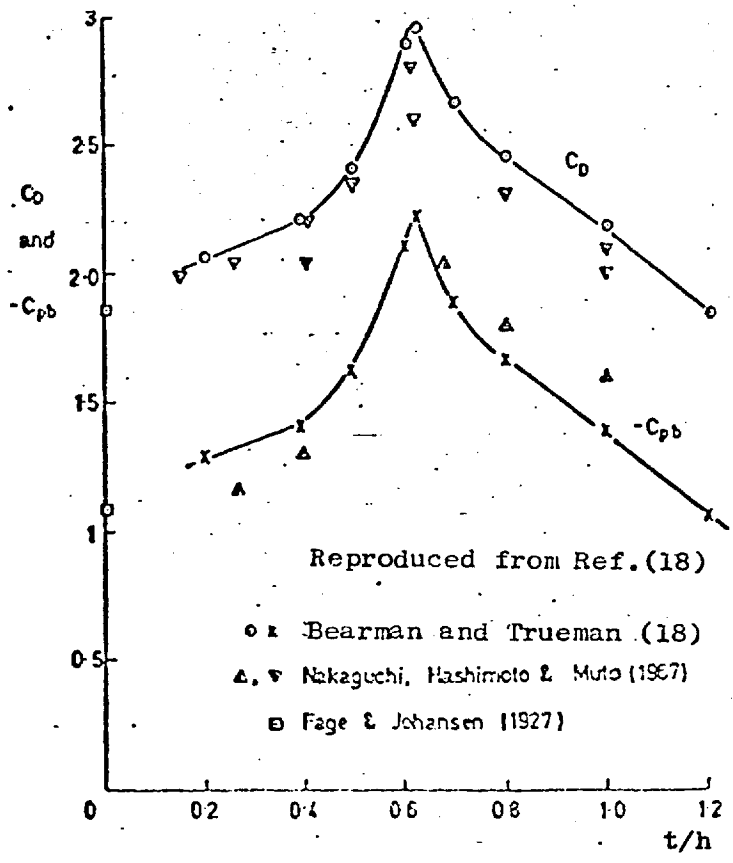

Figure 4.1 Drag and Base Pressure Coefficient on Rectangular Sections

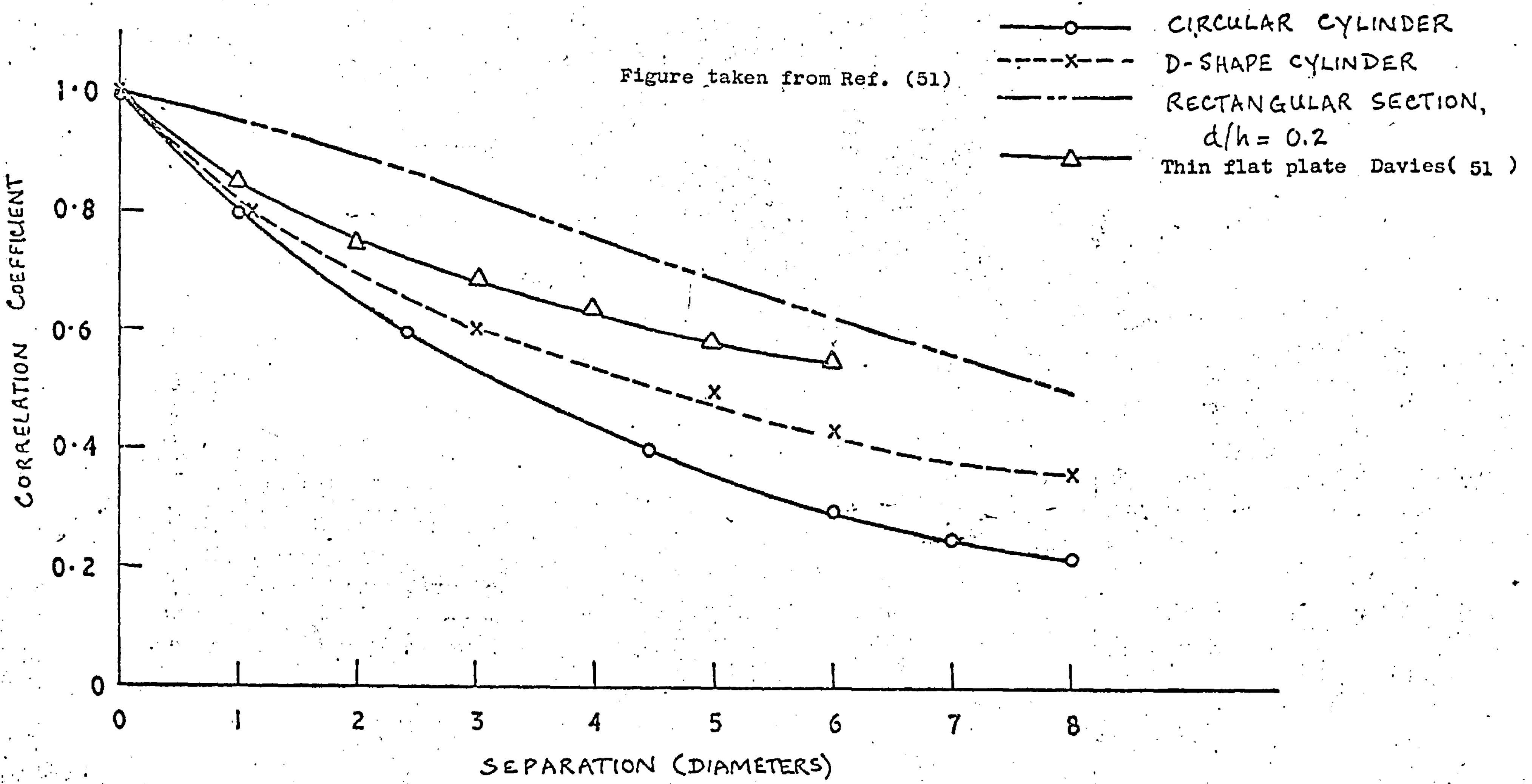

Figure taken from Ref. (51)

Figure 4.2 CORRELATIONS ALONG THE SPAN OF VARIOUS BLUFF BODIES

Figure taken from Ref.(53)

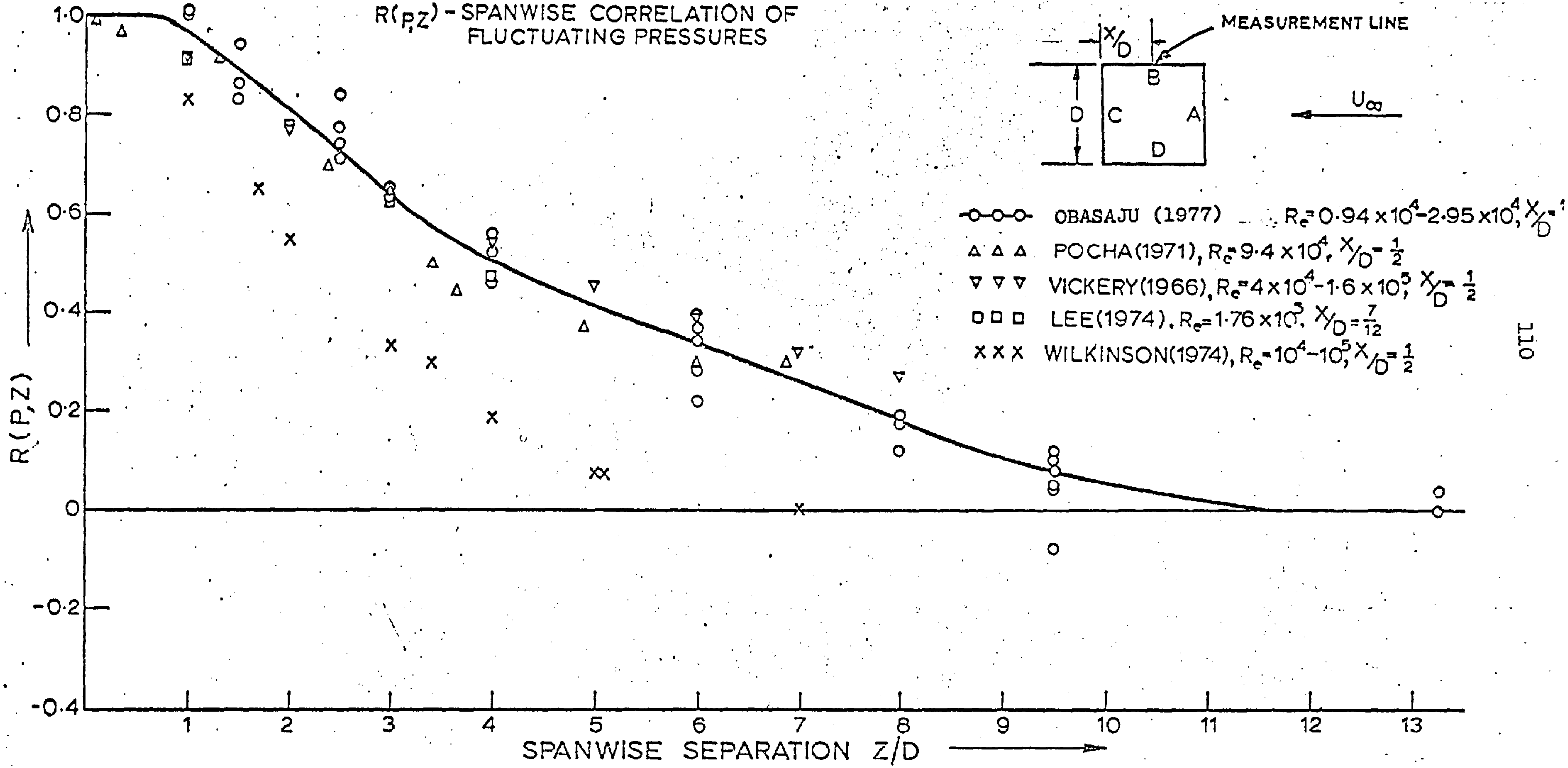

Figure 4.3 *Spanwise distribution of R(P,Z) on face B of a stationary square section cylinder at α = 0°*

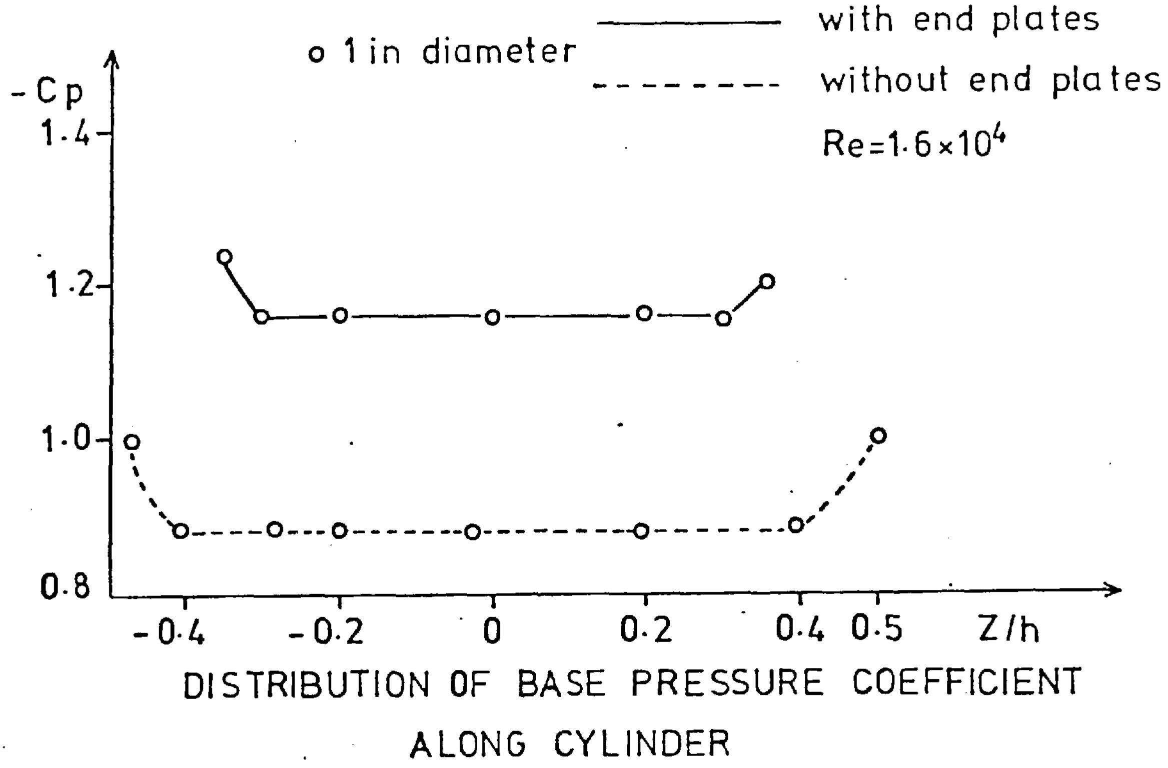

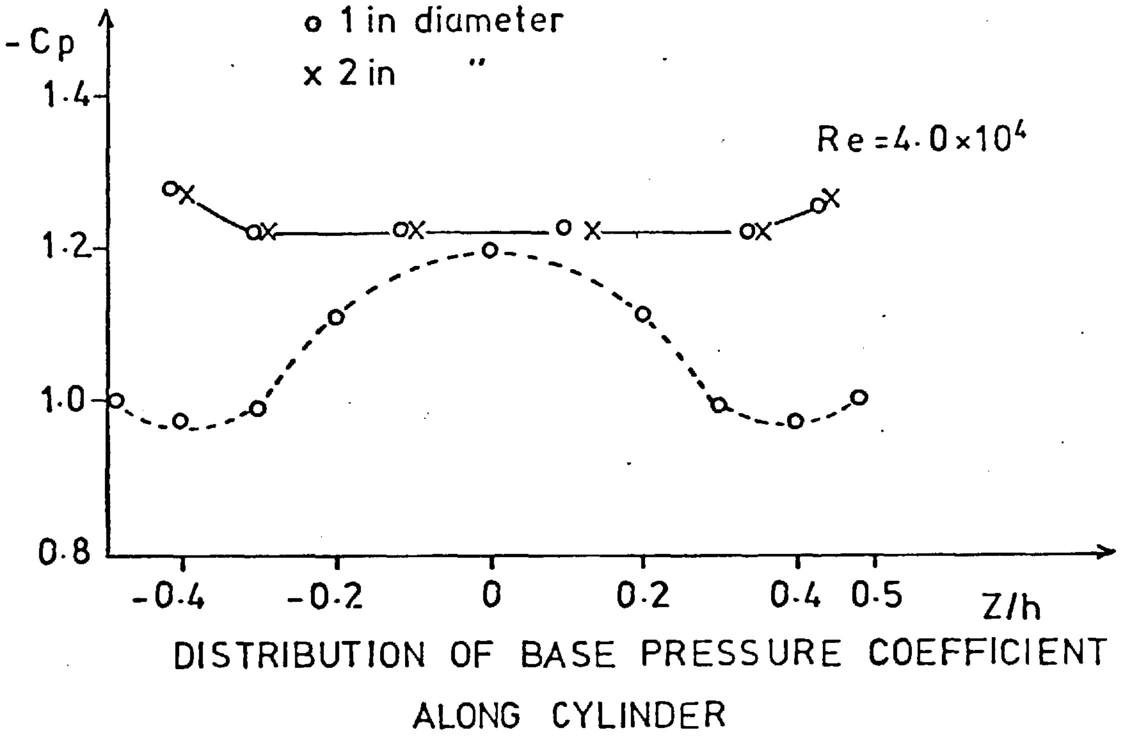

FIGURE 4.4 BASE PRESSURE OF CIRCULAR CYLINDER
(Data taken from reference 13)

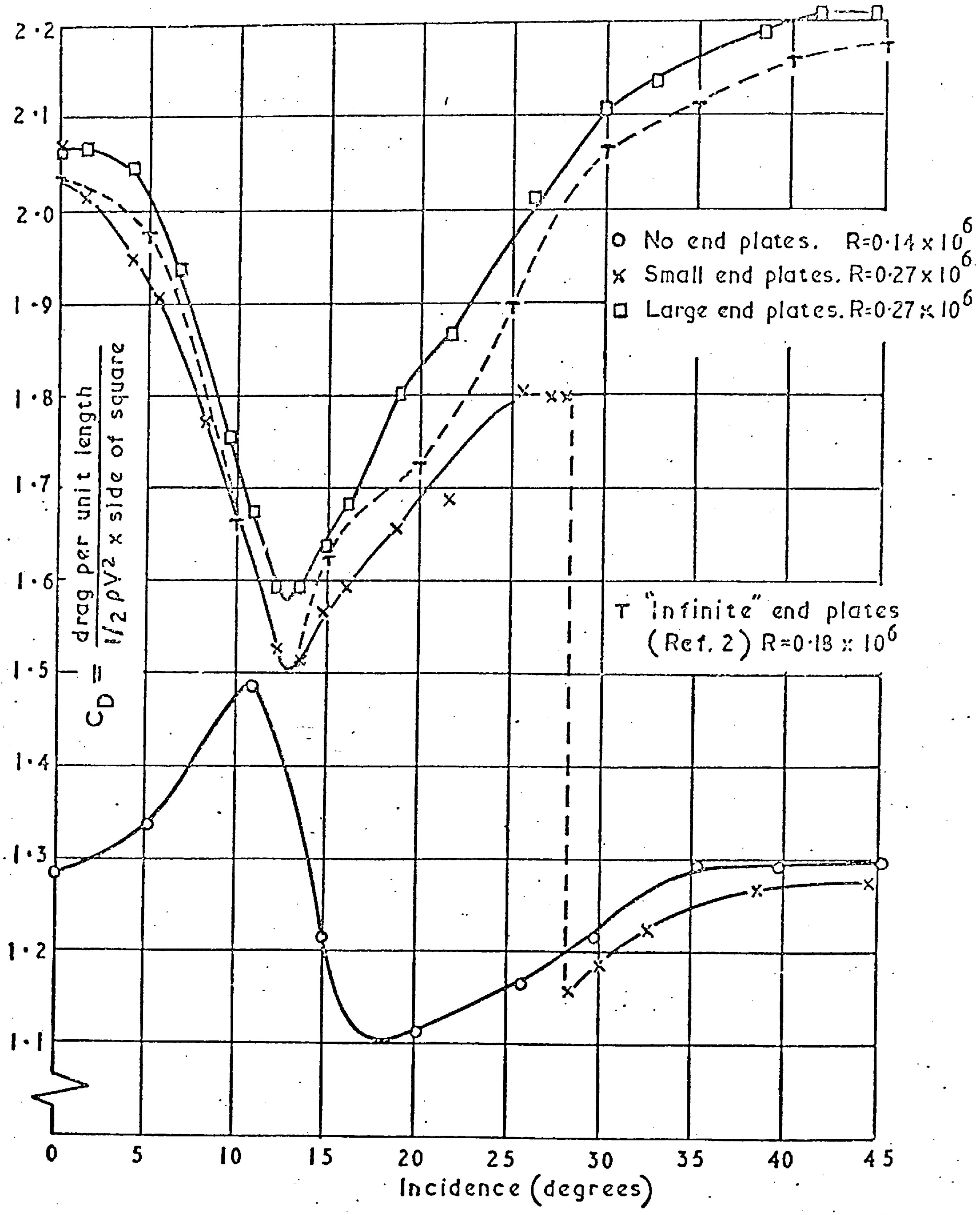

Figure 4.5 Drag of square-section cylinder

(Data taken from reference 14)

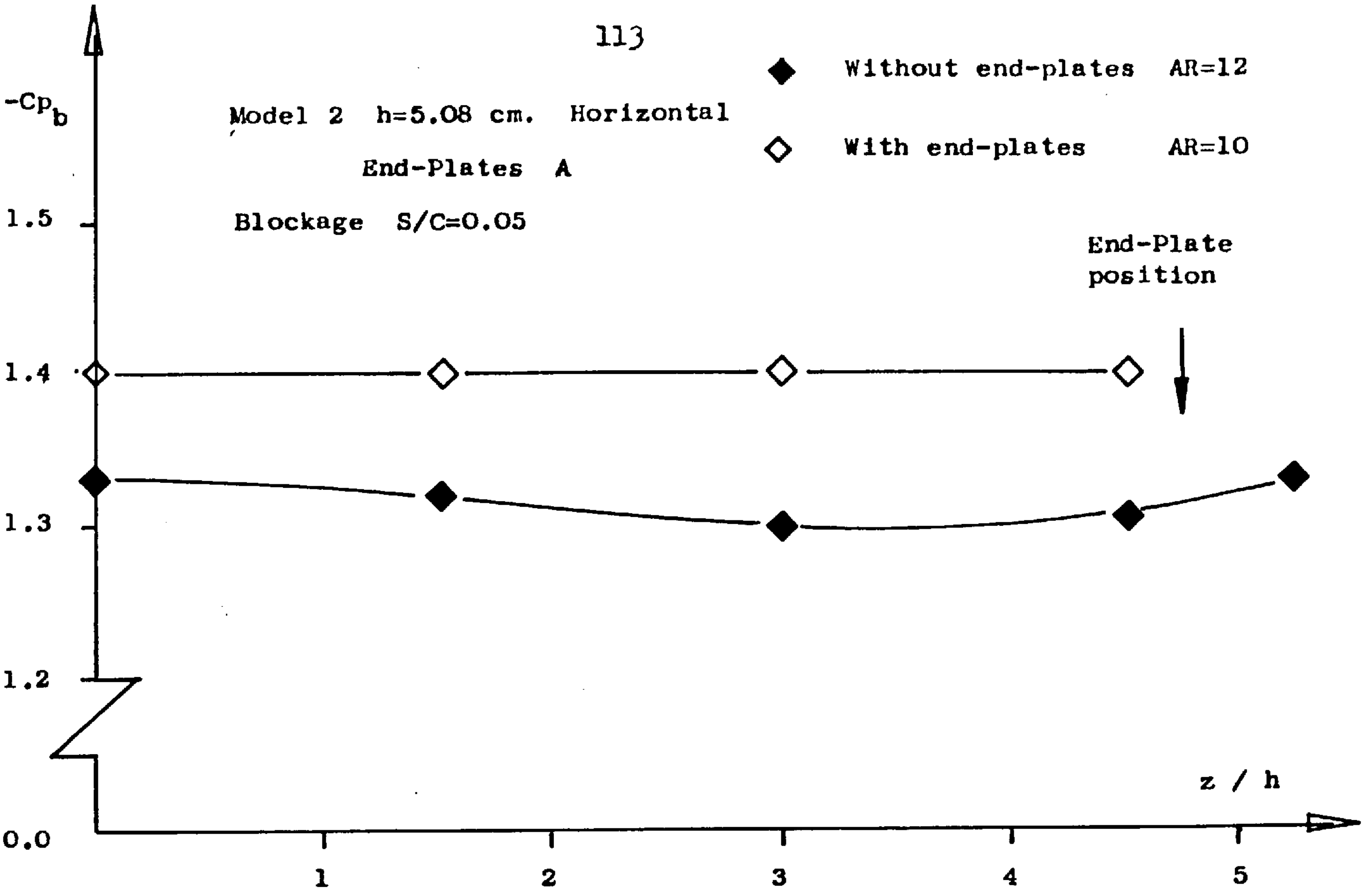

Figure 4.6 Spanwise Pressure Distribution in Smooth Flow
(Uncorrected for Blockage)

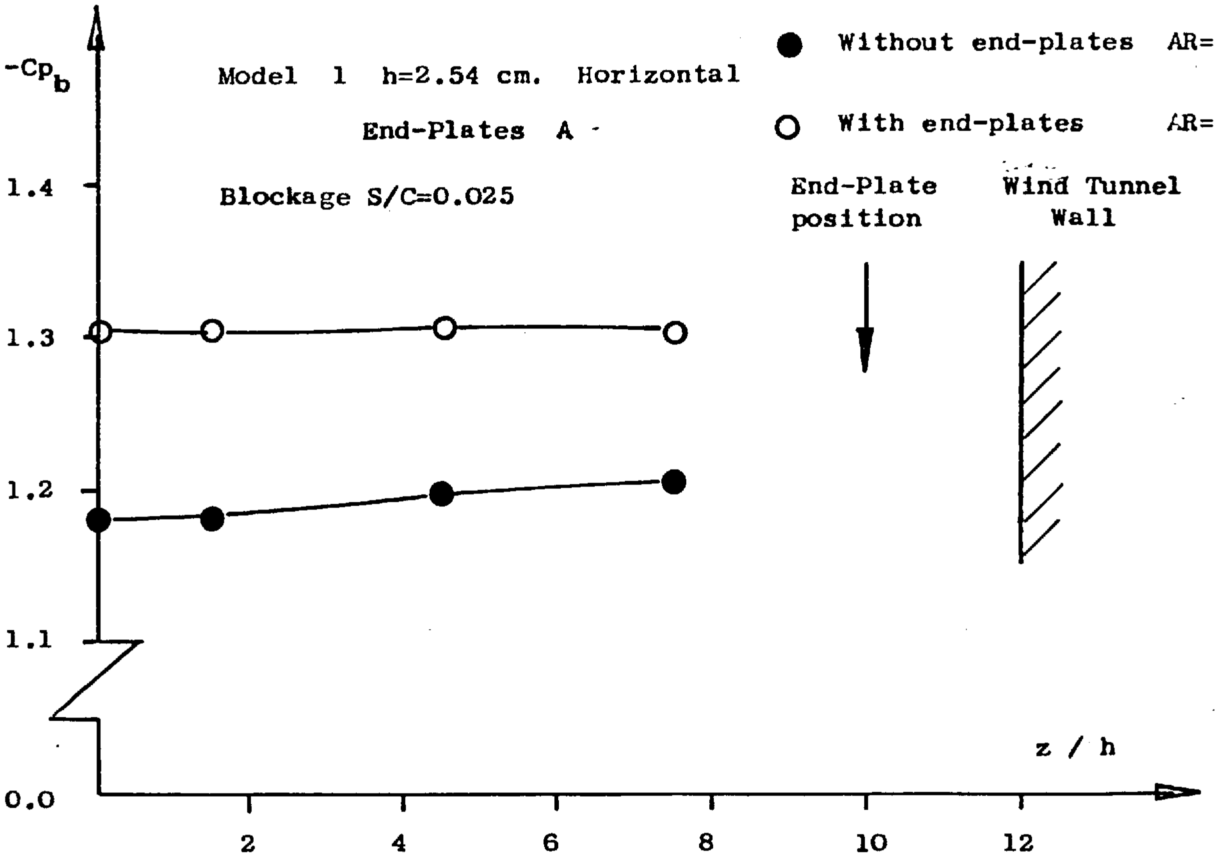

Figure 4.7 Spanwise Pressure Distribution in Smooth Flow
(Uncorrected for Blockage)

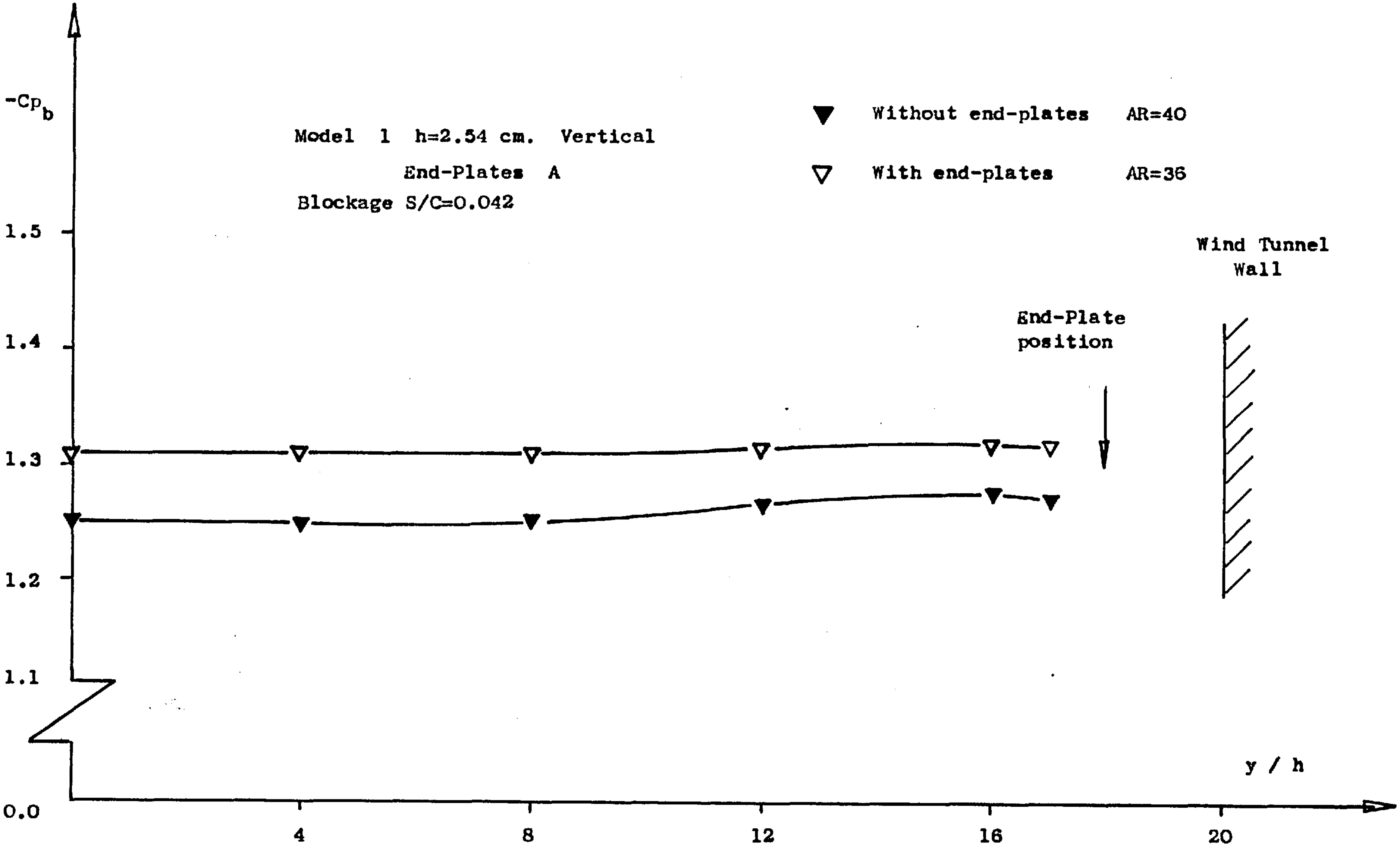

Figure 4.8 Spanwise Pressure Distribution in Smooth Flow (Uncorrected for Blockage)

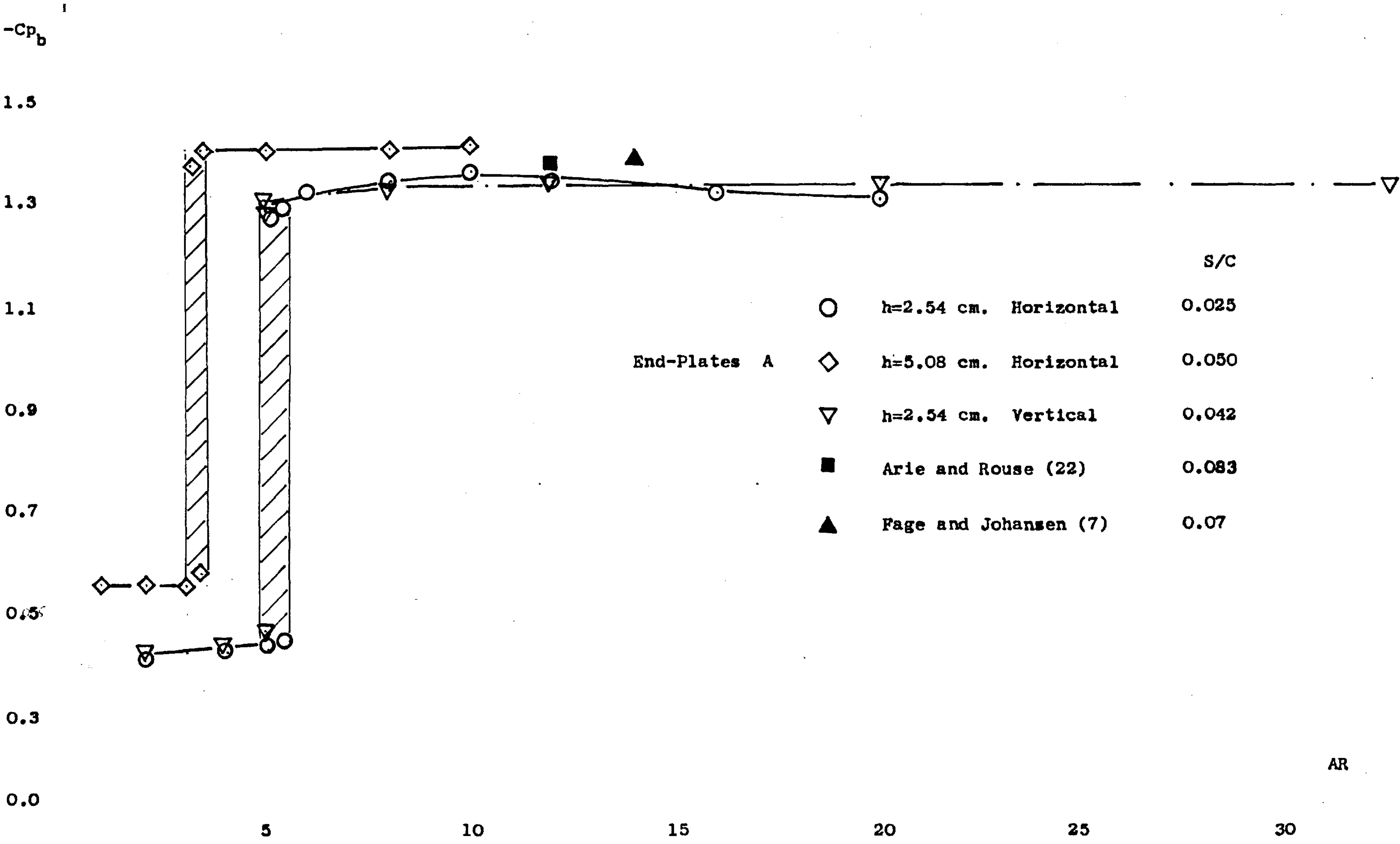

Figure 4.9 Base Pressure Coefficient at mid-span versus Aspect Ratio in Smooth Flow (Uncorrected for Blockage)

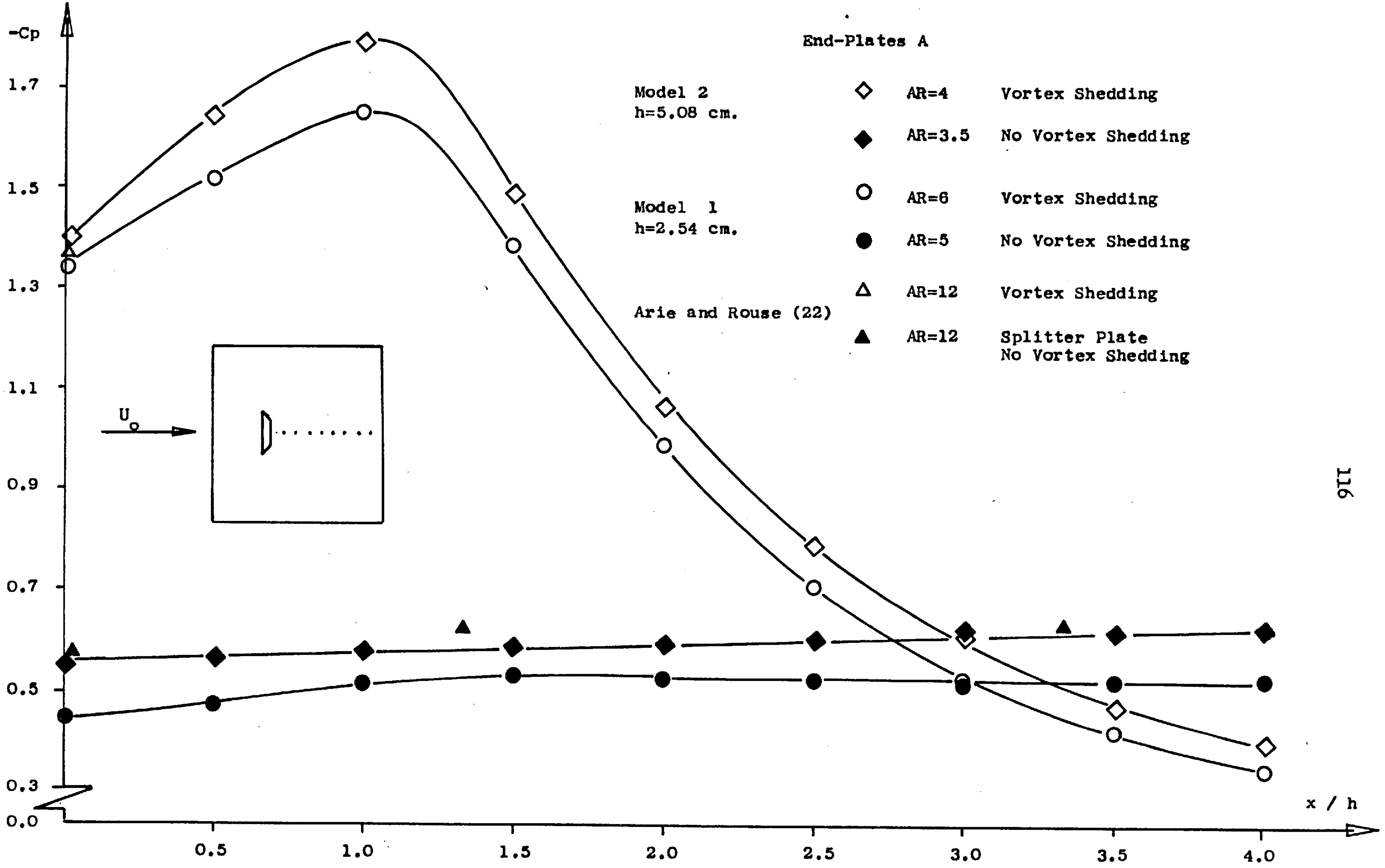

Figure 4.10 Base Pressure Coefficient Distribution (downstream) on the End-Plate Centre Line

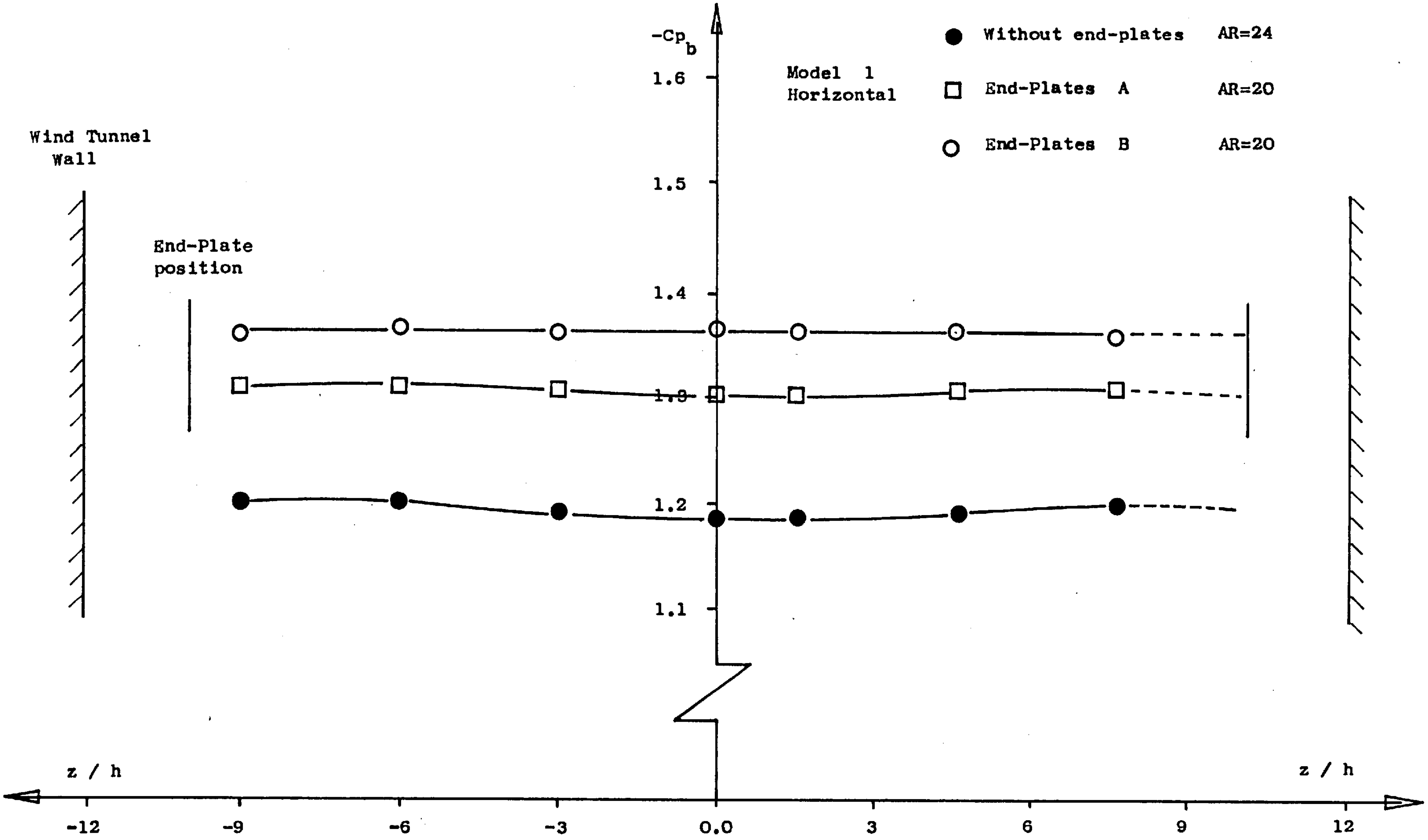

Figure 4.11 Spanwise Base Pressure Coefficient Distribution in Smooth Flow (Uncorrected for Blockage)

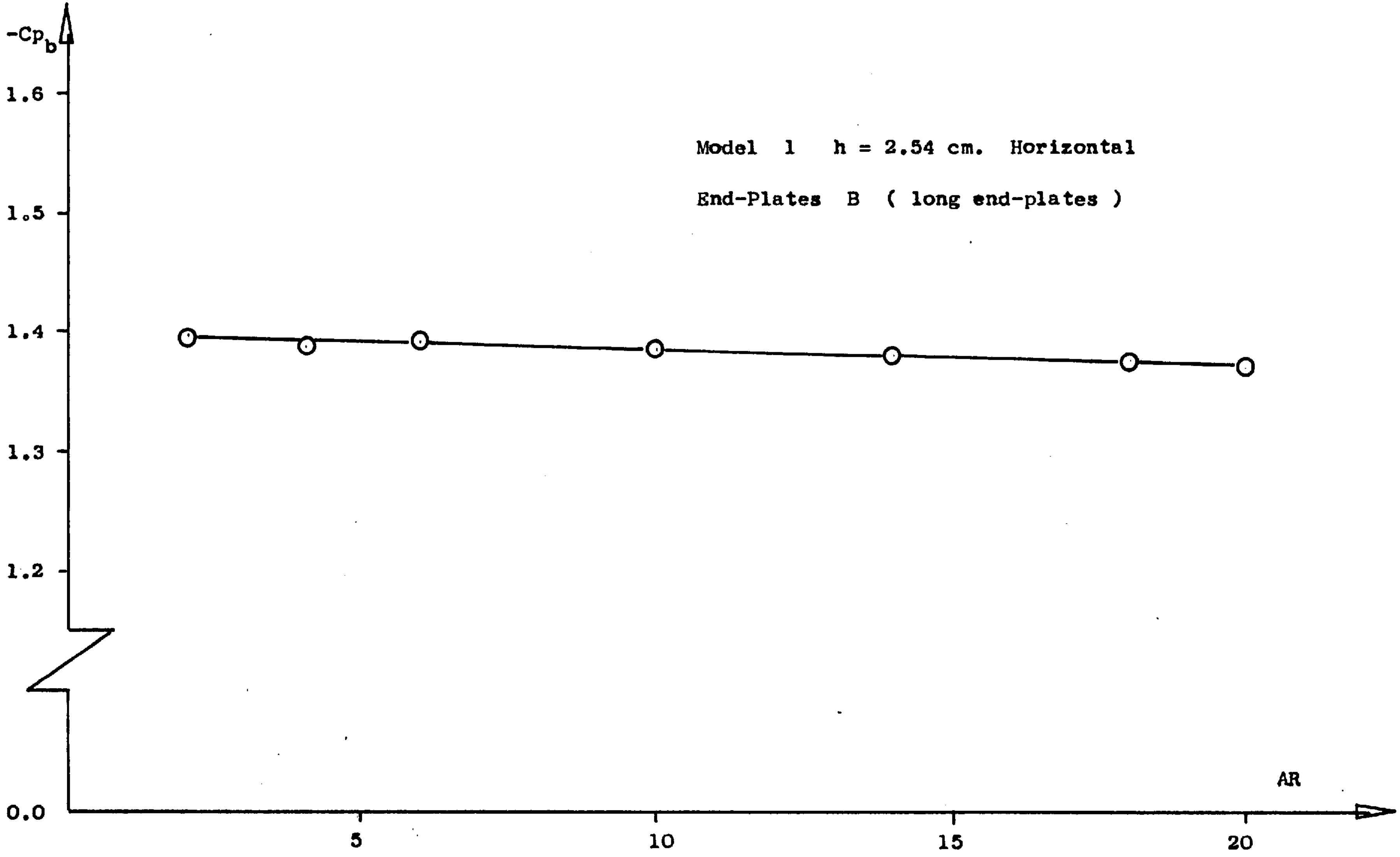

Figure 4.12 Base Pressure Coefficient at Mid-Span versus Aspect Ratio in Smooth Flow (Uncorrected for Blockage)

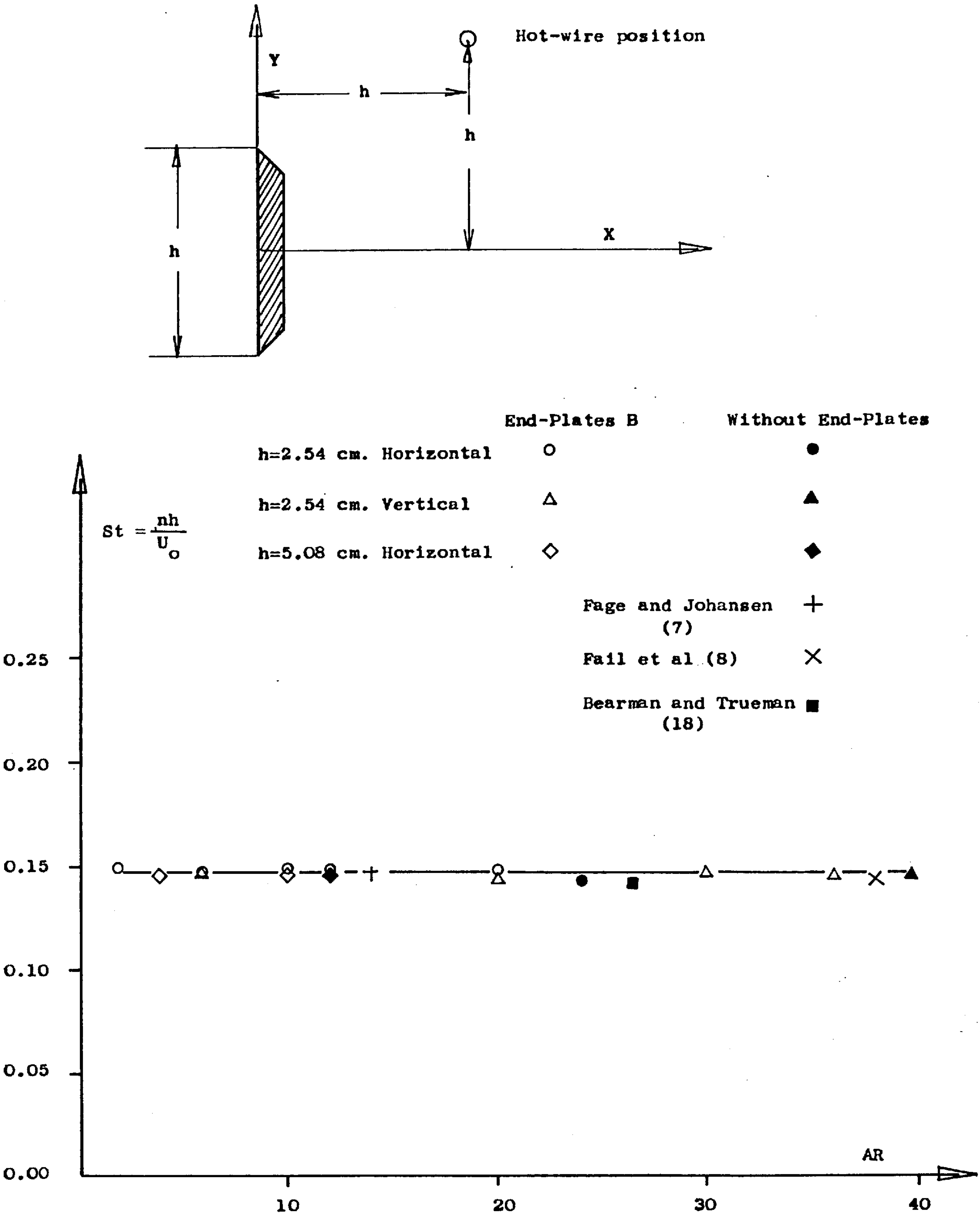

Figure 4.13 Strouhal Number versus Aspect Ratio in Smooth Flow
(Uncorrected for Blockage)

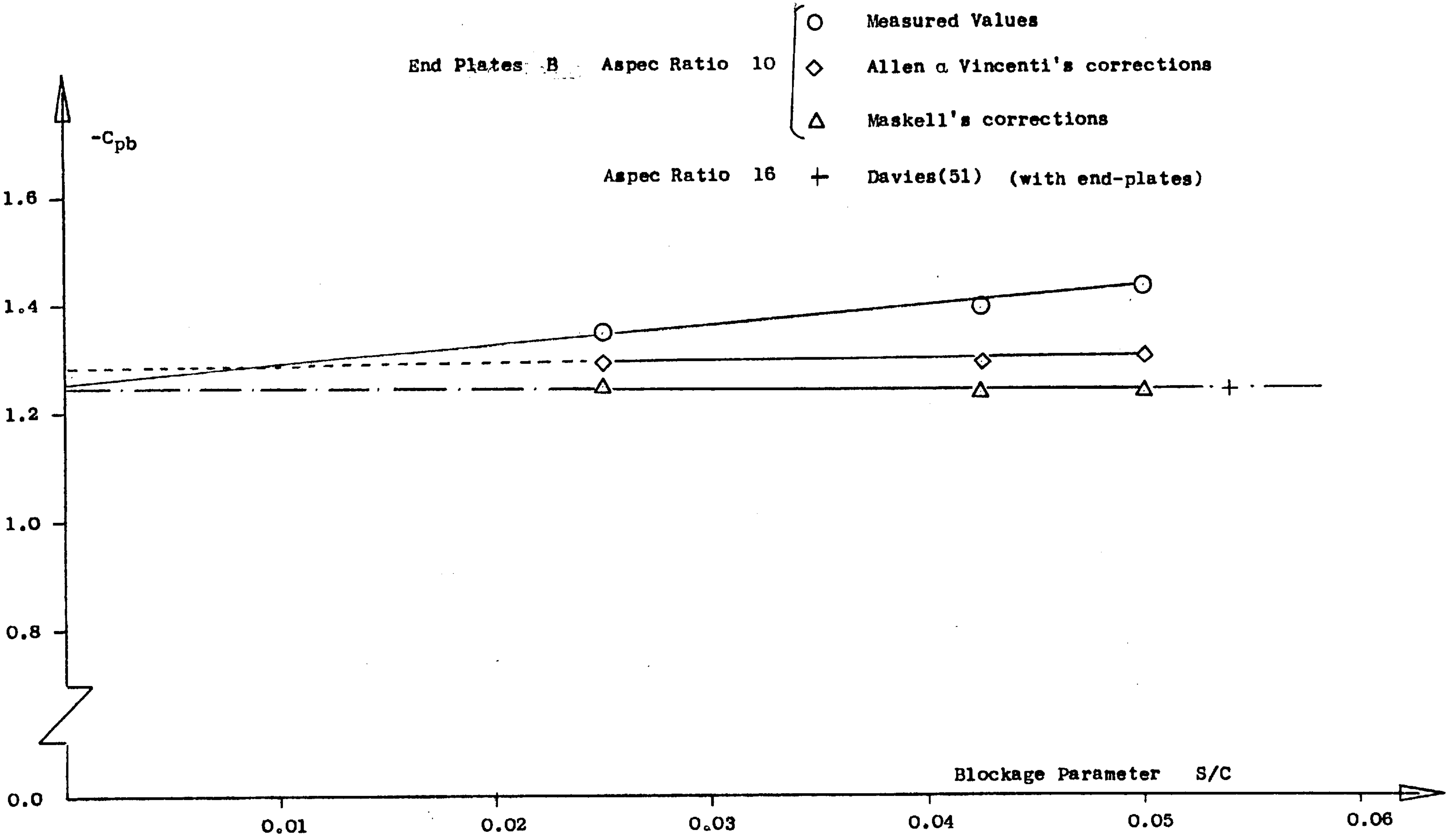

Figure 4.14 Base Pressure Coefficient corrected for Blockage in Smooth Flow

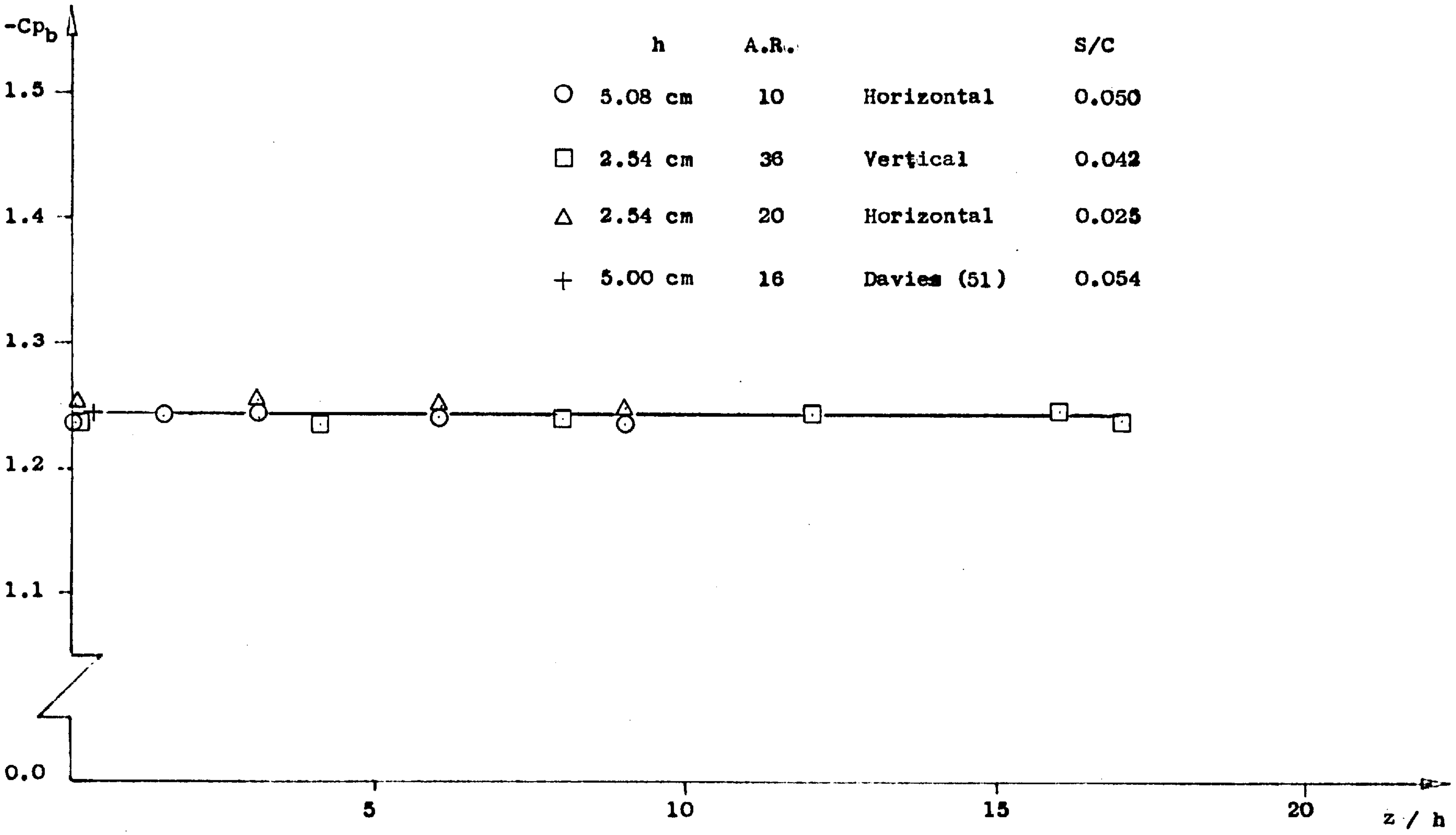

Figure 4.15 Corrected Base Pressure Coefficient Across the Span With End Plates in Smooth Flow

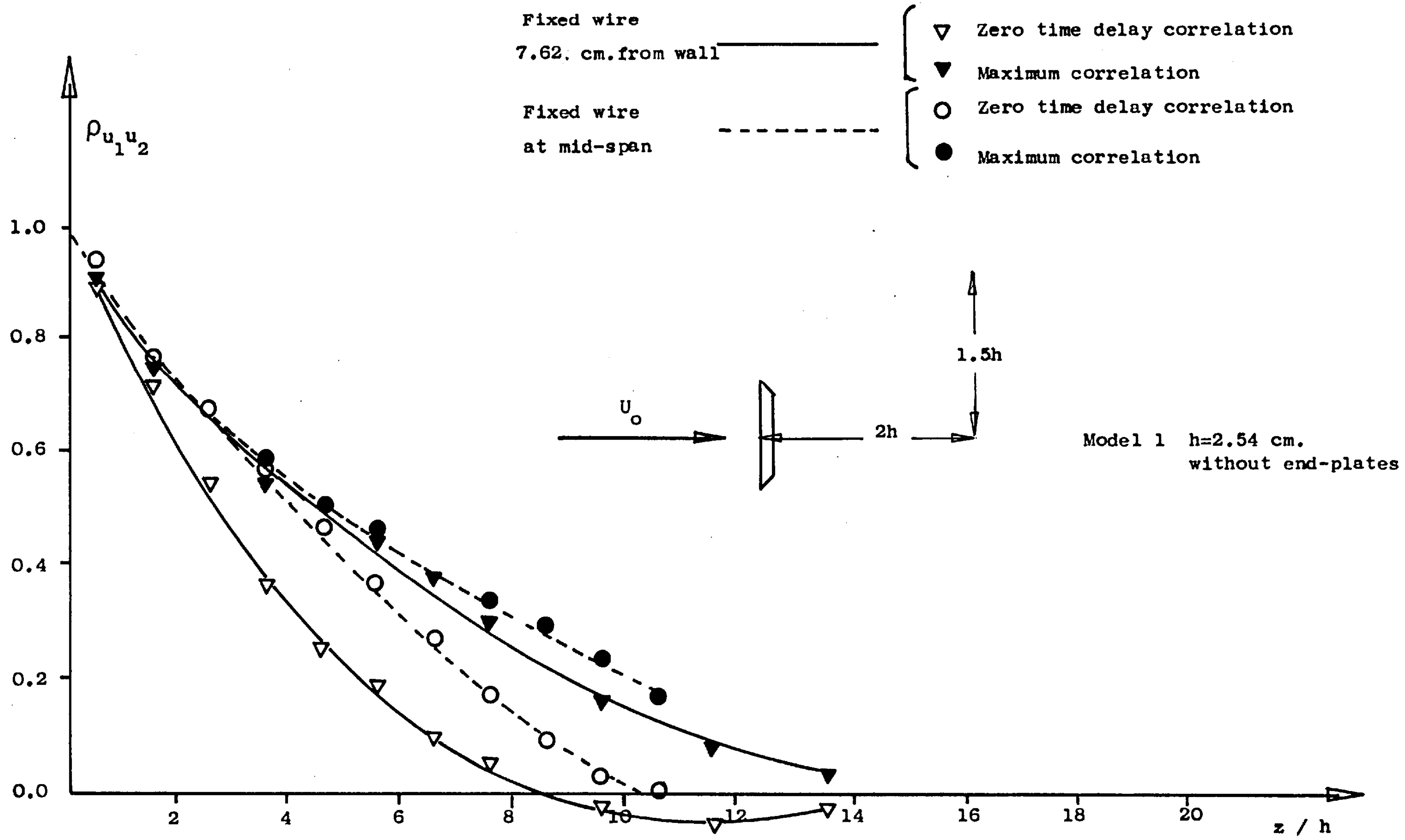

Figure 4.16 Lateral Velocity Correlation Coefficient Without End-Plates in Smooth Flow

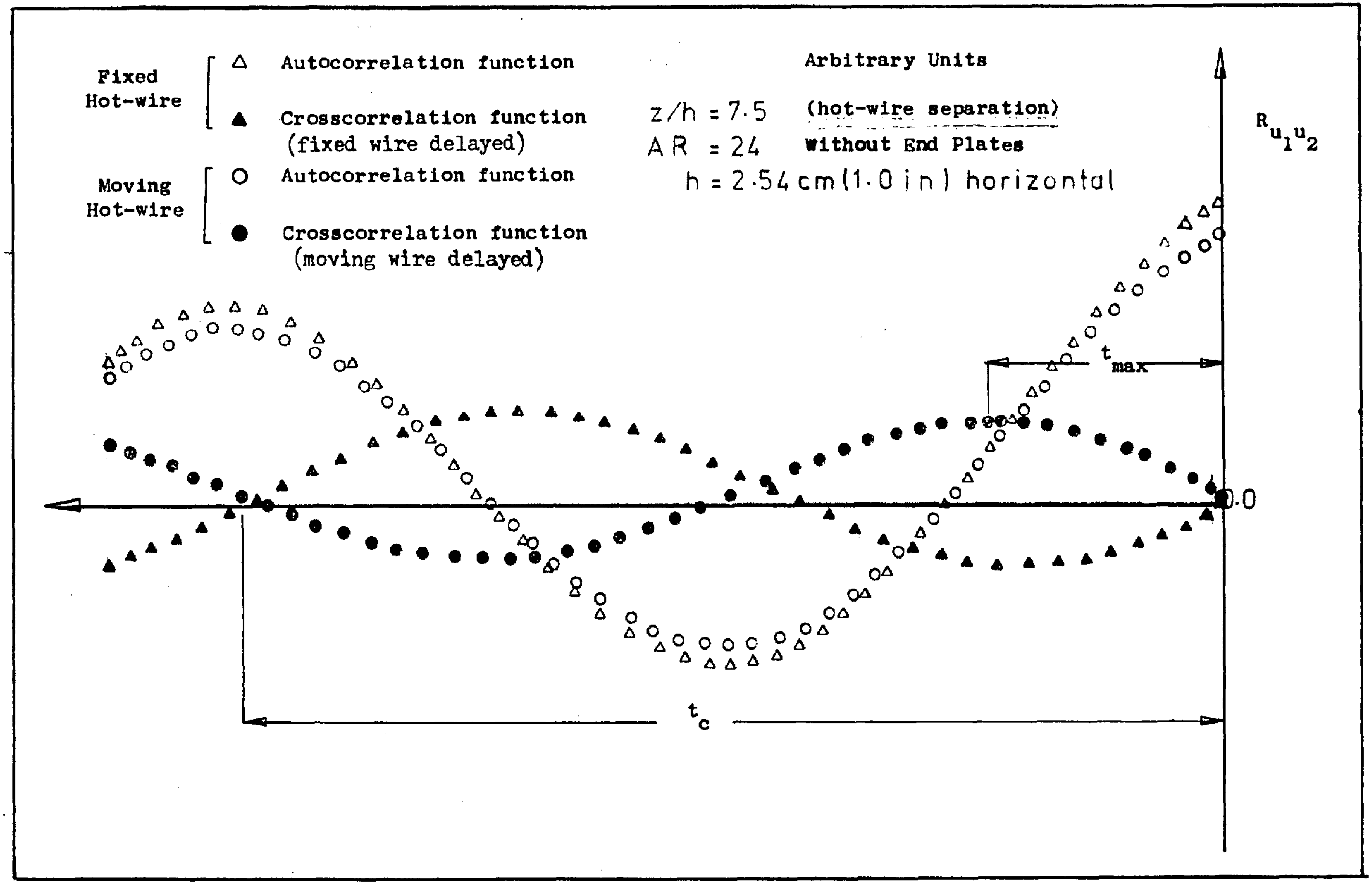

Figure 4.17 Space-time Correlations

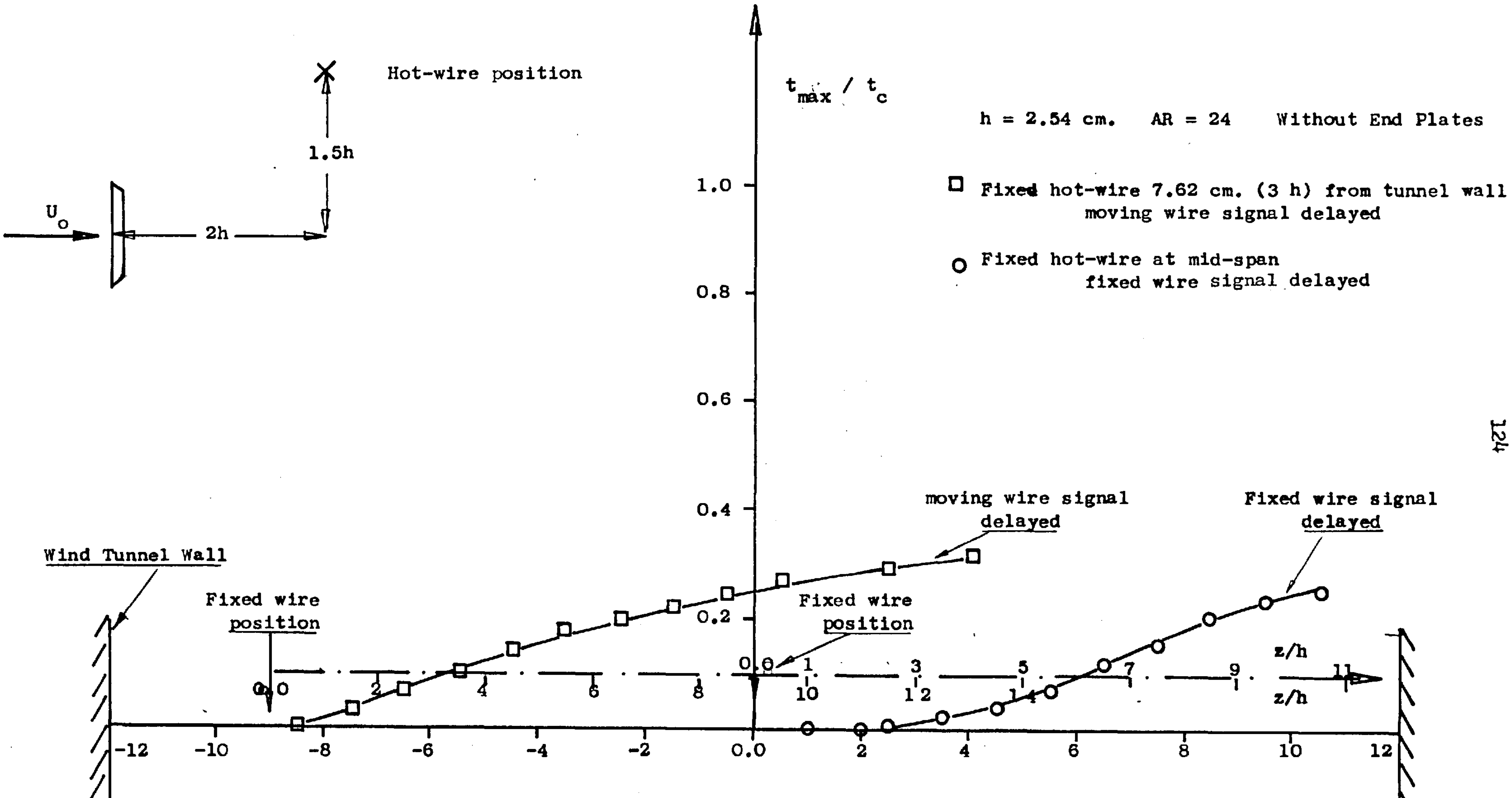

Figure 4.18 Time Delay Function for Maximum Lateral Correlation in Smooth Flow

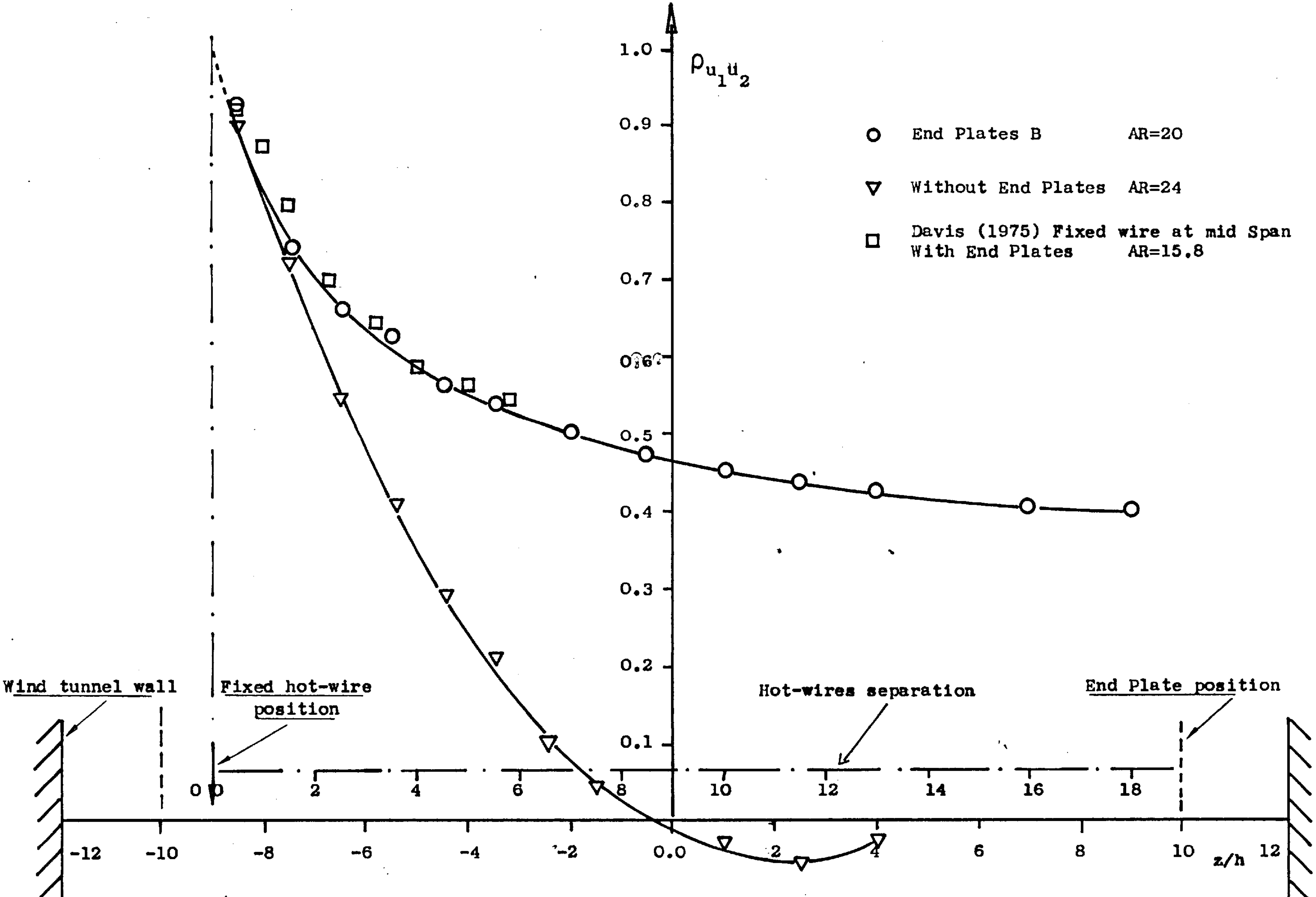

Figure 4.19 Lateral Velocity Correlation with and without End Plates in Smooth Flow

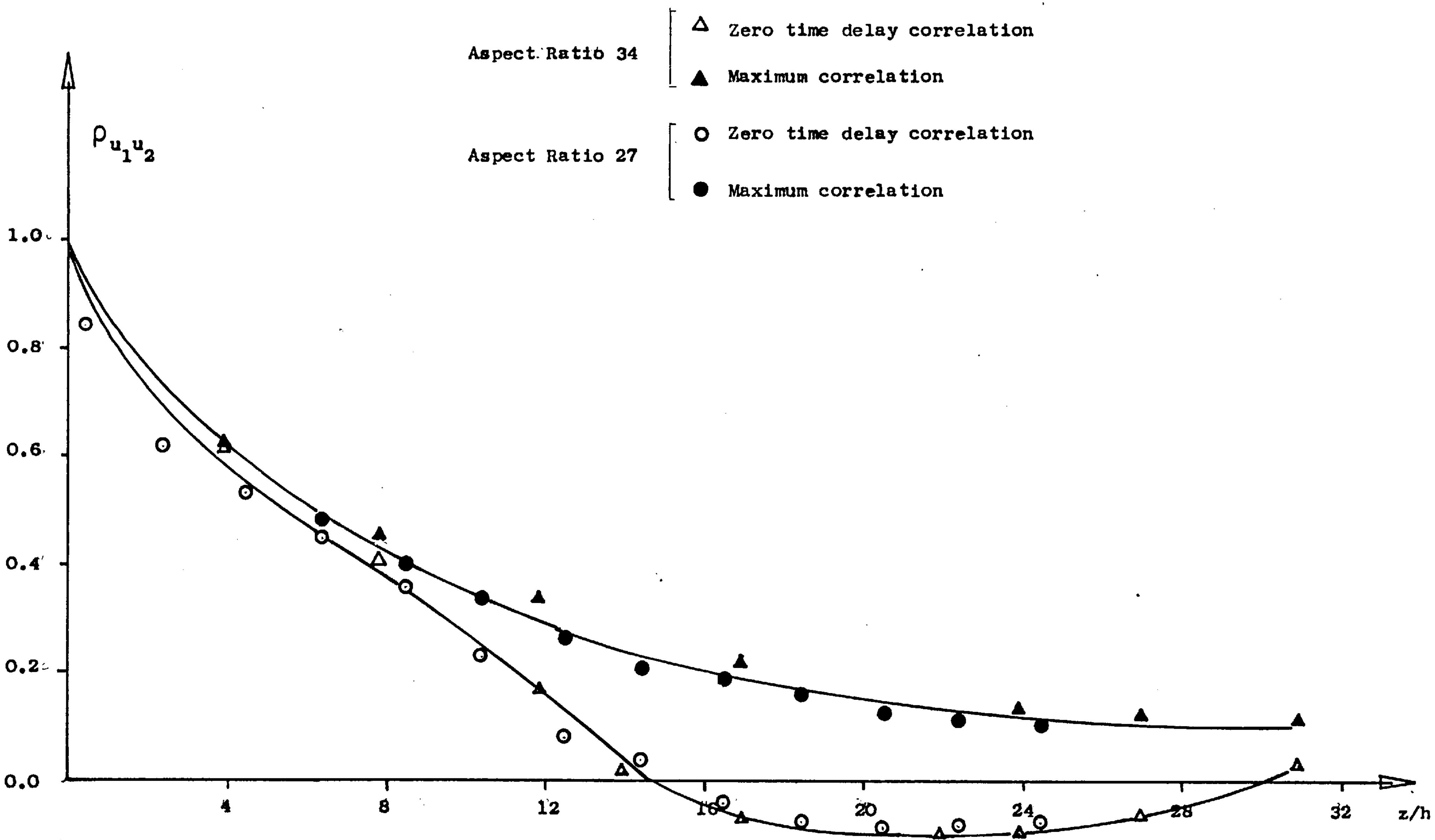

Figure 4.20 Lateral Velocity Correlation for Larger Aspect Ratios with End Plates in Smooth Flow

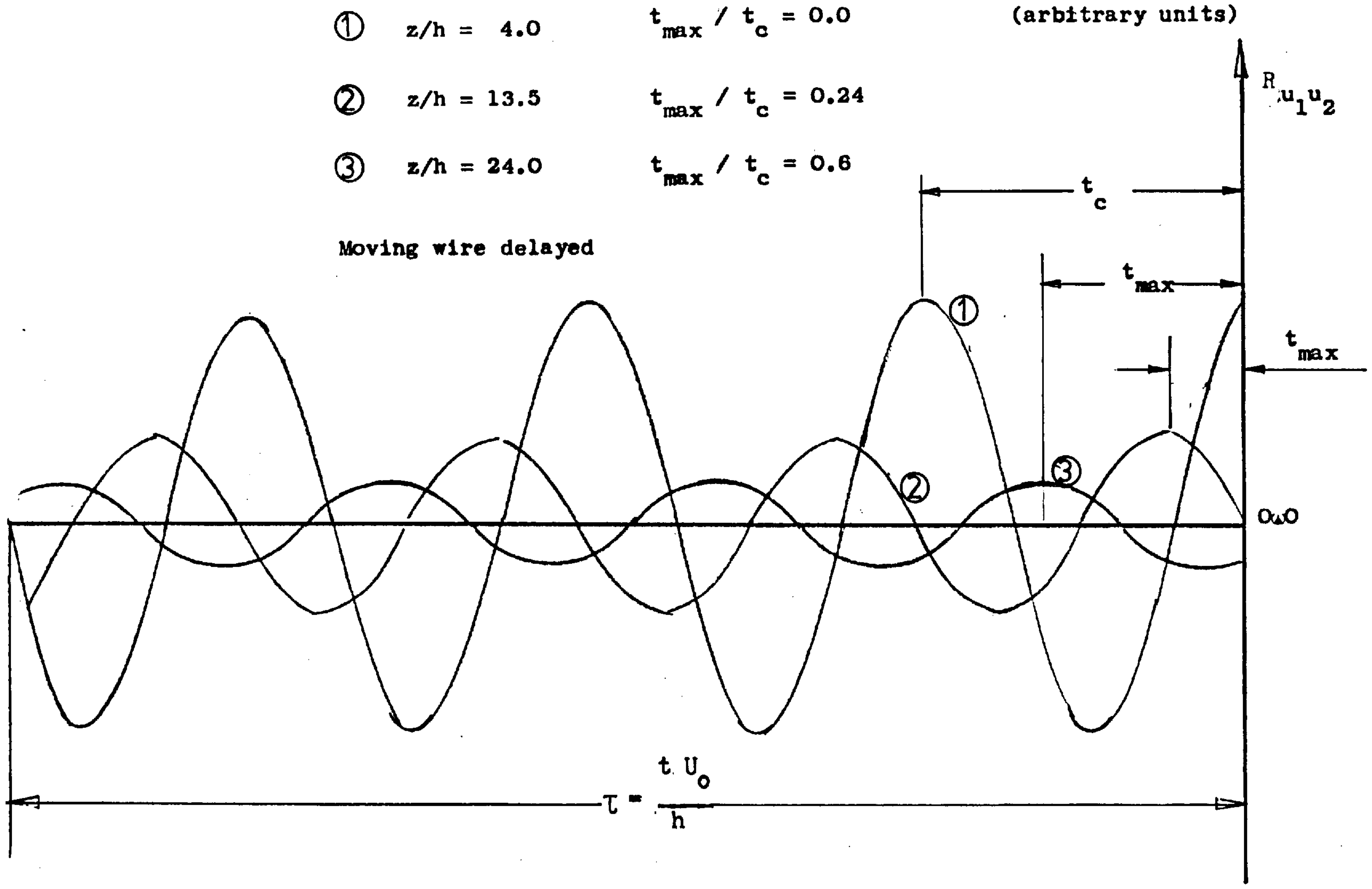

Figure 4.21 Crosscorrelation Funtion for differents Hot-Wires Separations in Smooth Flow with End Plates
(h=2.54 cm , AR=34 , fixed hot-wire 2.54 cm from end plate)

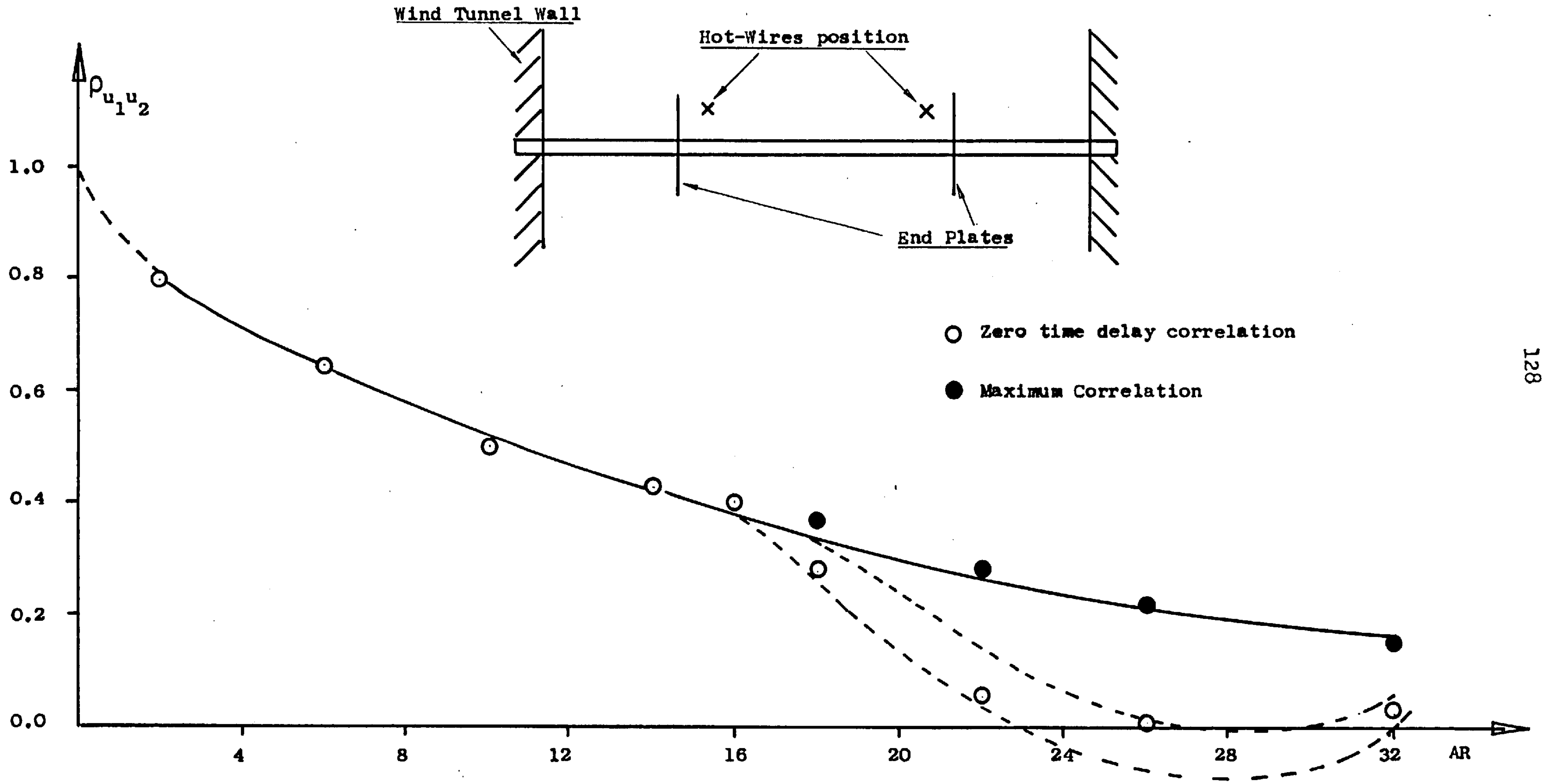

Figure 4.22 Lateral Velocity Correlation vs. End Plate Separation (hot-wires fixed 2.54 cm. apart of the End Plates)

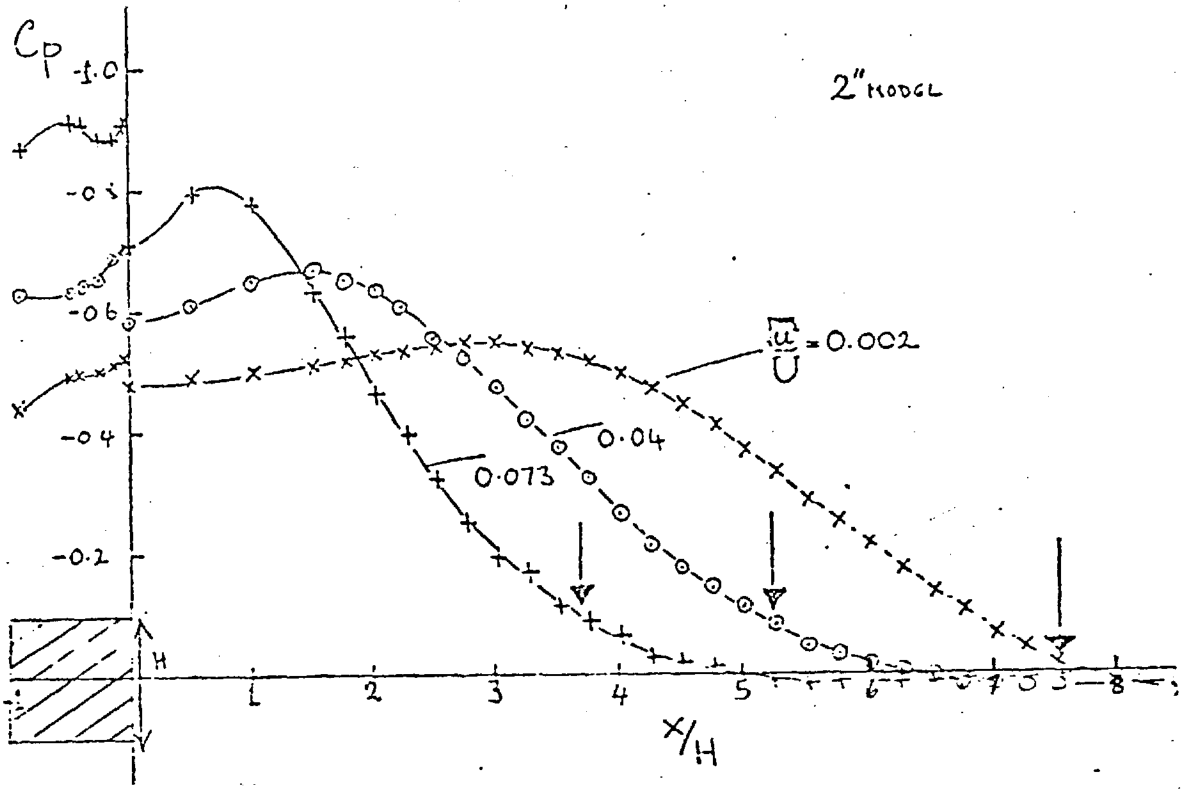

Pressure Distributions around a square section cylinder fitted with a splitter plate.

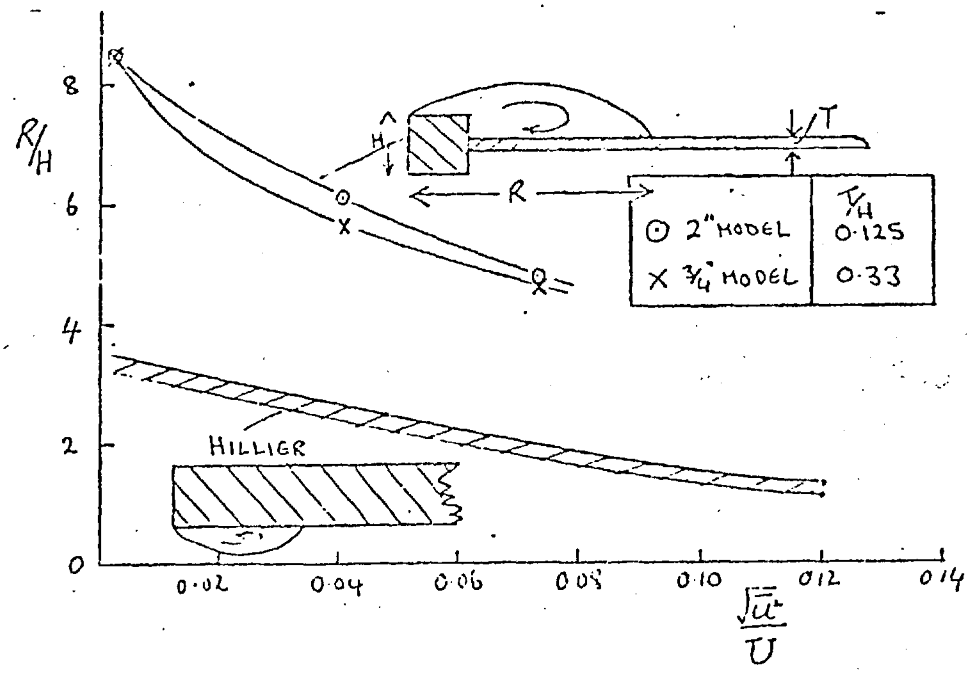

Reattachment length versus turbulence intensity.

Figure 5.1 Reproduced from reference (26)

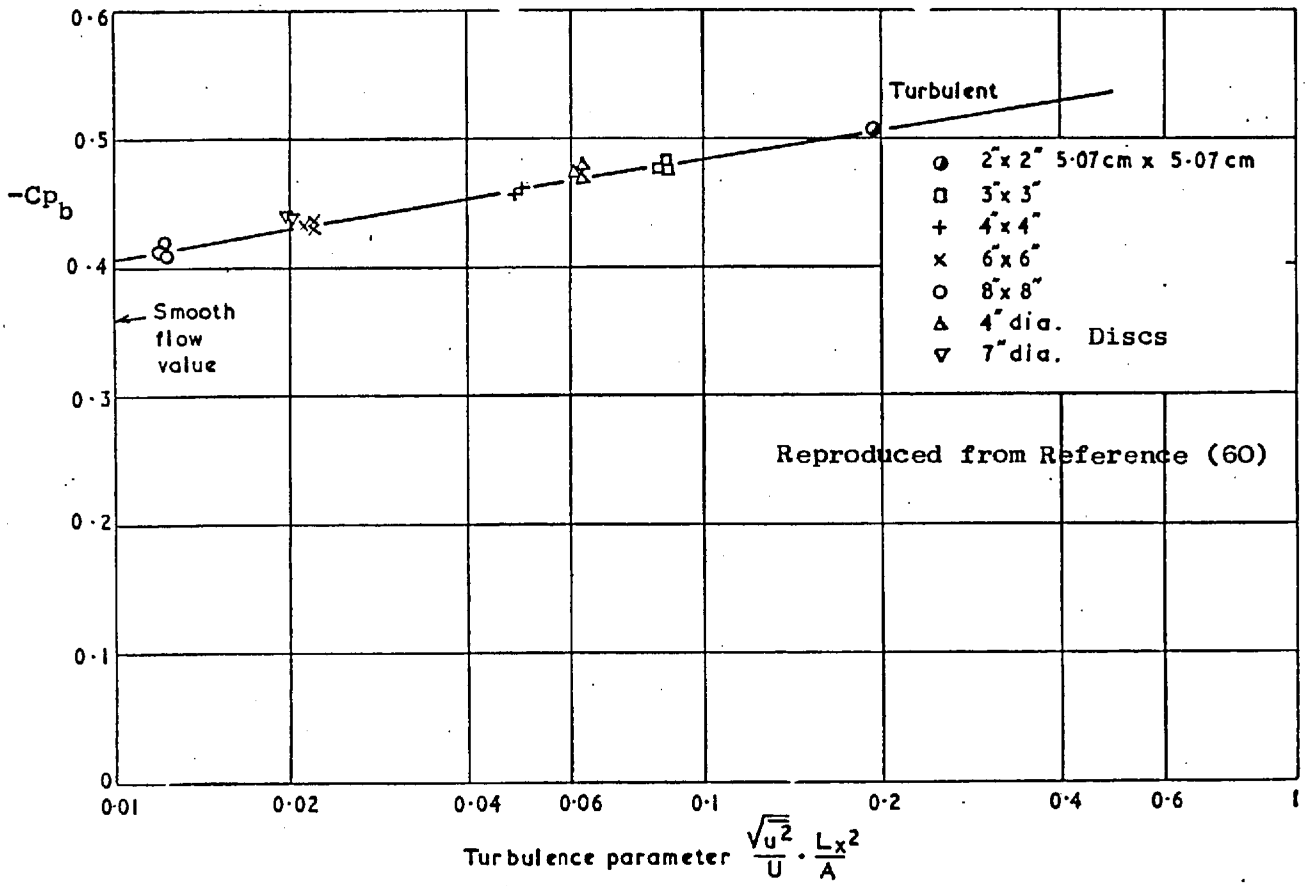

Reproduced from Reference (60)

Figure 5.2 Base pressure measurements on flat plates in turbulent flow

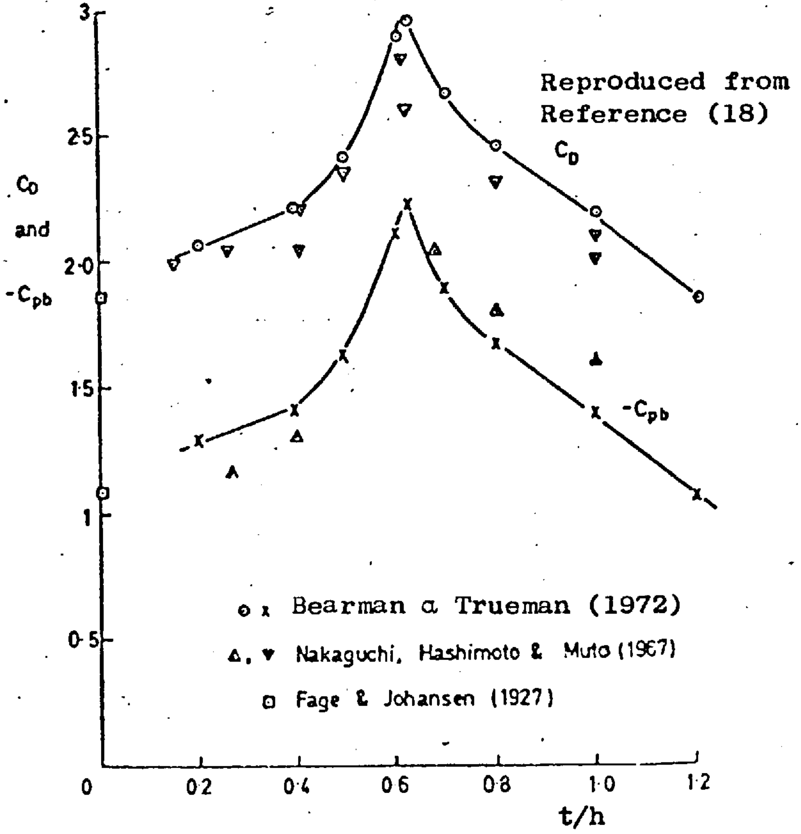

Reproduced from Reference (18)

Figure 5.3 Flow around Rectangular Cylinders

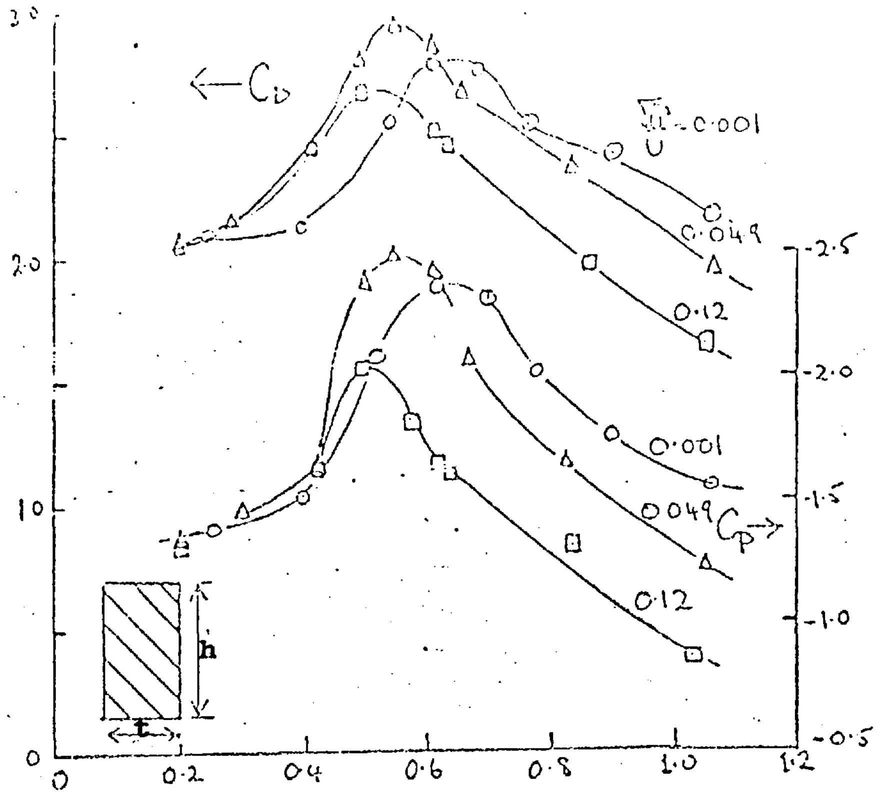

Figure 5.4 Influence of Turbulence on the Flow around Rectangular Cylinders (Nakamura and Tomonari (1976)).

The Effect of Intensity and Large Scale Turbulence

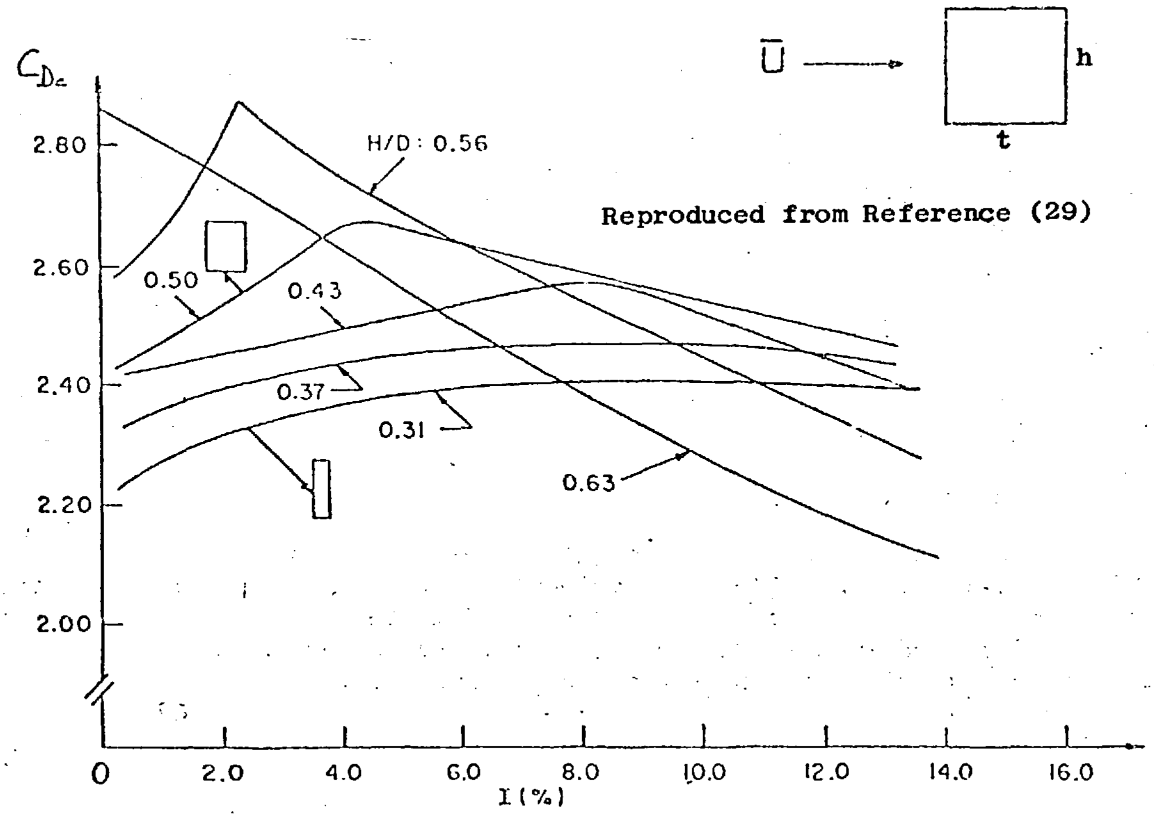

Reproduced from Reference (29)

Figure 5.5 Effect of Turbulence Intensity of the Drag Coefficient of Rectangular 2D Cylinders (after Ref. 6)

Petty (34) EUROMECH CONF. 1979

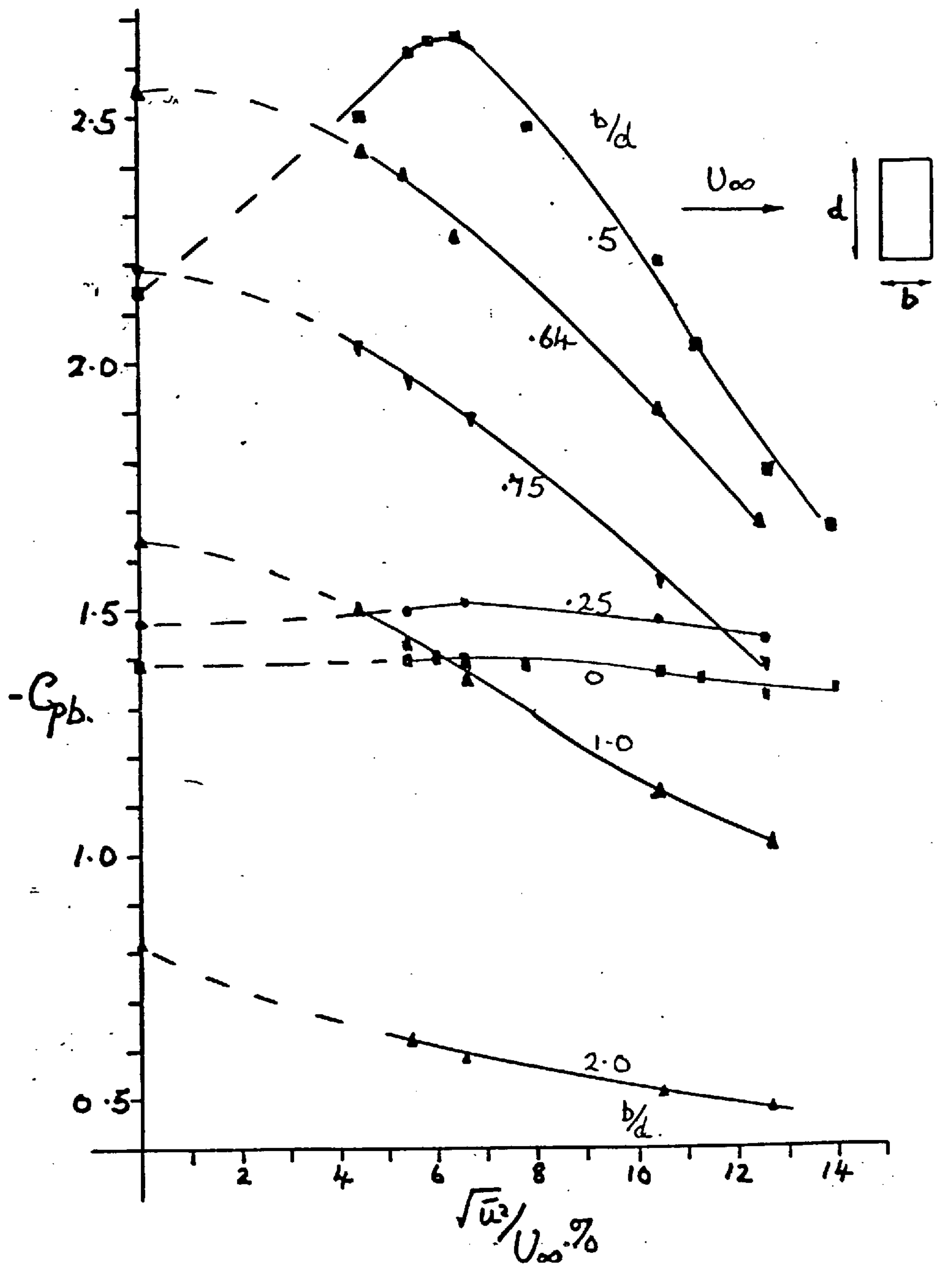

Figure 5.6 Effect of Turbulence Intensity on the Base Pressure Coefficient Of Rectangular Two-Dimensional Cylinder

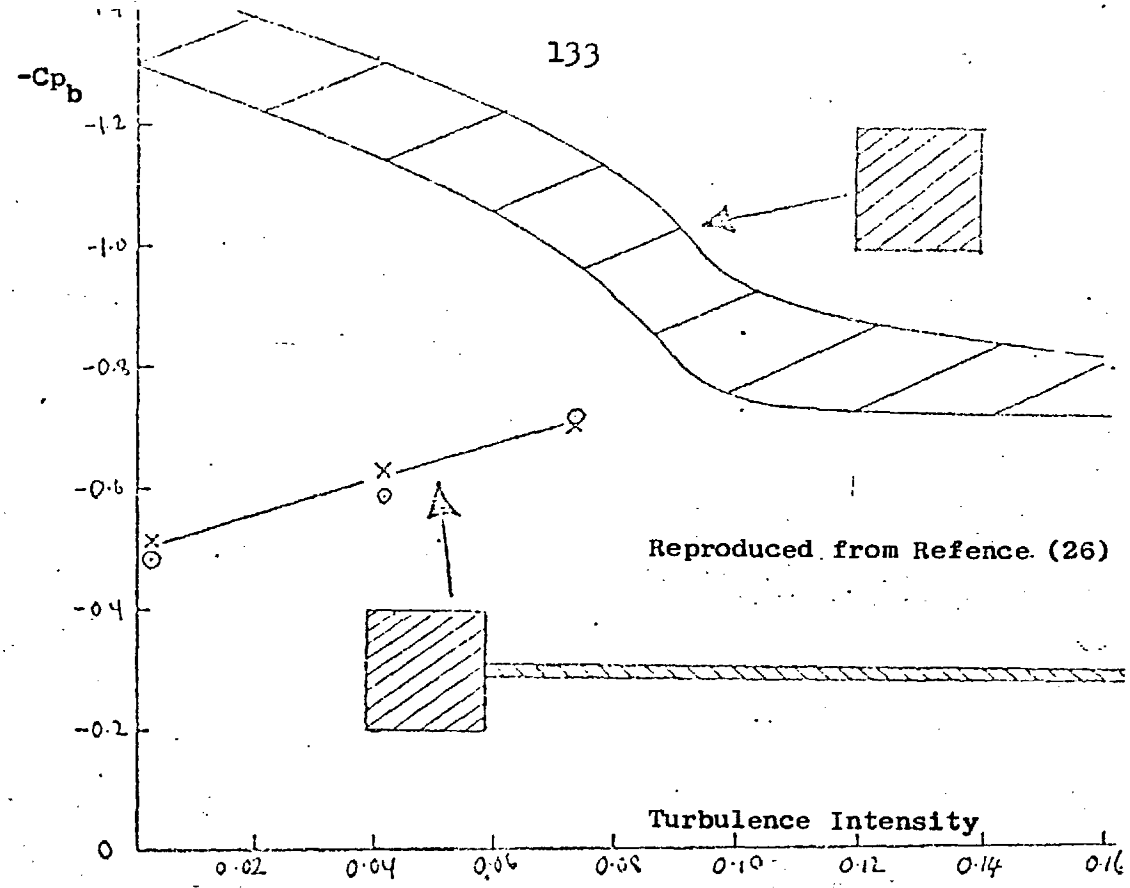

Figure 5.7 Base pressure on square section cylinders versus turbulence intensity.

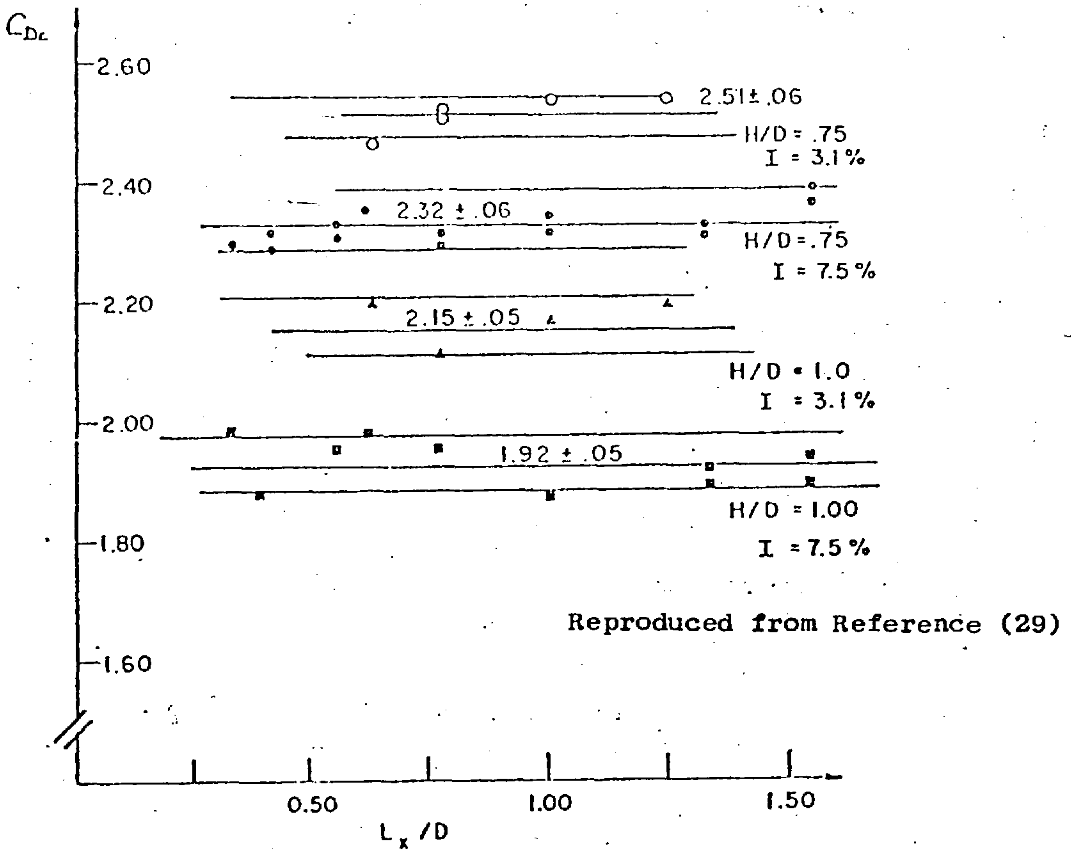

Figure 5.8 Effect of Longitudinal Scale of Turbulence on the Drag Coefficient of Rectangular 2D Cylinders (after Ref. 6)

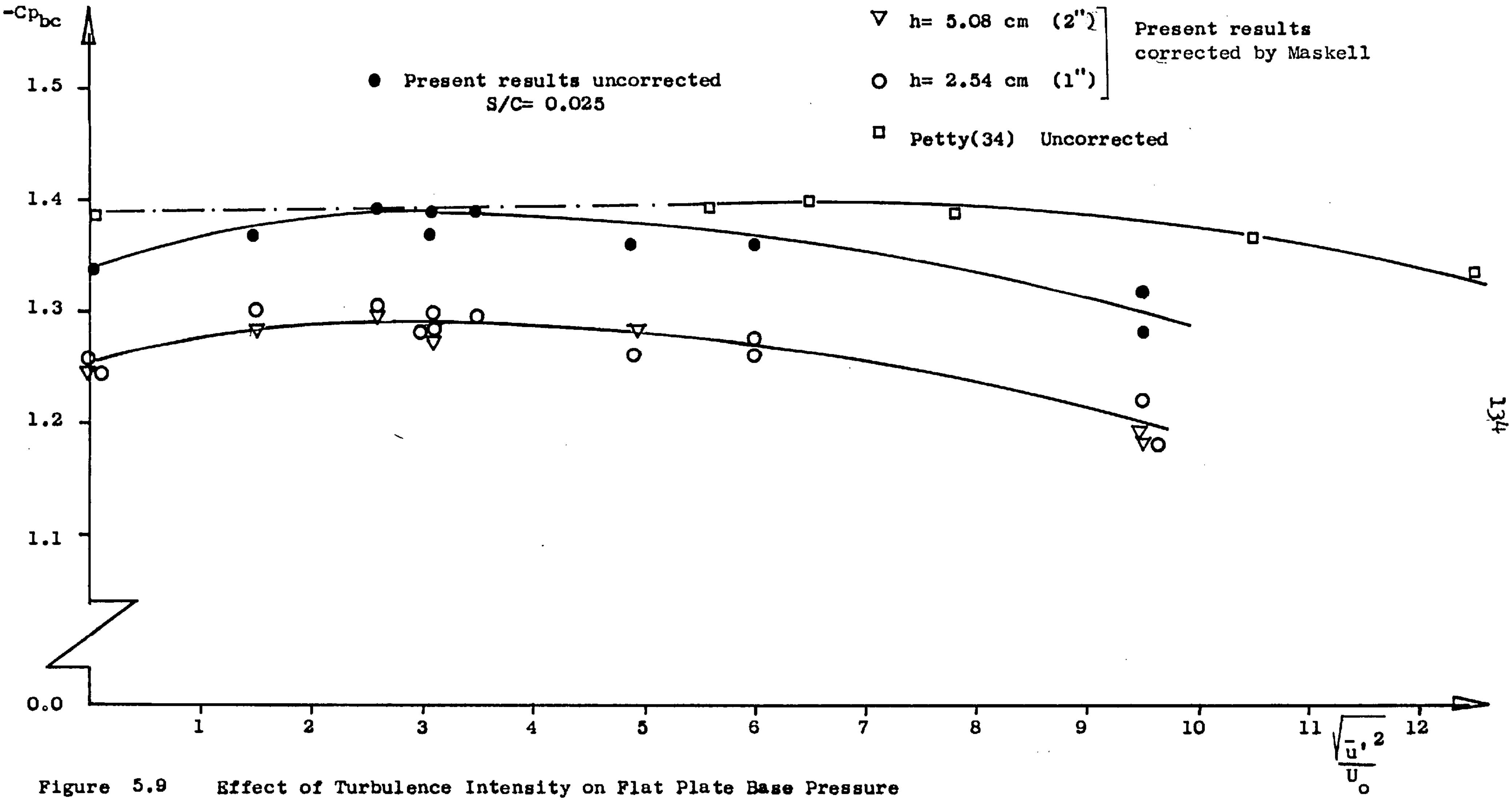

Figure 5.9 Effect of Turbulence Intensity on Flat Plate Base Pressure

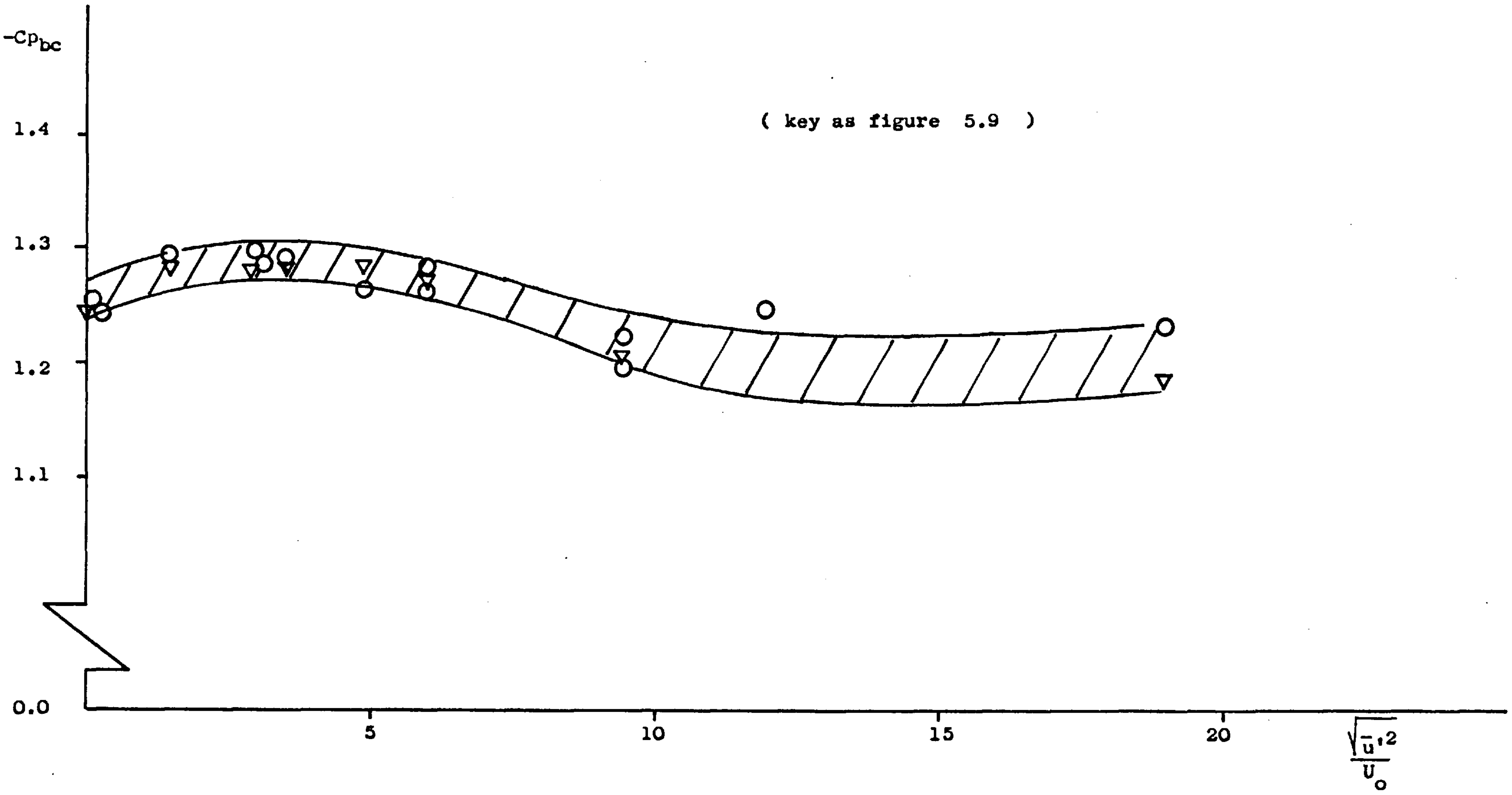

Figure 5.10 Base Pressure on Flat Plates in Turbulent Flows

Cp_b corrected for wind tunnel Blockage (Maskell's Method)

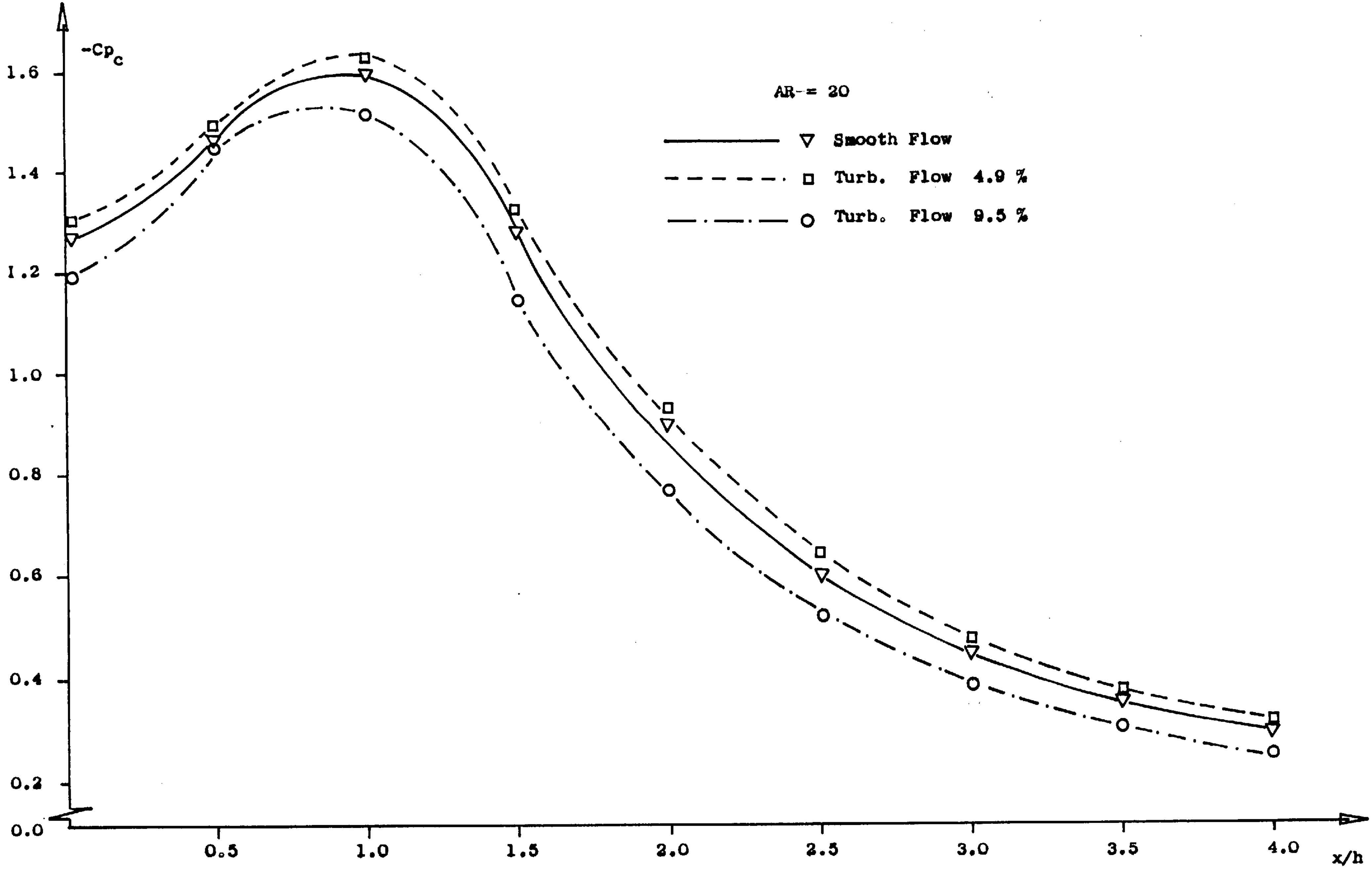

Figure 5.11 Corrected Pressure Coefficient along End Plate Centre Line in Smooth and Turbulent Flows

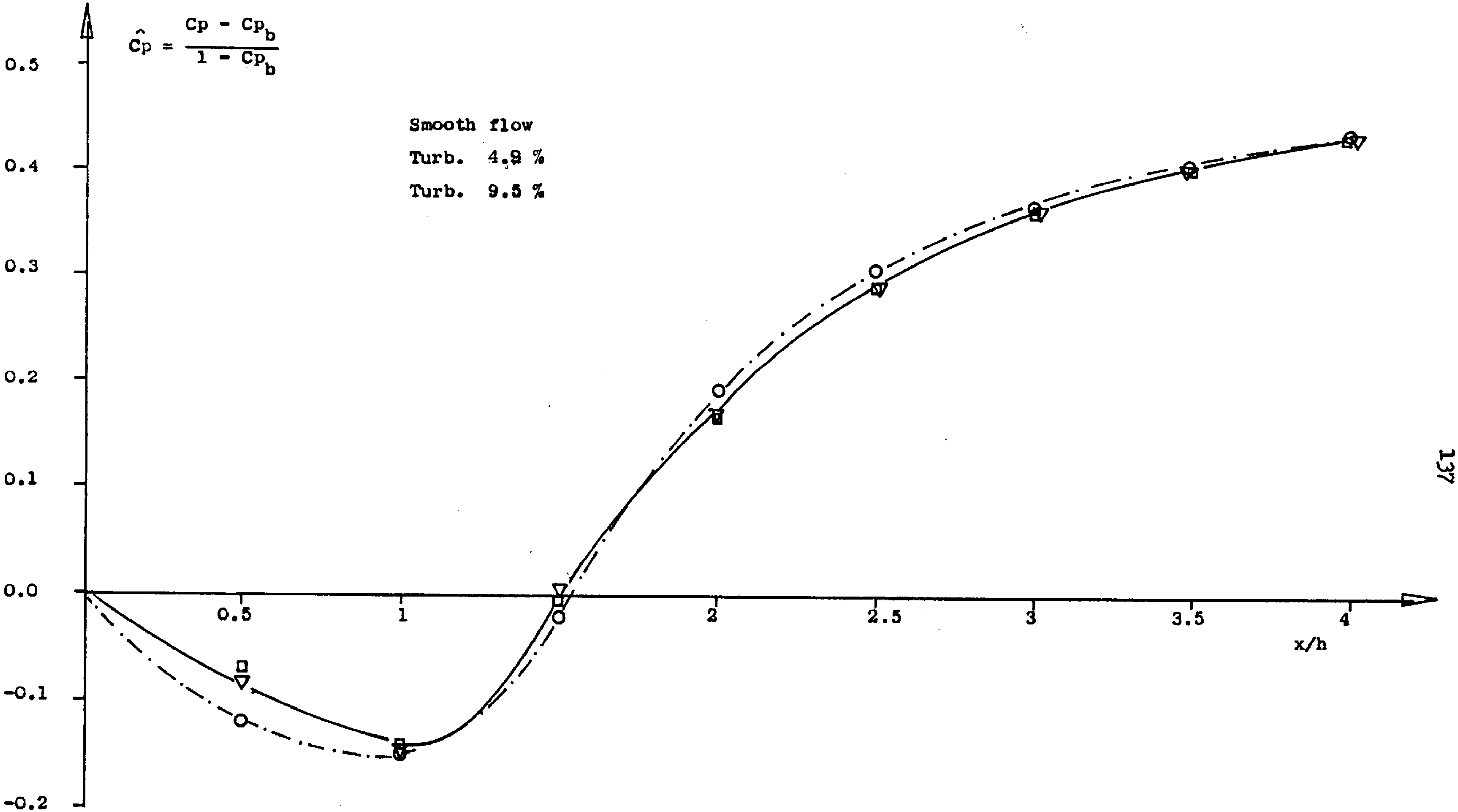

Figure 5.12 Pressure Recovery at the End-Plate in Smooth and Turbulent Flows.

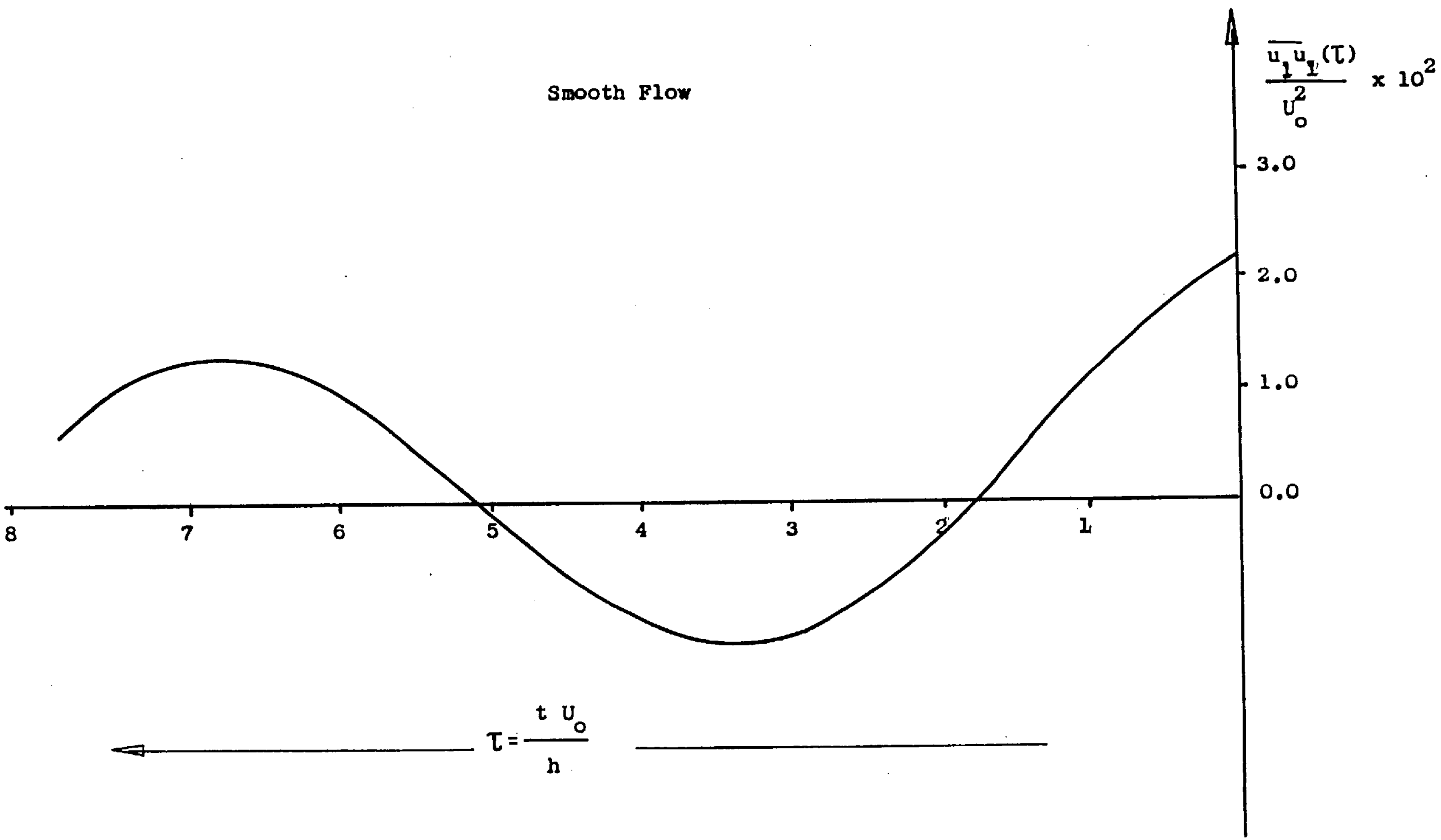

Figure 5.13 Non-dimensional Autocorrelogram

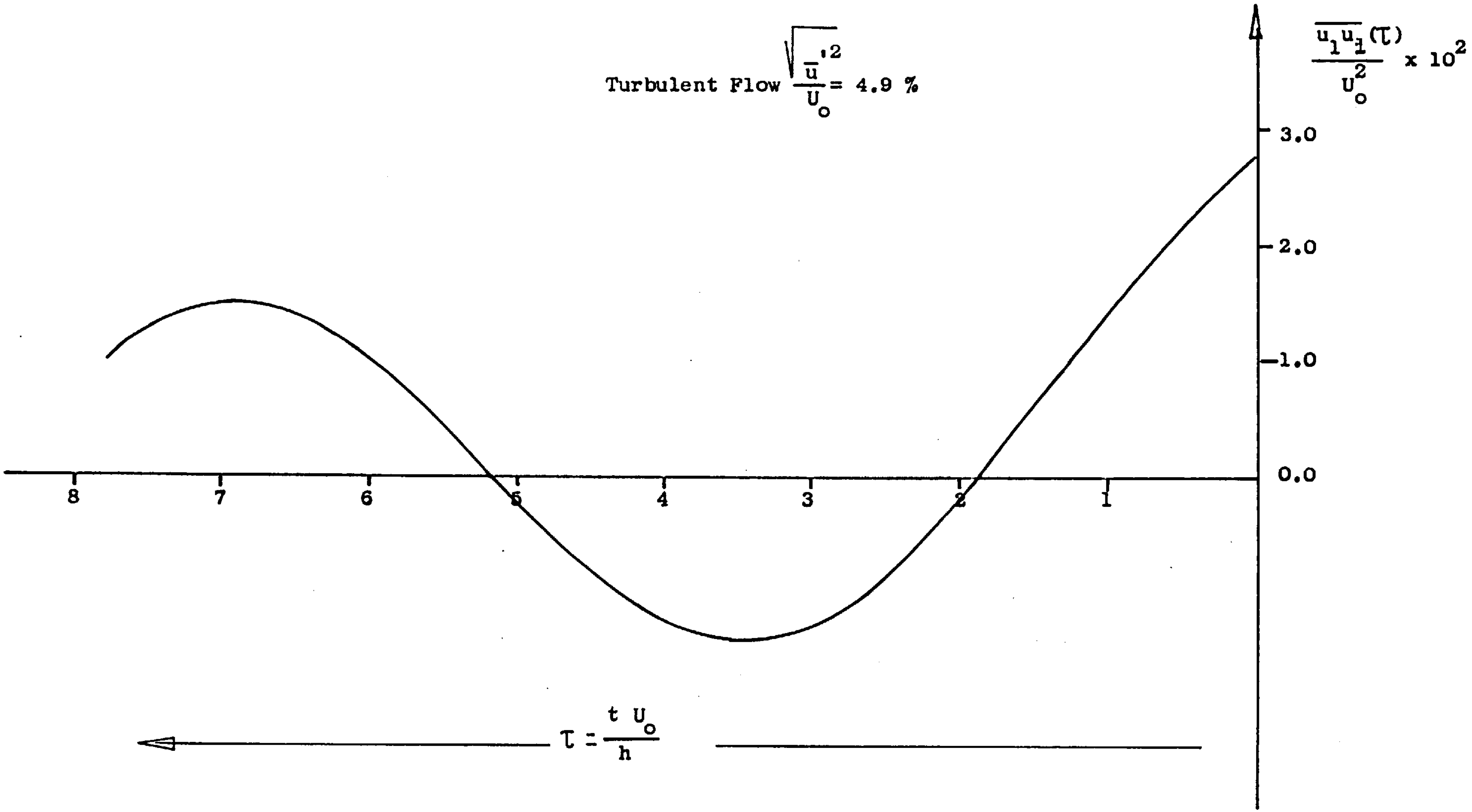

Figure 5.14 Non-dimensinal Autocorrelogram

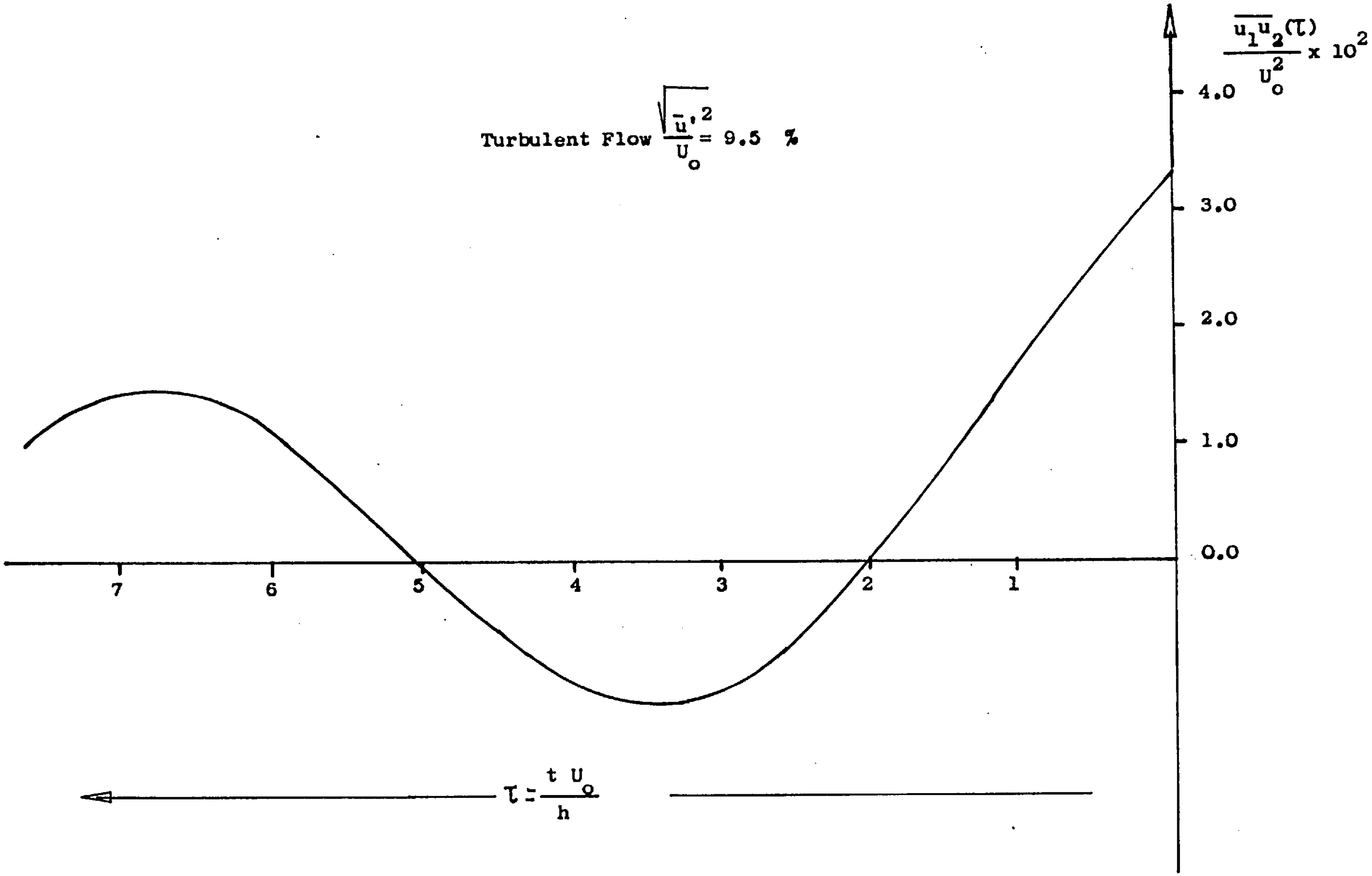

Figure 5.15 Non-dimensional Autocorrelogram

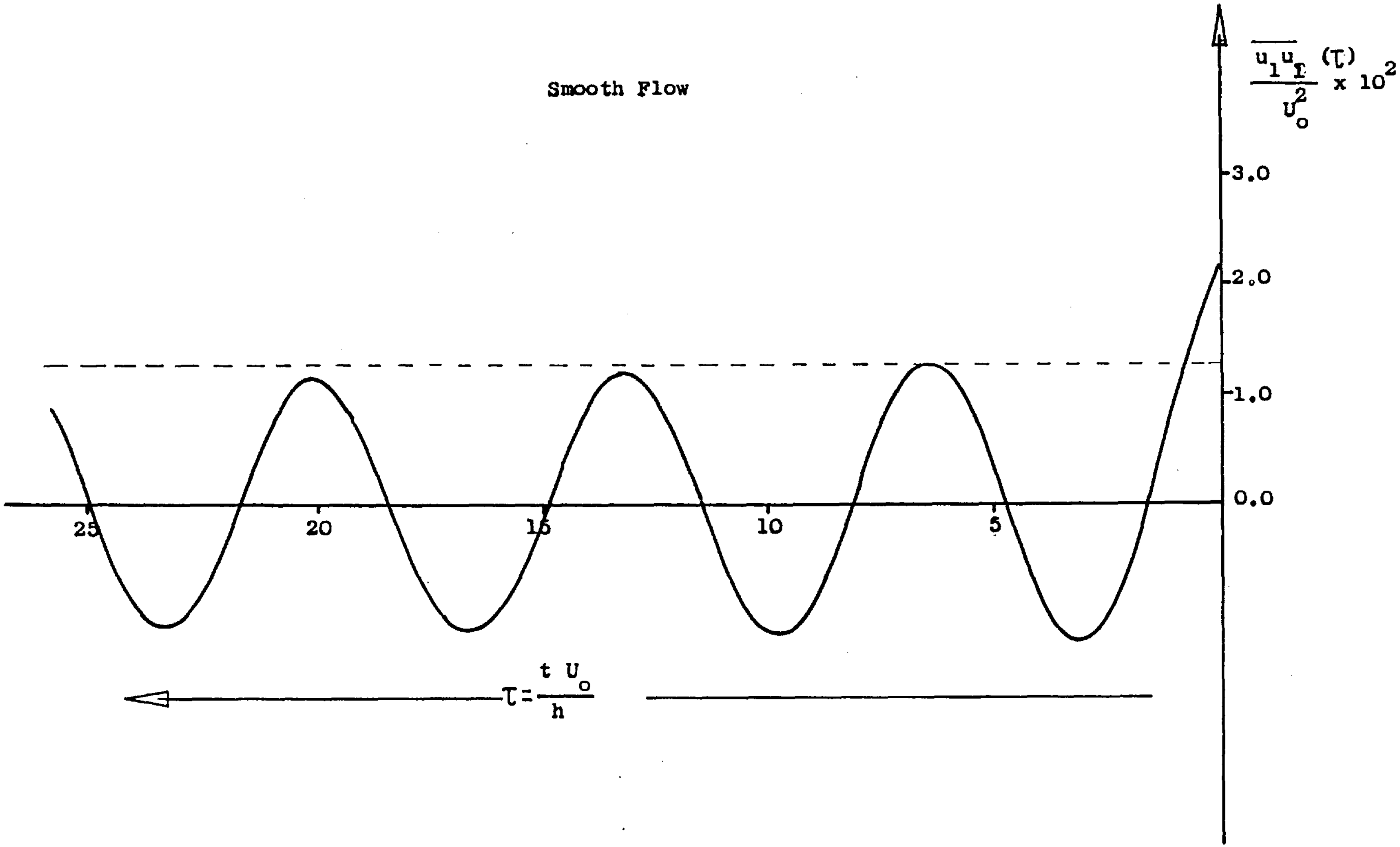

Figure 5.16 Non-dimensionl Autocorrelogram

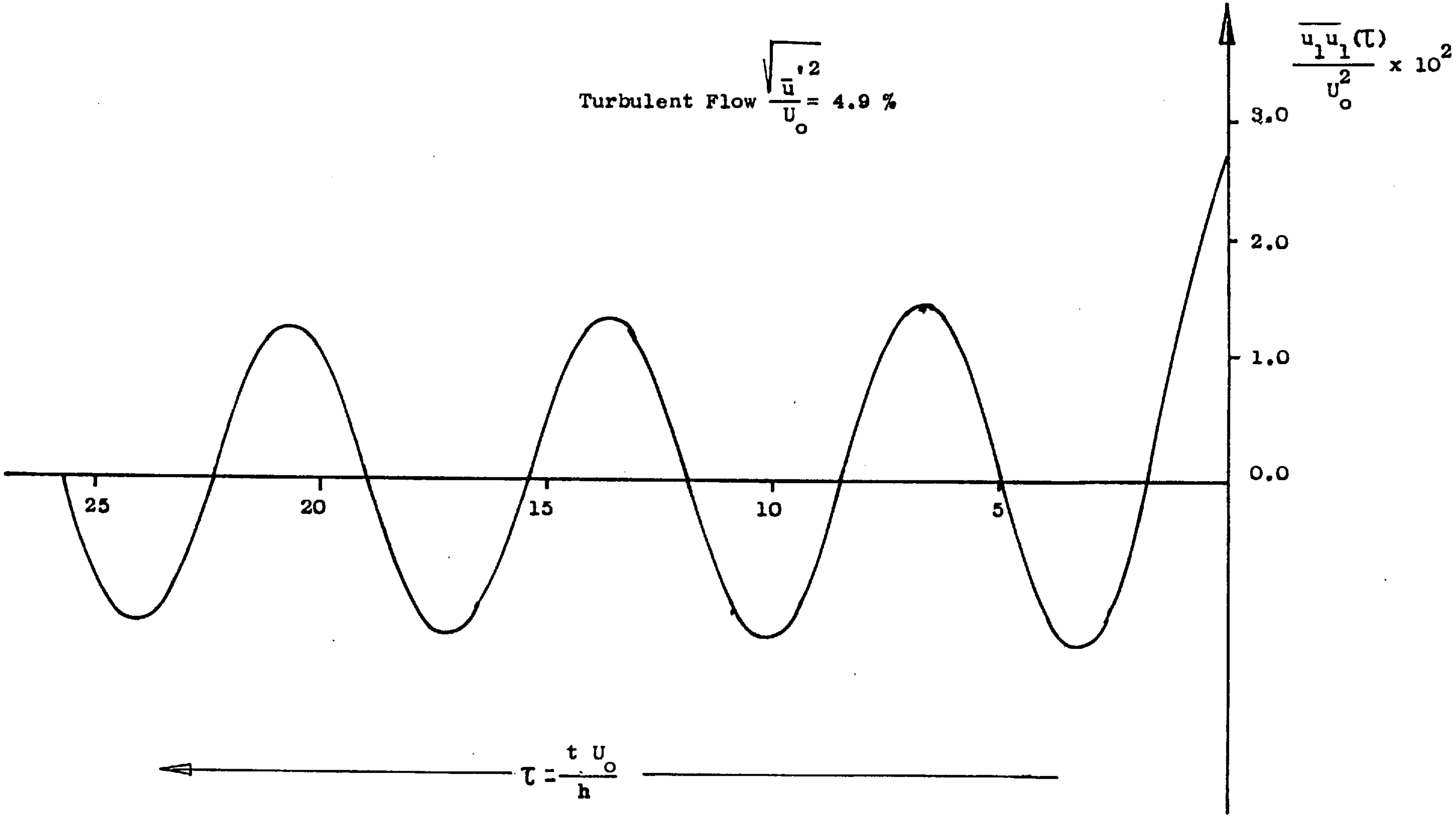

Figure 5.17 Non-dimensional Autocorrelogram

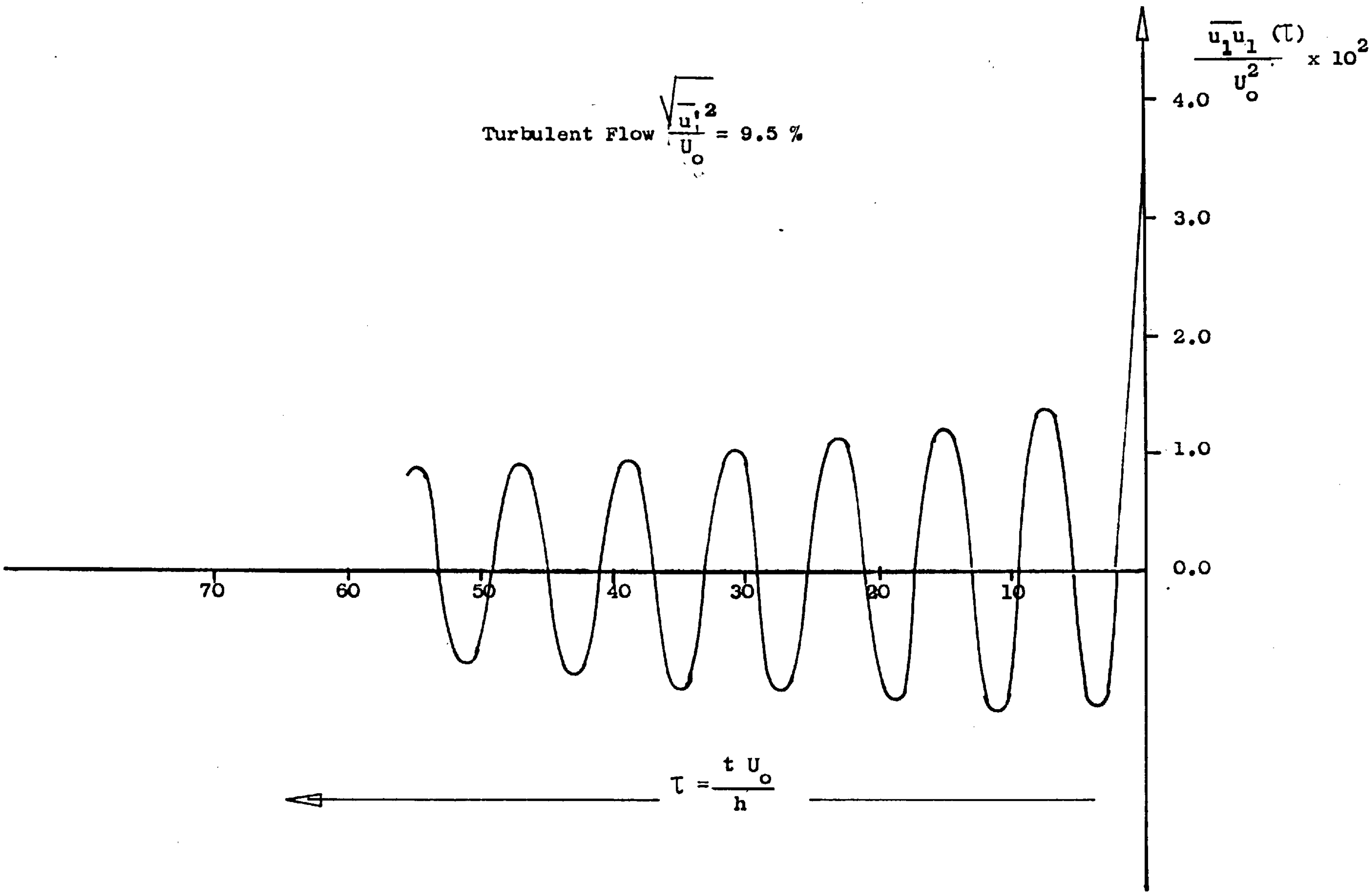

Figure 5.18 Non-dimensional Autocorrelogram

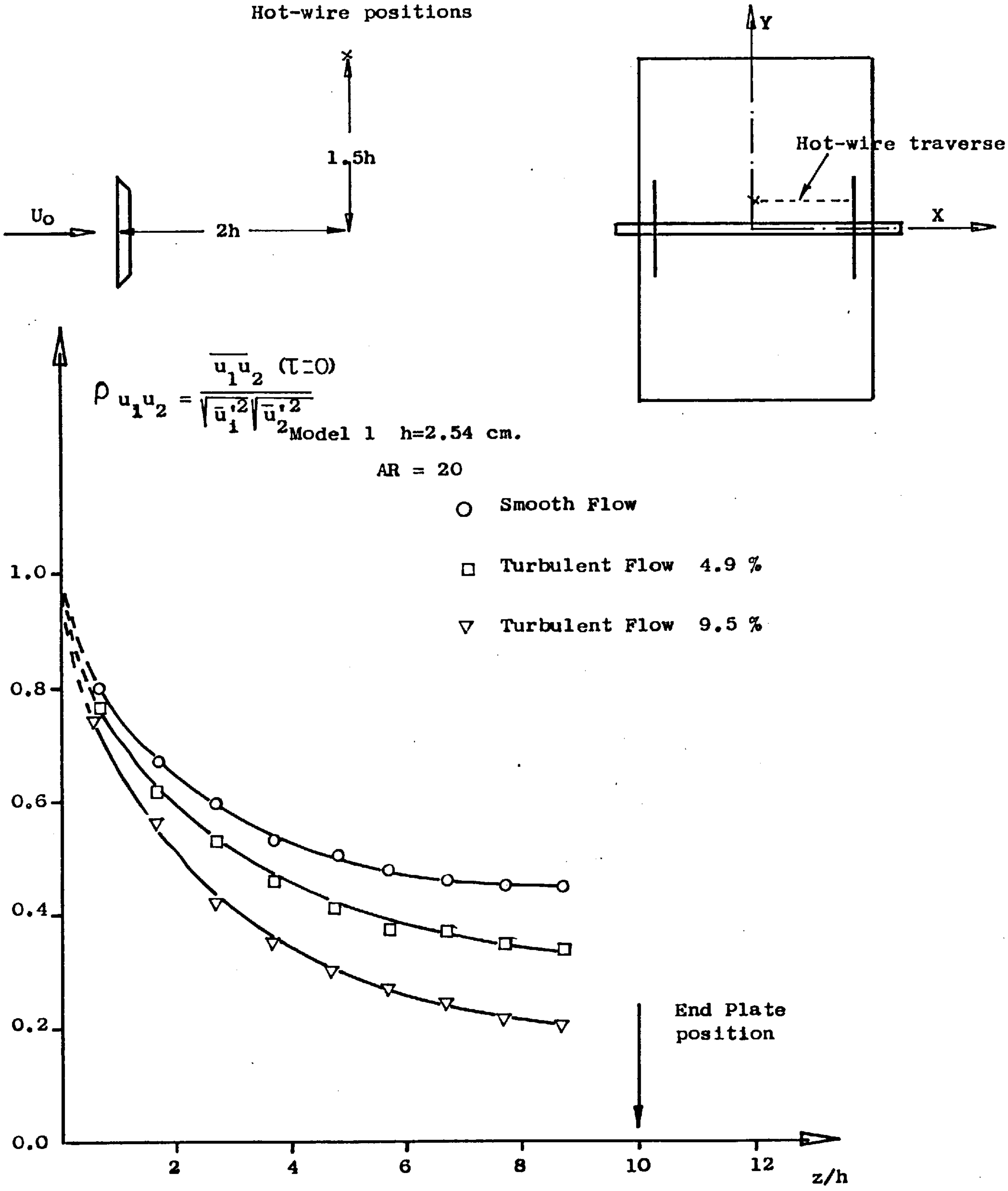

Figure 5.19 Effect of Turbulence Intensity on Lateral Velocity Correlation

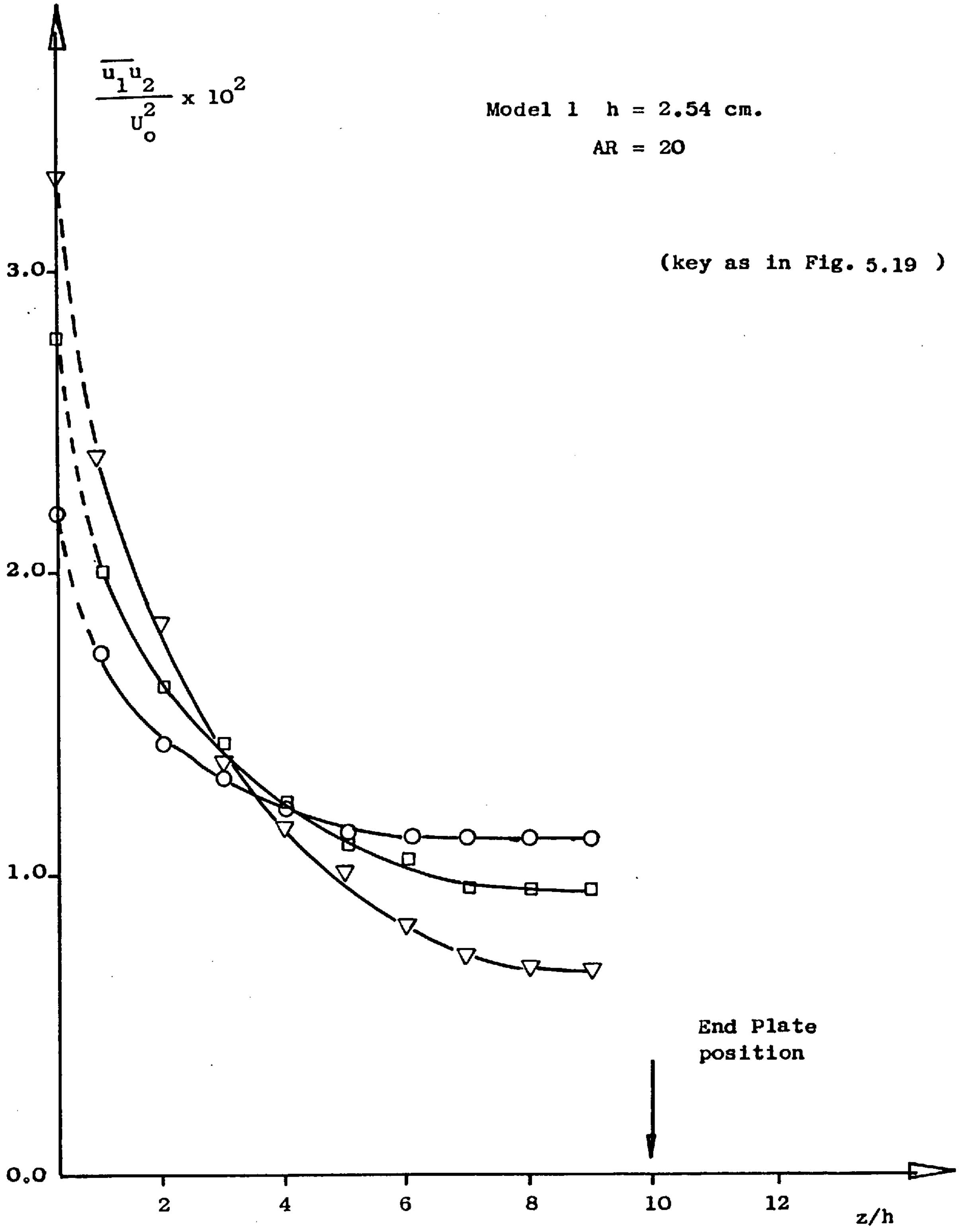

Figure 5.20 Effect of Turbulence on the Spanwise amplitude of the Correlated Velocity Fluctuations.

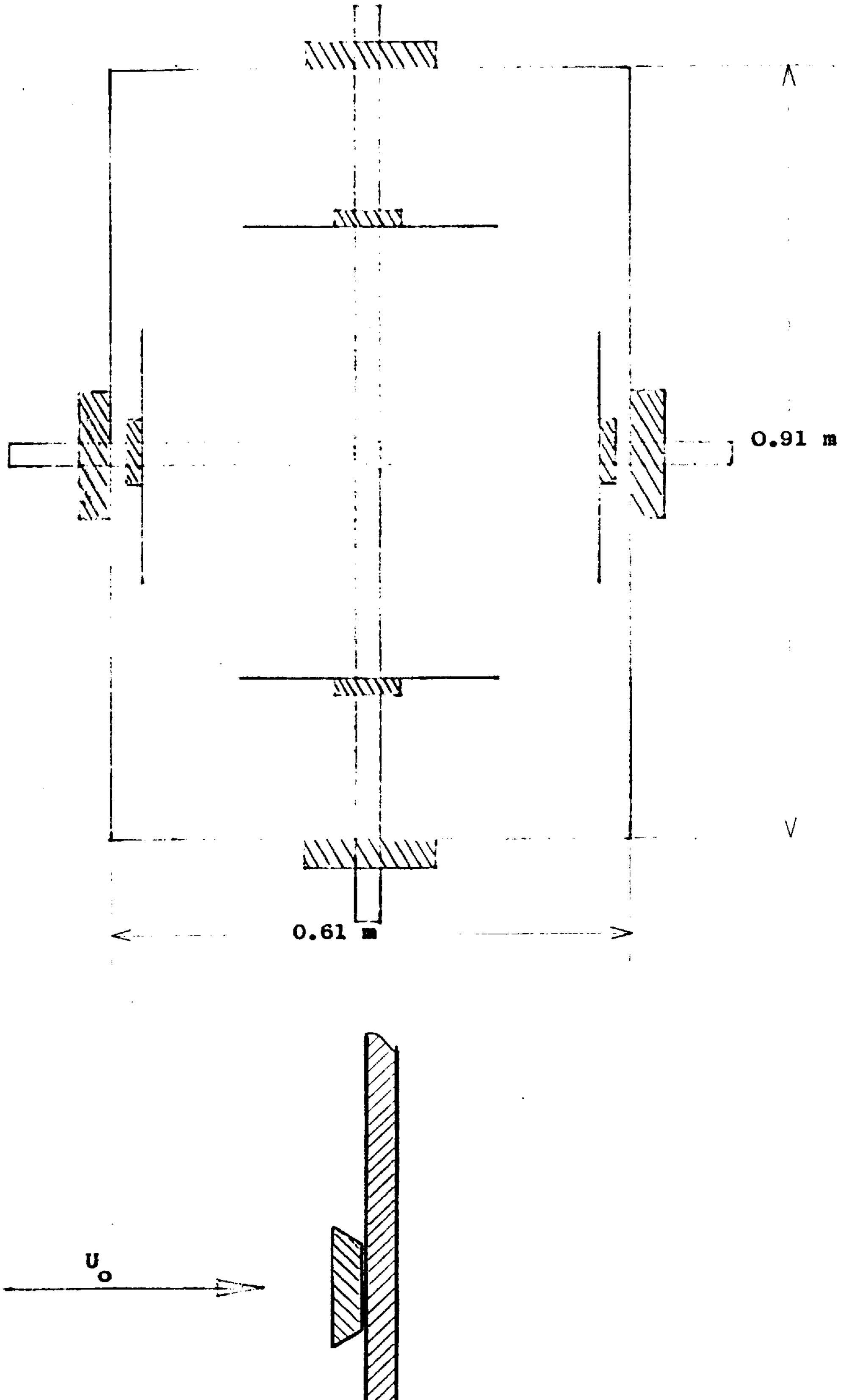

Figure 6.1 Sketch of the Overlapped Intersecting Flat Plates in the 0.91 m X 0.61 m Wind Tunnel

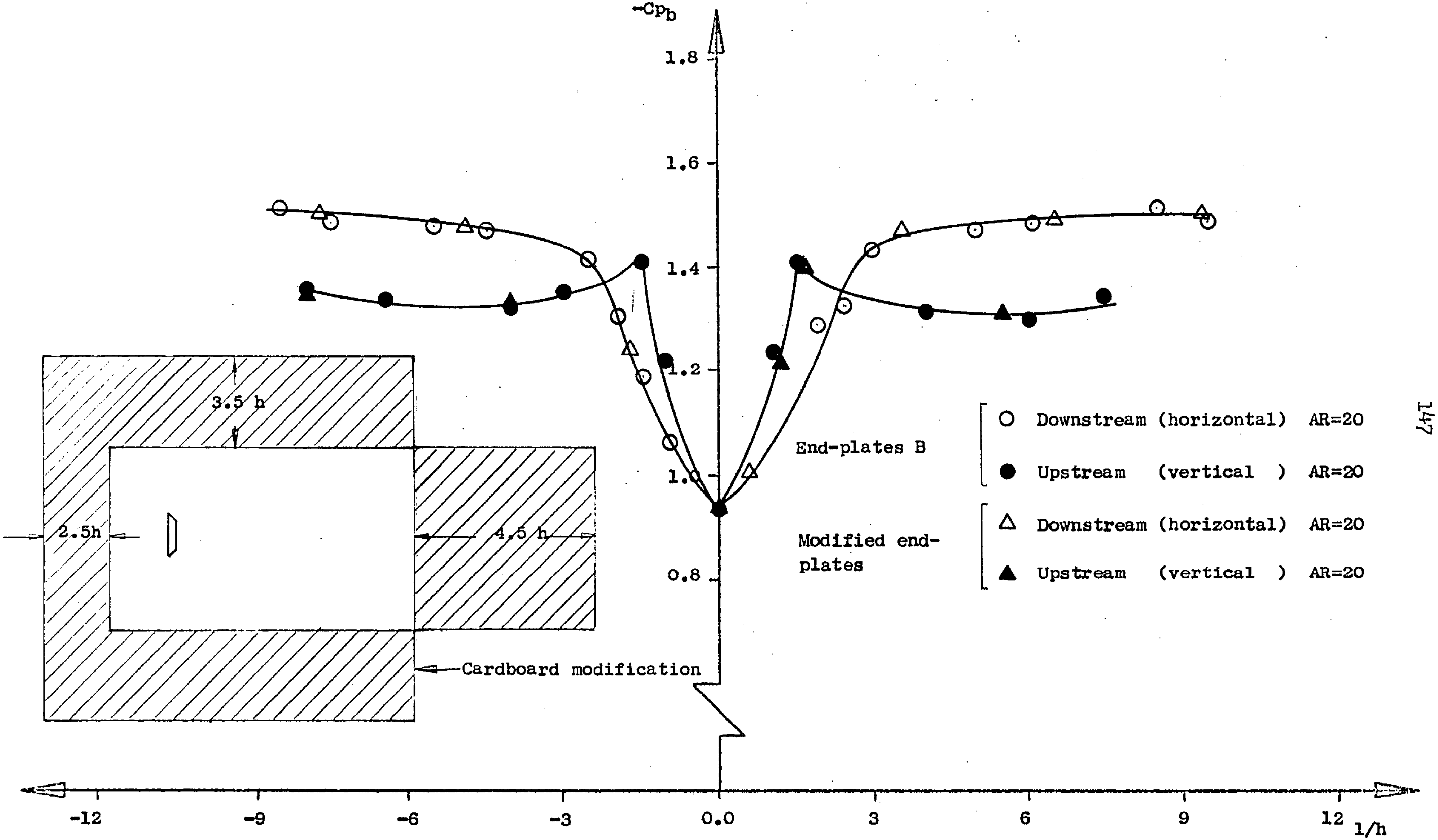

Figure 6.2 Spanwise Base pressure coefficient on overlapped intersecting flat plates

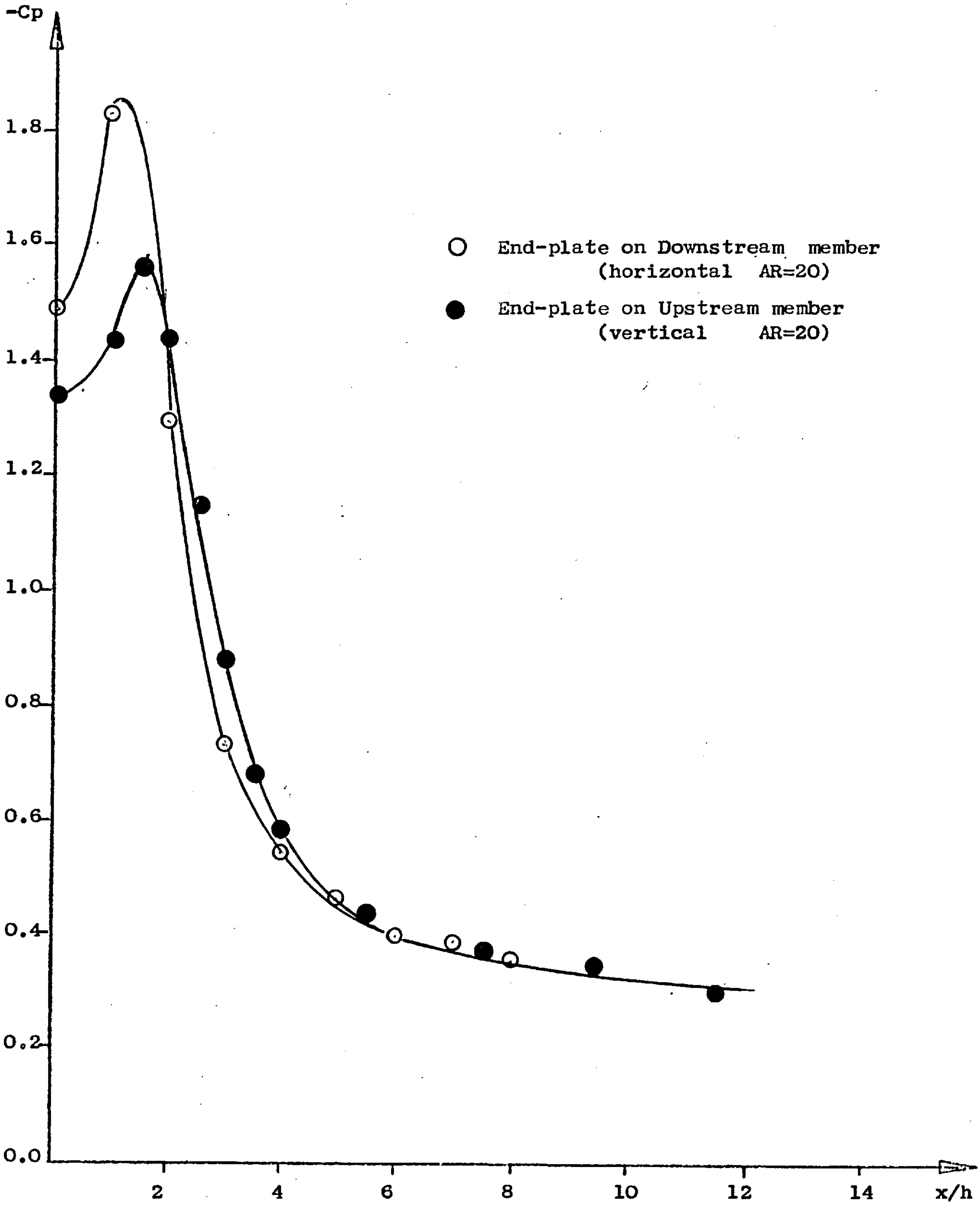

Figure 6.3 Pressure distribution on end-plate centre line for overlapped intersection

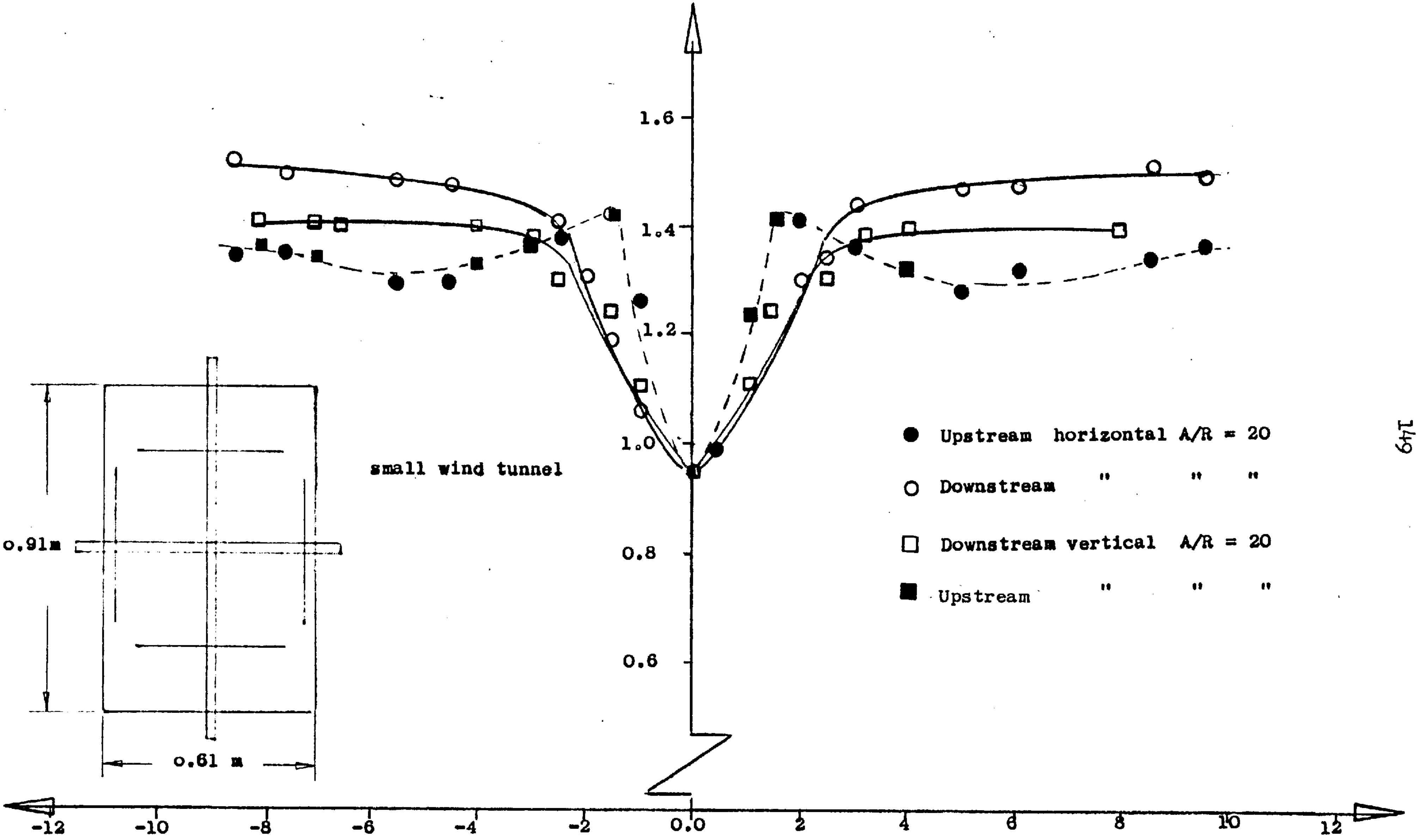

Figure 6.4 Spanwise pressure distribution on overlapped intersecting flat plates

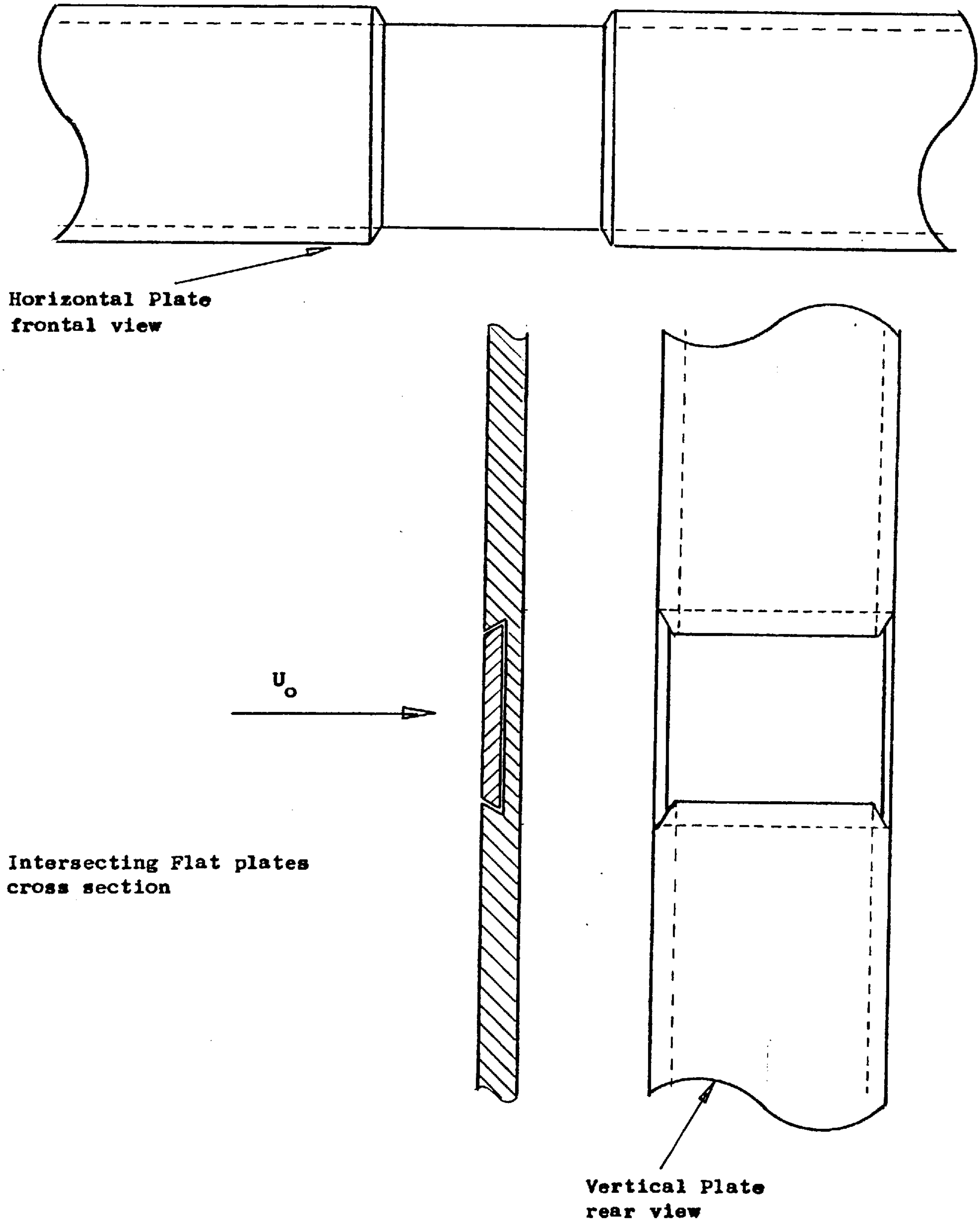

Figure 6.5 Sketch of the Intersecting Flat Plates (halflapped intersection)

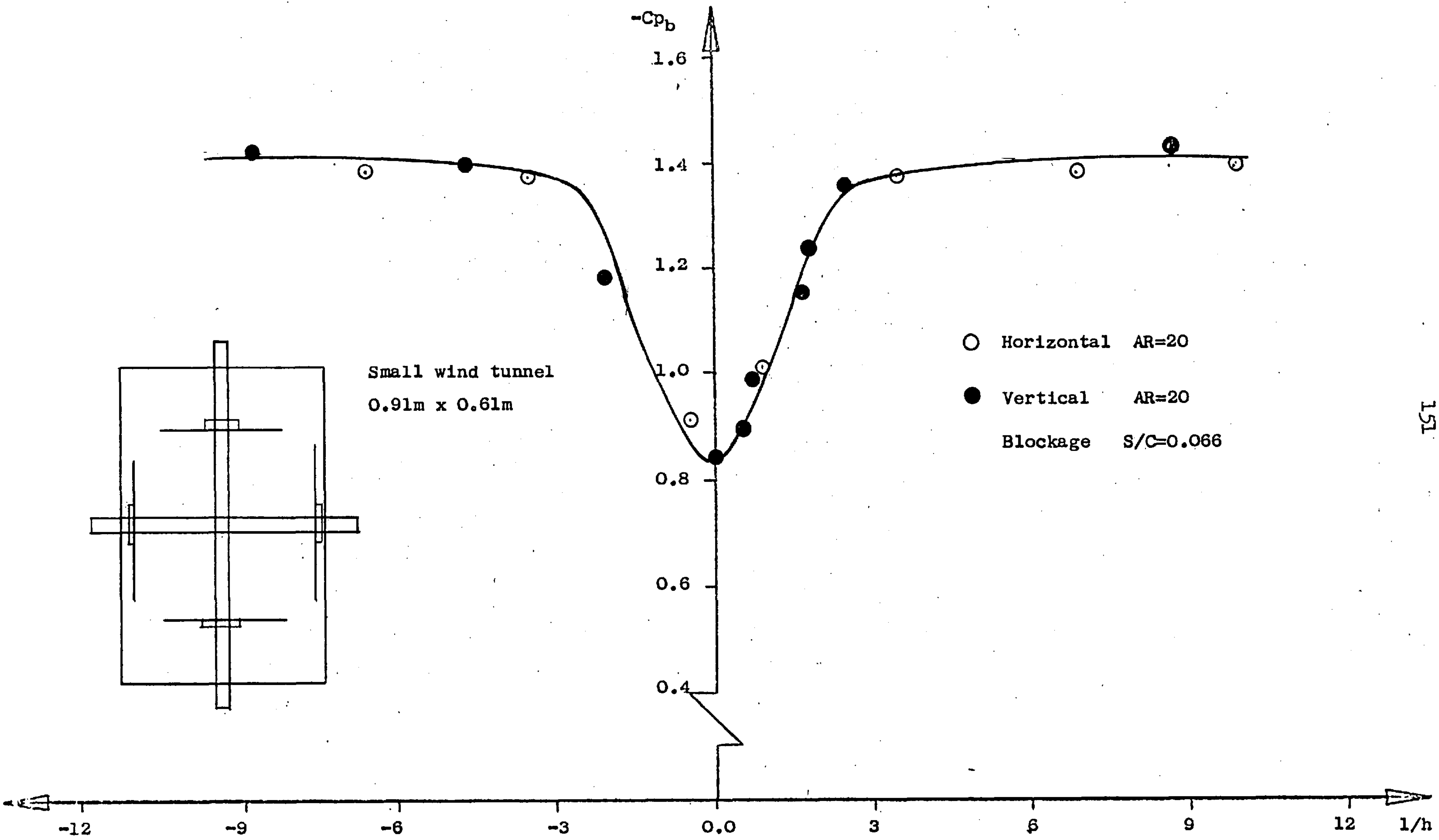

Figure 6.6 Uncorrected Spanwise Base Pressure Coefficient on intersecting flat plates

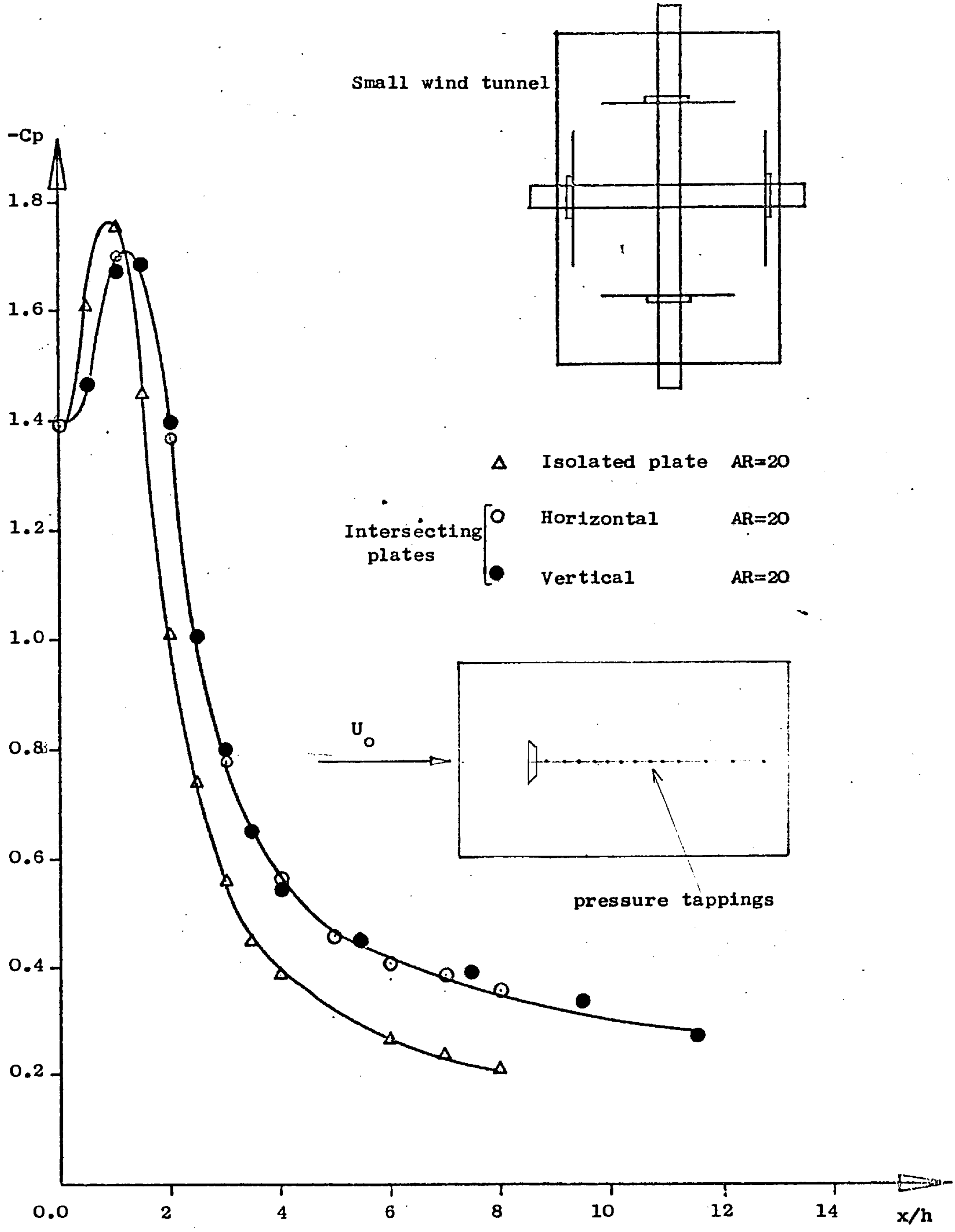

Figure 6.7 Pressure Coefficient downstream on end-plate centre line

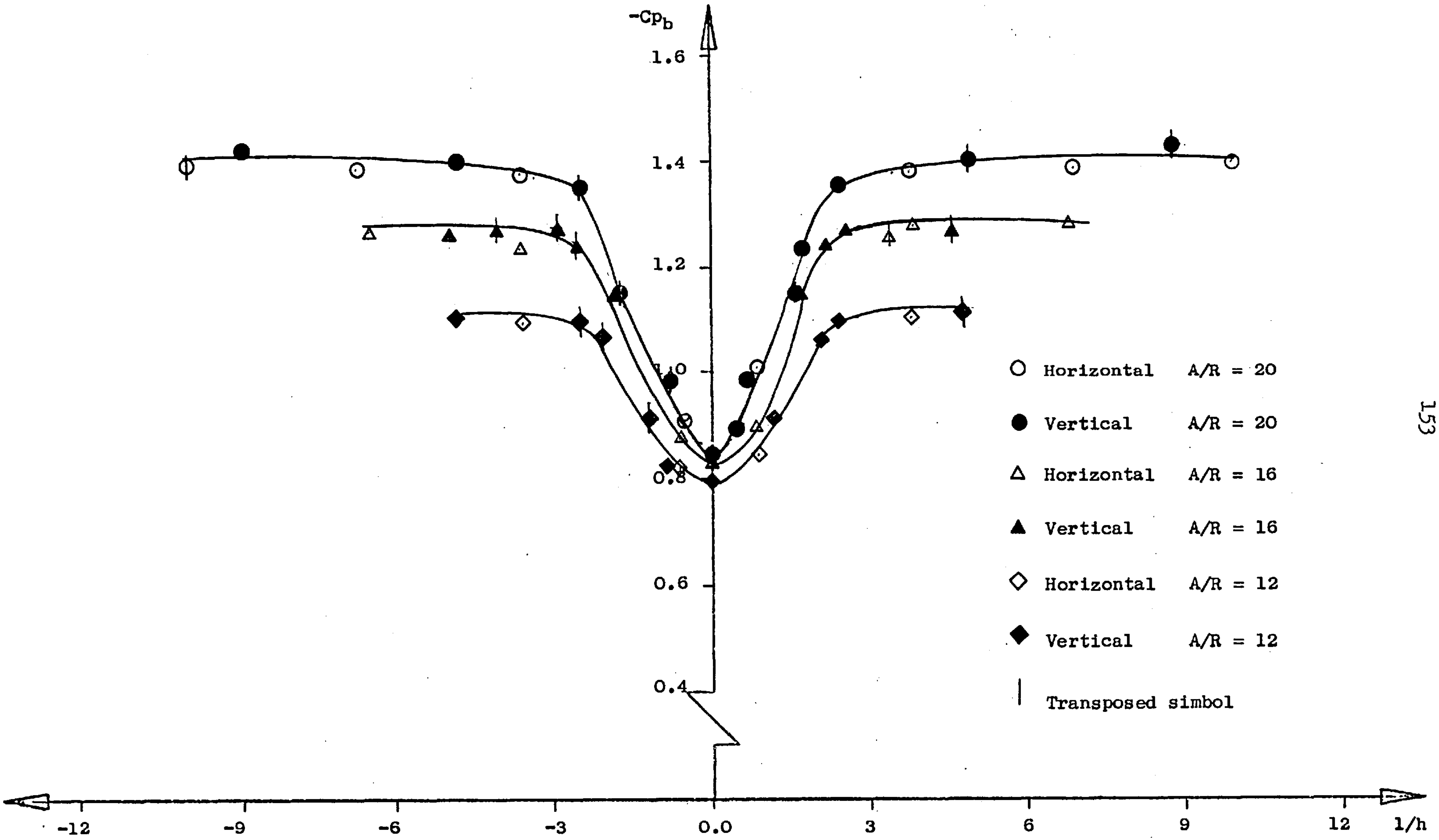

Figure 6.8 Spanwise Base pressure coefficient on intersecting flat plates and effect of Aspect Ratio

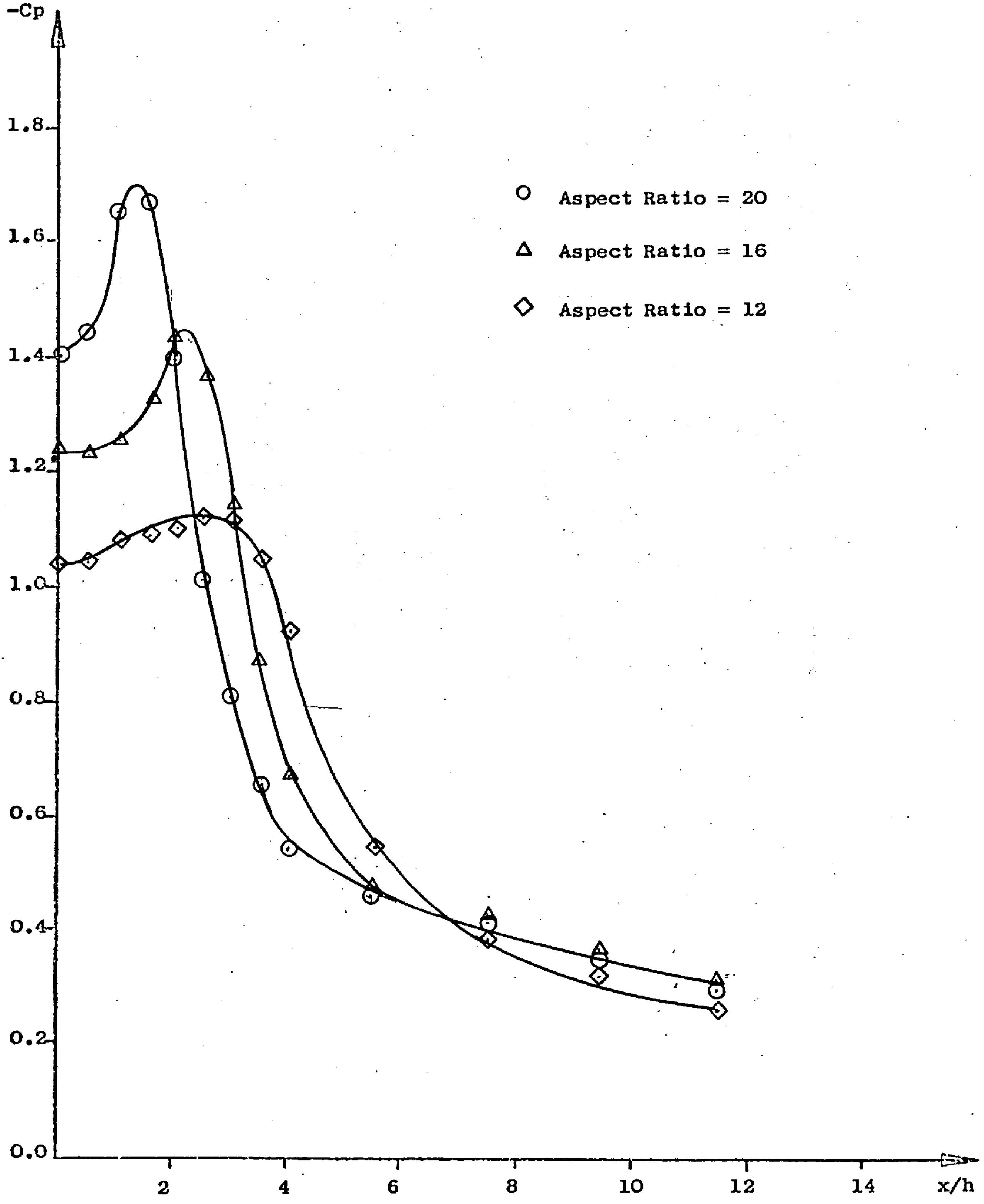

Figure 6.9 Pressure distribution on End-plate centre line and effect of Aspect Ratio

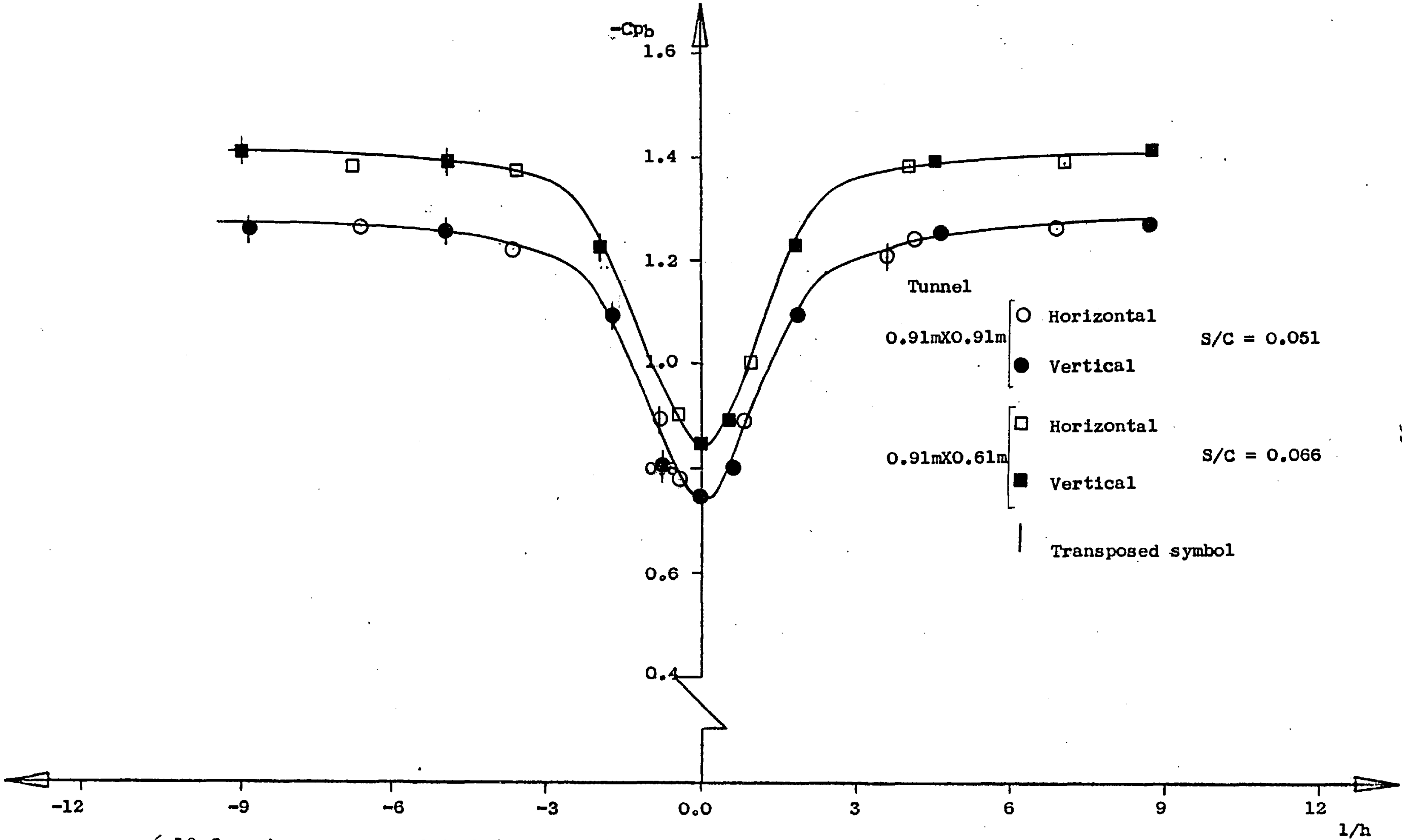

Figure 6.10 Spanwise pressure distribution on Intersecting Flat Plates (AR=20) in different wind tunnels

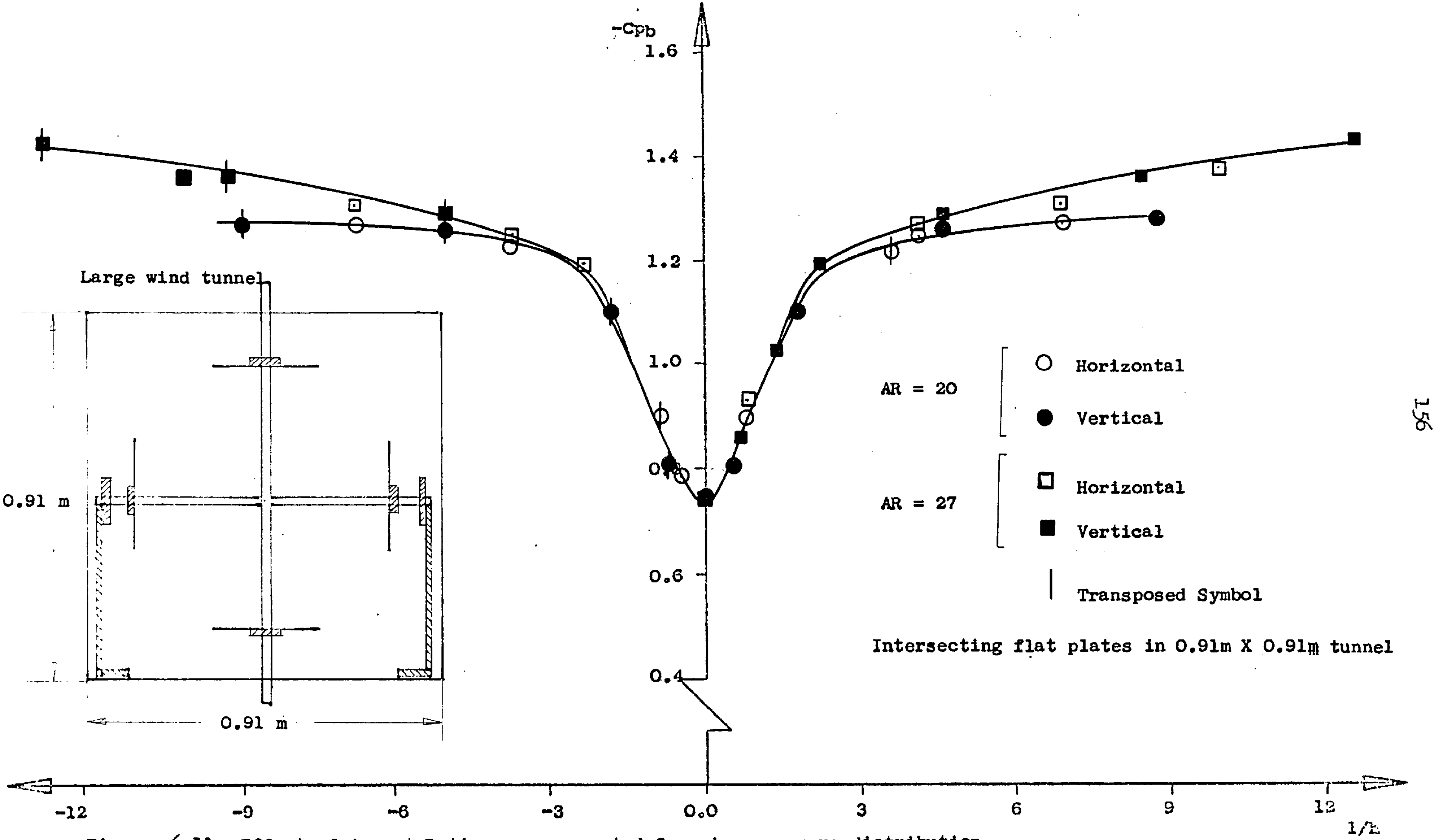

Figure 6.11 Effect of Aspect Ratio on uncorrected Spanwise pressure distribution

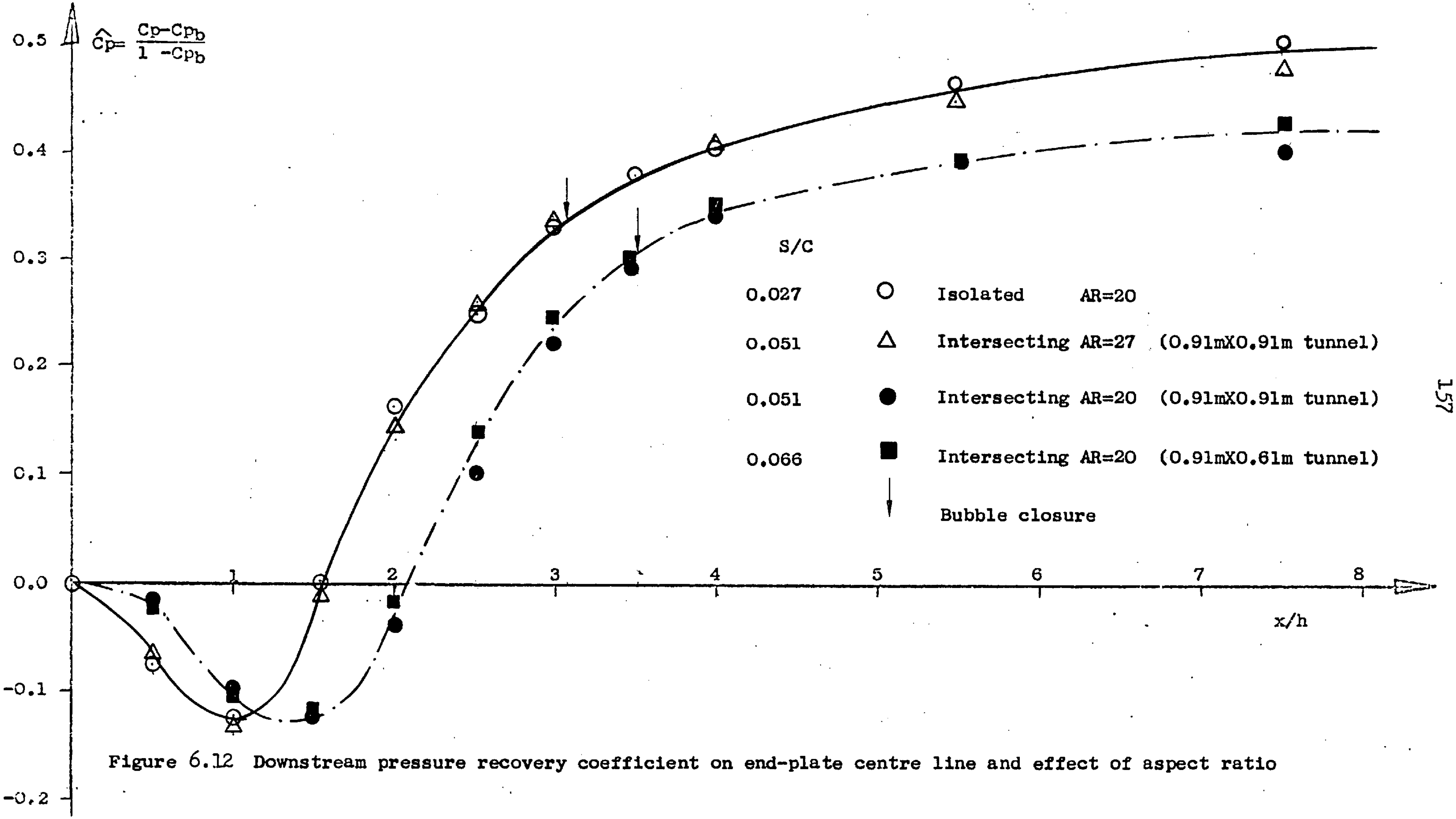

Figure 6.12 Downstream pressure recovery coefficient on end-plate centre line and effect of aspect ratio

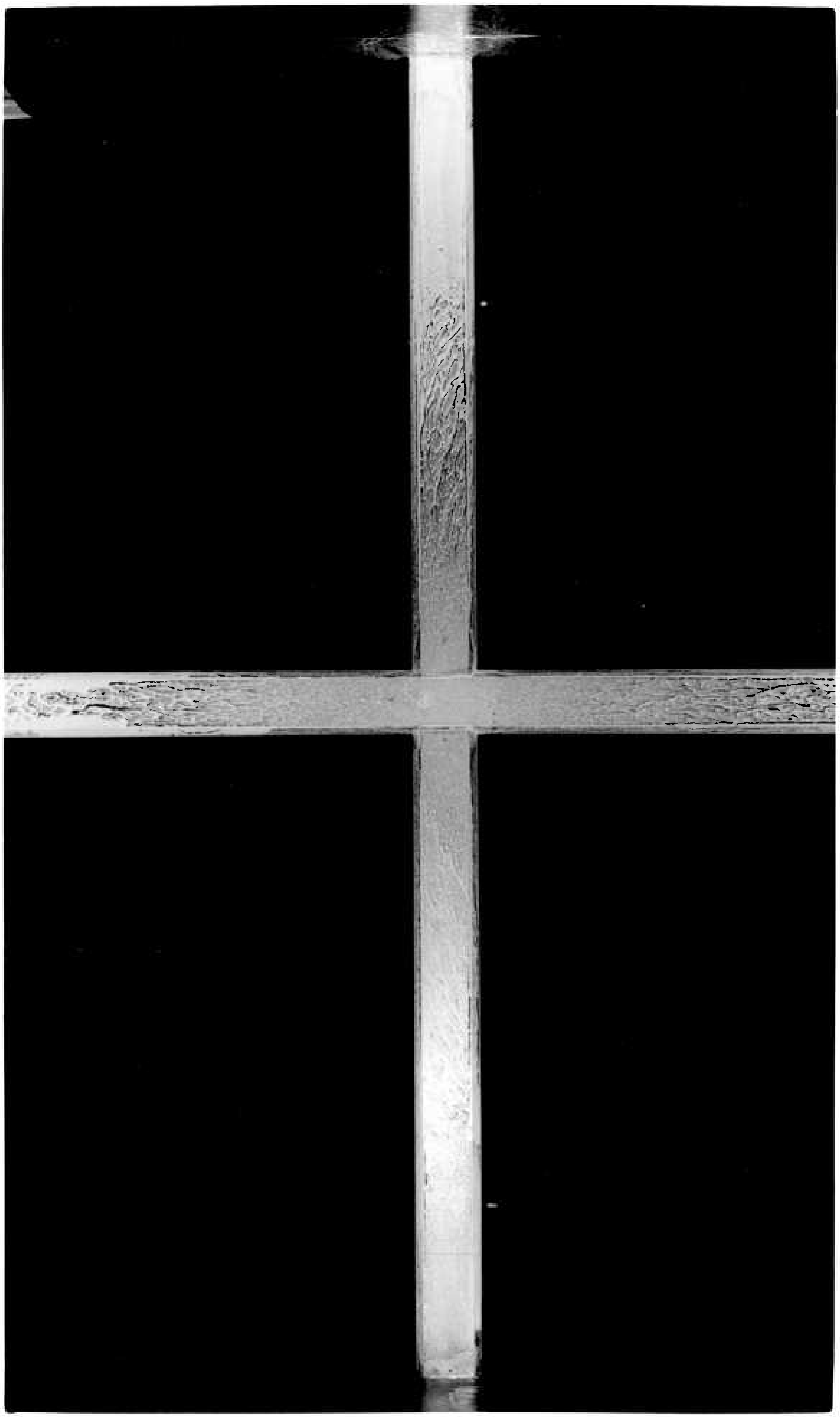

Figure 6.13 Oil flow visualisation on the base of the junction (AR = 20)

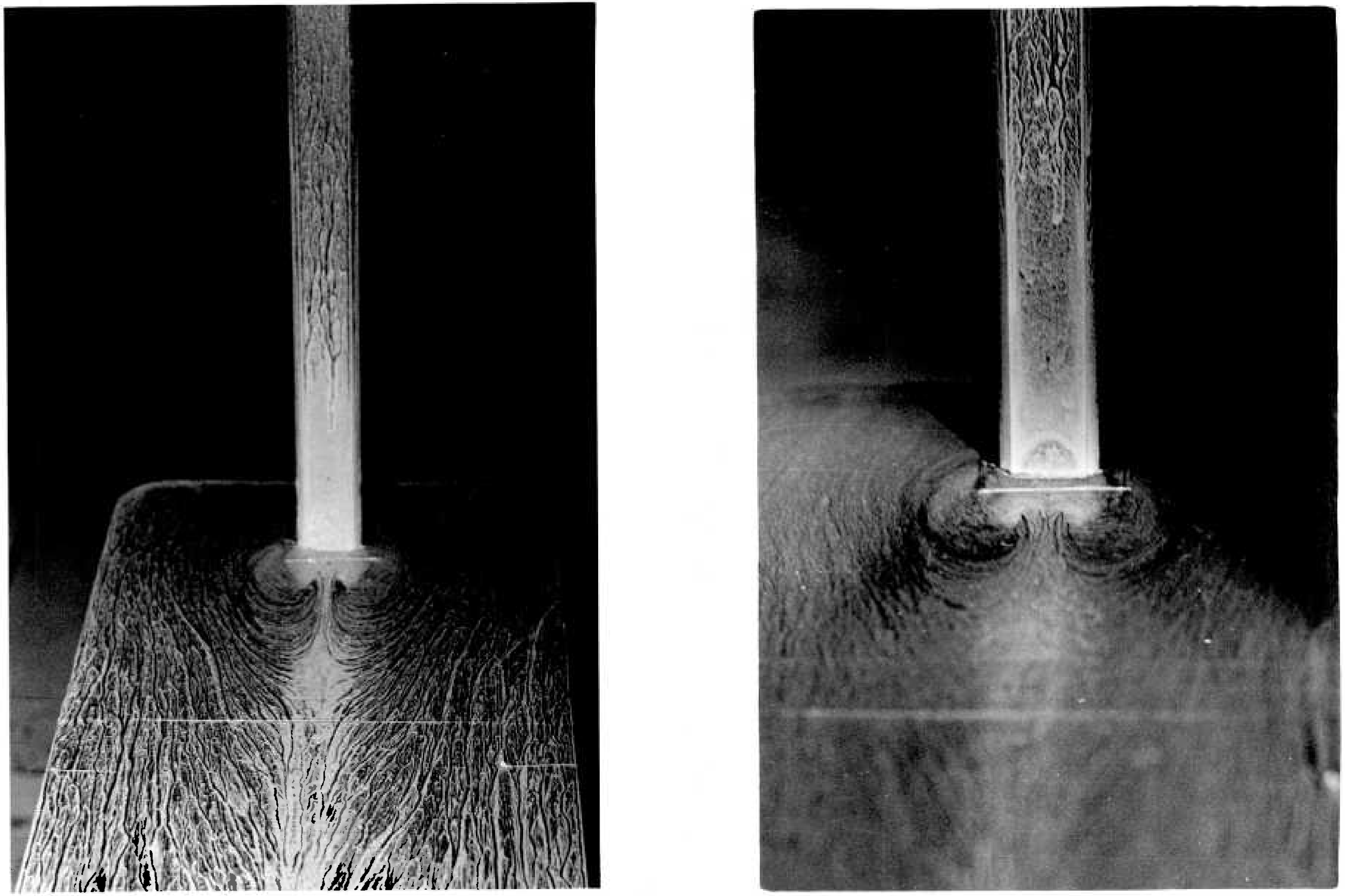

AR = 12

AR = 20

Figure 6.14 Oil flow visualisation on the end-plates

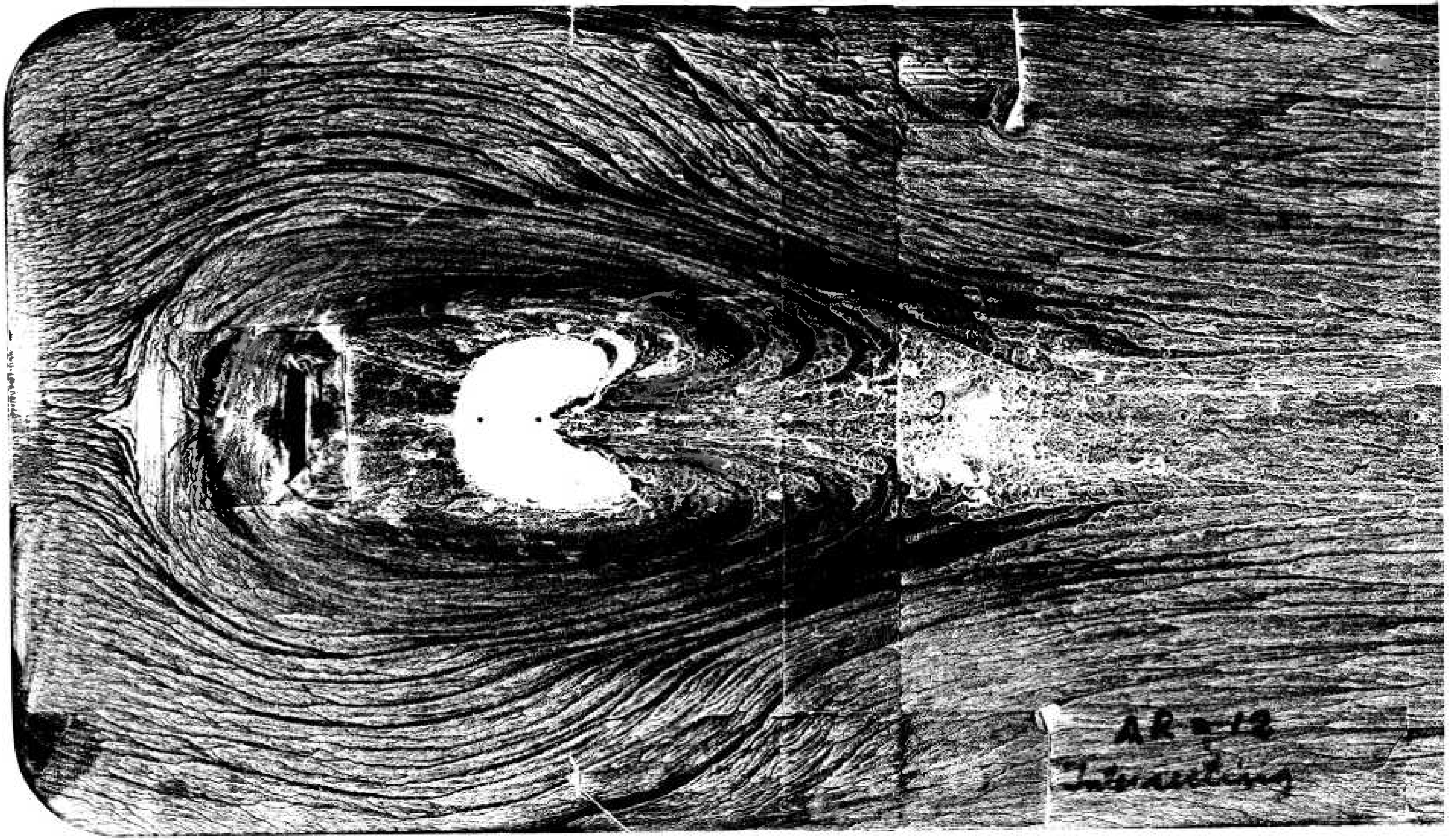

Figure 6.15 Oil flow on the end-plate (intersecting model AR = 12)

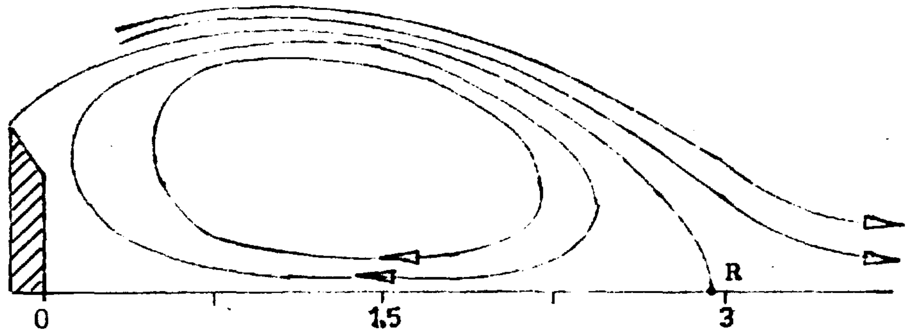

Isolated Flat Plate

Fail et al (8) Pitot measurements
R = 2.8 h

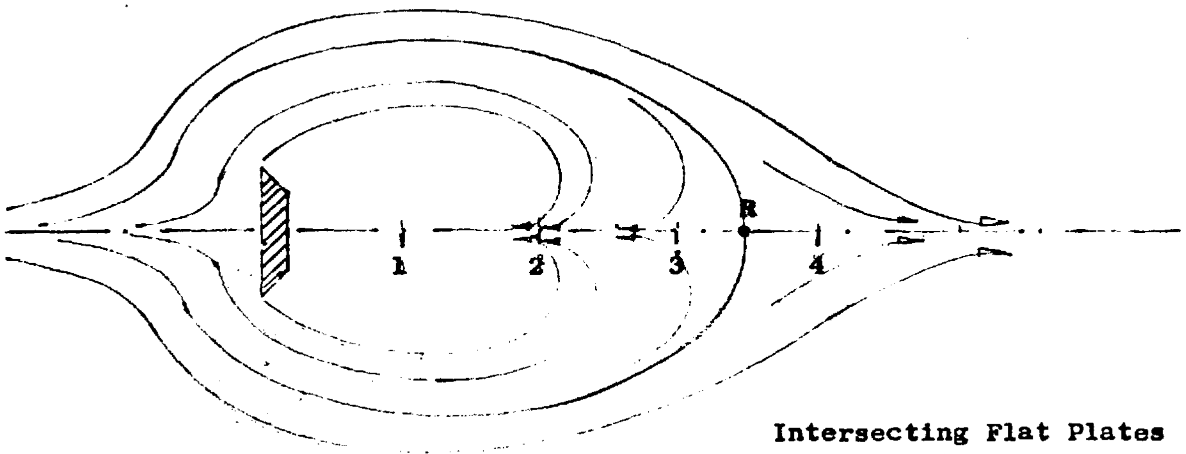

Intersecting Flat Plates
Aspect Ratio = 20
R = 3.5 h

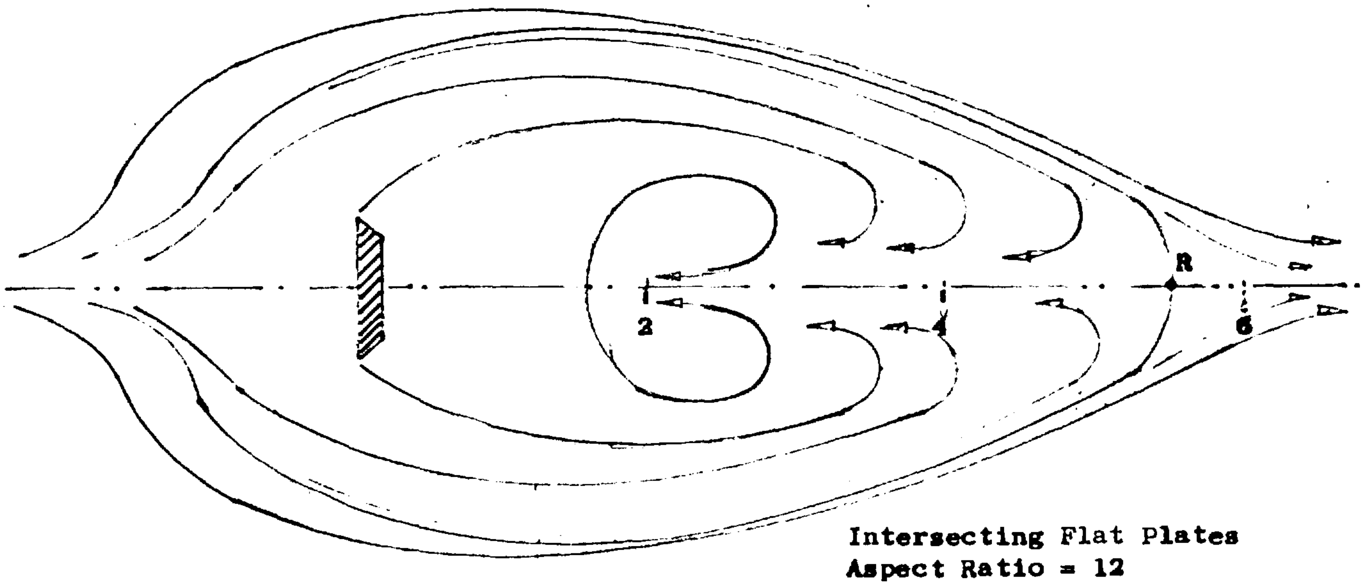

Intersecting Flat Plates
Aspect Ratio = 12
R = 5.5 h

Figure 6.16 Streamline pattern in the Wake of **Isolated** and **Intersecting Plates**

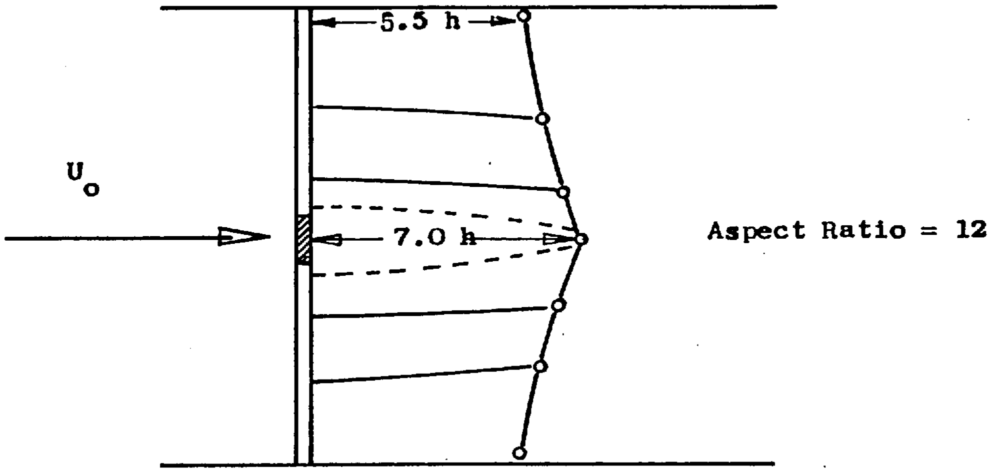

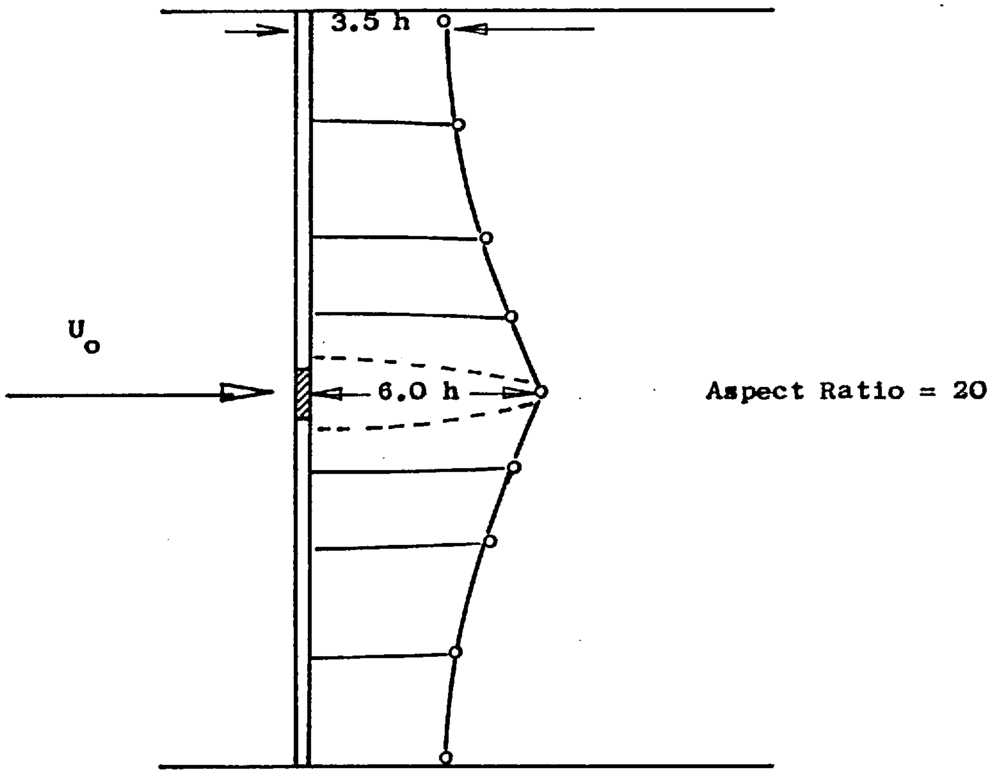

Figure 6.17Sketch showing Bubble length across the Span for intersecting plates

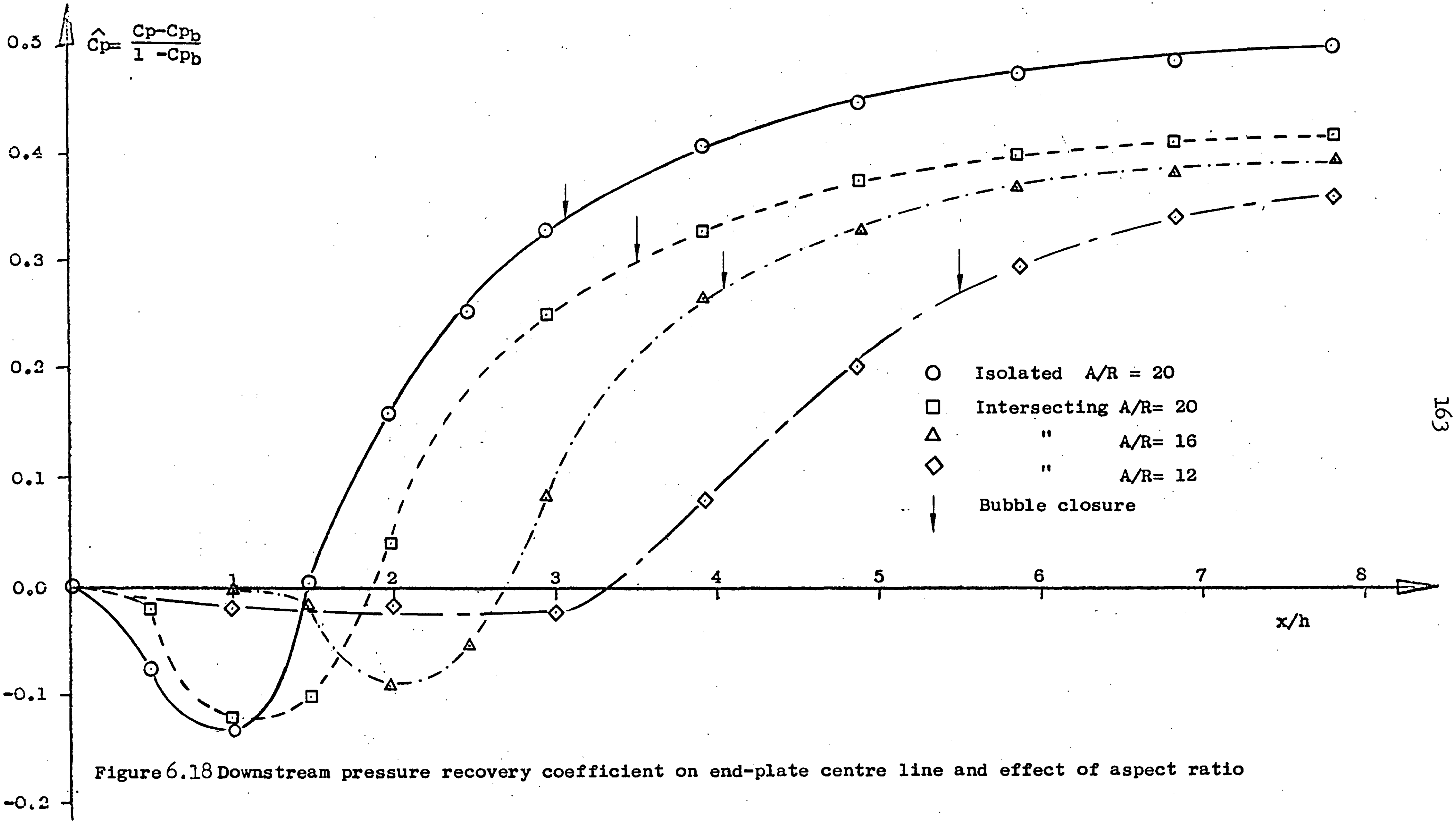

Figure 6.18 Downstream pressure recovery coefficient on end-plate centre line and effect of aspect ratio

Turbulent wake of a normal flat plate

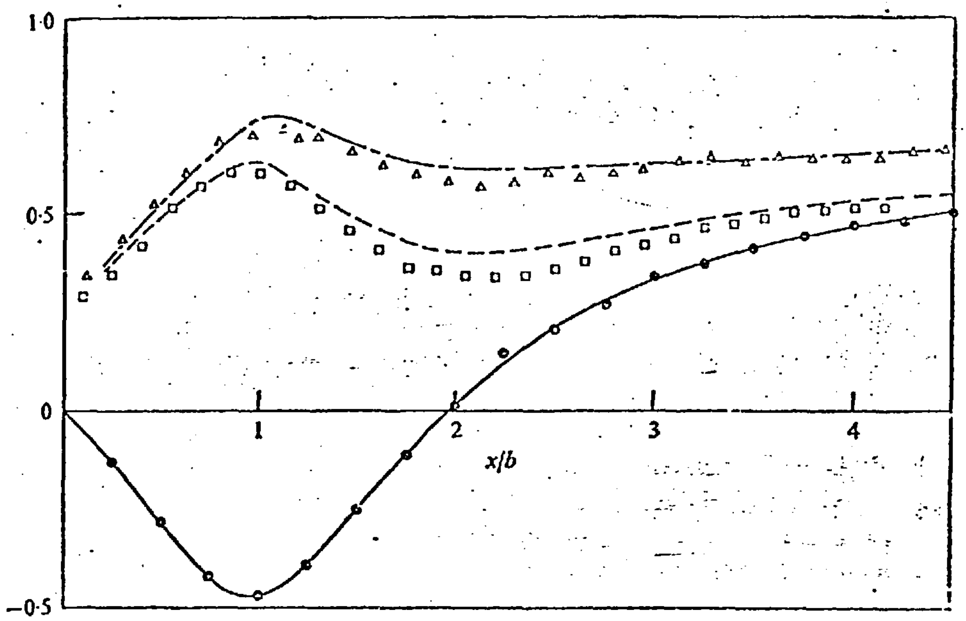

FIGURE 8. Mean velocity measurements downstream of the flat plate ($y/b = 0$). △, hot wire with axis in z direction; □, hot wire with axis in y direction; ⊖, pulsed wire; —·—, – – –, calculated hot-wire response.

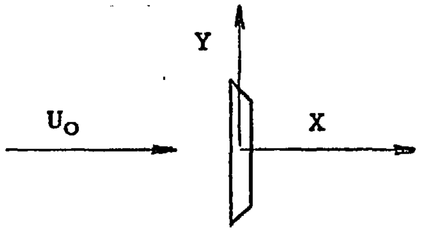

Turbulent wake of a normal flat plate

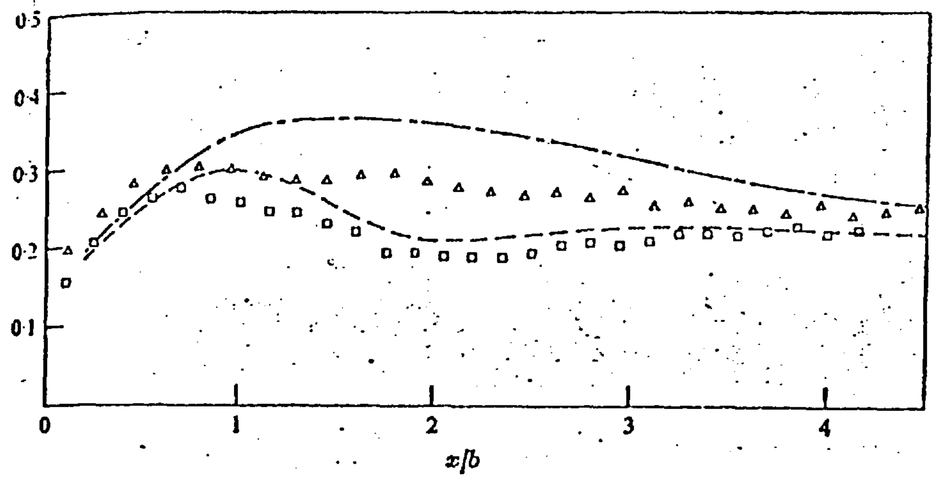

FIGURE 10. σ_u measurements with a hot-wire anemometer downstream of a flat plate. Notation as in figure 8.

Figure 6.19 Figures reproduced from Bradbury(41)

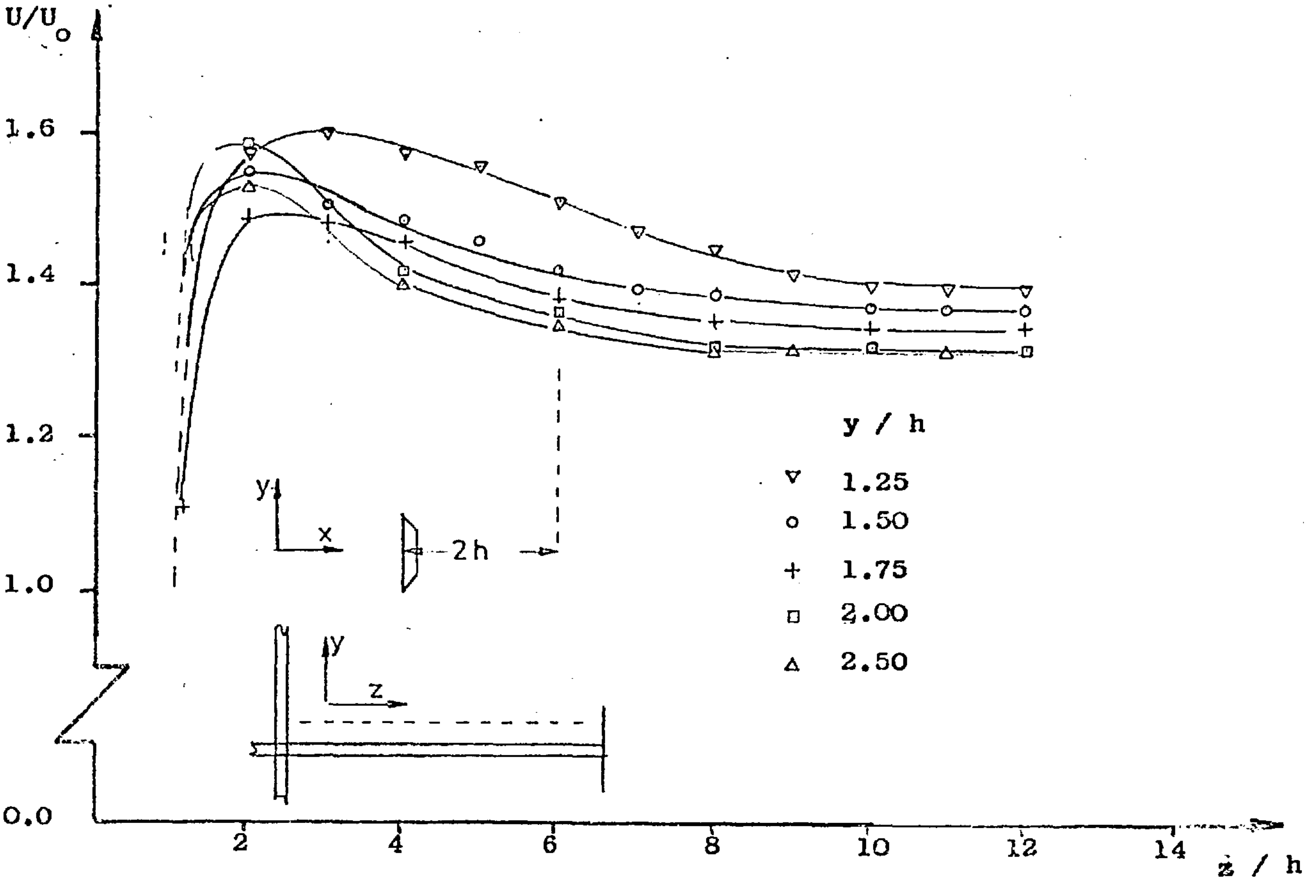

Figure 6.20 Spanwise velocity distribution (AR = 27 , S / C = 0.051)

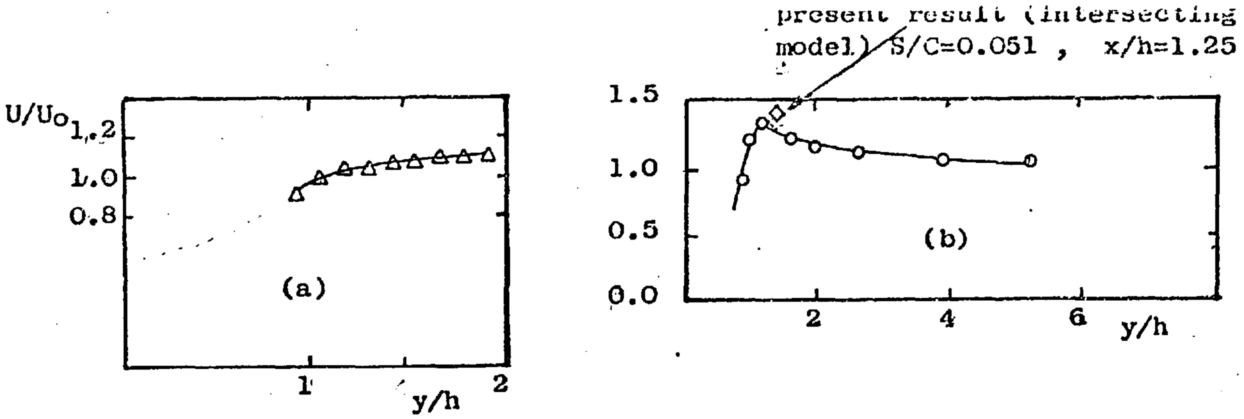

△ Bradbury(41) With end-plates
corrected values : S/C=0.1
measurement at x/h=2.0

○ Fail et al(8) Without end-plates
Corrected values S/C=0.025
measurements at x/h=1.25

◇ Present result
Intersecting
model

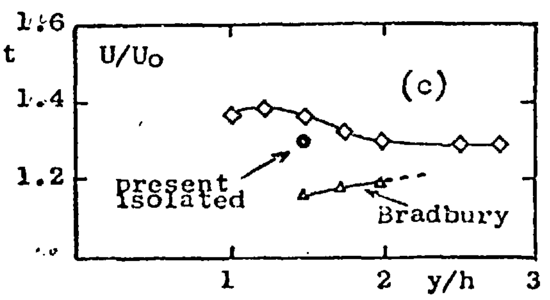

◇ measurements at x/h=2 ,
z/h=12.4

uncorrected for Blockage.

Figure 6.21 Chordwise velocity distribution (AR=27, S/C=0.051)

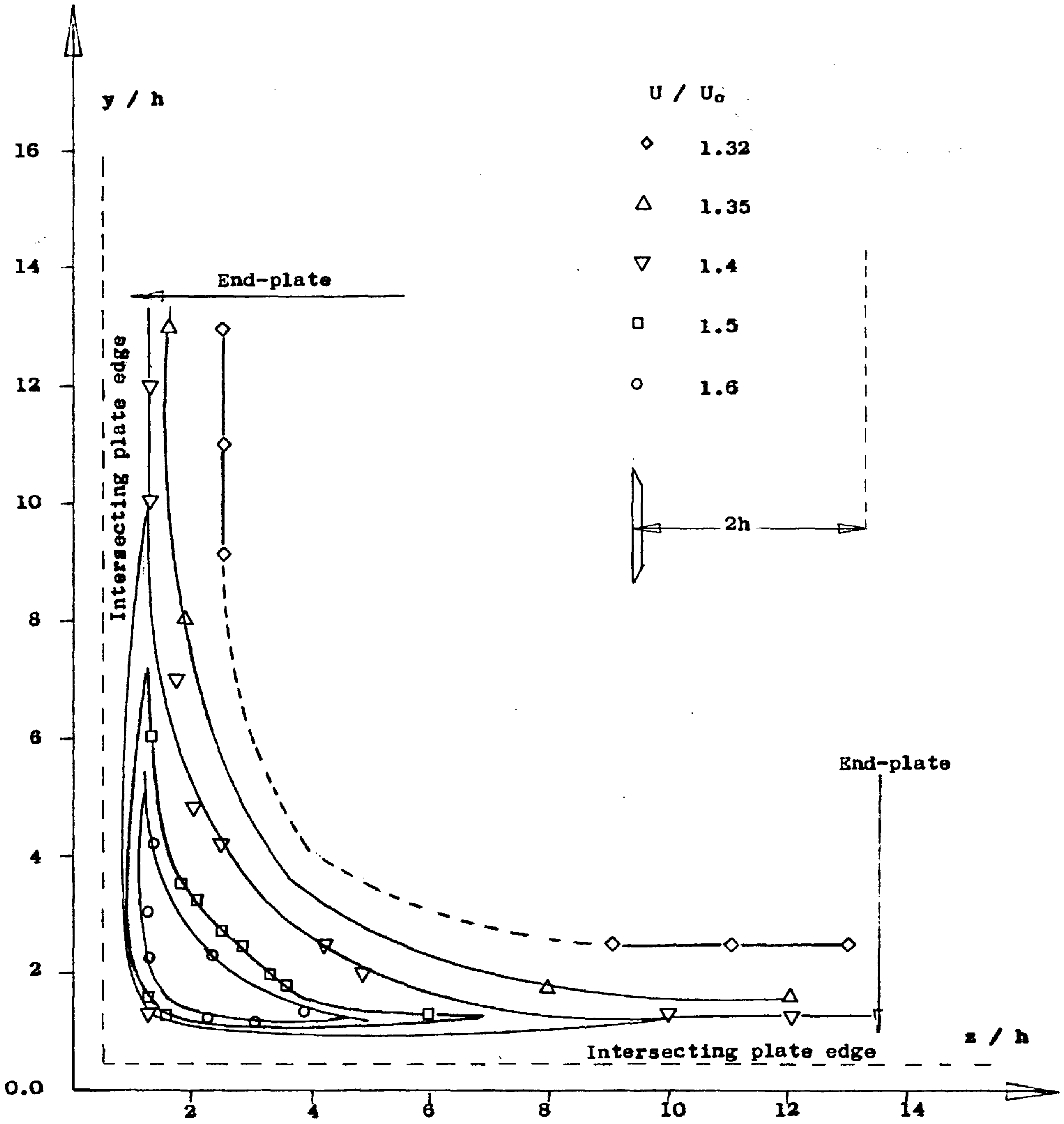

Figure 6.22 Mean Velocity distribution for intersecting flat plates

Aspect Ratio 27 (0.91m x 0.91m Wind tunnel S/C = 0.051)

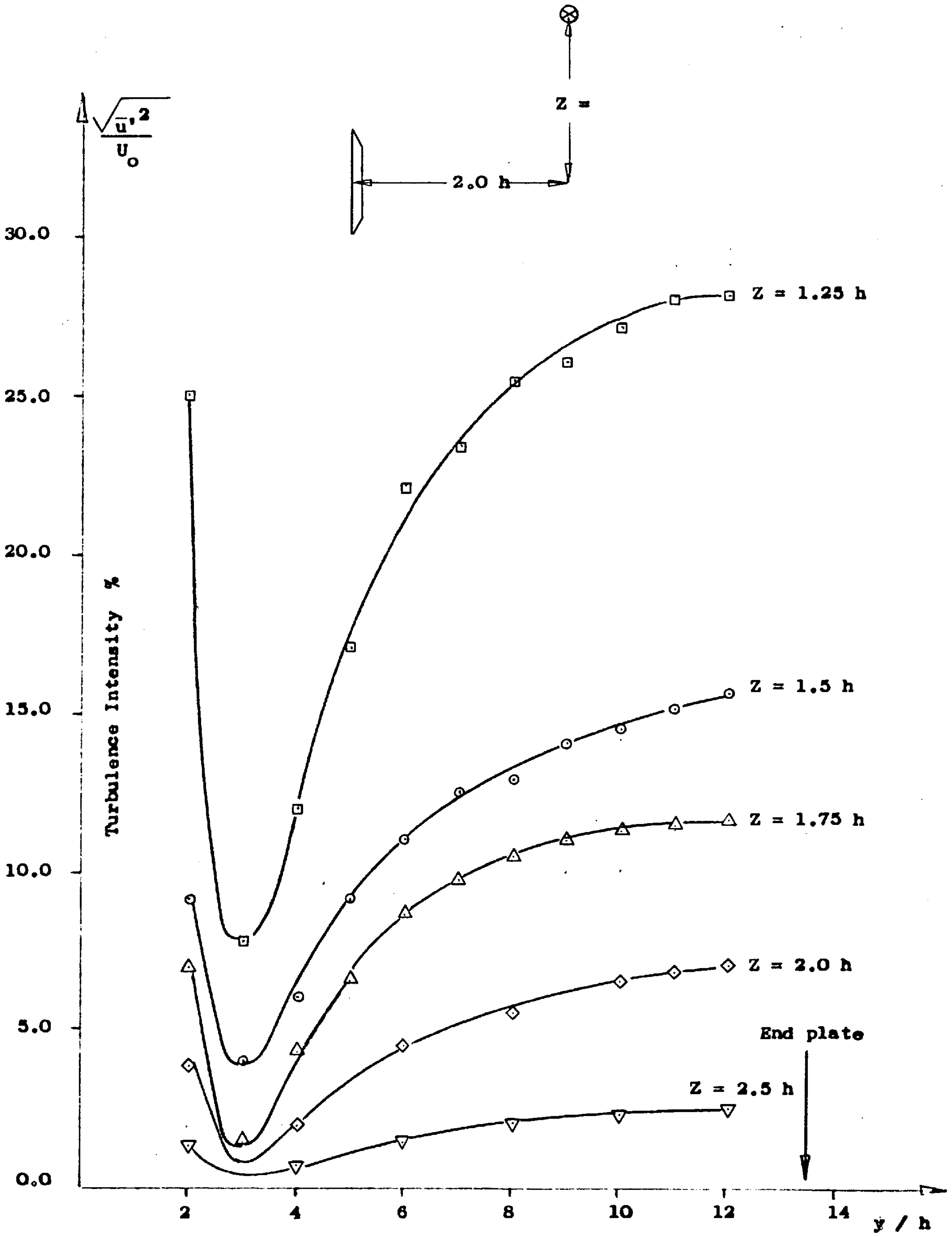

Figure 6.23 Velocity Fluctuation distribution across the Span for Intersecting Flat plates (AR = 27)

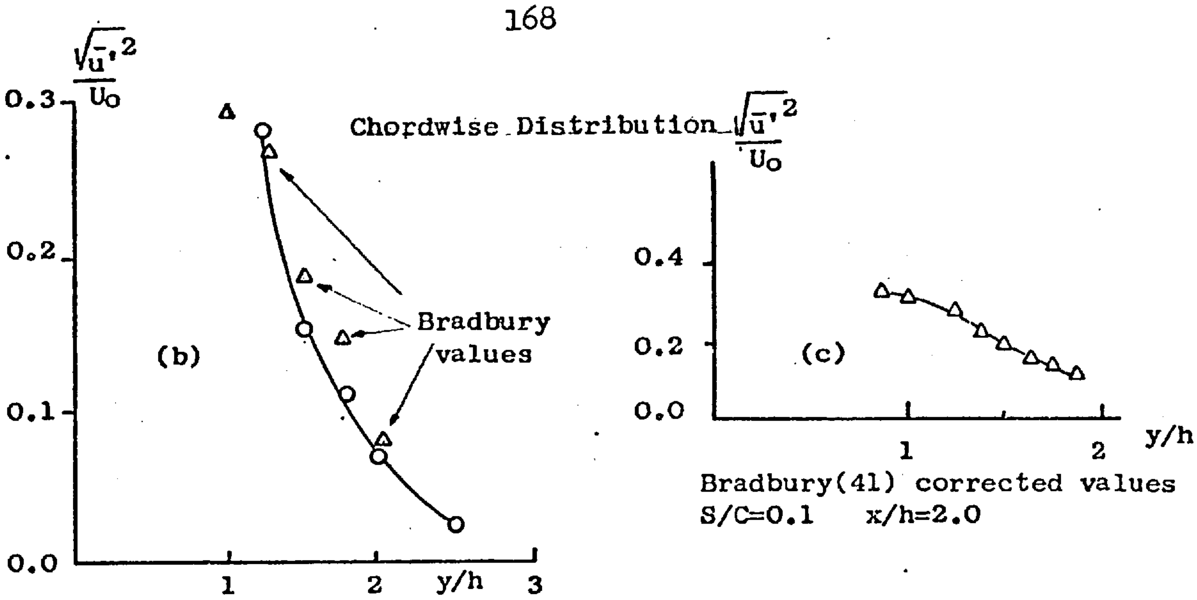

Present results Intersecting model uncorrected values S/C=0.051 x/h=2.0

Bradbury(41) corrected values S/C=0.1 x/h=2.0

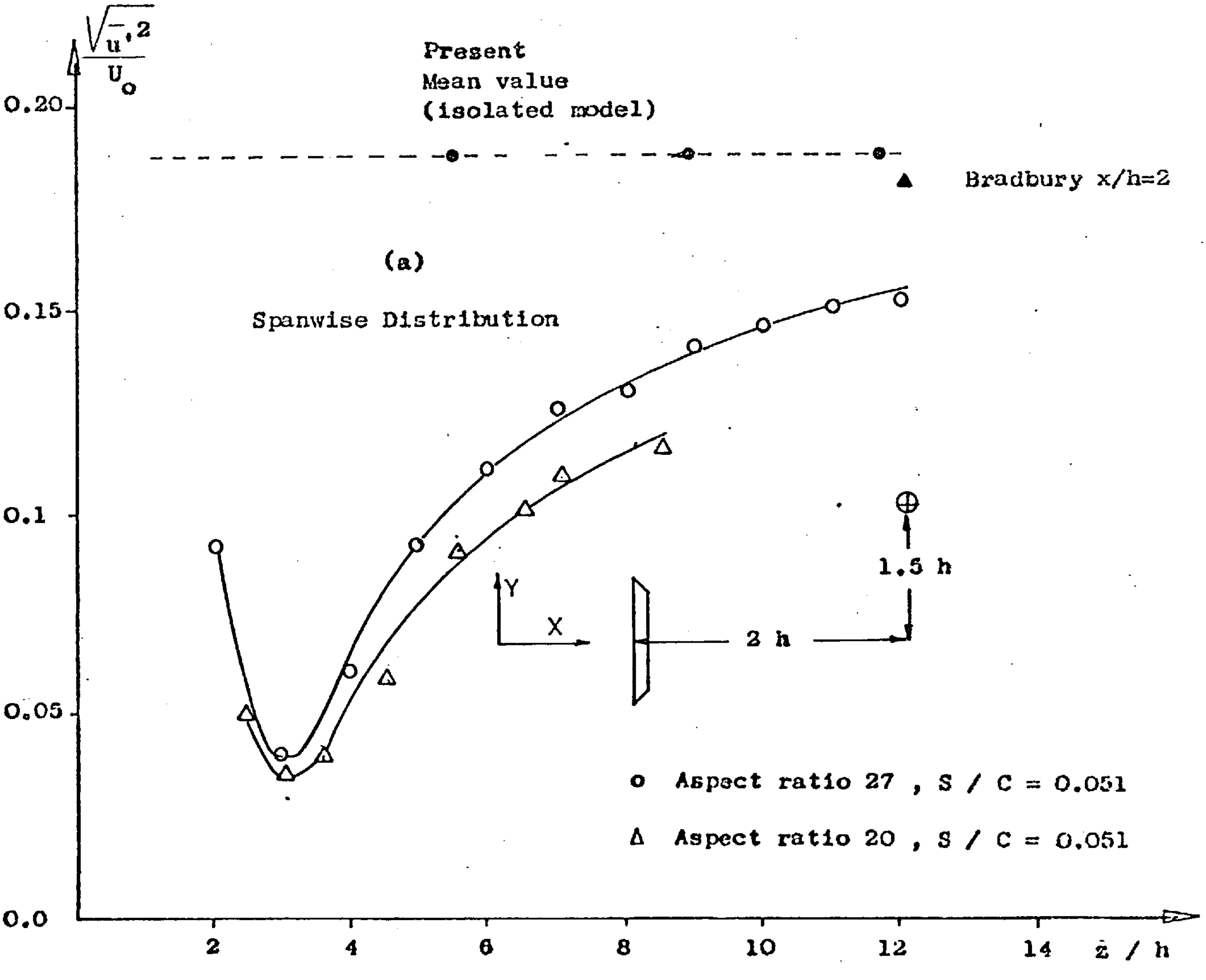

Figure 6.24 Intensity of the fluctuating velocities for intersecting plates

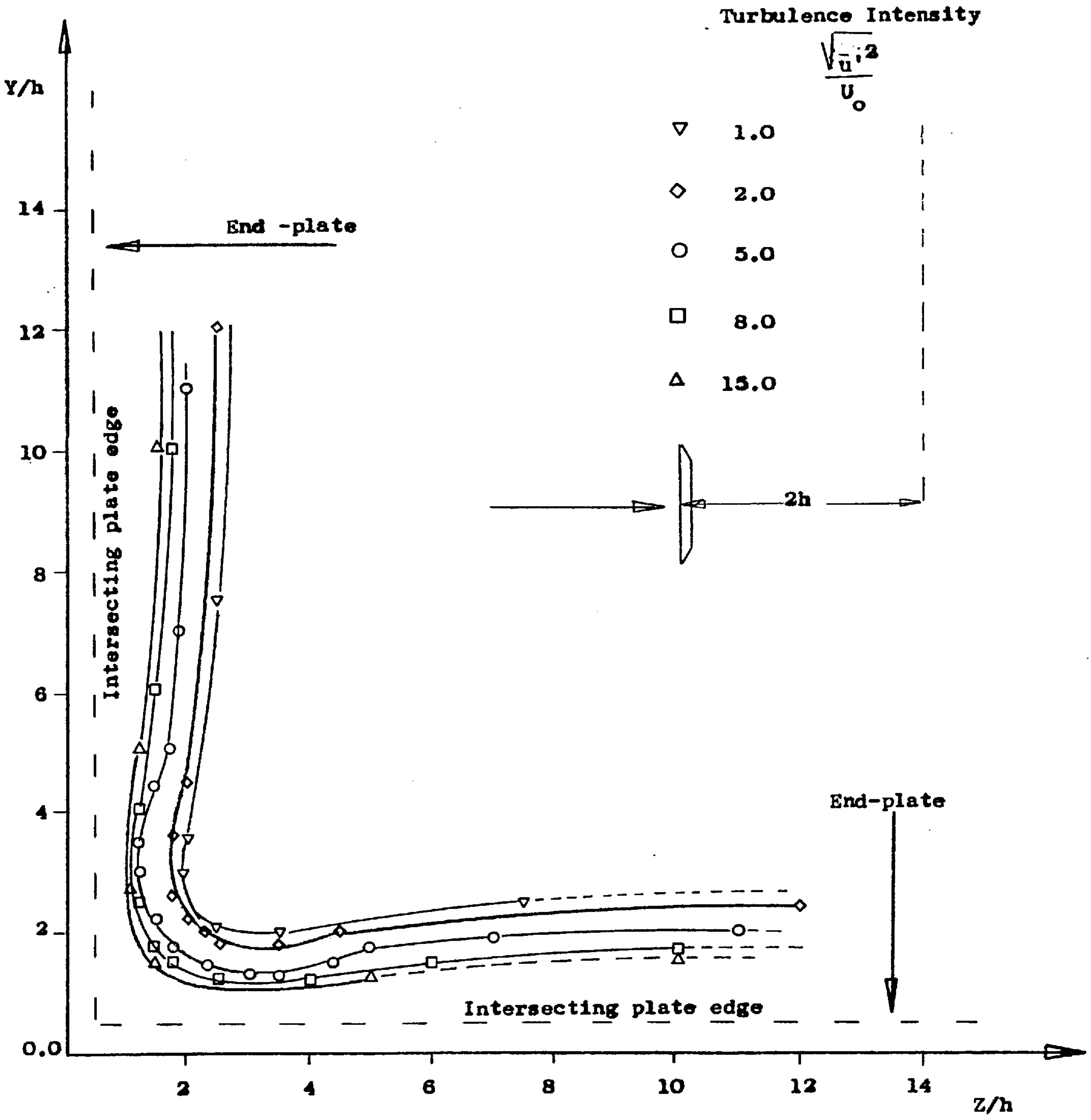

Figure 6.25 Intensity of the ~~Velocity~~ Velocity Fluctuation distribution for Intersecting flat plates Aspect Ratio 27 (0.91m X 0.91m wind tunnel)

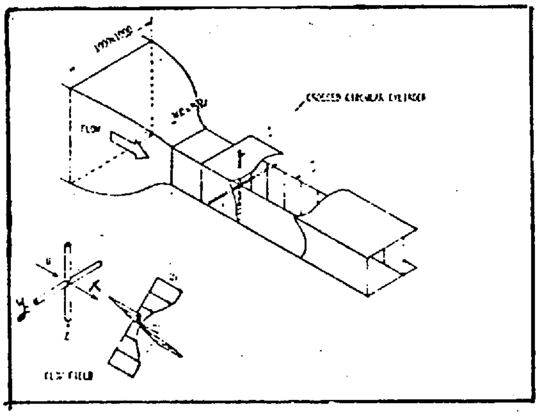

Intersecting Circular Cylinders mounted in the Wind Tunnel

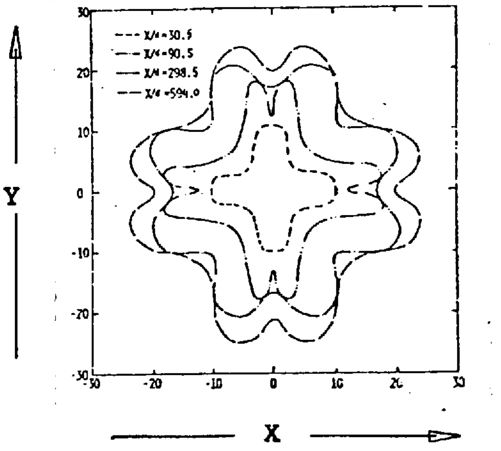

Mean Velocity contours downstream

Intensity of the Fluctuating Velocity distribution

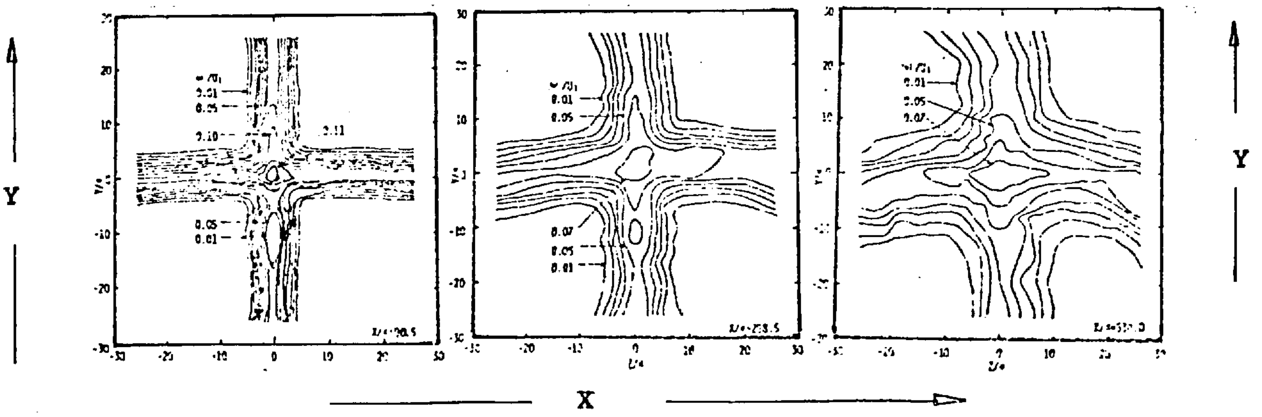

Figure 6.26 Figures Reproduced from Nakamura et al(62)

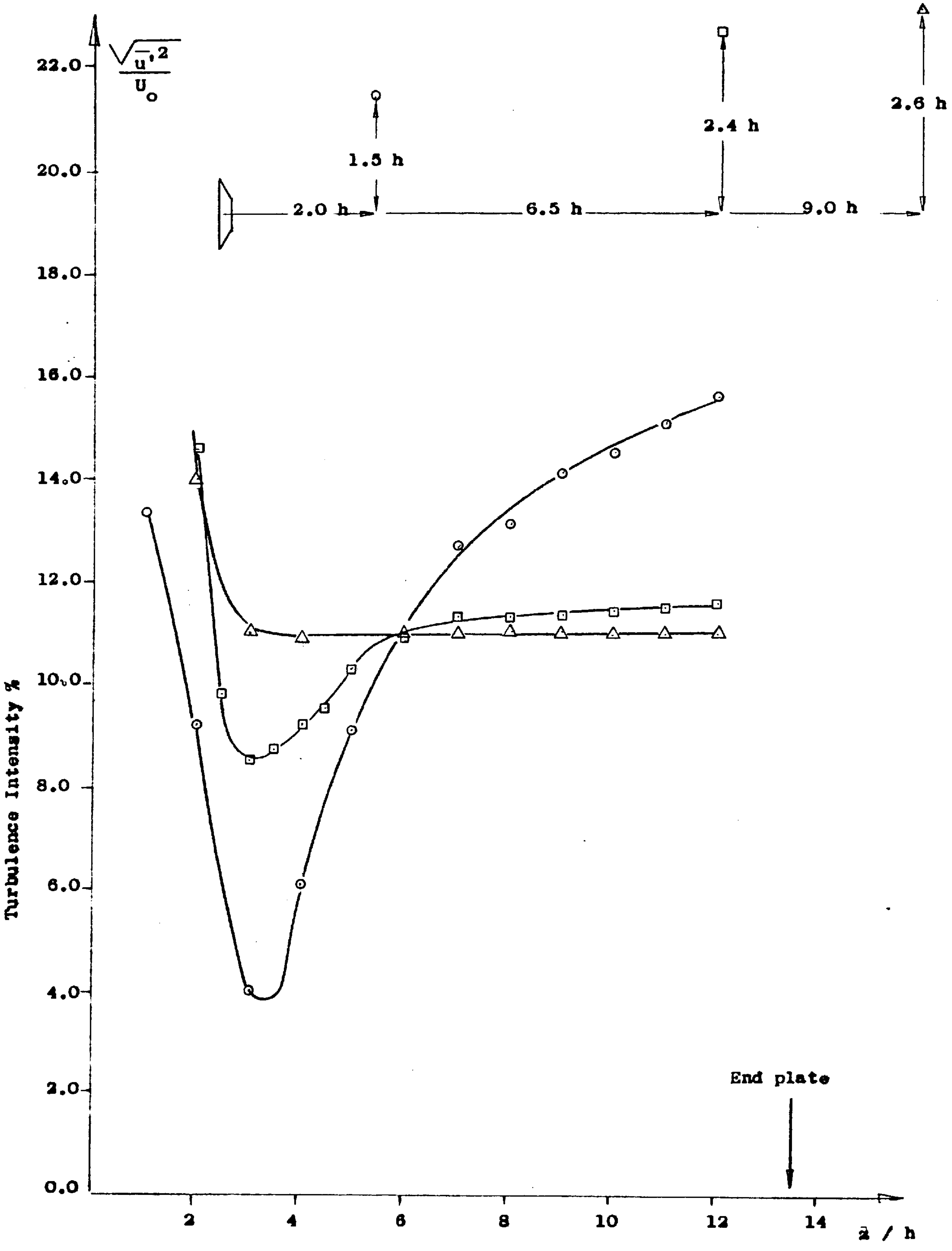

Figure 6.27 Velocity Fluctuation distribution across the span (AR = 27)

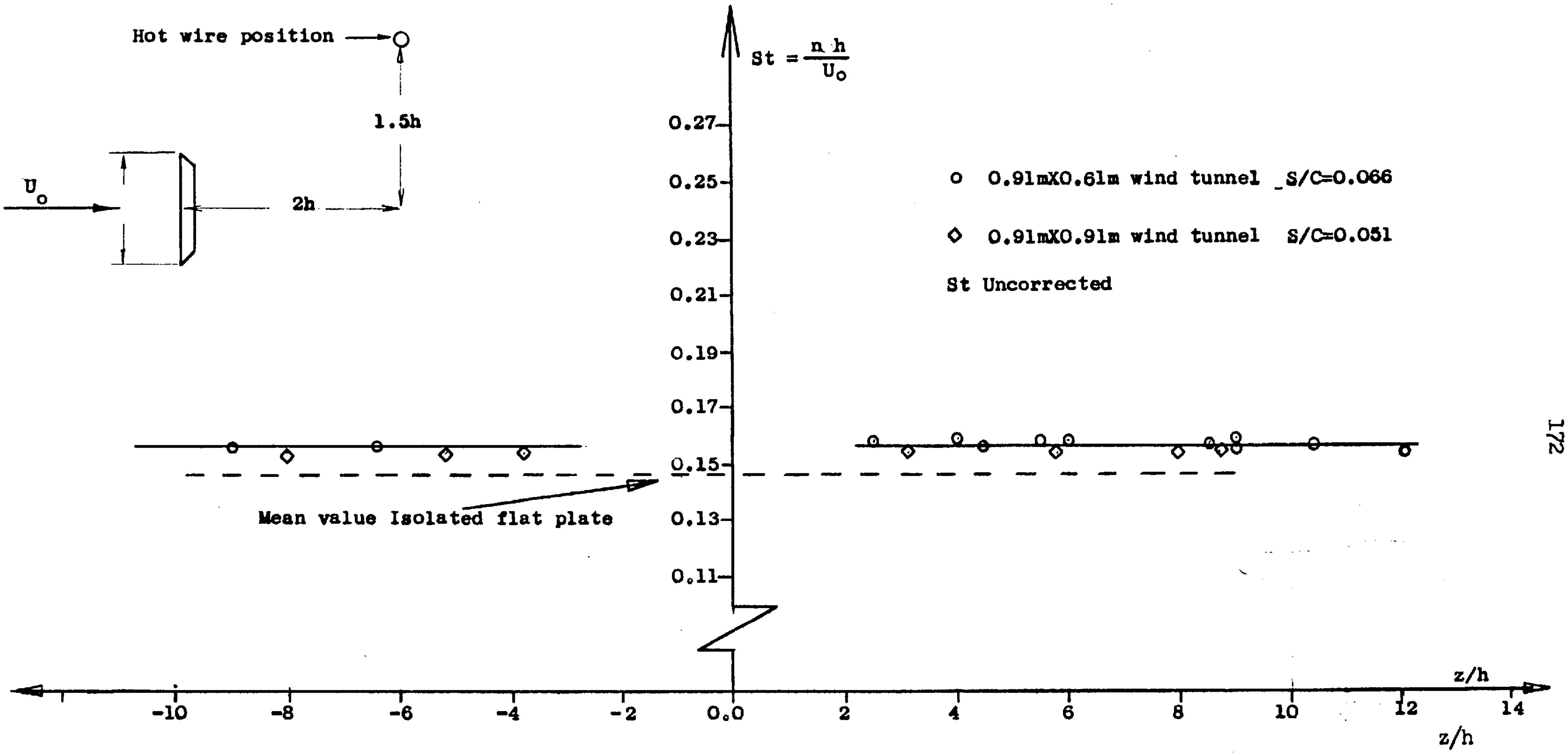

Figure 6.28 Spanwise Strouhal number distribution for intersecting flat plates

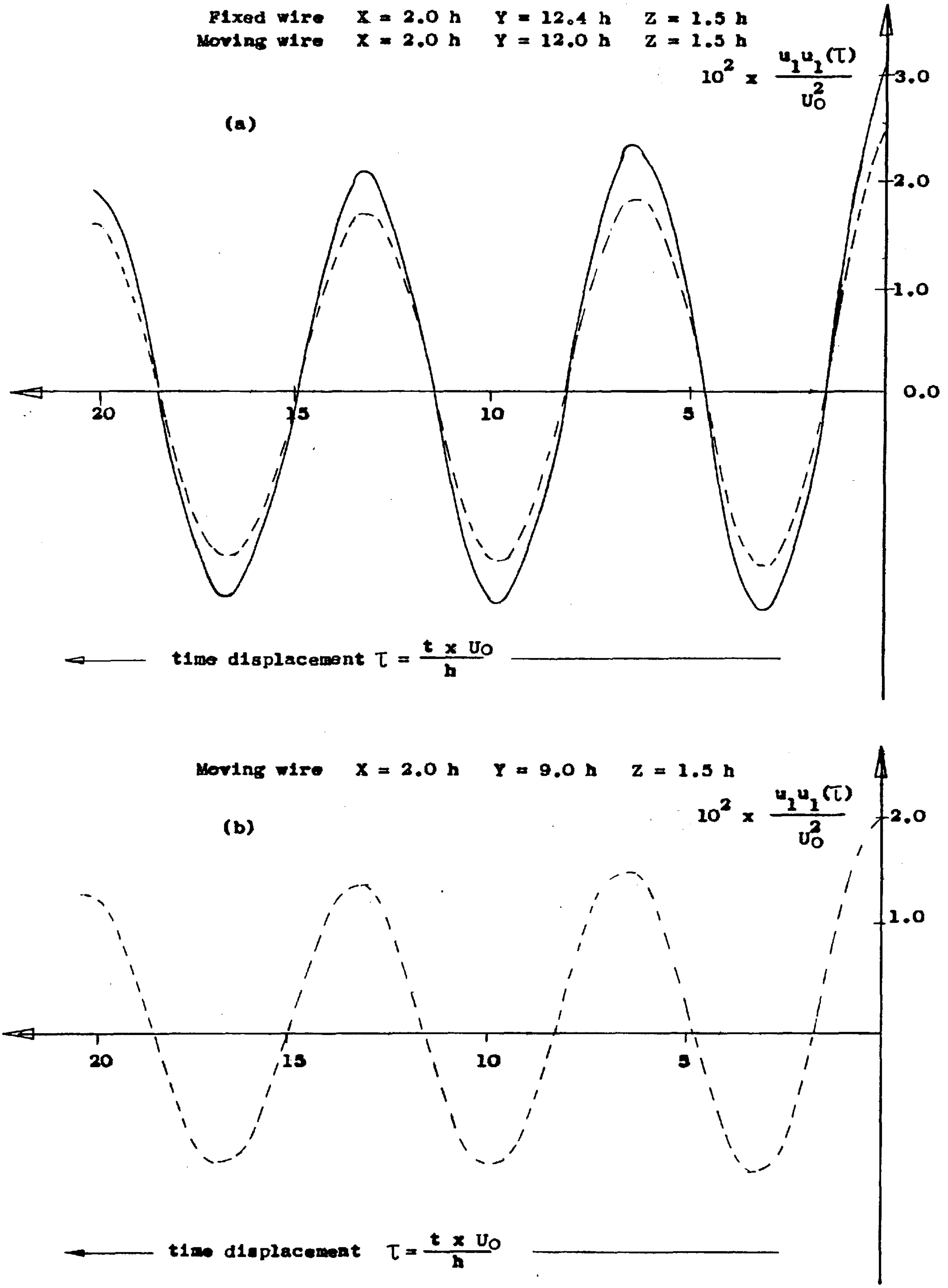

Figure 6.29 Non-dimensional Autocorrelogram showing decay of Energy at Shedding Frequency

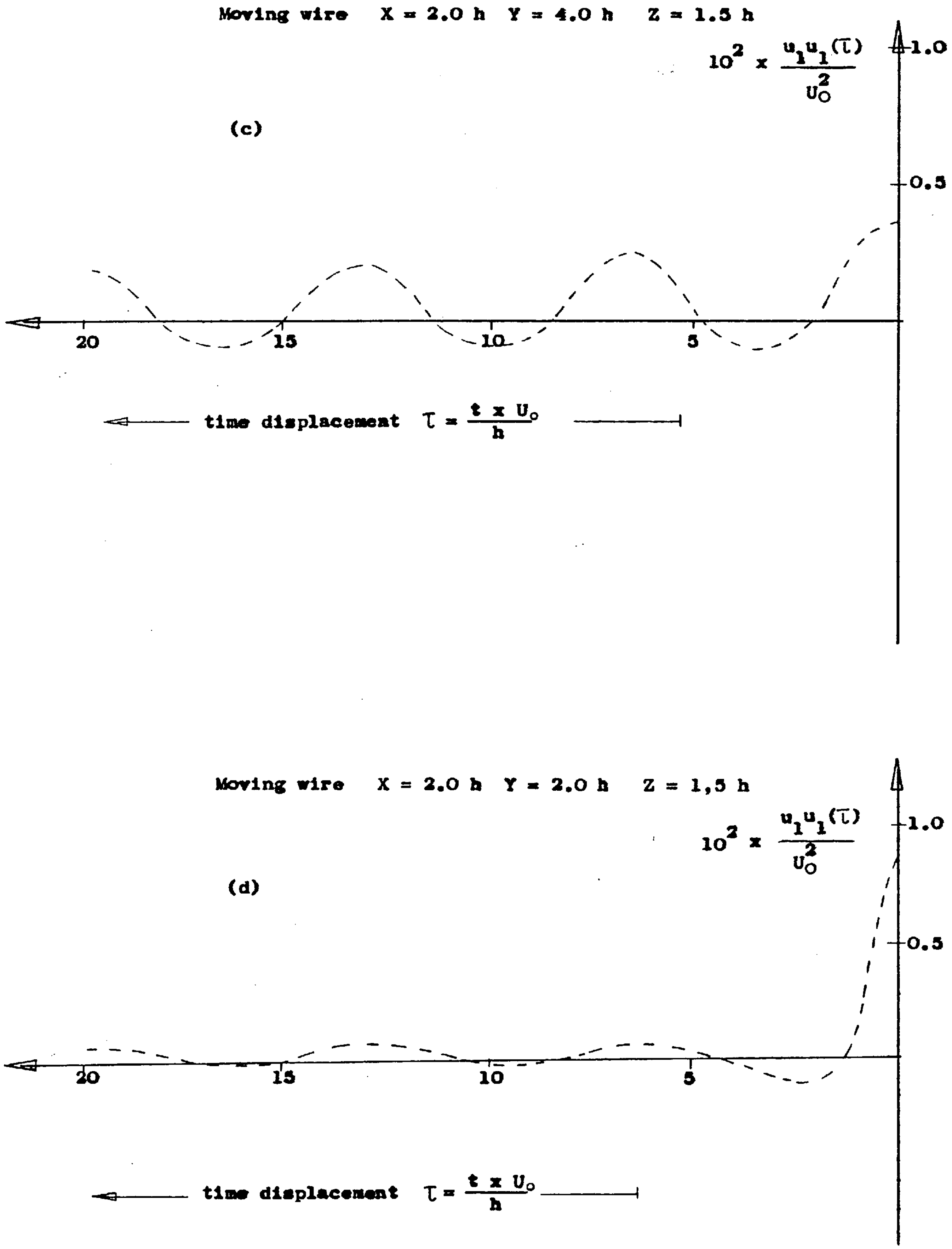

Figure 6.29 Non-dimensional Autocorrelogram showing decay of Energy at Shedding Frequency

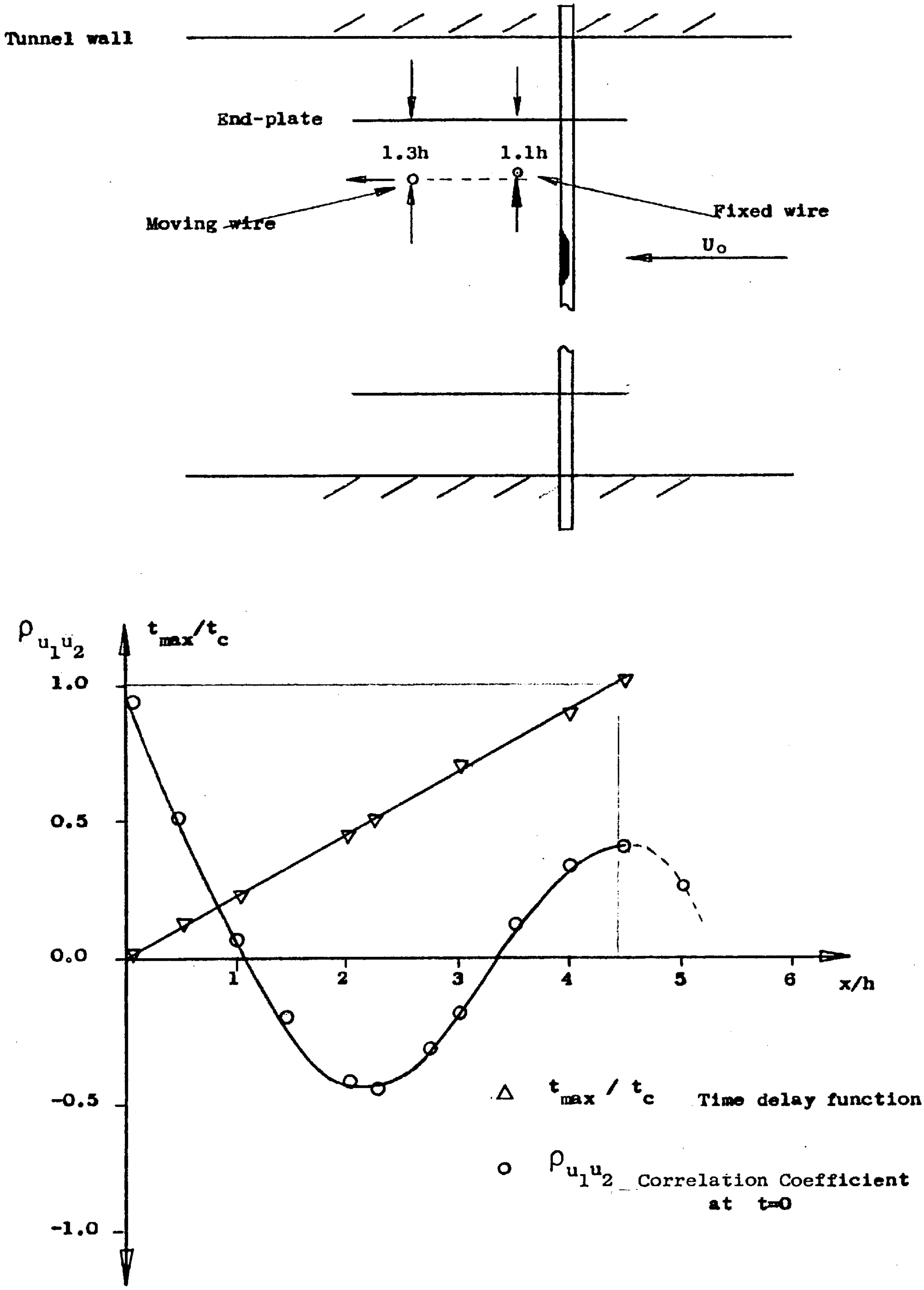

Figure 6.30 Streamwise velocity correlation for Intersecting flat plates (AR = 27)

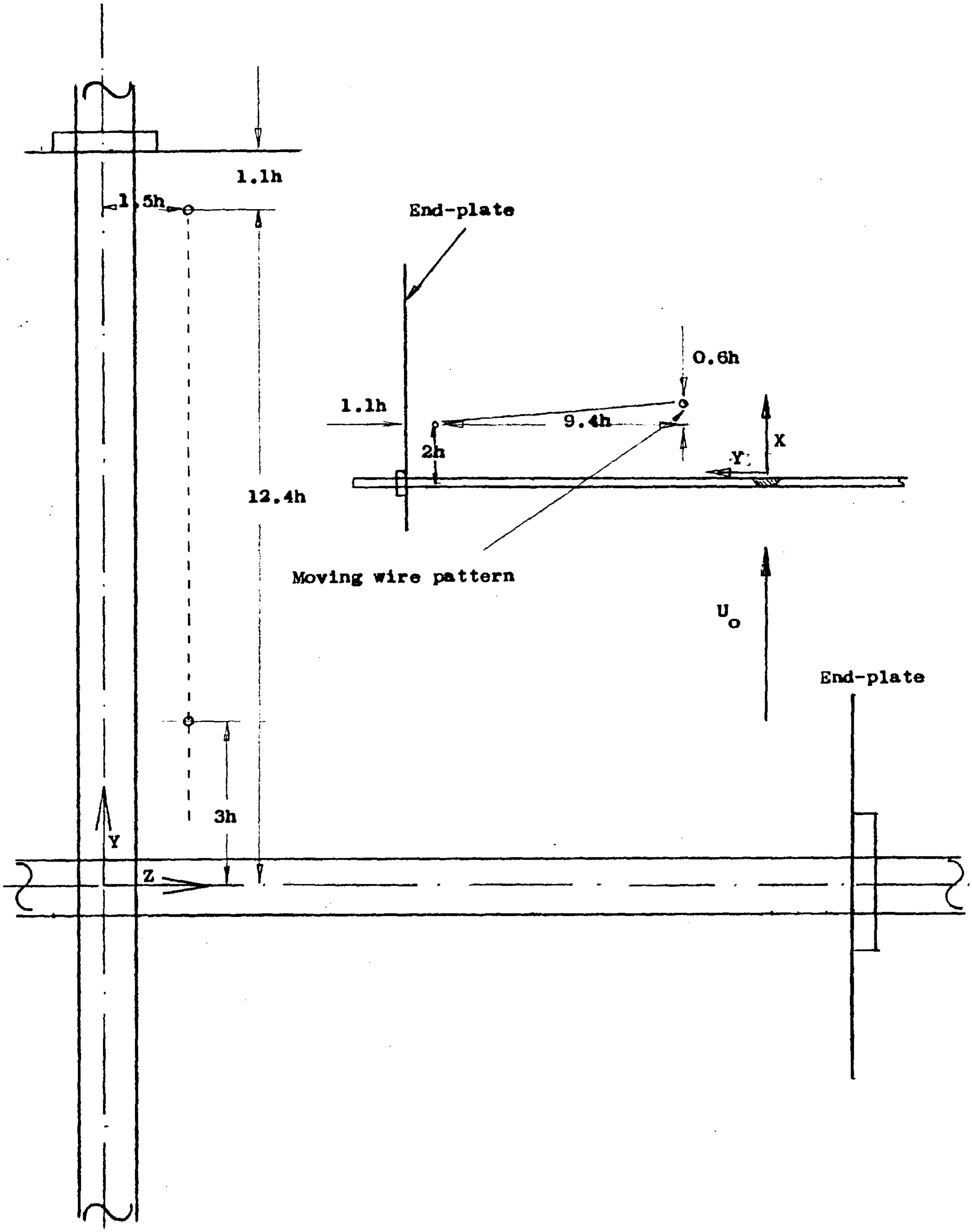

Figure 6.31 Sketch showing Hot-wires position to measure streamwise spacing of the vortices

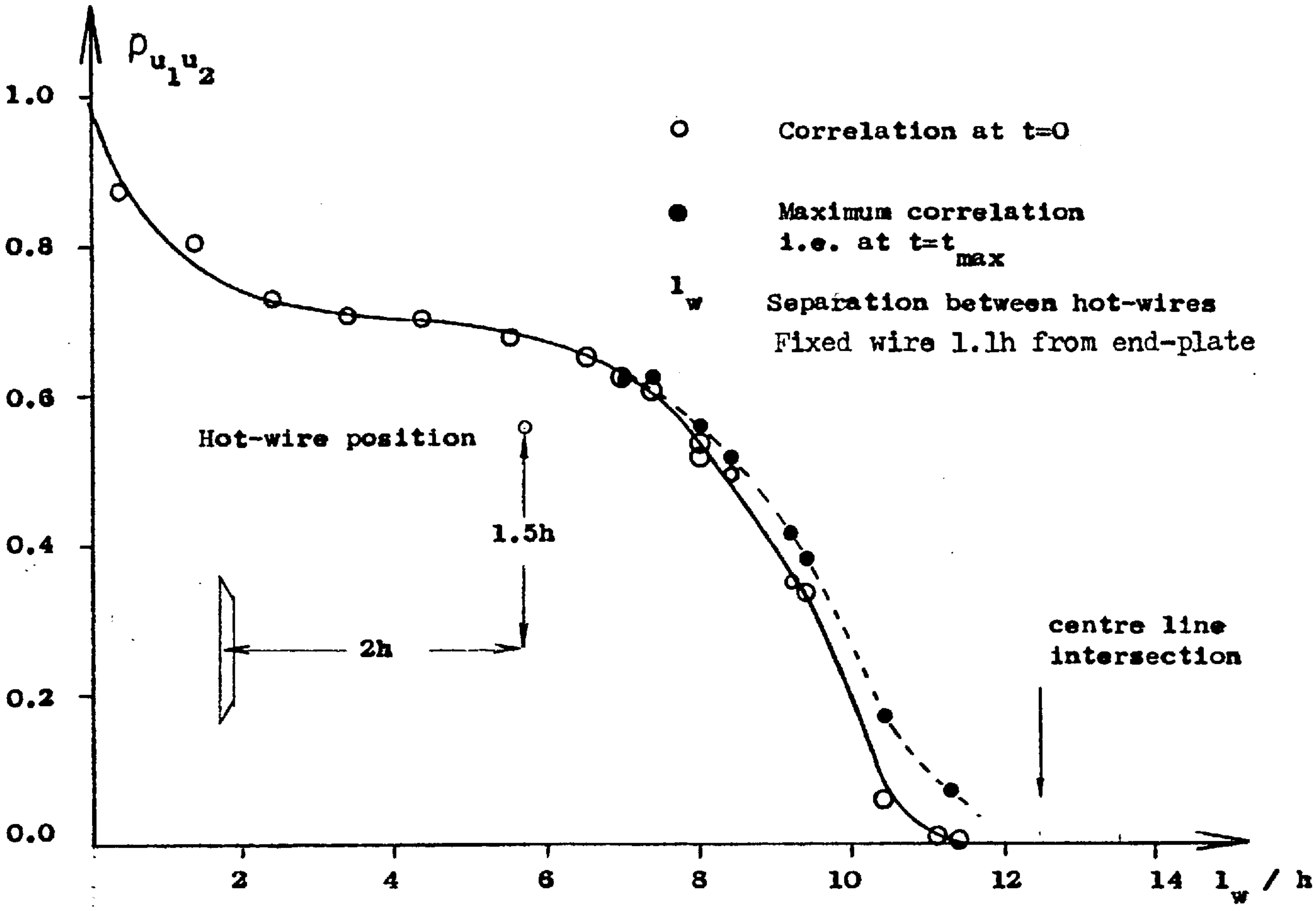

Figure 6.32a Lateral velocity correlation across the Span for intersecting Flat plates (AR = 27)

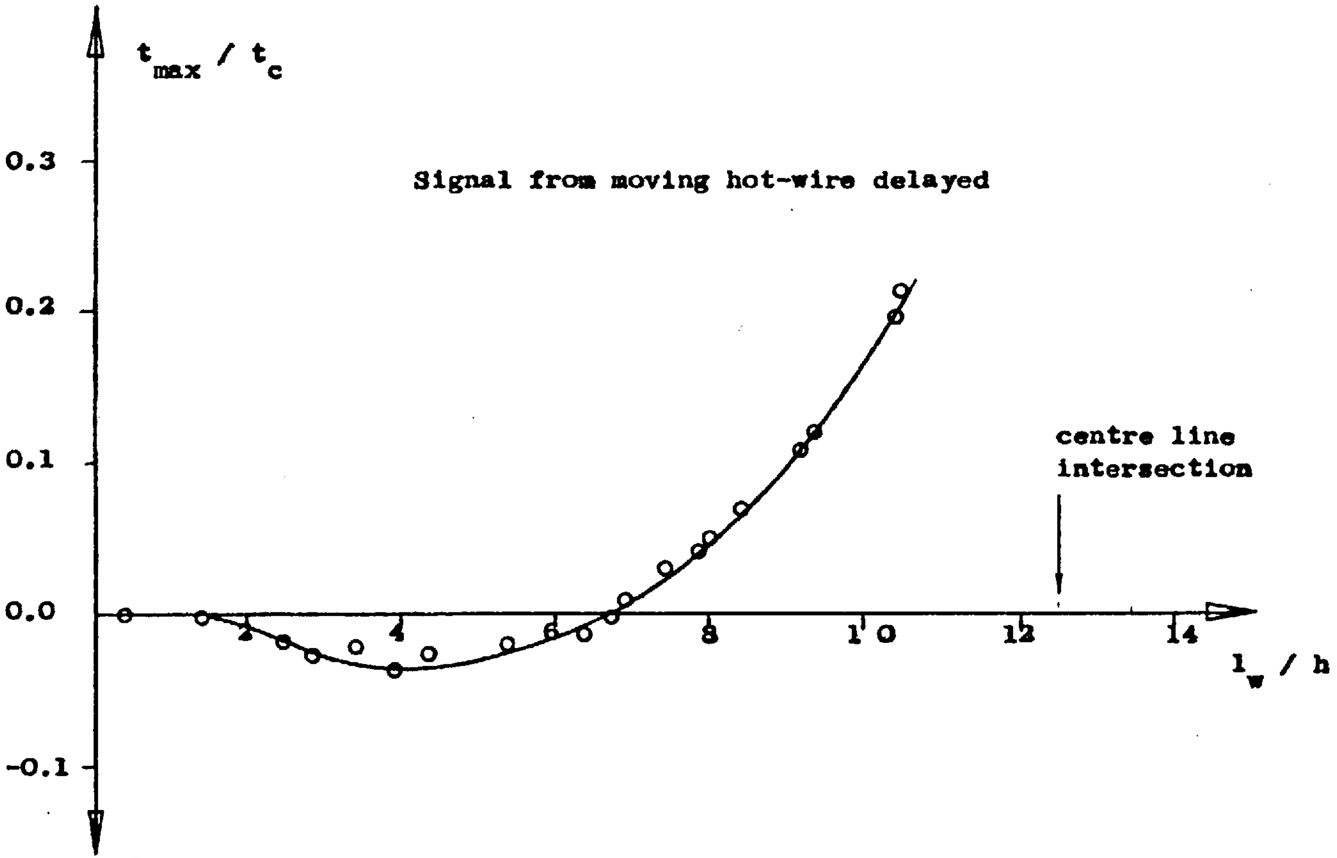

Figure 6.32b Time delay function across the Span for intersecting flat plates (AR = 27)

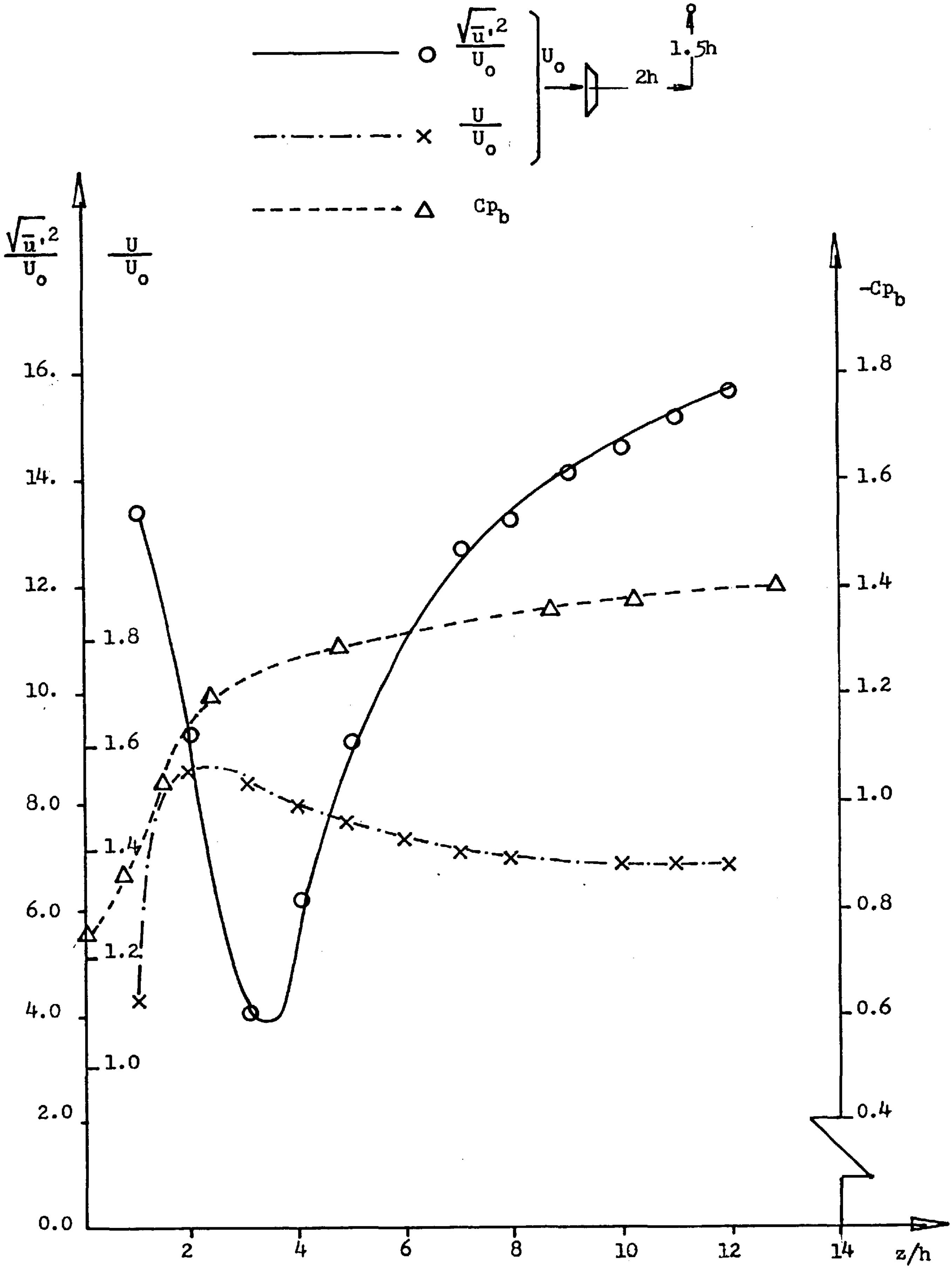

Figure 6.33 Spanwise mean Velocity, Base Pressure and Velocity Fluctuation Distributions for Intersecting Flat Plates.
(AR = 27 in the 0.91m x 0.91m wind tunnel, S/C = 0.051)

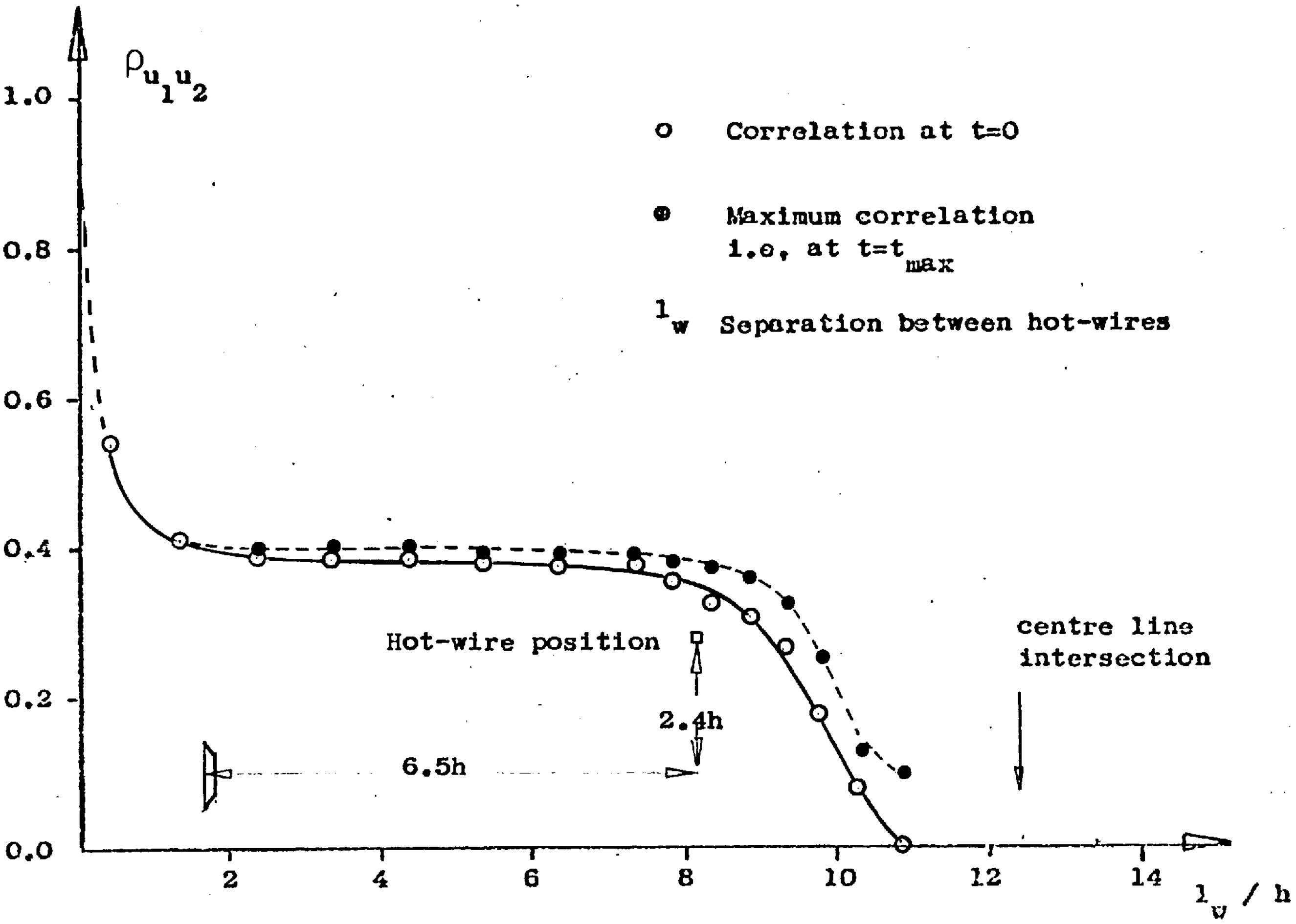

Figure 6.34a Lateral velocity correlation across the Span for Intersecting Flat plates (AR = 27)

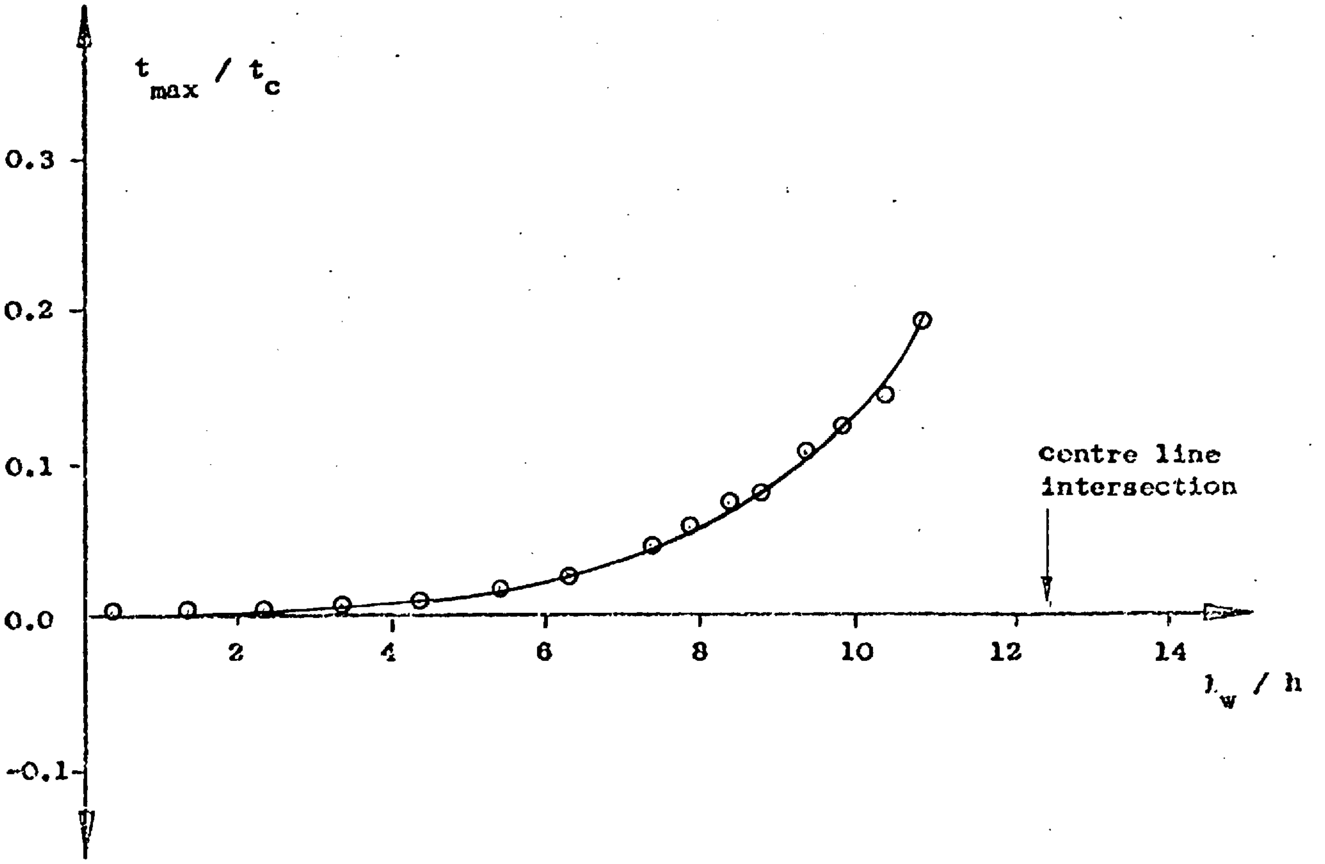

Figure 6.34b Time delay function across the Span for intersecting Flat plates (AR = 27)

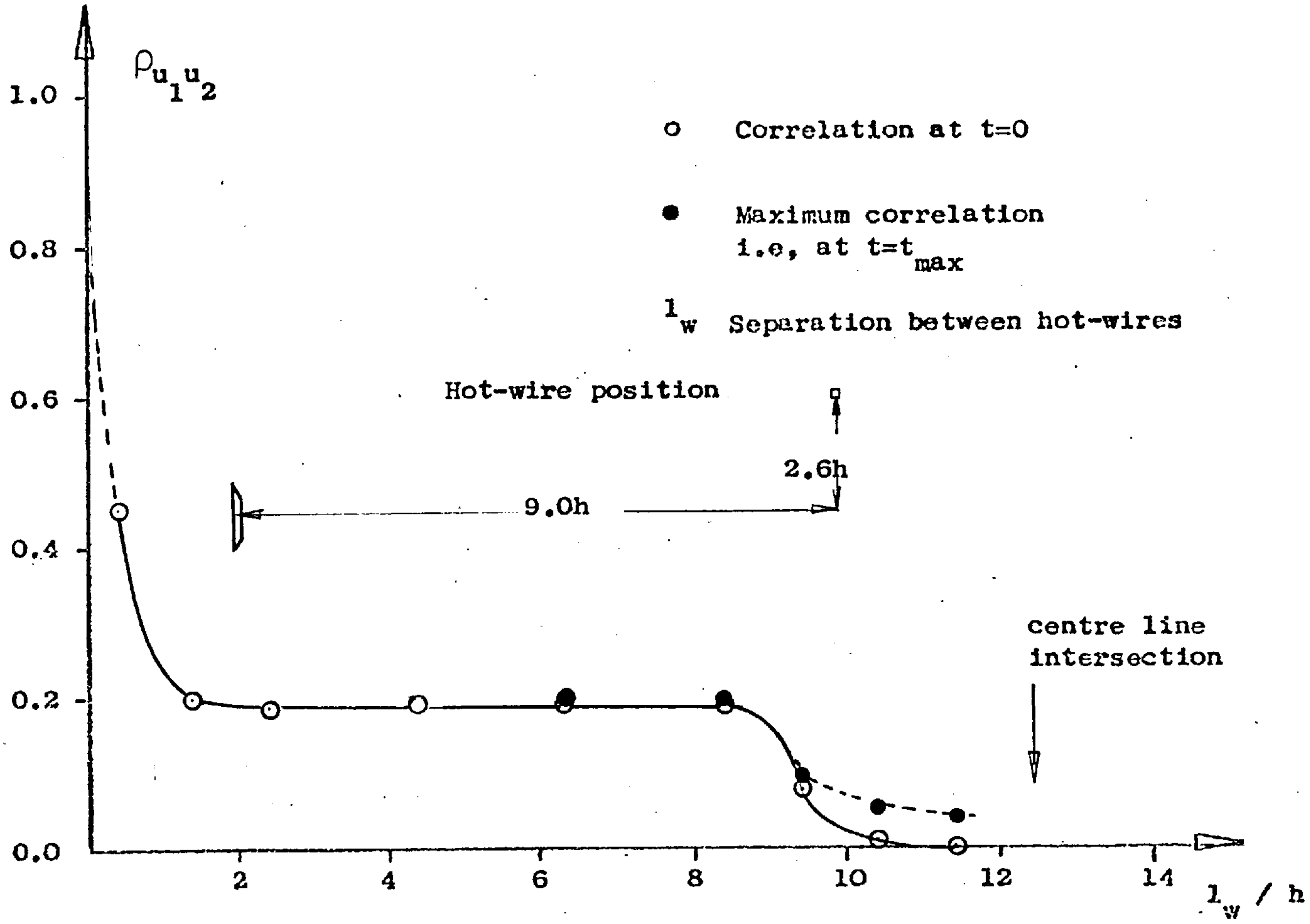

Figure 6.35a Lateral velocity correlation across the Span for Intersecting Flat plates (AR = 27)

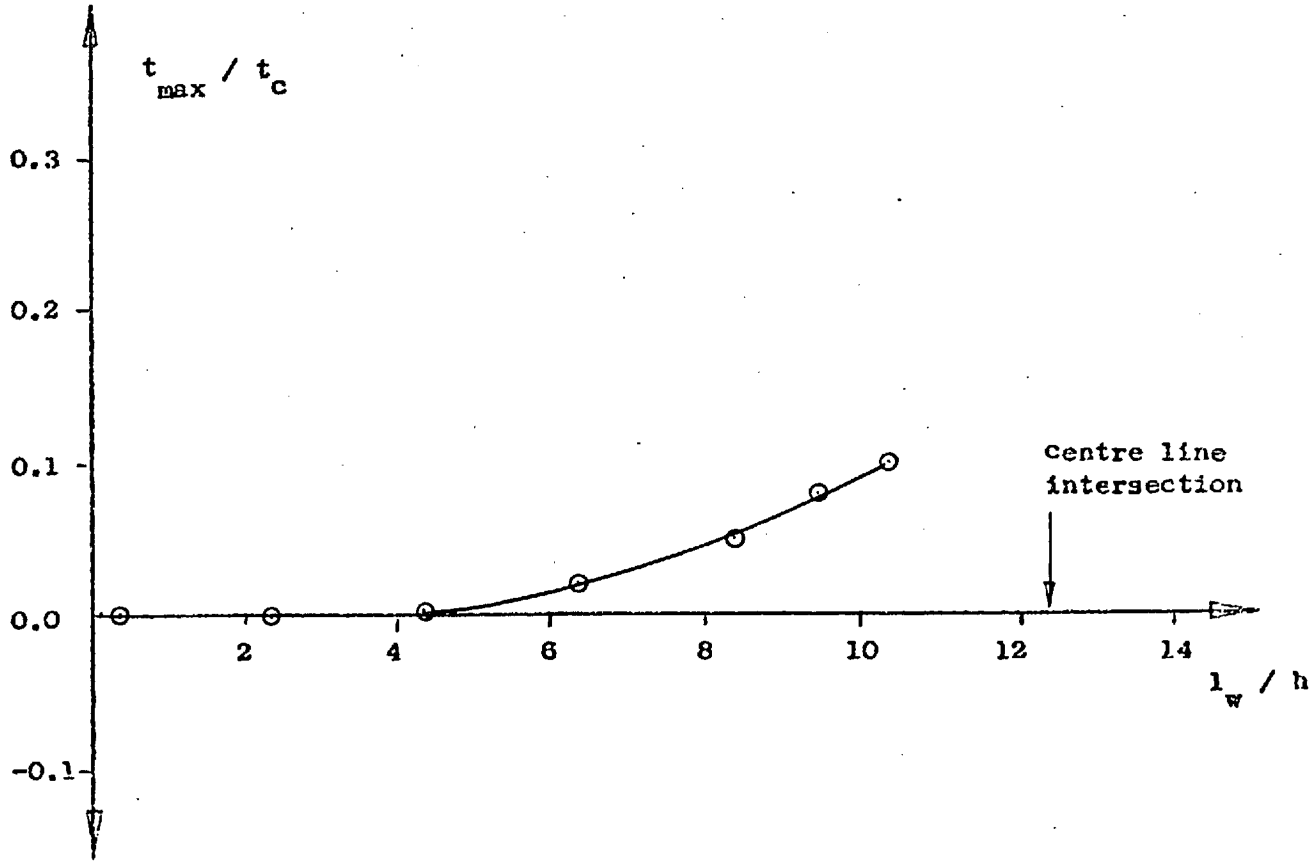

Figure 6.35b Time delay function across the Span for intersecting Flat plates (AR = 27)

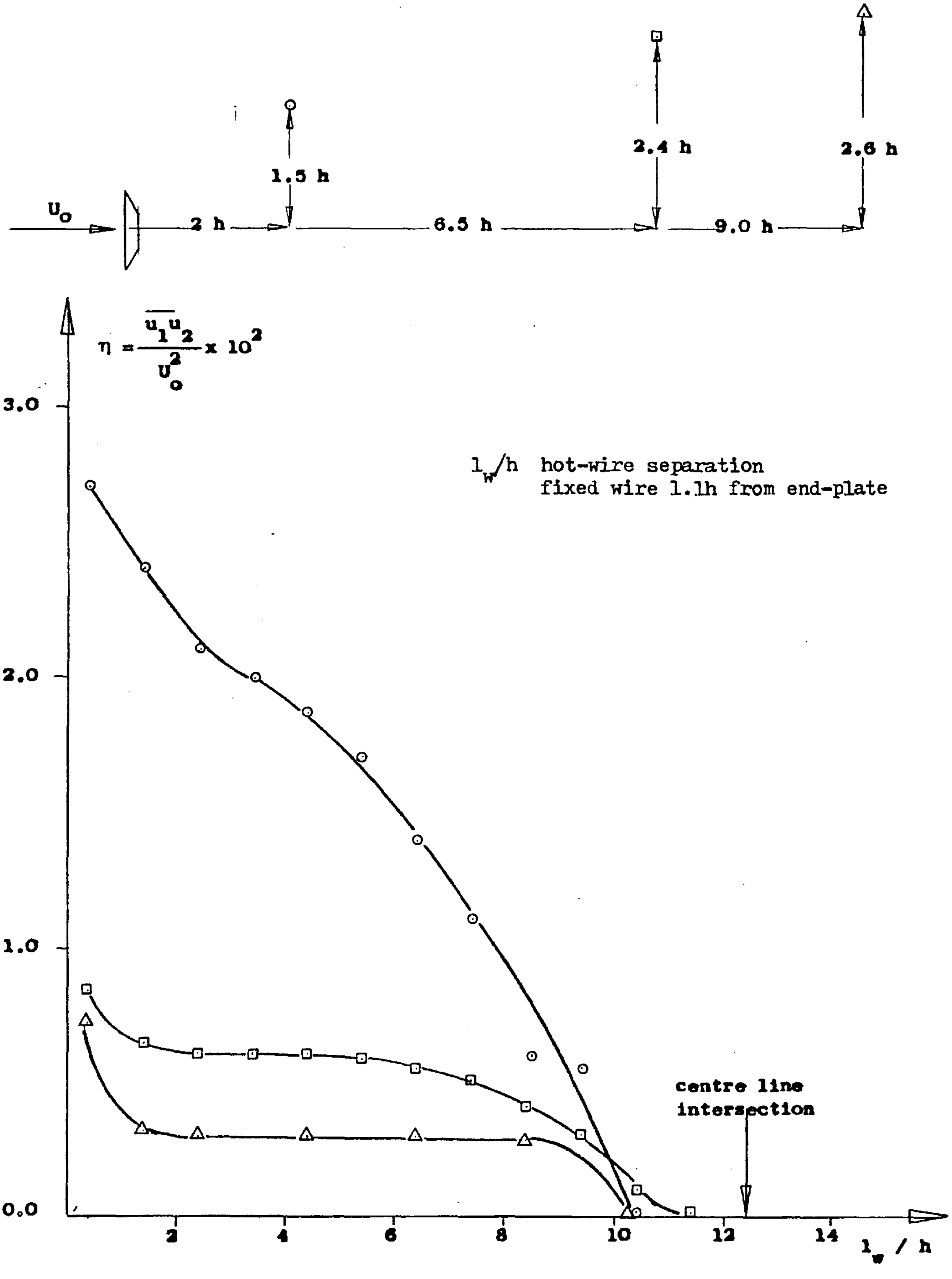

Figure 6.36 Spanwise correlated energy at shedding frequency

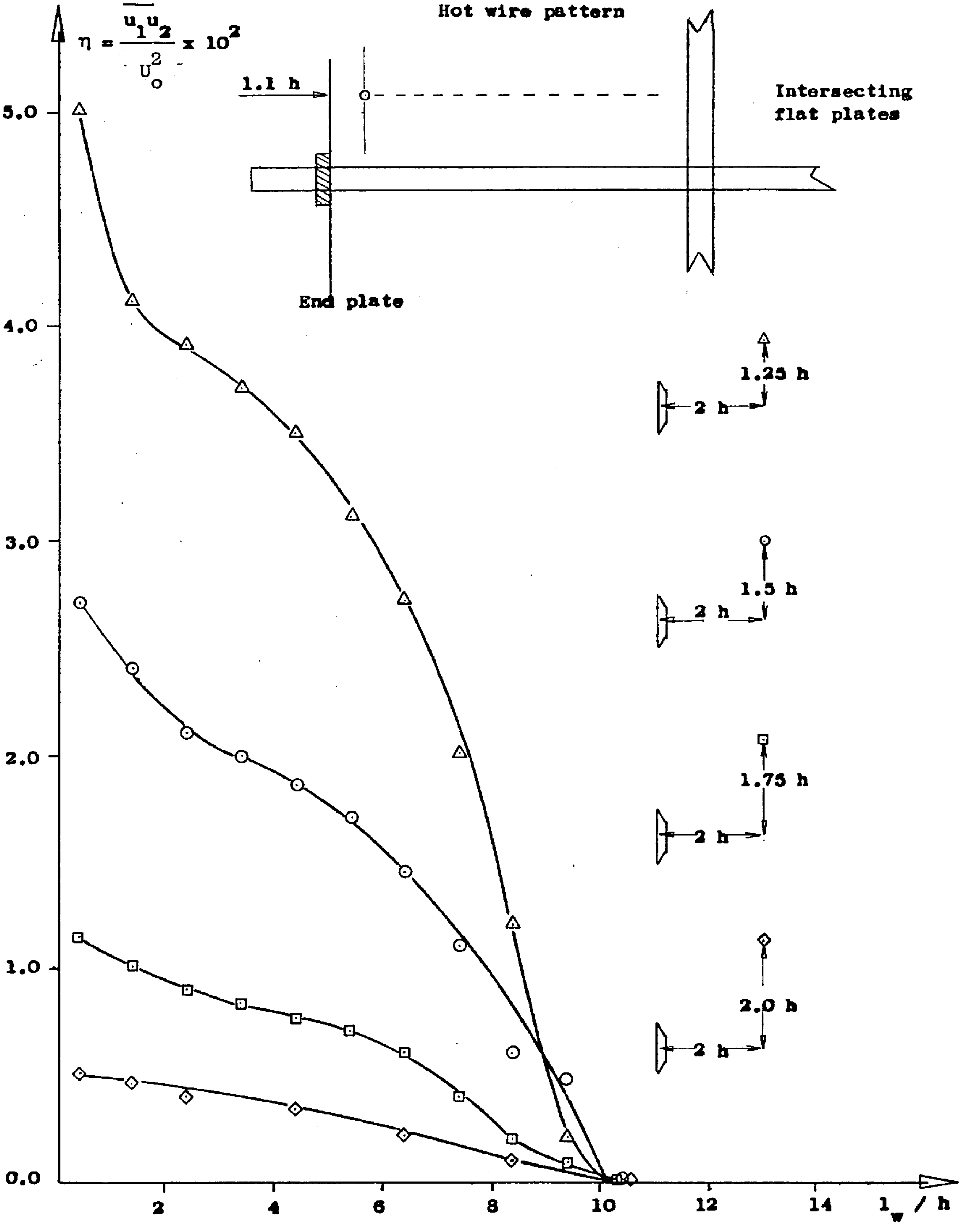

Figure 6.37 Spanwise correlated energy at shedding frequency

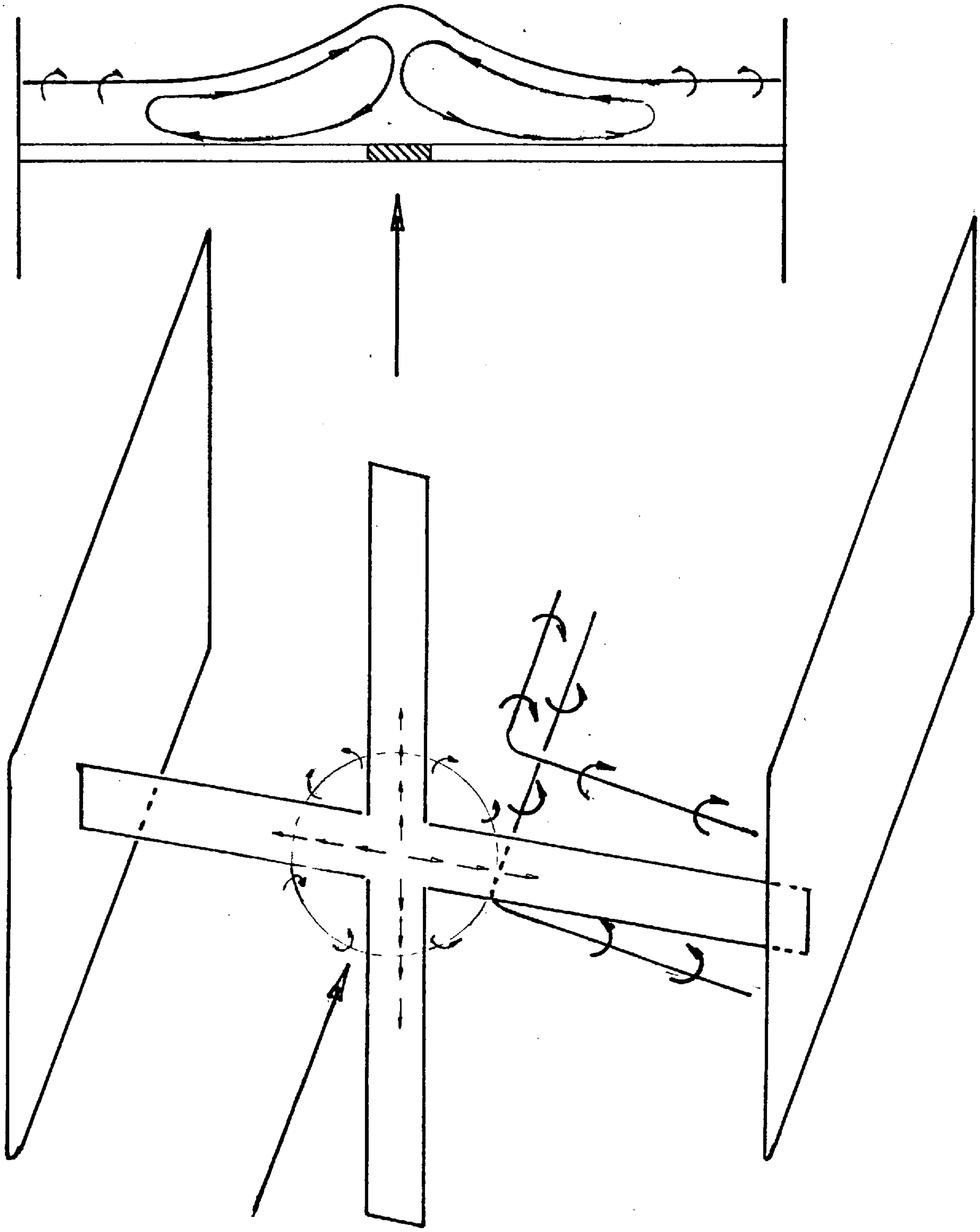

Figure 7.1 Base flow of the intersecting model

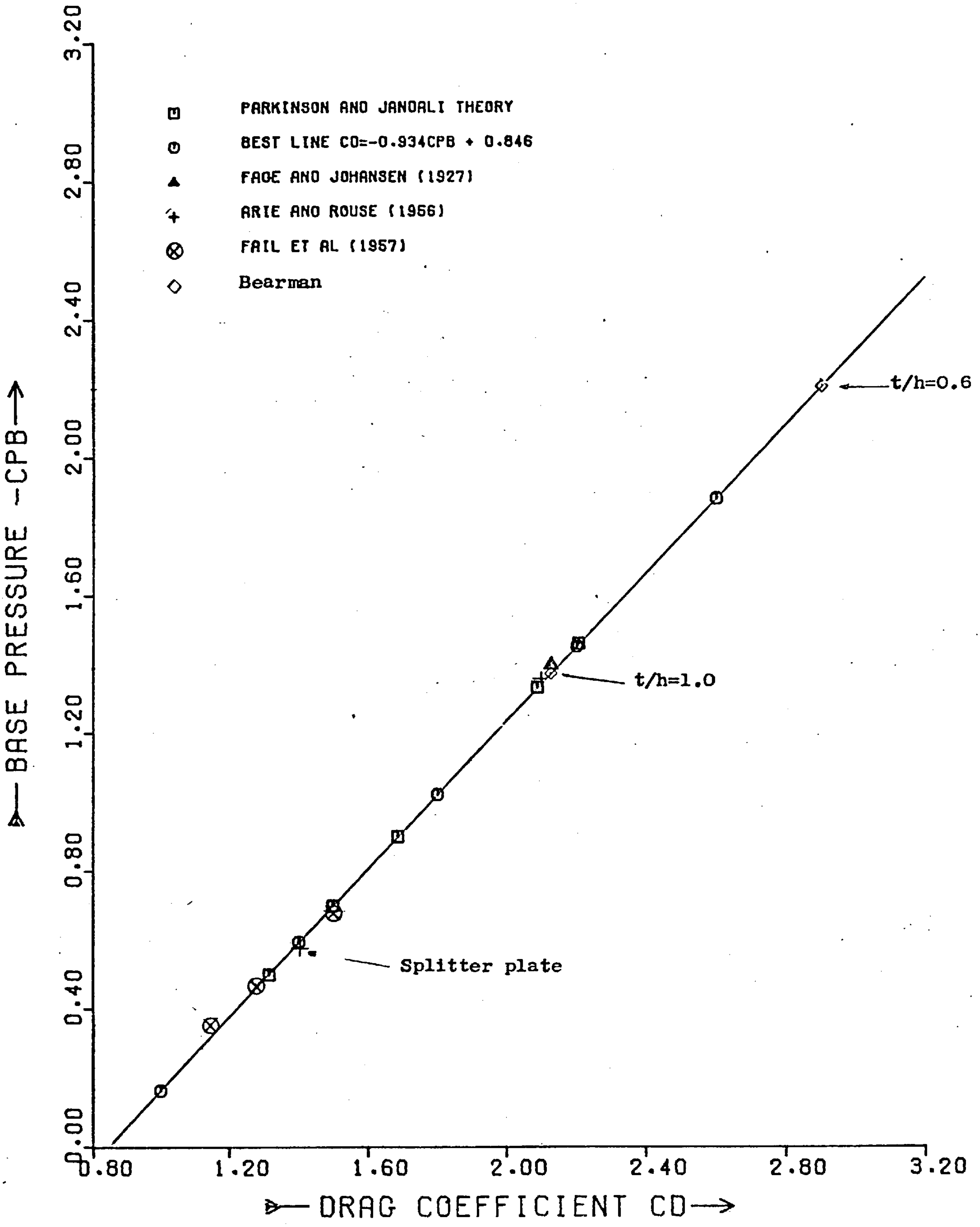

Figure A.1 Base pressure coefficient versus Drag coefficient

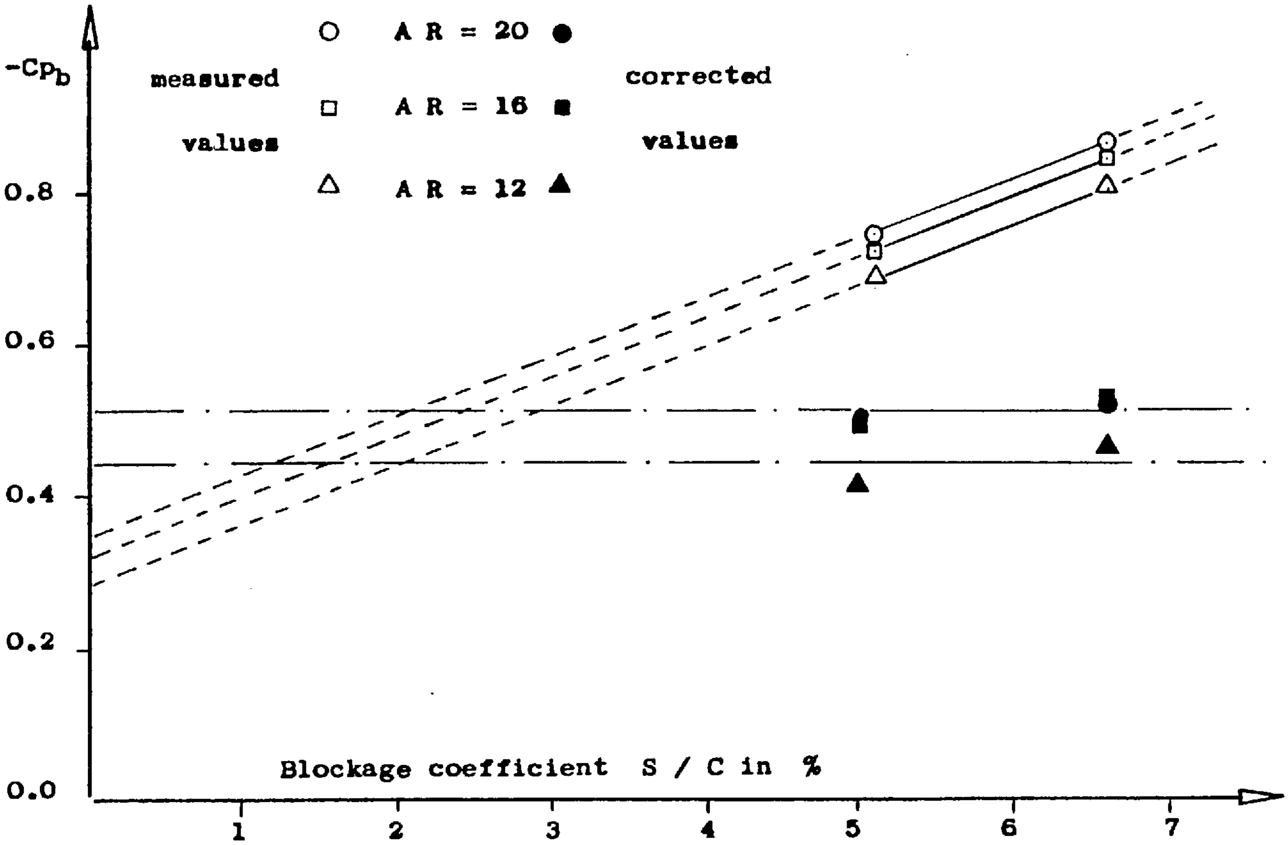

Figure A.2 Maskell's Corrections of the mid-span base pressure for intersecting flat plates (Cp_b of reference taken at mid-intersection)

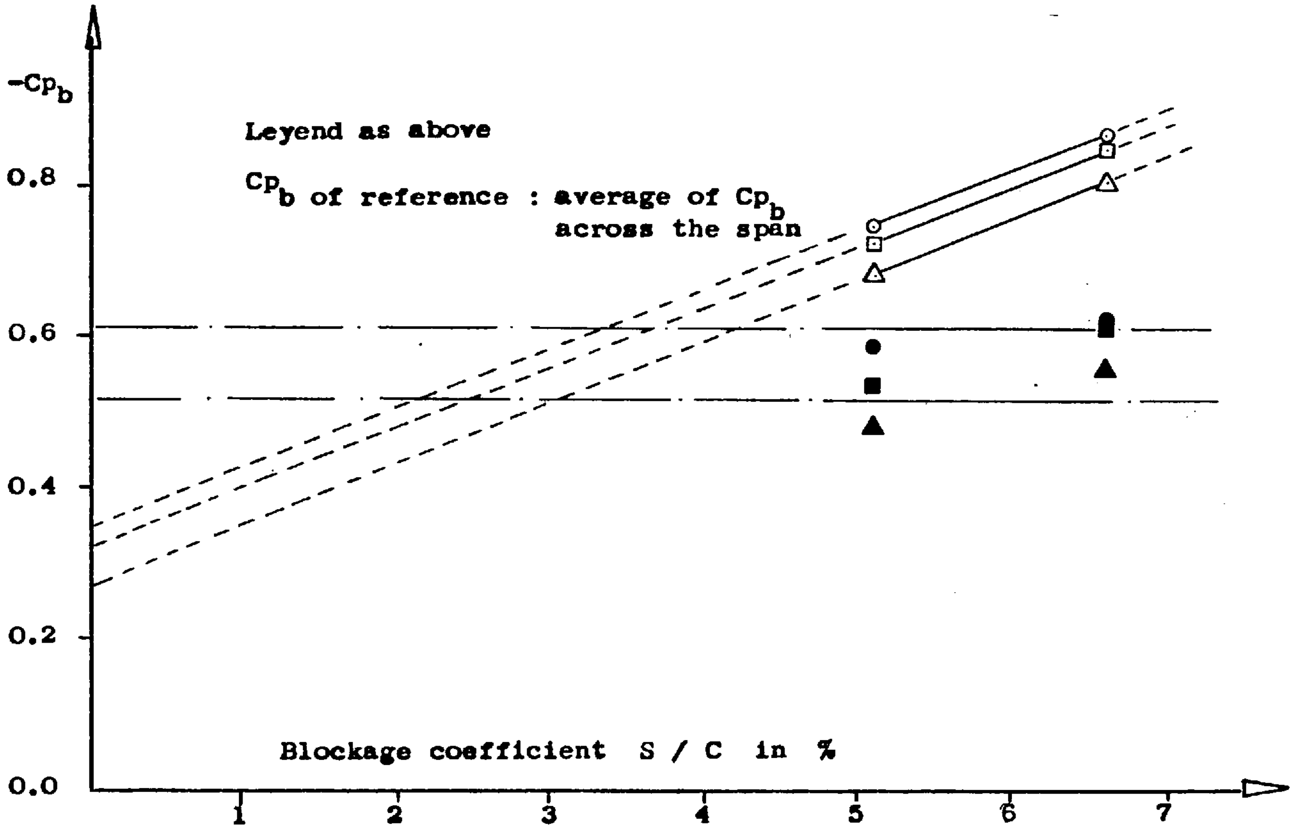

Figure A.3 Maskell's Corrections of the mid-span base pressure for intersecting flat plates

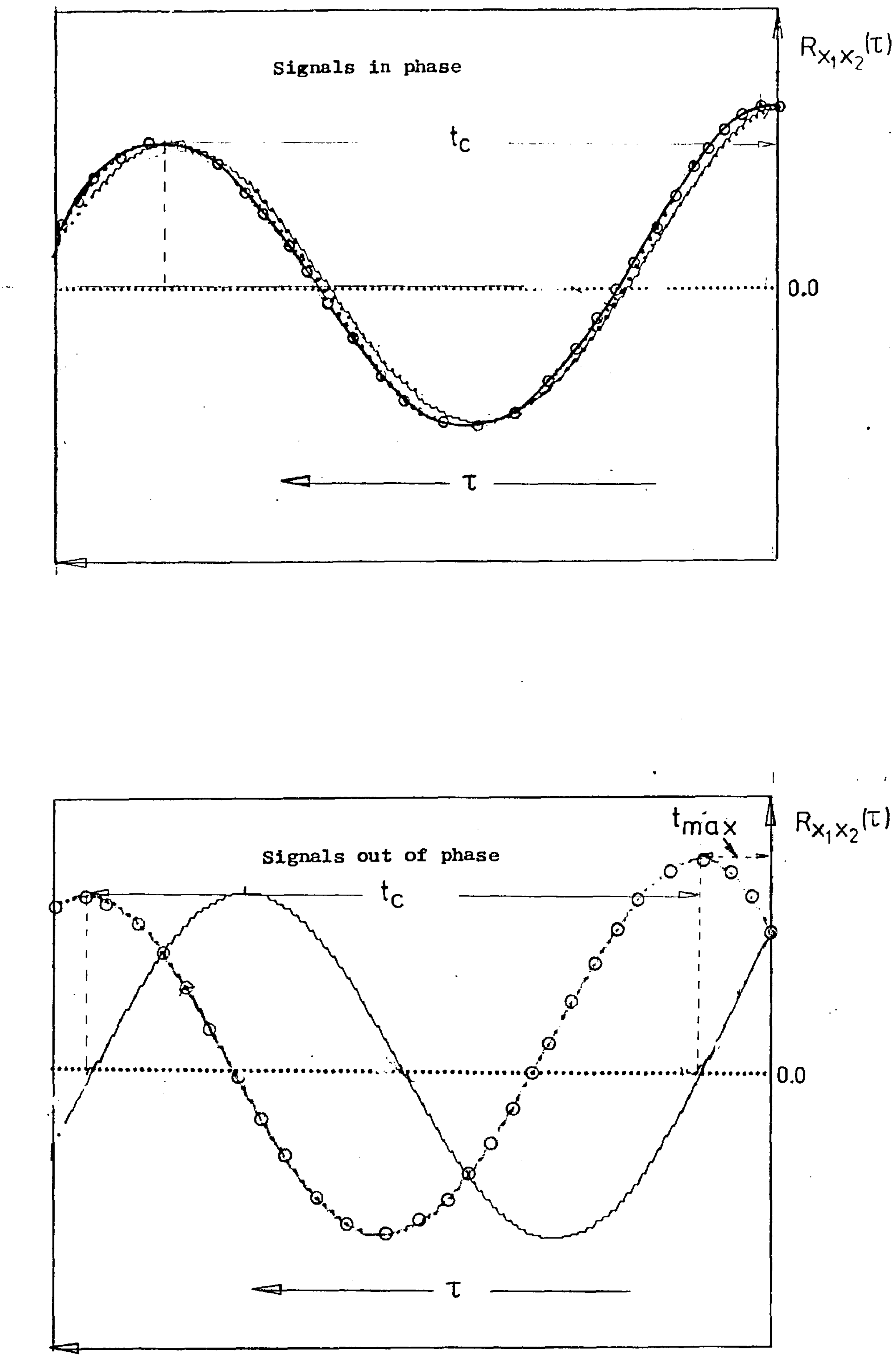

Figure C1. Crosscorrelogram showing phase angle and t_{max}